universitätbonn igg

Institut für
Geodäsie und Geoinformation

Schriftenreihe 14

Akbar Shabanloui

A New Approach for a Kinematic-Dynamic Determination of Low Satellite Orbits Based on GNSS Observations

Akbar Shabanloui • **A New Approach for a Kinematic-Dynamic Determination of Low Satellite Orbits Based on GNSS Observations**

universitätbonn igg

Institut für Geodäsie und Geoinformation

Schriftenreihe **14**

Akbar Shabanloui

A New Approach for a Kinematic-Dynamic Determination of Low Satellite Orbits Based on GNSS Observations

Diese Arbeit wurde am 5. August 2008 als Dissertation zur Erlangung des Grades Doktor-Ingenieur (Dr.-Ing.) der Landwirtschaftlichen Fakultät der Rheinischen Friedrich-Wilhelms-Universität Bonn vorgelegt.

Referent:	Prof. Dr.-Ing. Karl Heinz Ilk
Korreferent:	Prof. Dr.-Ing. Heiner Kuhlmann
Korreferent:	Prof. Dr. Manfred Schneider
Tag mündlichen Prüfung:	17. Oktober 2008

Diese Dissertation ist auf dem Hochschulschriftenserver der ULB Bonn
http://hss.ulb.uni-bonn.de/diss_online
elektronisch und durchgängig mit farbigen Abbildungen publiziert.

Schriftenreihe des Instituts für Geodäsie und Geoinformation
der Rheinischen Friedrich-Wilhelms-Universität Bonn

Herausgeber:
Prof. Dr.-Ing. Wolfgang Förstner
Prof. Dr.-Ing. Karl Heinz Ilk
Prof. Dr.-Ing. Theo Kötter
Prof. Dr.-Ing. Heiner Kuhlmann
Prof. Dr. Lutz Plümer
Prof. Dr. Wolf-Dieter Schuh

Die Aufnahme dieser Arbeit in die Schriftenreihe wurde von den Herausgebern der Reihe geprüft und gemeinsam beschlossen.

Bonn 2008 ISSN 1864-1113

Institut für Geodäsie und Geoinformation der Universität Bonn
Astronomische, Physikalische und Mathematische Geodäsie

A New Approach for a Kinematic-Dynamic Determination of Low Satellite Orbits Based on GNSS Observations

Inaugural–Dissertation zur
Erlangung des akademischen Grades
Doktor–Ingenieur (Dr.–Ing.)
der Hohen Landwirtschaftlichen Fakultät
der Rheinischen Friedrich–Wilhelms–Universität
zu Bonn

vorgelegt am 5. August 2008 von

M.Sc. Akbar Shabanloui
aus Salmas, Iran

D 98

Referent:	Prof. Dr.–Ing. Karl Heinz Ilk
Koreferenten:	Prof. Dr.–Ing. Heiner Kuhlmann
	Prof. Dr. rer. nat. Manfred Schneider
Tag der mündlichen Prüfung:	17. Oktober 2008
Publikation:	Diese Dissertation ist auf dem Hochschulserver der ULB Bonn `http://hss.ulb.uni-bonn.de/diss_online` elektronisch publiziert. (Erscheinungsjahr 2008)

Dedicated to my wonderful parents,
my mother Soghra and my father Najib,
in love and gratitude.

A New Approach for a Kinematic-Dynamic Determination of Low Satellite Orbits Based on GNSS Observations

Summary

A new approach for the integrated kinematical-dynamical orbit determination of low flying satellites based on high-low GPS-SST observations is proposed. These observations are code and carrier phase measurements between a Low Earth Orbiter (LEO) and the satellites of any of the Global Navigation Satellite Systems (GNSS) such as GPS, GLONASS or in future GALILEO. The orbit determination in this investigation is restricted to short arcs. The orbit determination technique is characterized by the fact that the satellite's arcs are represented by a semi-analytical series, consisting of a linear combination of the boundary vectors of the satellite's arc, a linear combination of Euler and Bernoulli polynomials up to a specific upper degree and a sine series up to a properly selected upper summation index. This kind of orbit representation does not only allow to determine arbitrary functionals of the satellite's orbits, such as velocities and accelerations of the satellite, it covers also the possibility to introduce geometrical and kinematical as well as dynamical observables for the determination of the orbit parameters. Furthermore, besides a pure kinematical orbit determination it is possible to introduce dynamical force function restrictions to realize a reduced-kinematical orbit determination – or in case of restricting each free orbit parameter – a pure dynamical orbit determination. The accuracy of the orbit representation depends primarily on the quality of the GPS-SST observation accuracy, the GPS satellite configuration and the number of GPS satellites at every individual observation epoch. The orbit determination approach has been tested based on simulation data sets and with real GPS observations of the satellite CHAMP. The proposed integrated kinematical-dynamical orbit determination opens a wide field of applications such as the orbit determination of satellite formation flight configurations and its application for the Earth system research.

Ein neuer Ansatz zur Bestimmung kinematisch-dynamischer Bahnen niedrig fliegender Satelliten aus GNSS Beobachtungen

Zusammenfassung

Eine neue Methode der integrierten kinematisch-dynamischen Bahnbestimmung von niedrig fliegenden Satelliten aus GPS-SST Beobachtungen wird vorgeschlagen. Diese Beobachtungen sind Code- und Trägerphasenmessungen zwischen dem Low Earth Orbiter (LEO) und den Satelliten eines der Global Navigation Satellite Systems (GNSS), wie beispielsweise GPS, GLONASS oder in Zukunft GALILEO. Die Bahnbestimmung in dieser Untersuchung ist begrenzt auf kurze Bahnen. Die Bahnbestimmungsmethode ist dadurch gekennzeichnet, dass die Satellitenbögen durch einen halb-analytischen Ansatz dargestellt werden, bestehend aus der Linearkombination der Randvektoren des Satellitenbogens, einer Linearkombination von Euler- und Bernoulli-Polynomen bis zu einem speziellen Grad und einer Sinusreihe bis zu einem geeignet gewählten oberen Summationsindex. Diese Art der Bahndarstellung erlaubt nicht nur, die Berechnung von beliebigen Funktionalen der Satellitenbahnen abzuleiten, wie Geschwindigkeiten und Beschleunigungen des Satelliten, sie ermöglicht auch die Nutzung geometrischer, kinematischer wie auch dynamischer Beobachtungstypen zur Bestimmung der Bahnparameter. Überdies ist es möglich, neben einer reinen kinematischen Bahnbestimmung dynamische Bedingungen der Kräftefunktion einzuführen und auf diese Weise eine reduziert-kinematische Bahnbestimmung zu realisieren – oder im Falle der Einführung von dynamischen Bedingungen für sämtliche freie Bahnparameter – eine reine dynamische Bahnbestimmung. Die Genauigkeit der Bahndarstellung hängt vor allem von der Genauigkeit der GPS-SST- Beobachtungen, der GPS Satellitenkonfiguration und der Zahl der GPS-Satelliten zu den einzelnen Beobachtungszeitpunkten ab. Die Bahnbestimmungsmethode wurde am Beispiel von simulierten Datensätzen aber auch mit realen Beobachtungen des Satelliten CHAMP getestet. Die vorgeschlagene Methode der integrierten kinematisch-dynamischen Bahnbestimmung öffnet ein weites Feld von Anwendungen, wie beispielsweise die Berechnung von Bahnen von Satelliten-Formationsflug-Konfigurationen und die Nutzung dieser Satellitenmissionen für die Erdsystemforschung.

Contents

1. Introduction

1.1 Orbit Determination (OD)

The development of orbit determination techniques especially for the bodies of our Solar System was one of the main topics of research during the last two centuries. Famous astronomers, physicists and mathematicians such as Gauss, Legendre, Lagrange and later Poincaré contributed significantly to the development and the progress of these techniques. This was also the time when many problems of Celestial Mechanics initiated the development of new mathematical methods. Only one example, important especially for the geodetic sciences, was the development of the least squares adjustment technique by Carl Friedrich Gauss as important numerical method to treat erroneous observations especially for the determination of the orbit of the planetoid Ceres. Within these two centuries, an overwhelming number of publications related to various questions of Celestial Mechanics and of the orbit determination problem of multi-body systems have been published.

Astronomy played an important role within Geodesy from the very beginning when it started to be a scientific discipline. All those observation and processing techniques which were necessary to derive geodetic latitudes, longitudes and azimuths are summarized within the knowledge domain "Geodetic Astronomy". These geodetic elements are used to orientate geodetic networks and to determine the figure of the Earth and the dimensions of best-fitting or of mean Earth ellipsoids. The techniques of "Astronomical Geodesy" developed to a high standard had been applied to derive reference ellipsoids for a subsequent mapping such as the International Ellipsoid, Hayford's ellipsoid, Bessel's ellipsoid or Clarke's ellipsoids. These ellipsoids are still important today as elements of geodetic datum systems and represent the basic fundaments of various worldwide mapping products.

Nevertheless, these techniques lost continuously their importance during the last fifty years since 1957 when the first artificial satellite Sputnik I was launched. This was the moment when "Satellite Geodesy" started to become one of the most important disciplines within Geodesy. During these five decades the determination of the orbits of artificial satellites became an extremely important task for geodetic research. Indeed the determination of precise orbits is the important pre-requisite for the determination of gravity field models and the geoid indispensable in Geodesy and many other Geo-disciplines but also for the determination of precise positions and the definition of celestial and terrestrial reference frames. Based on the principle techniques developed within Celestial Mechanics, the development of precise orbit determination methods for artificial satellites started and numerous articles have been published on this topic during these past five decades. Because of the decade-long tradition of Celestial Mechanics, the specific focus of the determination of orbits changed and with it also the terminology of the different orbit determination techniques. Nowadays, the various methods can be characterized based on different criteria. One of these criteria is related to the purpose of the orbit we want to determine. If we need a first impression of the orbit to derive, e.g., initial or boundary values as starting values for an orbit improvement procedure then we have to perform a ***preliminary orbit determination***. If we want to determine an orbit which fits the observations in the best possible way then we have to improve not only the various constituents of the force function model in the equation of motion and the determination quantities (initial or boundary values) but it is also necessary to correct the observations based on a proper stochastic model such that the residuals are minimized with respect to a specific norm. This procedural method of ***differential orbit improvement*** results in a final ***definitive orbit determination***. Indeed this is the procedure which is applied to improve gravity field parameters or parameters of any other force function constituents.

Another classification of the various orbit determination techniques with respect to the kind of orbit models is proposed by G. Beutler (Beutler 2005). He distinguishes ***kinematic methods*** which do not make use of any force function models and ***dynamic methods*** which require a specific force function model. In the first case the orbits are represented by a table of satellite positions where the table's spacing is defined by the measurement rate, in general by the measurement rate of the on-board GNSS (Global Navigation Satellite System) receiver. The result is a point-wise empirical representation of the orbit and a satellite-related

equivalent to the so-called kinematical positioning by GNSS. In the second case, the initial or boundary values of the satellite arcs are determined, or improved if they are approximately known from a preliminary orbit determination, so that a best fit to the observations is achieved. The notation "best fit" means usually a best fit in the sense of least squares, but also other norms are possible. The dynamical orbit determination is possible either numerically by any numerical integration method or analytically. The dynamical orbit can be represented in principle by an arbitrarily dense sequence of point positions (and velocities) or by an analytical expression. But it should be pointed out that the analytical solutions are possible only for specific cases and only at a certain level of approximation. In addition to the kinematic and the dynamic orbit determination technique, Beutler also introduced a further type of methods called ***reduced dynamic methods*** which lie somewhere in between the kinematic and purely dynamic methods. This group of methods is characterized by the fact that additionally to the parameters of the dynamic methods stochastic parameters of various types are introduced after a couple of minutes along the orbit. In this way the total orbit is divided into short arcs with different continuity properties at the arc boundaries, depending on the type of stochastic parameters. There are various articles which demonstrate the advantages of this method (e.g. Beutler et al. 2006, Jäggi et al. 2006).

We will modify this terminology of orbit determination techniques slightly, adapting the real meaning of the notation "kinematics" in physics, which is defined as the theory of the motion of mass points and closely related to terms such as velocity and acceleration. Therefore, if the orbit is determined point-wise by GNSS analysis techniques then we consider this determination of satellite position ephemerides as ***geometric orbit determination***. There is no connection between subsequent positions, and consequently, no information about the velocity or even the acceleration of the satellite. To describe the time dependency of the motion of a satellite, it is necessary to provide a properly constructed function which consistently connects positions, velocities and accelerations. Such a function can be a represented by an interpolation function or a function derived from the table of positions by a sophisticated approximation method. From these functions, velocities and accelerations can be derived consistently by numerical or analytical differentiation. With such a function, the kinematics of the satellite's motion is given. Because of the importance of these orbit representations we will define those methods which are directed to the determination of precise kinematical orbits by any approximation functions as ***kinematic orbit determination***. We would like to point out that no dynamic force model is used at all. The kinematic orbit is represented by a sufficient number of approximation parameters, including the initial or boundary values of the arc. These parameters are determined such that the observations are approximated in the best possible way with respect to a properly selected norm for the residuals. In this research, the kinematical orbit is, in principle, a solution of the equation of motion of the satellite. If the kinematical parameters are determined by a best fitting process based on the observations then we perform a kinematical orbit determination, if the parameters are determined by a model of the force function then we perform a dynamical orbit determination. Therefore, the ***dynamic orbit determination*** based on a dynamical model corresponds to Beutler's definition. There is also the possibility to use certain constraints based on the dynamical force function model. In this case, we come up with a ***reduced kinematical orbit determination*** of a specific level. It will be explained later in detail, that this formulation of the orbit determination problem allows a smooth transition from a kinematical orbit determination to a dynamical orbit determination. In the first case, the orbit parameters are determined without the force function information and in the second case, all parameters are functionals of the force function model.

1.2 Satellite Orbits in Satellite Geodesy

1.2.1 Mathematical-Physical Model of a Satellite's Motion

The three-dimensional motion of artificial satellites is caused by the various constituents of the force function acting on the satellite. In the following, we will consider only the free-fall motion of artificial satellites. This free-fall can be generated also by a compensation mechanism where the (non-gravitational) surface forces are transformed into active thruster accelerations by a specific feedback system to produce a pure

gravitational free-fall motion of the satellite. Forces acting on an artificial satellite can be volume forces such as gravitational forces which act on the mass elements of the satellite or surface forces such as atmospheric drag or solar radiation pressure which act on the surface elements of the satellites. This is the reason that the geometry of the satellite must be known up to a certain level of approximation. The total of all surface and volume forces causes a three-dimensional motion of the satellite in space.

The three-dimensional motion of a satellite can be separated in a translational motion of the mass center of the satellite and a rotation around this center of mass. The translational motion is described by the balance equation of the linear impulse and in case of a constant satellite mass by the equation of motion. The rotational motion is described by the balance equation of linear momentum or by Euler's equation of rotation in case of a rigid body with constant tensor of inertia. In Satellite Geodesy, only the translational motion of the artificial satellite is of importance; the rotation of satellites in space is treated within the so-called satellite attitude control and important for astrodynamics. The analysis of the rotational motion for geodetic purpose is of minor importance, therefore, the rotational effects are not considered here within the context of the orbit determination problem. Because of the fact that the gravitational force and the gravitational torque generated by the gravitational interaction of the satellite and the Earth are derived from the gravitational energy of mutual gravitational interaction of both bodies, the translation and the rotation are coupled (Ilk 1983a). But the coupling effects are very small because of the small size of the satellite with respect to the Earth dimensions; therefore it will be disregarded for orbit determination problems in this research.

There are various formulations in Classical Theoretical Mechanics to formulate the equations of motion of satellites, Newton's classical formulation, Lagrange's formalism or the Hamilton formalism. For the present applications Newton-Euler's equation of motion is sufficient as basic physical-mathematical formulation of the satellite's translational motion.

1.2.2 The Classical Techniques of Satellite Geodesy

The classical techniques of Satellite Geodesy are based on the use of satellites as high targets, as test bodies following the force functions acting on the satellites and as platforms carrying sensors to detect various features of the Earth system by remote sensing techniques. A combination of these techniques enables the recovery of the gravity field of the Earth together with very precise three-dimensional coordinates of selected observation stations but also area covering features of the Earth surface such as the sea surface and the topography at the continents. In most of these applications, the precise determination of satellite orbits plays a decisive role. We will give a short review of the development during the last decade and demonstrate that the high precision of the GNSS positioning and the innovative satellite technology led to a change of paradigm in geodetic applications, especially for the determination of gravity field models and here with regard to the orbit determination problem.

The determination of the gravitational field and of selected position coordinates by using the satellites as test masses can be performed by a definitive orbit determination procedure which is based on the classical (in most cases non-relativistic) Newton-Euler formalism,

$$\frac{d}{dt}\mathbf{p}(t) = \frac{1}{m}\mathbf{K}(\mathbf{r}, \dot{\mathbf{r}}; t) \qquad \rightarrow \qquad \ddot{\mathbf{r}} = \mathbf{a}, \tag{1.1}$$

with the force function $\mathbf{K}(\mathbf{r}, \dot{\mathbf{r}}; t)$ or the specific force function $\mathbf{a}$, the position $\mathbf{r}$, velocity $\dot{\mathbf{r}}$ and the acceleration $\ddot{\mathbf{r}}$ vectors as well as the linear momentum $\mathbf{p}$. To determine the parameters of the force function model and the determination quantities of the equation of motion (initial or boundary vectors of the satellite's arc) based on various types of observations of the satellite, a numerical as well as an analytical perturbation strategy has been applied, frequently in a complementary way.

The ***numerical perturbation concept*** can be characterized by the definitive orbit determination process where differential corrections to the various observed or unknown parameters are determined numerically. It is based on the basic geometric relation,

$$\mathbf{r}_i(t) = \mathbf{R}_{li}(t) + \mathbf{R}_l(t), \tag{1.2}$$

with the geocentric position vector $\mathbf{r}_i(t)$ to the satellite i, the topocentric position vector $\mathbf{R}_{li}(t)$, referred to the terrestrial observation station l and the station vector $\mathbf{R}_l(t)$. This equation represents the observation model which reads for a specific observation time t_k after inserting the observations $\bar{\mathbf{b}}_i$ (ranges, direction elements, etc.), the approximate values for the (unknown) station coordinates $\mathbf{x}_S^0$, the respective residuals $d\mathbf{b}_i$ and corrections to the station coordinates $d\mathbf{x}_S$,

$$\mathbf{r}_i(t_k) = \mathbf{R}_{li}\left(t_k; \bar{\mathbf{b}}_i + d\mathbf{b}_i\right) + \mathbf{R}_l\left(t_k; \mathbf{x}_S^0 + d\mathbf{x}_S\right). \tag{1.3}$$

The orbit model is based on Newton-Euler's equation,

$$\ddot{\mathbf{r}}_i(t) = \mathbf{a}_F(t; \mathbf{x}_F) + \mathbf{a}_D(t; \mathbf{x}_i), \tag{1.4}$$

where the specific force function is composed of the Earth-related specific force function $\mathbf{a}_F(t; \mathbf{x}_F)$ with the parameters $\mathbf{x}_F$ and the orbit-related specific disturbance forces $\mathbf{a}_D(t; \mathbf{x}_i)$ with the corresponding model parameters $\mathbf{x}_i$. This equation has to be integrated twice based on the initial values α_i^0 for the orbit i, so that the non-linear model results in

$$\mathbf{r}_i(t_k; \alpha_i^0 + d\alpha_i, \mathbf{x}_i^0 + d\mathbf{x}_i, \mathbf{x}_F^0 + d\mathbf{x}_F) = \mathbf{r}_i(t_k, \bar{\mathbf{b}}_i + d\mathbf{b}_i, \mathbf{x}_S^0 + d\mathbf{x}_S). \tag{1.5}$$

This equation has to be linearized in the usual way, building a so-called mixed adjustment model. The partial differentials are determined numerically by integrating the variational equations or by approximating the partial differentials by partial differences. Obviously, this model requires satellite arcs of sufficient lengths because of two reasons: On the one hand, the coverage of the satellite arcs with observations was very poor in the past compared to the situation nowadays. Therefore, to achieve a sufficient redundancy it was necessary to use medium or long arcs. On the other hand, to cover the characteristic periodic and secular disturbances caused by the small corrections to the approximate force function parameters it was necessary - at least useful - to use medium or long satellite arcs as well.

This fact becomes even more visible by having a closer look at the analytical perturbation strategy. The explicit Lagrange's perturbation equations expressed by classical Keplerian elements $a, i, e, \Omega\ \omega, \nu$ and the disturbing potential R read e.g. for the orbit inclination i (do not mix it up with the orbit number) and the right ascension of the ascending node, Ω, (e.g. Kaula 2000)

$$\begin{aligned}
\frac{di}{dt} &= \frac{1}{na^2\sqrt{1-e^2}\sin i}\left(\cos i\frac{\partial R}{\partial \omega} - \frac{\partial R}{\partial \Omega}\right), \\
\frac{d\Omega}{dt} &= \frac{1}{na^2\sqrt{1-e^2}\sin i}\frac{\partial R}{\partial i}.
\end{aligned} \tag{1.6}$$

Inserting Kaula's expansions of the disturbing function in terms of the Keplerian elements leads to the famous Kaula's perturbation equations,

$$\begin{aligned}
\frac{di}{dt} &= \sum_{n,m,p,q} GM_\otimes a_\otimes^n \frac{F_{nmp}G_{npq}S'_{nmpq}}{\sqrt{GM_\otimes a\,(1-e^2)}a^{n+1}\sin i}\big((n-2p)\cos i - m\big), \\
\frac{d\Omega}{dt} &= \sum_{n,m,p,q} GM_\otimes a_\otimes^n \frac{\partial F_{nmp}/\partial i\, G_{npq}S_{nmpq}}{\sqrt{GM_\otimes a\,(1-e^2)}a^{n+1}\sin i},
\end{aligned} \tag{1.7}$$

with the inclination function F_{nmp}, the excentricity function G_{npq}, etc. (refer to Kaula 2000, for an explanation of additional quantities). It becomes obvious that the secular effects and the various periodicities can be detected only with arcs of sufficient length which are able to cover these typical disturbance patterns of the Keplerian elements. As typical effects, we only want to mention the dependencies of the rotation of the nodal line of the orbit plane and the line of apsides by the zonal spherical harmonics of even degree of a spherical harmonic expansion of the disturbing function R. The situation is similar also in case of the numerical perturbation techniques. The practical experiences underline these numerical characteristics of the perturbation strategies.

1.2.3 A New Era of Satellite Geodesy

The success of the Global Navigation Satellite Systems (GNSS), the development of microcomputer technology and the availability of highly sophisticated sensors enabled space borne concepts of gravity field missions such as CHAMP and GRACE and – to be realized in a couple of months – GOCE. The innovative character of these missions is based on the continuous and precise observations of the orbits of the low flying satellites (high-low Satellite-to-Satellite Tracking – h-l SST) and the extremely precise range and range-rate K-band measurements between the satellites in case of GRACE (low-low Satellite-to-Satellite Tracking – l-l SST). In addition, the surface forces acting on these satellites are measured and can be considered properly during the recovery procedure. In case of GOCE, components of the gravity gradient are measured by a gravity gradiometer (Satellite Gravity Gradiometry – SGG). The orbit decay of GOCE is compensated by a feedback system coupled with the measurement of the surface forces acting on the satellite so that the kinematically computed orbit is purely gravity field determined.

In case of SST, the relative motion of free-falling test masses are measured as relative distances and velocities or as relative accelerations. The concept is possible either in the so-called low-low or in the high-low mode. In the former case, the satellites have approximately the same altitude (400 to 500km). In this case, both satellites are equally sensitive to gravity field irregularities. In the latter case, only one (the gravity field sensitive) satellite is placed into a low orbit while the observing satellites of the GNSS describe orbits with high altitudes. The latter high-low alternative is usually modified such that the observations of the satellites of the GNSS are used to derive precise kinematical orbits. In case of SGG, the elements of the gravity gradient or linear combinations thereof are intended to be measured simultaneously, depending on the sensitivity axes realized in the gradiometer instrument. It can be shown that the observations in these three cases can be related to the gravitational potential V in case of high-low SST or precise orbit determinations, to the gradient of the potential ∇V in case of low-low SST and to the gradient of the gradient of the gravitational potential $\nabla\nabla V$ (gravitational tensor) in case of SGG. A common feature of these various gravity field measurement techniques is the fact that the differences of the free-fall motion of test masses is used to derive more or less in-situ the field strength of the gravity field. This is obvious in case of SGG; here the relative acceleration of two test masses m_1 and m_2 in the sensitivity axis $\mathbf{r}_{12}$ is measured. The main part of the acceleration is represented by the (specific) tidal force field $\mathbf{G}_{(21)\otimes}$ of the Earth which can be approximated by the gravitational tensor $\nabla\mathbf{g}_{\otimes}$:

$$\ddot{\mathbf{r}}_{12} = \mathbf{r}_{12} \cdot \nabla\mathbf{g}_{\otimes}. \tag{1.8}$$

There is no basic difference to the measurement principle in case of the low-low-SST alternative where the Earth gravity field is measured also in form of the tidal field acting on the relative motion of both satellites. It reads with the reduced mass μ_{12} and the gravitational attraction of both satellites, $\mathbf{K}_{21}$,

$$\ddot{\mathbf{r}}_{12} = \frac{1}{\mu_{12}} \left(\mathbf{K}_{21} + \mathbf{G}_{(21)\otimes} \right). \tag{1.9}$$

In this case, the tidal force $\mathbf{G}_{(21)\otimes}$ cannot be approximated sufficiently accurate by the gravitational tensor. The same principle holds also in case of the free-fall absolute gravimetry or by the use of precisely determined kinematical orbits for gravity field recovery; here the free fall of a test mass with respect to the gravity field of the Earth is observed. The only difference to low-low-SST is the fact that the specific force function is dominated mainly by the gravitational acceleration of the Earth, $\mathbf{g}_{\otimes}$, and not by the tidal force field $\mathbf{G}_{(21)\otimes}$ as in case of low-low-SST or SGG:

$$\ddot{\mathbf{r}} = \mathbf{g}_{\otimes}. \tag{1.10}$$

Obviously, the in-situ character of these measurement principles does not require the analysis of long arcs with respect to accumulated gravity field effects, because the gravity field is detected more or less directly. It should be pointed out that in all these different measurement scenarios, the in-situ observations contain the complete spectral band of the gravity field. Therefore, the frequently expressed argument long wavelength features of the gravity field cannot be detected in such an in-situ way is certainly not true. The restrictions with respect to signal content in certain observables are caused by the spectral limitations of the measurement apparatus, such as in case of a satellite gravity gradiometer as envisaged for the GOCE mission.

There are various proposals to account for the special features of the new types of observations as already outlined in Sec. 1.2.3. These techniques have in common that they do not analyze accumulated perturbation effects of the gravitational field; they rather detect - more or less directly - the intrinsic structure of the gravitational field.
A very obvious and simple approach is the use of energy balance relations along the orbit. In this approach, the velocities derived by numerical differentiation from the satellite positions along the orbits (as result of a geometric orbit determination) are used to compute the kinetic energy which balances the potential energy, modeled by the unknown gravity field parameters. The application of the energy integral for problems of Satellite Geodesy has been proposed since its very beginning (e.g., O'Keefe 1960, Bjerhammar 1967, Reigber 1969, Ilk 1983a). But the applications did not lead to convincing results because of the type of observations and the poor coverage of the satellite orbits with observations available at that time. The situation changed with the new type of homogeneous and dense data distributions as demonstrated e.g. by Jekeli (Jekeli 1999) or discussed in Visser (Visser et al. 2003). Two gravity field models based on the energy balance approach and kinematical CHAMP orbits, TUM-1s and TUM-2Sp, have been derived by Gerlach (Gerlach et al. 2003) and Földvary (Földvary et al. 2004), respectively. Both models come close to the GFZ (GeoForschungsZentrum) gravity field models EIGEN-1 (Reigber et al. 2003a), EIGEN-2 (Reigber et al. 2003b), EIGEN-CHAMP3Sp (Reigber et al. 2003c), derived by the classical perturbation approach. Another approach is based directly on Newton's equation of motion, which balances the acceleration vector with respect to an inertial frame of reference and the gradient of the gravitational potential. By means of triple differences, based upon Newton's interpolation formula, the local acceleration vector is estimated from relative GPS position time series (again as a result of a geometric orbit determination) as demonstrated by Reubelt (Reubelt et al. 2003). The analysis techniques, mentioned so far, are based on the numerical differentiation of the GPS-derived ephemeris, in the latter case even twice. Numerical differentiation of noisy data sets is an improperly posed problem, in so far, as the result is not continuously dependent on the input data. Therefore, any sort of regularization is necessary to come up with a meaningful result. In general, filtering techniques or least squares interpolation or approximation procedures can be applied to overcome these stability problems. The respectable results of the energy approach in a real application, demonstrated by Gerlach (Gerlach et al. 2003) and Földvary (Földvary et al. 2004). Nevertheless, numerical differentiation remains the most critical step in these gravity field analysis procedures. An advanced kinematical orbit determination procedure which delivers directly velocities and accelerations can help to overcome these intrinsic problems.

An alternative is a gravity field approach which is based on a two-step procedure, representing, in principle, a definitive orbit determination strategy as mentioned in Sec. 1.1. In a first step, a kinematical orbit determination delivers the empirical orbit as observed from the GNSS measurements of different types. In a second step the parameters of a dynamical force function model is modified such that it fits in a best possible way the kinematical orbit, as derived in the preceding step. This gravity field recovery technique is based on Newton's equation of motion, formulated as a boundary value problem in the form of a Fredholm type integral equation. The idea has been proposed as a general method for orbit determination by Schneider in 1967 (Schneider 1968), modified for gravity field determination by Reigber (Reigber 1969) and successfully applied subsequently, especially as additional observation equations for zonal and resonant potential coefficients, by Reigber (Reigber 1989) in a series of gravity field models, which became well-known under the acronym GRIM (e.g., Balmino et al. 1976). In the following, the idea has been applied to the Satellite-to-Satellite Tracking (SST) problem by Ilk (Ilk 1983a) and later to the Satellite Gravity Gradiometry (SGG) analysis. After that, the method has been developed and tested based on various simulation scenarios, e.g. see Ilk et al. 1995 and Ilk et al. 2003. The method requires a dense coverage of the satellite arcs with observations so that it took some more years until its suitability for the processing of real data could be shown. When the Global Positioning System (GPS) became fully operational and the first gravity field satellite CHAMP was equipped with precise on-board GPS receivers and launched in 2000, a first convincing proof of the excellent properties of this method was possible by Mayer-Guerr (Mayer-Gürr 2006). The recovery procedure can be applied in the space domain or in the spectral domain (by a series of sine functions). In case of the gravity field recovery procedure, the observation equations are formulated in space domain by dividing the one-year orbit into short pieces of arcs. As already mentioned above, the subdivision of the total orbit is necessary because of discontinuities of the kinematical orbits. The length of the arcs is not critical at all and can be adapted to the discontinuities of the data set. Because of the

fact that a bias for each of the three components of the accelerometer measurements along a short arc will be determined, the arc length should be not too small to get a safe redundancy and not too long to avoid accumulated unmodeled disturbances. An arc length of approximately 30 minutes seems to be appropriate, taking the discontinuities of the kinematically determined arcs into account. The root of the gravity field recovery techniques developed so far is the orbit determination of short arcs which underlines again the importance of the improvement of the orbit determination techniques.

1.3 A Short Historical Review of Orbit Determination

1.3.1 Ground Based Orbit Determination

The observation of the direction vectors to artificial satellites (longitudes and latitudes or azimuths and zenith distances) by specialized cameras is the early observation technique of Satellite Geodesy. Approximately at the same time the distance measurement technique by lasers was developed and it was possible to measure the geometrical distances from the ground stations to the satellites equipped with retro-reflectors. In the early seventieth, the laser ranging replaced the optical measurements nearly completely. The processing of optical observations, either based on the astrometric or the photogrammetric method, was very time-consuming. This was the reason that the optical observation era in Satellite Geodesy came to a sudden end with the development of SLR systems and the use of the Doppler and GPS techniques for orbit determination. Another reason was the limited accuracy of the direction measurements: a directional accuracy of ± 0.1" corresponds to $\pm 3m$ in the orbit of a satellite at 6000 km altitude above ground (e.g. LAGEOS). Even if the direction vectors are complementary to the distance measurements and despite the fact that the optical measurements have some unique properties compared to the other observation types, the optical observation techniques were not competitive with respect to the accuracy compared to the cm accuracy available with laser ranging systems. Nevertheless, the optical tracking of satellites is of fundamental importance because it is the only observation technique in Satellite Geodesy which directly enables access to the inertial reference frame defined by the fixed stars. But recent progress made in the development of the Charge Coupled Device (CCD) technique may lead to a revival of optical satellite observations. All other methods such as the measurements related to the Global Positioning System (GPS) or by the Satellite Laser Ranging (SLR) provide only an indirect link to the celestial reference frame through the equation of motion (Seeber 2003). Nowadays, the observations within the GNSS play a dominant role in Satellite Geodesy but it shall be noticed that optical and laser observations are an independent tool to control and calibrate other observation systems, e.g. based on GPS and DORIS.

In the case of laser distance measurements to satellites (SLR), the travel time of a laser pulse between a ground station and a retro-reflector fixed to a satellite is measured with an extremely high accuracy. The development of pulsed laser-systems for the tracking of artificial satellites started in the USA as early as 1961/1962. The first satellite that carried a laser reflector was BEACON EXPLORER–B (BE-B) and the first successful signal returns were obtained in 1965 and yielded an accuracy of a few meters (e.g. Seeber 2003). In subsequent years, the progress in laser ranging was very fast and the accuracy of laser ranging has improved from several meters down to a few millimeters. In space distance measurements are possible with an accuracy of a couple of micro-meters with micro-wave measurement techniques (e.g. K-band measurement between the GRACE twin-satellites). Laser-interferometric distance measurements are in discussion that can reach even a much higher accuracy.

Satellite laser ranging systems have been deployed at many locations around the world. Despite the success of GNSS measurements for orbit determinations, laser ranging measurements are still indispensable in Satellite Geodesy and this will last for the next future. Nowadays, ground-based orbit determinations of Low flying Earth Orbiting satellites (LEO) such as CHAMP and GRACE are possible with an accuracy of a couple of centimeters and they can be used to calibrate and control other orbit determination techniques. DORIS (**D**oppler **O**rbitography and **R**adiopositioning **I**ntegrated by **S**atellite) is another navigation system to determine and validate the orbits of LEOs.The DORIS system was developed by the French Space Agency (CNES) with the objective to support the precise orbit determination of LEOs with the reverse Doppler

concepts. The DORIS system uses a stable frequency which is emitted from the ground beacon stations (beacons network). The Doppler measurements are performed by DORIS on-board the LEOs. Many of the remote sensing satellites like SPOT 2-5, TOPEX/POSEIDON, JASON and ENVISAT are equipped with the DORIS instruments to estimate their precise orbits. A first realization was used 1990 at the remote sensing satellite SPOT-2. In the DORIS system, the ground beacons broadcast continuously and omnidirectionally at frequencies of 2036.25 *MHz* and 401.25 *MHz*. A receiver on-board of the satellite receives the broadcasted signals and measures the Doppler shift over a short count interval, e.g. 10 seconds (Seeber 2003). The precise Doppler measurement is made at 2 *GHz*; the use of the second frequency allows to eliminate ionosphere effects. The DORIS results are of high quality because the DORIS stations are distributed well around the globe. The accuracy envisaged for DORIS was about 10 *cm* in the radial component after one month in the post processing mode, but with the improvement of the network configuration, a better theory and a sophisticated error modeling, the current accuracy is about 2.5 *cm* in the post processing mode (Seeber 2003). With the establishment of the autonomous real time orbit determination on-board the SPOT-4 satellite, the accuracy of a few meters for the real time orbit was reachable. For remote sensing applications, the delivery of the real time orbit of satellites is very important. The DORIS system offers three different orbit products (Seeber 2003),

- *Real time* orbits with an accuracy of sub-meter with the new DORIS generation,
- *Operational* orbits with an accuracy of sub-meter after 48 hours (<20 *cm* in the radial component),
- *Precise* orbits with sub-decimeter accuracy after one month (*cm* accuracy for radial component).

Besides the SLR and DORIS systems, PRARE (**P**recise **R**ange **A**nd **R**ange rate **E**quipment) is another system to determine precise orbits of the LEOs. The German PRARE system is a compact, space-borne, two-way, two-frequency (2.2 *GHz* S-band and 8.5 and 7.2 *GHz* X-band) microwave satellite tracking system. The primary objective of the PRARE system is to provide the precise orbit determination for LEOs missions. Based on a global network of PRARE ground stations, a radial orbit accuracy of better than 10*cm* has been achieved (Seeber 2003).

1.3.2 Space Based Orbit Determination

The dense coverage of the orbits of low flying Earth observation satellites with highly precise observations performed by the satellites of the GNSS changed the situation for the orbit determination dramatically. Already in the early years of the development of space navigation systems, it was observed that the precise and continuous global coverage of satellite orbits with measurements could significantly improve the quality of the orbits of LEOs. Because of the independency of Earth based observation stations, the accuracy of the determined orbits was much more homogeneous than ever before. A pre-requisite was that the satellites are equipped with precise multi-channel on-board GNSS receivers. The application of Space-borne GPS (SGPS) receivers on-board a LEO for the goal of the orbit determination began with the launch of Landsat 4 (Birmingham et al. 1983) and the GPS tracking system has demonstrated its capability of providing high precision POD products through the GPS experiment on the altimetric mission TOPEX/Poseidon (Melbourne et al. 1994). Geometric precise orbits computed from the GPS tracking data are estimated to arrive at a radial orbit accuracy comparable to or even better than the precise orbit ephemerides (POE) computed from the combined SLR and DORIS tracking data (Bock 2003). Precise orbits are especially important in those cases where the satellites are considered as free-falling test masses in the gravitational field as mentioned already. In these cases, the perturbations of the observed orbits from reference orbits are analyzed and considered as functionals of the improvements of the gravitational field parameters. This corresponds in principle to the definitive orbit determination procedure as mentioned before. This idea has been applied in various modifications with great success in case of the geodetic satellites CHAMP and GRACE and will be applied in the near future for GOCE. But also the altimetric satellites such as e.g. TOPEX/ Poseidon, JASON-1 as well as the satellites to investigate the polar caps as e.g. ICESAT and in near future CRYOSAT require very precise orbits to determine the sea surface topography and the sea level

heights as well as the ice thickness of the polar caps. But also the various remote sensing satellites require a precise geo-referencing of the sensors as in case of the magnetic missions Ørsted and SWARM or other remote sensing satellites such as ASTER and IKONOS etc. Because of the importance of the determination of satellite orbits, there were various approaches to solve this problem and the progress arrived so far is well documented in many books and papers.

1.4 The GNSS Revolution in Satellite Geodesy

1.4.1 Processing Techniques of GNSS Observations

The primary result of an orbit determination procedure based on GNSS observations is an ephemeris of three-dimensional coordinates referred to a terrestrial or celestial reference frame. The data processing procedures may be distinguished by their differencing level namely the zero-difference (ZD), double-difference (DD), or triple difference (TD) level of the original high-low GPS-SST observations. All strategies make direct use (in double and triple differences) or indirect use (zero difference) of the GNSS ground network (IGS network). Direct use is made if the GPS observations of the ground stations are used together with the LEO GPS-SST data for the processing procedure in case of DD and TD. Indirect use is made if the observations of the ground stations are not used for the LEO GPS data processing as in case of ZD. The ground based GPS observations are required in this case to estimate GPS satellite positions and clock corrections. In any case, ground station observations are required to compute precise GPS satellite orbits. All differencing techniques require GPS orbits, precise Earth rotation information, and LEO GPS-SST measurements as input for the data processing. The GPS satellite orbits and ERP (Earth Rotation Parameters) are taken either from the IGS (or one of its analysis centers) or they may be estimated together with the LEO orbit (within a one step or a two step procedure). In the following, the specific advantages of the GNSS for orbit determination are outlined and compared to the ground based observation systems and some important groups of orbit determination strategies applied so far will be described in more detail.

1.4.2 Conventional Ground Based Observations and High-Low GPS-SST Observations

The Global Navigation Satellite System provides a number of advantages over conventional (classical) tracking techniques from ground based observation stations. The excellent observation geometry of the GNSS provides three-dimensional information from the pseudo-range measurements as opposed to just range, range rate or angular measurements to a single satellite. Another appealing aspect of the observations from a GNSS receiver on-board a LEO is its continuous data collection property, provided sufficient power is available to sustain the receiver operation and a sufficient storage capacity to record the huge amount of measurements is available. Conventional ground based techniques are limited to those observation periods where the spacecraft is visible from the tracking stations, and, in case of laser ranging if the atmospheric conditions permit a measurement. The high costs (equipment and personal) involved with the operation of conventional tracking stations and their land based nature limits its use and hence reduces the data collection quantity and distribution. Space-borne GNSS receivers avoid the need of these expensive tracking stations, provided the IGS network consists of a sufficient number of observation stations. It is remarkable that GPS carrier phase observations and their differenced quantities taken from the ground station network (DD or TD) are the most accurate ones among all space observation techniques (Bisnath 2004). Only GPS measurement techniques allow a purely geometrical three dimensional orbit determination. The geometrical satellite positions can be estimated independently of the orbit altitude and without knowledge of force function models (Bock 2003). For validation of LEO orbits derived from GPS measurements, it is necessary to compare them with other independent orbit determination procedures such as those based on SLR.

1.4.3 Dynamical Precise Orbit Determination

The dynamical precise orbit determination approach requires a precise mathematical model of the physical forces acting on the LEOs and a precise mathematical model of the LEOs physical properties (Rim and Schutz 2002). The physical models are used to describe the motion of the LEO according to the physical laws of Theoretical Mechanics (e.g. Ilk 1976, Bisnath 2004). Double integration of the Newton-Euler equation of motion using initial or boundary values of the orbit results in a nominal trajectory. The task is to correct the initial or boundary values such that the orbit shows a best fit to the pre-processed (undifferenced or differenced) GPS tracking data with respect to a certain norm (differential orbit improvement). An example of the most accurate SGPS dynamical orbit determination results compared to SLR and DORIS orbits is that of the altimetry satellite TOPEX/Poseidon orbiting around the Earth at an approximate altitude of 1300 km. For an arc of ten days length, the radial RMS differences are in the size of approximately $3cm$, the along track RMS differences in the size of $10cm$ and the cross track RMS differences are in the size of $9cm$. The procedure applied in this example was based on double differenced ionosphere-free carrier phase and P-code GPS observations (Rim and Schutz 2002).

1.4.4 Geometrical Precise Orbit Determination

In case of a geometrical orbit determination procedure, only the geometrical observations between the receiver (LEO) and the sender (e.g. GPS, SLR, DORIS, etc.) are used to determine point-wise the positions of the receiver. Only the LEO positions and/or clock offsets at every observation epoch are determined, based on the SST observations. The geometrical orbit determination strategies do not need an information about the Earth gravity field and other parameters of the dynamical LEO orbit model. The input, in case of the zero-differenced geometrical orbit determination strategy, consists of precise GPS orbits and their clock offsets, Earth rotation parameters and dual frequency pseudo ranges (P_1, P_2, C/A) and carrier phase (ϕ_1, ϕ_2) space-borne GPS receiver tracking data. The precision of the geometrical LEO positions depends on the precision of the GPS-SST observations, on the configuration of the GPS-SST observation geometry and on the quality of the GPS orbit and clock products, provided by the IGS centers. The number of GPS satellites, simultaneously visible from the space-borne receiver, as well as the strength of the geometric configuration of the GPS satellites are the crucial criteria for the accuracy of the positions determined by the geometrical orbit determination method. If less than four GPS satellites are available per epoch, no LEO position can be estimated in zero-differenced mode. These missing positions as well as data gaps, e.g. due to receiver resets or orbit maneuvers lead to interrupts in the geometrically determined orbit of the LEO. This may cause problems if the geometrical positions are used for subsequent gravity field determination procedures where equidistant ephemerides are necessary to derive e.g. homogeneous velocities or accelerations. This is not the case for a dynamical orbit solution, because the dynamical orbits are determined continuously independent from data gaps. Poor and not homogeneous data coverage would also cause weaknesses in the specific parts of the determined satellite arcs. An example for a geometrical (denoted as "kinematical") strategy using triple differenced GPS-SST observations may be found in Grejner-Brzezinska (Grejner-Brzezinska et al. 2002) and in Byun (Byun 2003). In Švehla (Švehla and Rothacher 2002) geometrical (denoted also as "kinematical") zero and double-differenced precise orbit determination strategies of LEOs (e.g. CHAMP) including an ambiguity resolution are presented (see also Švehla and Rothacher 2003). The zero-differenced geometrical POD approach for the determination of LEO orbits (denoted as "kinematical") using subsequent filtering techniques can be found in Bisnath (Bisnath 2004). This approach is based on code pseudo-ranges and subsequently time differenced carrier phase observations.

1.4.5 Short Arc Kinematical Precise Orbit Determination of the LEO

The kinematic precise orbit determination procedure consists of two steps which can be integrated also into one determination procedure: (a) the geometrical precise orbit determination resulting in an ephemeris of point-wise positions and (b) the estimation of an approximation function representing the kinematical satellite orbit. Geometrical orbit determination is the process of determining an initial geometrical orbit

of the LEO from only geometrical high-low GPS-SST observations. This process consists of a point-wise determination of the absolute LEO positions from the ionosphere-free code pseudo-range and carrier phase observations. As outlined, the satellite orbit is given point-wise and may contain gaps along the ephemerides. In many applications (e.g. in case of Earth gravity field recovery techniques), a continuous LEO orbit is required. But as mentioned already, the densely with GPS-SST observations covered satellite arcs do not need to be very long provided the analysis procedure is properly adapted to the well-observed short arcs.

1.4.6 Reduced-Dynamical Precise Orbit Determination

As already pointed out, the dynamical orbit determination techniques require a precise mathematical model of all forces acting on the satellite and a mathematical model of the physical properties of the LEO. The equation of motion can be solved using numerical or analytical determination techniques. The high-low GPS-SST observations are approximated by a particular orbit as result of the least squares adjustment process where the initial or boundary values are determined as unknown parameters. Remaining model errors cause deviations of the dynamically determined orbit from the observed one, in most cases showing systematic patterns of the residuals. Usually, the model errors increase with the arc length of the LEO. The introduction of empirical parameters, modeling e.g. deviations proportional to the satellites revolution period or stochastic pulses once per a couple of minutes (Jäggi et al. 2006) can help to avoid the unlimited increase of modeling errors. This is the basic idea of the reduced-dynamical orbit determination strategies as proposed by Beutler (Beutler et al. 2006). Empirical parameters reduce the influence of possible deficiencies of the dynamic models on the estimated orbit. Lower flying satellites (e.g. GOCE) require more empirical parameters than higher flying ones (e.g. CHAMP) because it is virtually impossible to use adequate dynamical models for the non-gravitational surface forces (e.g. atmospheric drag), and it is difficult to model ocean tide effects (Bock 2003).

1.5 Thesis Statement

Due to the fact that the arcs of low Earth orbiting satellites are densely and homogeneously covered by code pseudo-range and carrier phase measurements, orbit determination based on various processing procedures is possible at a very high level of precision. This fact has revolutionized processing techniques and applications in Satellite Geodesy. It has been demonstrated recently that e.g. for gravity field recovery only short arcs of approximately 30 minutes length and covering the Earth homogeneously are sufficient to determine the complete spectrum of the gravitational field of the Earth. Therefore, the very precise determination of kinematical orbits becomes indispensable. As already defined, we understand the notation "kinematics" as a procedure which delivers not only three-dimensional positions but also velocities and accelerations in a consistent way. In this thesis, a procedure will be proposed which allows the determination of pure kinematical orbits as well as pure dynamical orbits; but even more, it allows a smooth transition from a kinematical orbit determination to a dynamical orbit determination. This hybrid orbit determination procedure is achieved by formulating a boundary value problem to Newton-Euler's equation of motion, either as absolute or relative orbits, in form of an integral equation of Fredholm type. The solution of this integral equation can be formulated as a function which consists of three parts: a first one describing a linear combination of the boundary position vectors (either a straight line or an ellipse connecting the end points of the arc or a dynamical reference orbit), a second one which consists of polynomials of Euler and Bernoulli type of various degrees and a third one consisting of a series of sine functions, described by an - in principle – infinite number of terms. Because of a limited number of observations, the number of parameters has to be restricted adequately, ensuring the envisaged accuracy. The free parameters of this approximation function can be determined partly by the adapted force function model and partly as free parameters in a least squares adjustment procedure representing the dynamical orbit or completely by a least squares adjustment procedure representing the kinematical orbit. In the case of the reduced-kinematical or reduced dynamical modification, certain constraints are introduced by the functional model. The observations are based on precise GNSS measurements of various types. GNSS provides accurate code

pseudo-range and carrier phase observations, which are used to estimate the geometrical absolute position of the LEOs. Results are presented based on different observables. Precise results have been achieved with the help of carrier phase high-low GPS-SST observations in the zero difference concept. In this method, the availability of the GPS precise orbits from the IGS centers and the physical models of the systematic errors in the high-low GPS-SST observations are necessary. Laser tracking to GPS and LEO satellites (e.g. GPS PRN 5-6, CHAMP, GRACE A/B) provides an opportunity to compare GPS and SLR systems directly or to combine the data of both in a single solution.

2. GPS Observables, Observation Time Delay and Reference Systems

2.1 Overview on GNSS

2.1.1 GPS Constellation

For the time being, the Global Positioning System (GPS) is the only operational Global Navigation Satellite System (GNSS). It consists of a constellation of at least 24 Medium Earth Orbiters (MEO, see Fig. 2.1) in nearly circular orbits with an altitude of about 20200 km above the Earth, in six evenly spaced planes (A to F) with an inclination of 55° and with four satellites per plane that transmit precise microwave signals. The system enables a GPS receiver to determine its location, time, speed and direction. It was developed by the United States Department of Defense (DOD) and was officially denoted as NAVSTAR GPS. Contrary to popular belief, NAVSTAR is not an acronym, but simply a name given by John Walsh, a key decision maker at the time where the GPS program has been established (Parkinson 1996). GPS has become a worldwide used aid to navigation at land, sea, air and space and a useful tool for map-making, land surveying, commerce and a very useful tool for various scientific applications. In geodesy, the Precise Orbit Determination (POD) of LEOs based on high-low GPS-SST observations and applied for gravity field recovery is one important task. Another important application out of many others is the determination of the positions of a worldwide net of IGS reference stations to define precise reference frames. GPS also provides a precise time reference used in many applications including scientific studies in the geo-sciences and the synchronization of telecommunication networks.

Figure 2.1: GPS-Block IIF Satellite (Credits: NASA)

2.1.2 GPS Satellite Categories

There are six types of GPS satellites, namely Block I, Block II, Block IIA, Block IIR, Block IIF, and Block III satellites. Eleven Block I satellites were launched in the period between 1978 and 1985 from Vandernberg

AFB, California. Today none of the original Block I satellites are in operation anymore. The Block II constellation is slightly different from the Block I constellation since the inclination of their orbital planes is 55° compared to the former 63° inclination. Apart from the orbital inclination, there is an essential difference between Block I and Block II satellites related to U.S. national security. The Block IIA satellites ("A" denotes advanced) are equipped with mutual communication capabilities. Some of them carry retro-reflectors to be tracked by laser ranging systems, i.e. SLR. Today no distinction is made between Block II and Block IIA satellites. Block IIR satellites ("R" denotes replacement) are equipped with improved facilities for communication and inter-satellite tracking. The Block IIR satellites have been launched after 2005 and will also transmit the new civil signal L_{2C} component and with the capability to improve the signal power to ground receivers. Furthermore, they transmit new military signals with an improved accuracy (M Signal). The Block IIF satellites ("F" denotes follow on) will be launched from 2009 onwards with an expected lifetime of 15 years. These satellites will be equipped with improved on-board capabilities such as inertial navigation systems and an augmented signal structure. The Block III GPS satellites are expected to carry the GPS into the year 2014 and beyond with a modern signal structure (e.g. L_{1C} and L_5) and an improved GPS satellite body structure (Hofmann-Wellenhof et al. 2001).

2.1.3 GPS Satellite Signals

The actual carrier signals in the GPS satellites are a spread spectrum that makes it less subject to intentional (or unintentional) jamming by the users. All GPS carrier signal components are derived from the output of a highly stable atomic clock, which is the key to the accuracy of the global navigation system. In the operational GPS (e.g. Block II/IIA) each satellite is equipped with four on-board time standards, i.e. two cesium and two rubidium atomic clocks. The long frequency stability of these clocks reaches a few parts of 10^{-13} and 10^{-14} over one day, respectively. The Block IIF satellites may be equipped with a space-qualified hydrogen maser with frequency stability of 10^{-15} over one day. The heart of the GPS satellites are stable atomic clocks, that generate a pure *sine* wave at a frequency $f_0 = 10.23MHz$, with a stability of the order of 1 part in 10^{-13} over one day. This is referred to as the fundamental L band frequency in GPS. Multiplying the L band fundamental frequency (f_0) by integer factors yields the three (later four with the new signal L_5) microwave L-band carrier waves L_1, L_2 and L_{2C}, respectively. The new signal L_5 has been proposed for the use as a civilian Safety-of-Life (SoL) signal. This frequency falls into an internationally protected range for aeronautical navigation, promising little or no interference under all circumstances. The first Block IIF satellite that would provide this signal is planned to be launched in 2009. The frequencies of the three active waves are obtained as follows:

$$\begin{aligned} f_{L_1} &= 154 f_0 = 1575.42MHz\,(\lambda_1 \approx 0.190m)\,, \\ f_{L_2} &= f_{L_{2c}} = 120 f_0 = 1227.60MHz\,(\lambda_2 \approx 0.244m)\,, \\ f_{L_5} &= 115 f_0 = 1176.45MHz\,(\lambda_5 \approx 0.255m)\,. \end{aligned} \tag{2.1}$$

The combination of all operational signals is very important to mitigate or eliminate some signal propagation errors (e.g. ionospheric error). It is remarkable that on the L_1 signal band a mix of navigation messages, coarse acquisition (C/A) and encrypted precision $P(Y)$ codes are propagated. On the L_2, $P(Y)$ code plus the new L_{2C} code on the Block IIR-M and newer satellites are transmitted to the users. In the case of LEOs all observation types (i.e. C/A, P_1, P_2, ϕ_1, ϕ_2 and ϕP_1) are tracked with their signal strength (i.e. SA, S_1 and S_2) to consider signal strength as statistical quantity in the precise orbit determination procedure.

2.2 The International GNSS Service

The International GNSS Service (IGS), formerly the International GPS Service, is a voluntary federation of more than 200 worldwide agencies that pool resources and permanent GPS and GLONASS station data to generate precise GPS and GLONASS products (orbits, clock offsets, etc.). The IGS is committed to provide the highest data quality and products as the standard for Global Navigation Satellite Systems in

support of Earth science research, multidisciplinary applications and education. The GNSS observations at the IGS permanent stations are transferred to the Data Centers and pre-processed and processed by the IGS Analysis Centers with respect to latency. The Analysis Centers produce diverse products specified as *predict*, *rapid* and *precise*. The analyzed data in the different analysis centers are transferred to the IGS center to produce the final products. Currently the IGS includes two GNSS, the USA GPS and the Russian GLONASS, and intends to incorporate future GNSS like the European GALILEO (IGS 2008). Obviously, in the post-processing of the LEO orbit determination procedure, the final precise products of the GNSS are necessary in this procedure. The GNSS positions and clock offsets can be used as fixed values (without variance-covariances) or as float values (with variance-covariances) in the processing of the GNSS observations.

2.3 Time Coordinate Systems

In space geodesy, measurement techniques usually measure travel times or travel time differences. Examples are the measurement of travel time differences of extraterrestrial signals from Quasars at two stations in case of VLBI and travel times of artificial signals from GNSS satellites to the GNSS receiver. In Satellite Geodesy, a time scale is regarded as one of the coordinates of a four-dimensional space-time reference frame. Two aspects of time scales are required in Satellite Geodesy, the time epoch and the time interval. The epoch defines the moment of an event, and the interval is the time difference between two epochs, which are measured in units of time of the adopted time scale. There are several time coordinate systems in Satellite Geodesy and in astronomic applications, which are based on various periodic processes such as the rotation of the Earth or atomic oscillations. Time scales in Satellite Geodesy can be classified in three basic main groups (Seidelmann 1992):

- Sidereal Time (ST): the time defined through the rotation of the Earth w.r.t the reference meridian of the Earth e.g. Greenwich meridian, local meridian or vernal equinox,
- Dynamical Time (TD): the time defined from planetary motions in the solar system, based on the theory of General relativity,
- Atomic Time (TA): the time realized in atomic clocks on the Earth's geoid. It is the basis for a uniform time scale on the Earth. This time is defined by the frequency of the basic oscillation of the frequency-determined element. The origin of the atomic time is defined by international conventions agreed by international organizations such as IAU (International Astronomical Union).

2.3.1 Sideral and Universal Time

Sidereal time and universal time are directly related to the periodic rotation of the Earth, and they are thus equivalent time scales. Sidereal time is a measure of the Earth's rotation and is defined as the hour angle between the observed local meridian and a point on the celestial sphere (e.g. the vernal equinox). If the measure is counted from the local meridian to the true vernal equinox, the sidereal time is called **L**ocal **A**pparent **S**idereal **T**ime (**LAST**) and if the measure is counted from the Greenwich meridian to the true vernal equinox, the sidereal time is called **G**reenwich **A**pparent **S**idereal **T**ime (**GAST**). Obviously, for the mean equinox, the Local and Greenwich sidereal time holds LMST and GMST respectively. The **U**niversal **T**ime (**UT**) is the Greenwich hour angle of the apparent Sun, which is orbiting uniformly in the equatorial plane. Universal time is not a uniformly scaled time, because the angular velocity of the Earth is not a constant. If the universal time is corrected for the polar motion (effect on the meridian, dUT_1), then the Universal Time is denoted as UT_1. The relationship between the corrected universal time (natural time scale) and universal time coordinate (artificial atomic time scale) is,

$$UT_1 = UTC + dUT_1. \tag{2.2}$$

In Eq. (2.2), $UT1$ is the astronomical observation at the ground station which is corrected for polar motion, and $dUT1$ is a correction which can be obtained from the IERS center. The practical importance of the Universal Time today is not as a time systems (it is too irregular compared to regular atomic time scales) but as an angular measurement used in the transformation between the Celestial and Terrestrial Reference Frames (Kleusberg and Teunissen 1998).

2.3.2 Atomic Time

The atomic time is the basis of a uniform, continuous time scale on the geoid, and is kept by atomic clocks. The fundamental time scale is *International Atomic Time (TAI, Temps Atomique International)* based on atomic clocks operated by various national agencies. It is kept by the IERS and BIPM who are responsible for the dissemination of the standard time and of the EOP. The fundamental interval (scale) of the atomic time is one *SI* second that has been defined at the 13^{th} general conference of ICWM based on the Cesium 133 atom and its origin point was established with Universal Time (UT) at midnight on the 1^{th} of January 1958. There is a fundamental problem of using the TAI in practice: the rotation of the Earth around its rotation axis is slowing down. Thus TAI would eventually become inconveniently out of synchronization with the solar day. This problem has been overcome by introducing *Universal Time Coordinate (UTC)*, which runs at the same rate as TAI, but incremented by the leap seconds when necessary. The IERS is responsible to publish them on January, 1st or July, 1st. The time signal broadcast by GPS satellites are synchronized with the atomic clock at the GPS master control station in Colorado. GPS time was set to 0^h UTC on 6^{th} of January 1980, but it is not incremented by UTC leap seconds. Therefore, at the moment of writing this lines, there is a 19^s offset between GPS time ($GPST$) and Atomic time (TAI) and the transformation reads,

$$GPST = TAI - 19^s, \tag{2.3}$$

UTC is the atomic time scale, which can be determined from the TAI and the leap seconds (n) as (McCarthy and Petit 2003),

$$UTC = TAI - n^s. \tag{2.4}$$

In space geodesy applications, the time epoch denoted by the *Julian Date (JD)* is expressed by a certain number of integer days and a fraction of a day after a fundamental epoch in the past, chosen to be at 12^h UT on January 1, 4713 BCE. The JD of the standard epoch of UT is called *J2000.0* as (Kleusberg and Teunissen 1998),

$$J2000.0 = 2451545.0(JD) = 2000, \quad January, \quad 1^d.5, \quad UT, \tag{2.5}$$

The Modified Julian Day *(MJD)* was introduced by space scientists in the late 1950's. It is defined as

$$MJD = JD - 2400000.5. \tag{2.6}$$

2.3.3 Dynamical Time

In 1952, the IAU introduced the so-called *Ephemeris Time(ET)* as a theoretically uniform time scale for the use with ephemeris. In practice, the ephemeris time was derived from lunar observations, and it depends on a theory of the Sun and the system of astronomical constants. Ephemeris time has never been disseminated as time signals from a time service. It was made available only through the publication of differences with respect to UT_1, and later to TAI (Seeber 2003). The Dynamical time is the independent variable in the equation of motion of bodies moving under gravitational interaction in the Solar System according to the theory of General Relativity. The best approximation of an Inertial Reference Frame to which we have access based on General Relativity is located at the mass center of the Solar System. The Dynamical time measured in this mass center is called *Barycentric Dynamical Time(TDB)*, and in the mass center of the Earth it is called *Terrestrial Dynamical Time(TDT)*(Kleusberg and Teunissen 1998). In the concepts of

General Relativity, a clock located at the geoid and moving with the Earth experiences periodic variations of up to 1.6 *msec.* which is caused by the annual motion of the Earth within the gravitational field of the Sun (and the other planets). In the computation of LEO orbits, this effect can be neglected, because LEOs move together with the Earth. Because of neglecting this effect in the orbit determination and by adapting as basic Newton's theory, TDT is the appropriate time scale in Satellite Geodesy. The application of the TDB time scale has to be considered for VLBI (Seidelmann 1992). Later in 1991, IAU has defined the *Terrestrial Time(TT)* as a new time scale based on the general theory of relativity to clarify the relationship between space and time coordinates. The unit of TT is the SI second and is realized through the atomic time scale TAI with a constant offset of 32.184^s between both time scales as,

$$TT = TAI + 32.^s184. \tag{2.7}$$

Because of this constant shift between TT and TAI time scales and the realization of TT by the TAI time scale, these two time scales are practically identical.

2.4 Reference Systems and Reference Frames

2.4.1 Introduction

In satellite geodesy, reference frames play a basic role for the representation of satellite orbits and as reference for station positions. The latter ones refer to an Earth-fixed reference frame while the equations of motion of satellites refer to an inertial system. There are three types of reference systems:

- **Galilei system**, with arbitrarily accelerated rotational motion of the reference system,
- **Newton system** (Quasi-inertial system), with arbitrarily accelerated translational motion of the reference system,
- **Inertial system**, with translational motion of the reference system along a straight line with constant velocity.

These reference systems can be used to describe the motion of satellites, the moon, sun, and the planets. The use of an inertial system has the advantage that the equation of motion has the simplest form compared to the equation of motion formulated with respect to other arbitrarily rotating reference systems. Nevertheless, inertial systems cannot be realized rigorously. This is the reason that Newton systems are used instead of inertial systems which represent local inertial systems in the vicinity of the origin (quasi inertial systems). Let us consider a Newton system, fixed at the center of mass of the Earth. The free fall motion of the geocenter, and with it, the motion of the origin of the reference system is ruled by the mutual gravitational forces with the sun, the moon, the planets, etc. The relative motion of an artificial satellite with respect to the geocenter then is determined by the gravitational interaction with the Earth, but also by the inhomogeneities of the mutual gravitational interaction of the Earth with the other bodies. The latter forces are so called tidal forces caused by these bodies. In case of LEOs which are close to the Earth, the direct gravitational force caused by the Earth is, of course, the largest constituent.

Newton systems can be used to describe the equation of the Earth in space, of celestial bodies and artificial satellites. Frequently, this sort of systems are called ***celestial reference system.*** If we want to describe positions and motions on the surface of the Earth, then another type of reference systems has to be introduced, so called ***terrestrial reference systems*** which are, in a certain way, fixed to the Earth. At a first glance the problem to define a terrestrial reference system seems to be a simple task. Because of the fact that any point on the Earth is moving with respect to the other points of the Earth's surface then again we have to search for an idealization of terrestrial reference systems. Ideal terrestrial systems could be defined in such a way that with respect to this system the crust should have only deformations and no rotations.

Besides the definition of these two basic concepts of reference systems, celestial and terrestrial ones, we also need the ***relationship between terrestrial and celestial reference systems***. This need can be clearly seen if we want to describe the motion, e.g. of an artificial satellite with respect to a terrestrial reference system. The inertia forces have to be considered properly in this case. To determine these forces, we need the time-dependent rotation vector of the terrestrial reference system with respect to the celestial system. Also many Earth related observation techniques in physical geodesy, e.g. to model the dynamical observations as in case of gravity measurements at the Earth surface, at sea or on-board of an airplane it is necessary to know the relationship between terrestrial and celestial systems.

2.4.2 Realizing Reference Frames

Space fixed reference systems in the sense of inertial systems (celestial reference systems) and Earth fixed reference systems (terrestrial reference systems), arbitrarily rotating with respect to the celestial system, are both necessary in practical applications. Yet, the definition of these two systems are just concepts. These theoretical concepts define ideal reference systems. The basic concepts comprise the structure of space and time. Therefore, the points in space and time have to be described accordingly. The problem to define space and time points can be realized by introducing space and time coordinates. A reference system equipped with coordinates is denoted as ***coordinate system***. Yet, it is not possible to connect to an ideal reference system in practice. In realizing these systems, we have to follow certain steps, suggested by Kovalevsky and Müller (Kovalevsky and Müller 1981) and discussed, e.g. in detail in Kovalevsky (Kovalevsky and Müller 1989) and in Moritz and Müller (Moritz and Müller 1987):

- Statement of a theoretical concept as ***an ideal reference system***: For example, an ideal celestial reference system is an inertial system, on which Newtonian's mechanics is based on,
- Choice of the physical structure of the ***reference system***: Besides the basic concept it is necessary to identify the physical bodies that are part of the physical system. For example, the solar system with its planets and moons defines such a physical structure including constants, equations of motion etc.,
- Modeling the physical structure as ***conventional reference system***: For example, to define a dynamical celestial reference system based on the solar system one has to adopt a specific model including the masses of the planets, precession constant etc. ("system of fundamental constants", periodically updated by IAU and IUGG),
- Realization of the reference system as ***conventional reference frame***: The materialization of conventional reference systems consists of a list of coordinates of points which represent the conventional reference system (fiducial points). For example a conventional dynamical celestial frame can be represented by the ephemerides of the fiducial points and a conventional kinematical celestial frame is realized by the coordinates of a selection of stars, accessible to observation, e.g. the fundamental star catalogue FK5, defined by the directions of about 1500 stars. Obviously, the number of fiducial points must be available in a sufficient number,
- Extensions and densifications of a conventional reference frame as ***a secondary conventional reference frame***: If the number of fiducial points of a conventional reference frame is not sufficient to connect to them, then extensions are necessary as for example secondary star catalogues referring to the same conventional reference frame.

2.4.3 Coordinate System

The problem to describe space and time points can be realized by introducing space and time coordinates. A reference system equipped with coordinates is referred to a coordinate system. Beside the three space coordinates, it is necessary to introduce another coordinate for the time. For both types of coordinates it is necessary to define proper measurement procedures.

In case of an ideal reference system, Newtonian mechanics based on an Euclidean or a flat space, respectively, is implicitly introduced. In Euclidean spaces, it is possible to introduce Cartesian coordinates but also curved coordinates. It should be pointed out that the introduction of curved coordinates, e.g., spherical polar coordinates, does not change the flatness of the space. Today we know that we live in a curved space an Euclidean or flat space can be introduced only locally. This is the reason that we may use also Cartesian coordinates locally.

To describe the geometrical positions of space points we can use orthogonal Cartesian coordinates. But also spherical polar coordinates or (rotational) ellipsoidal or geodetic coordinates. These types of coordinates are frequently used in geodesy. Ellipsoidal or geodetic coordinates consist of ellipsoidal longitudes and latitudes as well as of ellipsoidal heights. The application of modern satellite based observation techniques or geodetic space techniques allows to derive directly three dimensional absolute positions referred to a unique global reference system without separating it into two dimensional surface coordinates and a one dimensional height coordinate. E.g., the transformation of these three dimensional positions into surface coordinates "ellipsoidal latitude" and "ellipsoidal longitude" as well as into a height coordinates "ellipsoidal height" is simply accessible once a reference ellipsoid is introduced.

2.4.4 Conventional Reference Systems

2.4.4.1 Conventional Celestial Reference System (CCRS)

Conventional celestial reference systems can be defined by its various system components, a certain concept, a physical structure and the model of this structure, which is defined by certain conventions. There are two concepts of conventional celestial reference systems depending on the type of relations of the "carrier points" of these systems. Both definitions should lead to the same reference system at least in Newtonian mechanics. The relation between the carrier points can be defined kinematically by time-dependent coordinates or dynamically by the equation of motion of the corresponding mass points. In case of Newtonian Systems, e.g. there are various possibilities as shown in Table 2.1. The "relations" in this table contain implicitly

Table 2.1: Conventional Newton Systems.

Carrier points	Relations	
	Kinematic	Dynamic
compact radio sources (quasers)	position catalogue (including proper motion, etc.)	cosmology
stars	position catalogue (including proper motion, etc.)	stellar dynamics
planets	planet ephemerides	planet theory
moon	moon ephemerids	moon theory
artificial satellites	satellite ephemrides	satellite orbit theory

the physical structure and all numerical values of these parameters which are necessary to describe the mathematical-physical foundation of the reference systems. Obviously, most of the elements of such a reference system are, to a certain amount, arbitrary. One has to decide by convention how the reference system has to be constructed. Conventional kinematical and dynamical reference systems are not used exclusively but frequently in a certain combination. One has to keep in mind that this procedure can cause inconsistencies. Frequently used conventional Newton systems are space fixed ecliptic systems with the origin at the heliocenter or space fixed equator systems with the origin at the geocenter.

2.4.4.2 Conventional Terrestrial Reference System (CTRS)

A similar procedure as before to define conventional celestial reference system is necessary to define "Earth fixed" Galilei systems. In case of a rigid Earth, any Earth fixed triad is suitable for the definition of a

conventional terrestrial reference system. Because of the fact that the Earth is deformable and certain parts of the Earth move with respect to other parts, it is necessary to set up conditions for the definition of a terrestrial reference system. One possibility is (Kovalevsky and Müller 1989) to define it such that the overall rotation of certain parts of the Earth vanish ("no net rotation"). Another choice would be to define a conventional terrestrial reference system by material points of the Earth's surface such that these points only show deformations but no common rotations with respect to the adopted CTRS. Many other concepts are possible and have been proposed in the past. A certain concept for such a reference system (models, algorithms, constants, etc.) defines a "Conventional Terrestrial Reference System (CTRS)".

2.4.5 Conventional Reference Frames

With the choice of the system components, conventional reference systems are specified, conventional celestial reference system (CCRS) as well as conventional terrestrial reference systems (CTRS). Based on the basic system components, a certain number of representative points "fiducial points", have to be selected. These fiducial points are identical with the carrier points of the conventional reference systems. They must be available in a sufficient number and accessible to observation to connect to them and to derive the coordinates of other points. It is necessary to provide the coordinates of these points together with their time variations. Then materializations of a CCRS and a CTRS of a conventional celestial reference frame (CCRF) and a conventional terrestrial reference frame (CTRF) are available. Of special importance are the realizations of the International Earth Rotation Service (IERS). The IERS reference system contains the IERS standards and the IERS reference coordinate systems. The IERS standards contain a set of constants and models published in the IERS conventions 2003 (McCarthy and Petit 2003), e.g. the IAU 2000A/B precession theory and the IERS 2000A/B nutation theory, rates of continental drift, gravity constants, etc., which are used by the IERS. The IERS reference coordinate systems consist of:

- **I**nternational **T**errestrial **R**eference **F**rame (**ITRF**) and the
- **I**nternational **C**elestial **R**eference **F**rame (**ICRF**).

Both coordinates systems are realized by lists of coordinates of reference points, terrestrial collocation points or compact extra galactic radiation sources and its epochs. These frames and its mutual transformations are explained in more detail in Sec. 2.5.

2.4.5.1 Conventional Celestial Reference Frame (CCRF)

The stellar conventional celestial reference frame which is important in astronomy and geodesy and which is accessible with the techniques of geodetic astronomy is the fundamental catalogue FK5. The conventions of the FK5 are referred to the epoch J2000.0 (Julian date 2000.0). The axes coincide with a mean equatorial system, i.e. the x- and y-axes are located in so-called mean (dynamical) vernal equation. The stars are given by spherical polar coordinates α (right ascension) and δ (declination). These coordinates, the proper motions of the stars and various quantities are given in the FK5. The FK5 has been introduced end of the eighties. It contains 1535 stars; an FK5-extension is being prepared and shall contain around 3000 additional stars. More details on the FK5 can be found in Fricke (Fricke et al. 1988).

Of special importance is the International Celestial Reference Frame (ICRF). A detailed description is given in the IERS conventions 2003 (McCarthy and Petit 2003). The origin of the ICRF coincides with the barycenter of the solar system and the directions of the axes are fixed with respect to extragalactic radio sources. The accuracy of the axes is approximately 0.0001. The J2000.0 equatorial coordinates of extragalactic objects are determined from Very Long Baseline Interferometry (VLBI) observations. The $z-$axis corresponds to the (mean) Earth rotation axis at epoch J2000.0. The motion of the rotation axis in space is determined by the theories for precession and nutation (IAU 2000A/B), adopted by the International Astronomical Union (IAU). The VLBI analysis provide corrections to the conventional IAU models for

precession and nutation (Seidelmann 1980). The $x-$axis coincides with the intersection of the equatorial plane with the ecliptic plane. It is directed to the vernal equinox and is referred also to the epoch J2000.0. The change of this intersection line in time is determined also by the IAU-theories of precession and nutation. The $y-$axis is orthogonal to the $z-x-$plane and builds a right hand oriented system. ICRF is a frame whose directions are consistent with those of the fundamental catalogue FK5 within the observation accuracy of approximately 0.01 (Fricke et al. 1988).

2.4.5.2 Conventional Terrestrial Reference Frame (CTRF)

Especially for GPS users, the so-called World Geodetic System 84 (WGS84) is still very important. The user adopts this frame automatically if he uses the broadcast ephemeris predicted by the GPS control segment. Besides the errors of the orbit determination for the GPS satellites, the falsifications of the orbit parameters by the owner of the Global Positioning System reduce the accuracy of a connection to WGS84 to approximately a couple of meters. WGS84 is a terrestrial reference frame represented by the system satellites as carrier marks. Therefore, the orbit dynamics is included in the frame definition. The frame has its origin in the geocenter and the orientation of the coordinate axes is defined by a modification of the coordinate system NSWZ9z-c from the Defense Mapping Agency of the USA (DMA).

An alternative to get improved results consists in determining precise ephemerides by a network of globally distributed tracking stations. Such a network is run by DMA consisting of the five ground stations of the control segment and five additional tracking stations globally distributed. Besides, there exist some private tracking networks, or being established. Important is the Cooperative International GPS Network and the International GNSS Service (IGS). The precise ephemerides based on these tracking networks enable a much better realization of WGS84 than based on the predicted ephemerides of the GPS control segment.

Another conventional terrestrial reference frame is the ITRF (International Terrestrial Reference Frame) of the International Earth Rotation Service (IERS). It is a realization of the International Terrestrial Reference Frame (ITRF). The frame is materialized by a network of tracking stations whose position coordinates have been derived from a combination of laser ranging to satellites and to the moon, from VLBI observations, from GPS measurements and others. The origin, the orientation of the coordinate system and the scale of ITRF are implicitly defined by the coordinates of the observation stations. The origin of ITRF is the geocenter; the accuracy is in the size of a couple of centimeters. The $z-$axis coincides with the mean rotation axis of the Earth defined by the International Reference Pole (IRP). The $y-$axis is in the 0° International Reference Meridian (IRM) plane, which is defined by the adopted longitudes of the reference stations. IRP and IRM coincide with the corresponding directions of the BIH Terrestrial System (BTS) 1984 within an accuracy of 0.003. The BIH Reference Pole was adjusted to the CIO 1967 (Conventional International Origin) with an accuracy of approximately 0.03. Changes of the positions in time caused by plate tectonics or shift vectors are derived from repeating measurements. IERS publishes updates to the reference station coordinates, including shift vectors, as far as they are available. The solutions for every year are marked by the year code, e.g. ITRF2000.

2.5 Transformation between Celestial and Terrestrial Reference Frames

The transformation between conventional reference frames (CCRF) and conventional terrestrial reference frames (CTRF) could be performed by three rotations in space with three time-dependent angles, e.g. Eulerian angles or Cardano's angles. There are various theoretical reasons why this total rotation is split up in a series of successive rotations. There are two basic steps:

- Transformation from the mean celestial reference frame at epoch $T_0 = J2000.0$ to the true celestial reference frame at epoch T; these transformations include the transformations due to precession and due to nutation:

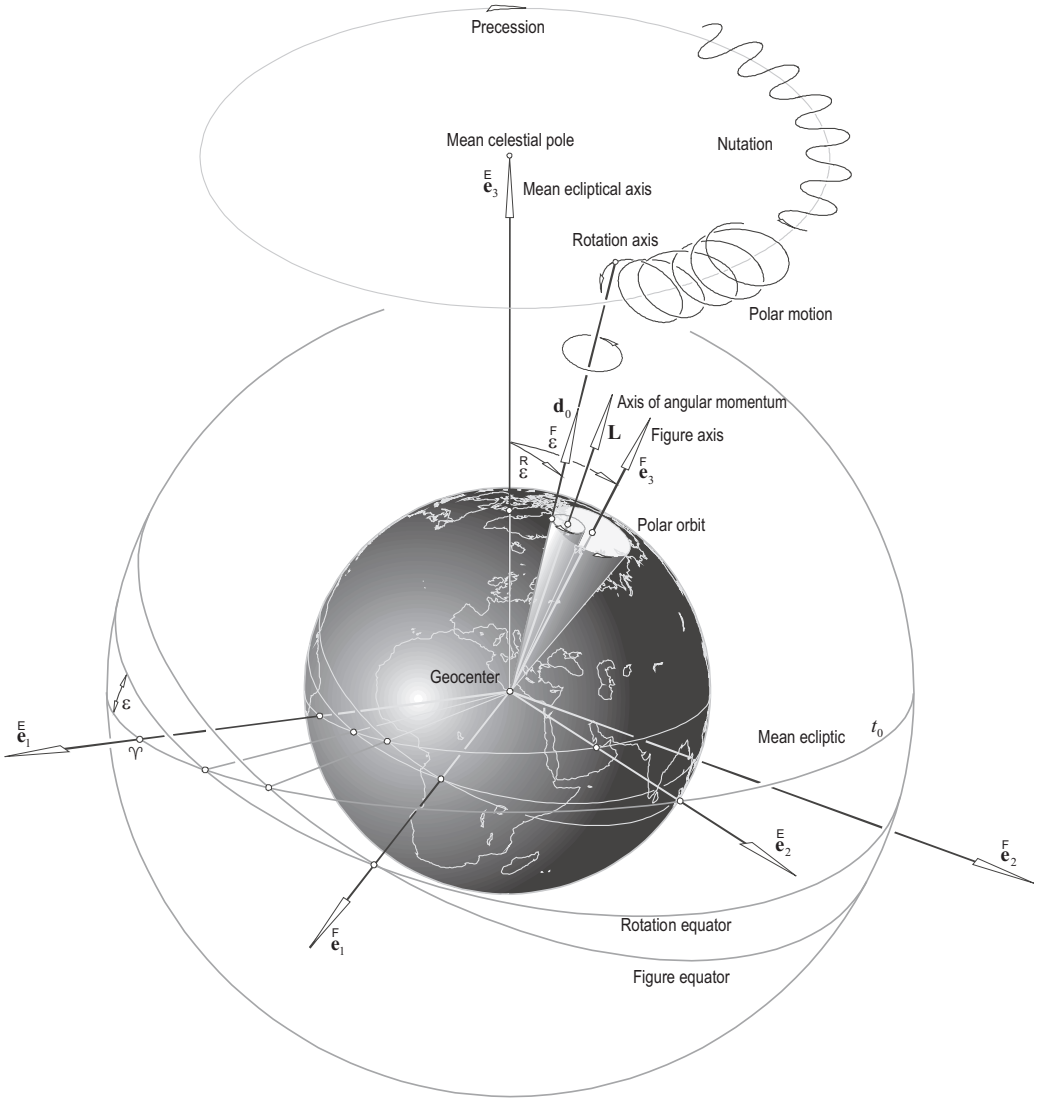

Figure 2.2: Celestial and Terrestrial Reference Frames.

- transformation from the mean celestial reference frame at epoch $T_0 = J2000.0$ (CCRF T_0) to the mean celestial reference frame at epoch T (CCRF T): ***precession,***
- transformation from the mean celestial reference frame at epoch T (CCRF T) to the true celestial reference frame at the same epoch T (CRF T): ***nutation,***

- Transformation from the true celestial reference frame at epoch T to the conventional terrestrial reference frame at epoch T; these transformations include the transformations due to the daily rotation and due to the polar motion:
  - transformation from the true celestial reference frame at epoch T (CRF T) to the true terrestrial reference frame at the epoch T (TRF T): ***daily rotation,***
  - transformation from the true terrestrial reference frame at epoch T (TRF T) to the conventional reference frame at the epoch T (CTRF T): ***polar motion.***

The total transformation of the orthogonal Cartesian coordinates referred to the frame (CCRF T_0) to coordinates referred to the frame (CTRF T) is given by the rotation matrix:

$$\begin{pmatrix} x \\ y \\ z \end{pmatrix}_{\text{CTRF } T} = \mathbf{S}(\text{GAST}, y_P, x_P)\mathbf{N}(\varepsilon, -\Delta\psi, -\varepsilon - \Delta\varepsilon)\mathbf{P}(-\zeta_A, \vartheta_A, -z_A) \begin{pmatrix} x \\ y \\ z \end{pmatrix}_{\text{CCRF } T_0} . \tag{2.8}$$

The first transformation from the mean celestial reference frame at epoch $T_0 = J2000.0$ (CCRF T_0) to the mean celestial reference frame at epoch T (CCRF T) is due to the general (lunisolar and planetary) precession between the epochs $T_0 = J2000.0$ and T (precession matrix),

$$\mathbf{P}(-\zeta_A, \vartheta_A, -z_A) := \mathbf{R}_3(-z_A)\mathbf{R}_2(\vartheta_A)\mathbf{R}_3(-\zeta_A). \tag{2.9}$$

The equatorial precession parameters for precession between the epoch T_0 and epoch T are given by the IERS conventions 2003 (McCarthy and Petit 2003):

$$\begin{aligned} \zeta_A &= 2.5976176'' + 2306.0809506''t + 0.3019015''t^2 + 0.0179663''t^3 - 0.0000327''t^4 - 0.0000002''t^5, \\ \vartheta_A &= 2004.1917476''t - 0.4269353''t^2 - 0.0418251''t^3 - 0.0000601''t^4 - 0.0000001''t^5, \\ z_A &= -2.5976176'' + 2306.0803226''t + 1.0947790''t^2 + 0.0182273''t^3 + 0.0000470''t^4 - 0.0000003''t^5, \end{aligned} \tag{2.10}$$

where the time difference t is given in Julian Centuries of TDB (Barycentric Dynamical Time) according to:

$$t = (T - J2000.0)/36525.0, \tag{2.11}$$

and T is given in Julian years of TDB. These parameters are based on a numerical model adopted by the IAU in 2000.

The second transformation from the mean celestial reference frame at epoch T (CCRF T) to the true celestial reference frame at the same epoch T (CRF T) is due to astronomic nutation at the epoch T. It can be computed by the following combination of rotations (nutation matrix):

$$\mathbf{N}(\varepsilon, -\Delta\psi, -\varepsilon - \Delta\varepsilon) := \mathbf{R}_1(-\varepsilon - \Delta\varepsilon)\mathbf{R}_3(-\Delta\psi)\mathbf{R}_1(\varepsilon). \tag{2.12}$$

The rotations contain the mean obliquity of the ecliptic ε and the astronomic nutation components in longitude $\Delta\psi$ and in obliquity $\Delta\varepsilon$, respectively. The mean obliquity of the ecliptic at epoch T, ε, which represents the rotation angle from the mean ecliptic system to the mean equator systems, is calculated by:

$$\varepsilon = 23^\circ 26' 21.448'' - 46.8150''t - 0.00059''t^2 + 0.001813''t^3. \tag{2.13}$$

The true obliquity of the ecliptic at epoch T is given by the sum $\varepsilon + \Delta\varepsilon$. The astronomic nutation components in longitude $\Delta\psi$ and in obliquity $\Delta\varepsilon$, respectively, are calculated by series expansions, according to the above mentioned theory. The first terms read:

$$\begin{aligned} \Delta\psi &= (-17.1996'' - 0.01742''t)\sin(\Omega) + (0.2062'' + 0.00002''t)\sin(2\Omega) + \cdots, \\ \Delta\varepsilon &= (9.2025'' + 0.00089''t)\cos(\Omega) + (-0.0895'' + 0.00005''t)\cos(2\Omega) + \cdots. \end{aligned} \tag{2.14}$$

The complete series terms are given, e.g. in the IERS conventions 2003 (McCarthy and Petit 2003), as well as an improved theory of precession and nutation. The final transformation from the true celestial reference frame at epoch T (CRF T) to the conventional terrestrial reference frame at epoch T (CTRF T) includes a first rotation due to the daily rotation expressed by the Greenwich Apparent Sidereal Time (GAST) and two rotations around small angles due to the polar motion, expressed by the polar coordinates (x_P, y_P):

$$\mathbf{S}(\text{GAST}, -y_P, -x_P) := \mathbf{R}_2(-x_P)\mathbf{R}_1(-y_P)\mathbf{R}_3(\text{GAST}). \tag{2.15}$$

The coordinate systems involved are illustrated in Fig. 2.2 (Ilk 2007). The true celestial reference frame (CRF T) is defined by the true celestial equator and the true Celestial Intermediate Pole (CIP) of epoch

T. The Conventional Terrestrial Reference Frame (CTRF T) is defined by the conventional mean terrestrial equator and the Conventional Terrestrial Pole (CTP) at the same epoch T. The position of CIP with respect to CTP is described by the parameters of polar motion (polar coordinates), x_P, y_P. The angle between the $x-$axis of CTRF (which is in the Greenwich mean astronomical meridian) is defined by the Greenwich hour angle of the true vernal equinox, the Greenwich Apparent Sidereal Time (GAST). GAST is changing continuously because of the rotation of the Earth but not completely uniformly. The GAST can be calculated from the Greenwich Mean Sidereal Time (GMST) and GMST itself by a time polynomial from the difference of the Universal Time 1 ($UT1$), which can be derived from observations and an atomic time scale, the Universal Time Coordinated (UTC):

$$\Delta t = UTC - UT1. \tag{2.16}$$

The integration of Δt over one day results in changes of the Length Of Day (LOD). The time difference Δt cannot be expressed by an analytical formula and is published together with the polar coordinates x_P, y_P by IERS.

A consistent system of reference frames, as for example the IERS reference coordinate frames consisting of the **I**nternational **T**errestrial **R**eference **F**rame (**ITRF**) and the **I**nternational **C**elestial **R**eference **F**rame (**ICRF**), include also the relations between these frames to be able to transform between these frames. The basic transformations are identical to those sketched before. A detailed description of the transformations between the current IERS reference frames, ICRF and ITRF, are given in the IERS conventions 2003 (McCarthy and Petit 2003). The (numerical) deviations from the more general transformation models given above are outlined in this publication. From the point of view of a *conventional reference system*, that means from the model point of view, there are only minor differences. The IERS Earth Oriented Parameter (EOP) describe the rotation of ITRF with respect to ICRF based on the conventional model of precession and nutation; they model the non-predictable portions of the Earth rotation. The polar coordinates x_P and y_P describe the Celestial Intermediate Pole (CIP) with respect to the IERS Reference Pole (IRP) (see Fig. 2.2). The CIP deviates from the true rotation axis by quasi-daily fluctuations with amplitudes below 0.01. The $x-$axis is directed to the IERS Reference Meridian (IRM); the $y-$axis is orthogonal to the $x-$axis in a westerly direction. $UT1$ is related to the Greenwich Mean Sidereal Time (GMST) by conventions; it defines the orientation of the IRM within ICRF, countable around the CEP-axis. $UT1$ is represented by the difference to very uniform atomic time scale, TAI, by $UT1 - TAI$; the instability of TAI is about six orders of magnitudes smaller than those of $UT1$.

2.6 Overview of GPS Observations

GPS observables are either ranges which are deduced from the measured travel times of electro-magnetic wave signals between the GPS satellites and the receivers or phase differences based on a comparison between the received electro-magnetic wave signals from GPS satellites and the signals which are generated in the receivers. Unlike the classical terrestrial electronic distance measurement, GPS uses the "one way concept" where two clocks are used, one is located in the GPS satellite and the other in the receiver. Thus, the ranges are biased by the satellite and receiver clock errors and, consequently, they are denoted as pseudo-ranges (Hofmann-Wellenhof et al. 2001). Obviously, the measured pseudo-range is different from the geometrical distance between the antenna at the GPS satellite and the receiver's antenna because of the errors of both clocks, the influence of the transmission medium and other physical influences on the GPS signals. It is also notable that the path of the signal transmission differs slightly from the geometric signal propagation path. The medium not only delays the signal, but also bends the path of the transmitting signal (Gao and Wojciechowski 2004). For GPS satellites, three basic observables can be identified:

- Code pseudo-range observations,
- Carrier phase observations and
- Doppler observations.

They will be discussed in more details in the following sections.

2.6.1 Code Pseudo-range Observables

Pseudo-ranges derived from code measurements are the fundamental observables in a code dependent receiver (Seeber 2003). The code sequence, generated in the receiver, is shifted stepwise against the code sequence, received from the satellite, until a maximum correlation is achieved. At the moment of maximum correlation, the internal code sequence is measured in the receiver time frame (Seeber 2003). The signal emission time of the GPS satellite is denoted by t^s, and the GPS signal reception time at the receiver by t_r. In the case of vacuum and an error free situation, the measured pseudo-range is equal to the geometrical distance and can be derived from (Xu 2007),

$$P_r^s(t_r, t^s) = (t_r - t^s)c, \tag{2.17}$$

where c is the speed of light and the subscripts r and s denote the receiver and GPS satellite, respectively. t^s and t_r are considered as true emission and reception times of the GPS signal. Taking both, GPS satellite and receiver clock errors, into account then the pseudo-range can be represented by,

$$P_r^s(t_r, t^s) = (t_r - t^s)c + [\delta t_r(t_r) - \delta t^s(t^s)]c, \tag{2.18}$$

where $\delta t_r(t_r)$ and $\delta t^s(t^s)$ denote the clock errors of the receiver and the GPS satellite, respectively. The GPS satellite clock error $\delta t^s(t^s)$ is known from the GPS satellite orbit determination procedure, performed by the IGS analysis centers. The receiver clock offset can be estimated within the GPS data processing in case of precise point positioning or it can be modeled in case of lower accuracy demands from the coefficients received from the navigation message. Considering the influences of the transmitting medium, e.g. the ionospheric, tropospheric, as well as the multi-path effects and other model corrections, e.g. Earth and ocean tide loading effects, relativistic effects and antenna mass center offsets as well as remaining error effects, the code pseudo-range observable at frequency i can be written as (Xu 2007),

$$\begin{aligned} P_{r,i}^s(t_r, t^s) = \rho_r^s(t_r, t^s) + [\delta t_r(t_r) - \delta t^s(t^s)]c + I_i^r(t_r) + d_O^s(t_r) + d_{Tr}^r(t_r) + d_{Ti}^r(t_r) + d_{C,i}^r(t_r) + \\ + d_{V,i}^r(t_r) + \ d_R^r(t_r) - d_R^s(t_r) + d_{M,P_i}(t_r) + \varepsilon_{r,P_i}^s. \end{aligned} \tag{2.19}$$

The measured code pseudo-range at frequency i at the left-hand side represents the geometrical distance between the satellite s at the signal emission time t^s and the GPS receiver antenna r at the reception time t_r as well as several correction terms as,

$I_i^r(t_r)$, $d_{Tr}^r(t_r)$	the ionospheric path delay at frequency i and the tropospheric effect, respectively,
$d_{Ti}^r(t_r)$	the Earth tide and ocean loading effects,
$d_O^s(t_r)$	orbital error of s^{th} GPS satellite at time t_r,
$d_{C,i}^r(t_r)$, $d_{V,i}^r(t_r)$	the receiver antenna phase center offset and its variation,
$d_R^r(t_r)$, $d_R^s(t_r)$	the special relativistic effects of the receiver r and GPS satellite s,
$d_{M,P_i}(t_r)$, ε_{r,P_i}^s	the multi-path effect on code pseudo-range observation and remaining (un-modeled) errors in the code pseudo-range observation model.

The GPS signal travel time between the GPS satellite s and the GPS receiver r, based on the corresponding geometrical distance $\rho_r^s(t_r, t^s)$, can be written

$$\tau_r^s = \rho_r^s(t_r, t^s)/c, \tag{2.20}$$

with taking frequency and time stability of the GPS satellites and GPS signal travel time into account, the GPS satellite clock offset reads,

$$\delta t^s(t^s) = \delta t^s(t_r - \tau_r^s) \approx \delta t^s(t_r). \tag{2.21}$$

If we assume that all error effects of the receiver r and the GPS satellite s have been considered, either by specified models or by elimination through the data combination procedures, then the error effects can be summarized as follows,

$$\begin{aligned} e_{r,P_i}^s(t_r) = -c\delta t^s(t_r - \tau_r^s) + I_i^r(t_r) + d_O^s(t_r) + d_{Tr}^r(t_r) + d_{Ti}^r(t_r) + d_R^r(t_r) - d_R^s(t_r) + \\ + d_{C,i}^r(t_r) + d_{V,i}^r(t_r). \end{aligned} \tag{2.22}$$

The observation equation can be written with the error term from Eq. (2.22) inserted into Eq. (2.19),

$$P^s_{r,i}(t_r) = \rho^s_r(t_r, t^s) + c\delta t_r(t_r) + d_{M,P_i}(t_r) + e^s_{r,P_i}(t_r) + \varepsilon^s_{r,P_i}. \tag{2.23}$$

The above discussed code pseudo-range model is generally valid for both C/A and P code pseudo-range observations. The precision of the code pseudo-range measurements depends on the electronic characteristics. Nowadays, it is no problem to measure with a precision of up to 1% of the chip wavelength. This corresponds to a precision of about $3m$ for the C/A code and of $30cm$ for the P-code observations (Xu 2007).

2.6.2 Carrier Phase Observables

The carrier phase observable is the measurement of the phase of the received satellite signal relative to the receiver generated phase at the reception time. The observable is the difference between the transmitted and the doppler shifted carrier phase, defined in the satellite time frame, and the phase of the reference signal, defined in the receiver time frame (Seeber 2003). The number of full carrier phase waves between the receiver and the GPS satellite cannot be accounted for at the initial signal acquisition time. Therefore, the measured carrier phase is the measurement of the fractional phase and it is necessary to register changes in the cycles. The carrier phase observable results from an accumulated carrier phase observation process. The fractional carrier phase can be measured electronically with a precision of better than 1% of the carrier phase wavelength, which corresponds to a millimeter precision. This is the reason why the carrier phase measurement is more precise than the code pseudo-range observation. A full carrier wave is called a cycle. The ambiguity integer number of cycles in the carrier phase measurement is called ambiguity parameter. The measurement consists of a correct fractional phase and an arbitrary integer cycle count setting at the start epoch. Such an arbitrary initial cycle of carrier phases will be adjusted to the correct one by modeling an ambiguity parameter (Xu 2007). Note that the receiver, the GPS satellite clock offset, the atmospheric delay, the ambiguity parameter and the hardware signal delay at the receiver and at the satellite are linear dependent. Hence, ambiguity fixing is not a trivial problem (Wuebbenna et al. 2001). In the vacuum or an error-free situation, the measured carrier phase can be written as (Xu 2007),

$$\phi^s_r(t_r) = \phi_r(t_r) - \phi^s(t_r) + N^s_r, \tag{2.24}$$

where the subscripts r and s denote the receiver and the GPS satellite, respectively. ϕ_r, ϕ^s and N^s_r are the phases of the receiver oscillator and the received signal phase of the GPS satellite as well as the ambiguity related to the receiver and the GPS satellite. The received phase of the satellite signal at the reception time is exactly the same as the phase of the emitted satellite signal at the emission time (Remondi 1984, Leick 1995)

$$\phi^s(t_r) = \phi^s_e(t_r - \tau^s_r), \tag{2.25}$$

where ϕ^s_e and τ^s_r denote the emitted phase of the GPS satellite and the travel time of the signal, respectively. The Eq. (2.24) can be rewritten as,

$$\phi^s_r(t_r) = \phi_r(t_r) - \phi^s_e(t_r - \tau^s_r) + N^s_r. \tag{2.26}$$

Suppose the initial time is t_0 and the received satellite signal and the reference carrier of the receiver have the nominal frequency f then the carrier phase measurement with the GPS satellite clock offset δt^s and the receiver clock error δt_r reads,

$$\begin{aligned} \phi_r(t_r) &= \phi_r(t_0) + f(t_r + \delta t_r(t_r) - t_0 - \delta t_r(t_0)), \\ \phi^s_e(t_r - \tau^s_r) &= \phi^s(t_0) + f(t_r + \delta t^s(t_r - \tau^s_r) - \tau^s_r - t_0 - \delta t^s(t_0)), \\ \tau^s_r &= \rho^s_r(t_r, t^s)/c. \end{aligned} \tag{2.27}$$

Inserting Eq. (2.27) in Eq. (2.26), then the observed carrier phase can be rewritten as,

$$\begin{aligned} \phi^s_r(t_r) &= \phi_r(t_0) + f(t_r + \delta t_r(t_r) - t_0 - \delta t_r(t_0)) - [\phi^s(t_0) + f(t_r + \delta t^s(t_r - \tau^s_r) - \tau^s_r - t_0 - \delta t^s(t_0))] + N^s_r \\ &= f\rho^s_r(t_r, t^s)/c + f(\delta t_r(t_r) - \delta t^s(t_r - \tau^s_r)) + \phi_r(t_0) - \phi^s(t_0) - f\delta t_r(t_0) + f\delta t^s(t_0) + N^s_r. \end{aligned} \tag{2.28}$$

If we assume A_r^s as real ambiguity parameter between the GPS satellite and the receiver:

$$A_r^s = N_r^s + \phi_r(t_0) - \phi^s(t_0) - f\delta t_r(t_0) + f\delta t^s(t_0), \tag{2.29}$$

and taking the special relativistic effect, the medium errors (e.g. tropospheric and ionospheric effects), multipath and ocean and the Earth tide loading into account, then Eq. (2.28) can be expressed in the cycle unit at frequency i (f_i) as:

$$\begin{aligned}\phi_{r,i}^s(t_r) = \rho_r^s(t_r,t^s)f_i/c + f_i[\delta t_r(t_r) - \delta t^s(t_r - \tau_r^s)] + A_{r,i}^s + \frac{1}{\lambda_i}[-I_i^r(t_r) + d_O^s(t_r) + d_{Tr}^r(t_r) + d_{Ti}^r(t_r) + \\ + d_{C,i}^r(t_r) + d_{V,i}^r(t_r) + d_R^r(t_r) - d_R^s(t_r) + d_{M,\phi_i}(t_r)] + \varepsilon_{r,\phi_i}^s,\end{aligned} \tag{2.30}$$

or in units of length,

$$\begin{aligned}\Phi_{r,i}^s(t_r) = \lambda_i\phi_{r,i}^s(t_r) = \rho_r^s(t_r,t^s) + c[\delta t_r(t_r) - \delta t^s(t_r - \tau_r^s)] + \lambda_i A_{r,i}^s - I_i^r(t_r) + d_O^s(t_r) + \\ + d_{Tr}^r(t_r) + d_{Ti}^r(t_r) + d_{C,i}^r(t_r) + d_{V,i}^r(t_r) + \ d_R^r(t_r) - d_R^s(t_r) + d_{M,\Phi_i}(t_r) + \varepsilon_{r,\Phi_i}^s.\end{aligned} \tag{2.31}$$

If we assume that all error effects of the receiver r and the GPS satellite s have been considered, either by specified models or by elimination through the data combination procedures, then the error effects can be summarized as follows,

$$e_{r,\Phi_i}^s(t_r) = -c\delta t^s(t_r - \tau_r^s) - I_i^r(t_r) + d_O^s(t_r) + d_R^r(t_r) - d_R^s(t_r) + d_{C,i}^r(t_r) + d_{V,i}^r(t_r). \tag{2.32}$$

The observation equation can be written with the error term from Eq. (2.32) inserted into Eq. (2.31),

$$\Phi_{r,i}^s(t_r) = \rho_r^s(t_r,t^s) + c[\delta t_r(t_r) - \delta t^s(t_r - \tau_r^s)] + \lambda_i A_{r,i}^s + d_{M,\Phi_i}(t_r) + e_{r,\Phi_i}^s(t_r) + \varepsilon_{r,\Phi_i}^s. \tag{2.33}$$

During GPS signal tracking, the phase and integer accounts are continuously modeled and frequently measured. In this way, the changing oscillator frequency is accounted for. Every time the phase is measured, the coefficient in the tracking loop model is updated to ensure a sufficient precision of the measurement (Remondi 1984).

2.6.3 Doppler Observables

The Doppler effect is a frequency shift phenomenon of the electromagnetic wave, caused by the relative motion of the emitter and receiver. Some of the first solution strategies proposed for GPS were based on the Doppler effect as observable for the TRANSIT system. This system used the integrated Doppler shifts (i.e. the phase differences) which were scaled to the ranges (Hofmann-Wellenhof et al. 2001). Suppose the emitted signal has the nominal frequency f then the radial velocity of the GPS satellite with respect to the receiver is,

$$v_\rho = \mathbf{v}.\mathbf{u}_\rho = \|\mathbf{v}\|\cos\alpha, \tag{2.34}$$

with

- $\mathbf{v}$ the velocity vector relative to the receiver,
- $\mathbf{u}_\rho$ the unit vector directing from the receiver to the GPS satellite,
- α the projection angle of the satellite velocity vector to the receiver-satellite direction and
- ρ the distance between the GPS satellite and the receiver.

Then the frequency of the received signal reads (Xu 2007):

$$f_\rho = f(1 + \frac{v_\rho}{c})^{-1} \approx f(1 - \frac{v_\rho}{c}), \tag{2.35}$$

and the Doppler frequency shift can be written as,

$$f_D = f - f_\rho \approx f\frac{v_\rho}{c} = \frac{v_\rho}{\lambda} = \frac{d\rho}{\lambda dt}. \tag{2.36}$$

The Doppler count (or integrated Doppler shift) is the integral of the frequency shift over a specific time interval (e.g. one minute). If the time interval is small enough, then the Doppler count is identical to the instantaneous frequency shift,

$$D = f_D = \frac{d\rho}{\lambda dt}. \tag{2.37}$$

An approximate Doppler frequency shift is required to get the GPS satellite signal. The prediction of D is part of the GPS signal tracking process. D is used to predict the phase change first, then the phase change is compared with the measured value to get the precise value of the Doppler frequency shift. The accumulated integer account of cycles is obtained through a polynomial fitting of a series of predicted phase changes and the measured values (Remondi 1984). Therefore, the Doppler frequency shift is a by-product of the carrier phase measurements. However, the Doppler frequency is an independent observable and a measurement of the instantaneous range-rate (Xu 2007). Notice that in an error-free environment the Doppler observable can be written as,

$$D = \frac{d\Phi}{\lambda dt} = \frac{d\rho_r^s(t_r, t^s)}{\lambda dt} - f\frac{d(\delta t_r - \delta t^s)}{dt} + R_f + \zeta, \tag{2.38}$$

with

D	the Doppler frequency shift,
f, λ	the frequency and the wavelength of the GPS signal, respectively,
R_f	the frequency correction of the relativistic effect,
ζ	the measurement error.

Effects with low frequency properties such as ionospheric, tropospheric, multi-path and tide effects are canceled out (Xu 2007).

2.7 The Corrections and Error Sources on the GPS Observations

2.7.1 Signal Travel Time and Sagnac Effect

The GPS observations (code pseudo-range and carrier phase) can be considered in a simplified way as geometrical distances ρ from the GPS satellite at the signal emission time to the receiver at the signal reception time. In case of the Precise Point Positioning (PPP) method, the precise satellite ephemerides (precise coordinates and the clock offset) provided by the IGS center must be corrected for the signal travel time. Then it is necessary to correct the observation time (epoch) t by subtracting the travel time of the signal to obtain the signal emission time and subsequently the GPS satellite position and its clock offset at the emission time. Therefore, it is necessary to compute the signal travel time through an iterative process. The computation of the GPS satellites position at the time of the signal transmission $\mathbf{r}(t - \tau_r^s)$ can be performed either by an interpolation of adjacent position values (e.g. by a Chebyschev interpolation method) or by a Taylor expansion,

$$\mathbf{r}(t - \tau_r^s) \approx \mathbf{r}(t) - \dot{\mathbf{r}}(t)\tau_r^s + \frac{1}{2}\ddot{\mathbf{r}}(t)(\tau_r^s)^2, \tag{2.39}$$

where $\dot{\mathbf{r}}(t)$ and $\ddot{\mathbf{r}}(t)$ are velocity and acceleration of the satellite at the time t. The travel time iteration is usually performed in an inertial system with the inertial receiver position $\mathbf{r}_{ICRF}$ and the inertial GPS satellite position vector $\mathbf{r}_{ICRF}^s$. It is necessary to transform the receiver positions from the inertial reference frame (ICRF) to the terrestrial reference frame (ITRF). The signal path given by Montenbruck (Montenbruck and Gill 2000) reads,

$$\rho_r^s(t_r, t^s) = \left\| \mathbf{R}_{ITRF}(t)(\mathbf{r}_{ICRF}^s(t - \tau_r^s) - \mathbf{r}_{ICRF}(t)) \right\|, \tag{2.40}$$

where $\mathbf{R}_{ITRF}(t)$ is the rotation matrix from the ICRF to the ITRF at epoch t. With the approximation,

$$\mathbf{R}_{ITRF}(t) \approx \mathbf{R}_z(\omega_e \tau_r^s)\mathbf{R}_{ITRF}(t - \tau_r^s), \tag{2.41}$$

where $\mathbf{R}_z$ is the rotation matrix causing a rotation around the z-axis of the ITRF and ω_e the angular velocity of the Earth. The inertial position of the GPS satellite can be substituted by the corresponding ITRF position, so that it follows,

$$\mathbf{r}^s_{ITRF}(t - \tau_r^s) = \mathbf{R}_{ITRF}(t - \tau_r^s)\mathbf{r}^s_{ICRF}(t - \tau_r^s). \tag{2.42}$$

The geometrical distance between the sender (GPS) and the receiver reads in ITRF,

$$\rho_r^s(t_r, t^s) = c\tau_r^s = \left\| \mathbf{R}_z(\omega_e \tau_r^s)\mathbf{r}^s_{ITRF}(t - \tau_r^s) - \mathbf{r}_{ITRF}(t) \right\|, \quad \mathbf{r}^s_m(t) = \mathbf{R}_z(\omega_e \tau_r^s)\mathbf{r}^s_{ITRF}(t - \tau_r^s). \tag{2.43}$$

The rotation matrix, $\mathbf{R}_z(\omega_e \tau_r^s)$, is necessary if the coordinates are referred to the ITRF (Strang and Borre 1997). The correction related to the rotation of the Earth is called Sagnac correction (Xu 2007). From Eq. (2.43) we see that when using the LEO coordinates in the ITRF system, one has to rotate the GPS satellite position vector around the z-axis. The amount equals the angular rotation of the earth in the time the signal needs to travel from the GPS satellites to the GPS receiver on-board LEO. For example, the altitude of a GPS satellite is about $20200km$, thus the GPS signal travel time to the LEO satellite is about $66msec$ and the earth rotates within this time span at an amount of about 15 *arcsec*. Therefore, the angular displacement of the earth around its rotation axis during the signal travel is roughly 1 *arcsec*. So, if the earth rotation effect is not applied to the GPS satellite coordinates then the estimated LEO absolute positions will be biased by about 1 *arcsec* in longitude. Therefore, the Sagnac effect can be corrected by inserting the rotation matrix, i.e. $\mathbf{R}_z(\omega_e \tau_r^s)$, in the Eq. (2.43) to calculate the true range between the LEO and GPS satellites in the ITRF system. The signal transmitting time τ_r^s can be solved through iteration of Eq. (2.43). This procedure has been applied in the LEO precise orbit determination with the code pseudo-range and the carrier phase observations. This computation is not affected by the receiver and the GPS clock offset. However, the computed nominal emission time is corrupted by the ionospheric, hardware and multi-path errors. All these effects are negligible in the present context (Montenbruck and Gill 2000).

2.7.2 Tropospheric Delay Correction

Satellite signals travel through the atmosphere which affects the propagation of the signal by the ionosphere and the troposphere. Each effect influences the satellite signals differently. Since the troposphere is a non-dispersive medium, tropospheric refraction causes an identical effect on both code and carrier phase modulation. The neutral atmosphere, which is the non-ionized part of the atmosphere, can normally be divided into two components, the dry and the wet part of the troposphere. The dry component consists mainly of dry gases (normally referred to as the dry part), whereas the wet component is a result of water vapor. The hydrostatic fraction contributes 90% of the total tropospheric refraction (see Leick 1995p. 308). The tropospheric effect is frequency independent and cannot be eliminated by combination of the observations based on different frequencies as in case of the ionospheric effects. There are different models to compute the wet and the dry tropospheric components, e.g. the models of Saastamoinen and Hopfield as well as the modified Hopfield model. These models depend on the absolute temperature, the partial pressure of the dry gases, the water vapor (from relative humidity) and the receiver elevation to the GPS satellite. In other words, the tropospheric models are based on the physical information at the receiver and the geometric receiver-GPS constellation. The tropospheric path delay can be represented as a function of the zenith path delay (*zpd*) and the mapping function (e.g. Marini or Marini and Murray or Niell mapping function, etc.). For zero differenced (ZD) observables in case of a LEO, there is no tropospheric delay to be taken into account between the LEO and the GPS satellites (Švehla and Rothacher 2002). In case of double differenced (DD) observables between the IGS GPS ground stations and the LEO satellite(s), the tropospheric zenith path delay effect (*zpd*) must be modeled or estimated based on a properly selected mapping function within the least squares estimation procedure.

2.7.3 Ionospheric Delay

The ionosphere influences the electromagnetic waves traveling through the atmosphere from the GPS satellites to the receiver antenna. The effect varies inversely with the square of the frequency f of the signals and directly with the Total Electron Content(TEC). The TEC represents the total number of free electrons contained in a column with a cross section area of one square meter along the path of the signal between the satellite and the receiver. The ionosphere path delayed of the code pseudo-range (P) and time advanced of the carrier phase (ϕ) observations at frequency f can be represented as:

$$I_{P,f} = \frac{40.28}{f^2} TEC = -I_{\phi,f}. \tag{2.44}$$

It is noticeable that there are only few ionosphere models available to estimate the ionosphere effects. Examples are the ionosphere plate model, the daily cosine model and the ionosphere point model. The ionosphere coefficients of the cosine model is included in the navigation message components which can approximate only 50% of the actual ionospheric group delay. Because of the low precision of the ionosphere models, they cannot be used for precise point positioning tasks. Better results to eliminate the ionosphere path delay can be achieved by a combination of observables at different frequencies. In case of dual frequency observations, almost all of the ionosphere range errors can be removed from code pseudo-range and carrier phase observations by the following linear combination as(Leick 1995),

$$P_3 = n_1 P_1 + n_2 P_2, \quad \Phi_3 = n_1 \Phi_1 + n_2 \Phi_2, \quad n_1 = \frac{f_1^2}{f_1^2 - f_2^2}, \quad n_2 = -\frac{f_2^2}{f_1^2 - f_2^2}, \tag{2.45}$$

where P_i and Φ_i are the code pseudo-range and carrier phase observations at the frequency f_i; P_3 and Φ_3 are the ionosphere-free code pseudo-range and carrier phase observations, respectively. Even the most dominant ionosphere correction is the lowest order term ($\frac{1}{f^2}$), the higher order terms ($\frac{1}{f^3}$) and ($\frac{1}{f^4}$) might be important in case of an observation accuracy of a few millimeters to centimeters, respectively (Bassiri and Hajj 1992). If the code pseudo-range observations ($P^s_{r,1}, P^s_{r,2}$) and the carrier phase observations ($\Phi^s_{r,1}, \Phi^s_{r,2}$) between the GPS satellite s and the receiver r under the frequencies f_1 and f_2 are given, ionosphere parameter can be derived from the linear combination of the pseudo-range and carrier phase observations as,

$$P^s_{r,I} = P^s_{r,1} - P^s_{r,2} = (1-\alpha) I^r_1 + c(1-\alpha) T^s_{GD} + \varepsilon^s_{r,P_I}, \tag{2.46}$$

$$\Phi^s_{r,I} = \Phi^s_{r,1} - \Phi^s_{r,2} = -(1-\alpha) I^r_1 + \lambda_1 N^s_{r,1} - \lambda_2 N^s_{r,2} + \varepsilon^s_{r,\Phi_I}, \tag{2.47}$$

where $\alpha = \frac{f_1^2}{f_2^2}$. The largest part of the receiver clock offset cancels out in the code combination and T^s_{GD} is a constant over a period of time, as given in the broadcast message. The dual frequency carrier phase ionosphere-free combination can be used to detect cycle slips and outliers in the carrier phase observations. Since the ionospheric effect disrupts the code (time delaying) and carrier phase (time advancing) observations in the same way, it is possible to eliminate common ionospheric errors under the same frequency based on the combination,

$$P\Phi^s_{r,3} = \frac{P^s_{r,i} + \Phi^s_{r,i}}{2}. \tag{2.48}$$

$P\Phi^s_{r,3}$ (index $i = 3$) is the ionosphere-free observation under the frequency $f_i, i = 1, 2$. This combination can be used to estimate the precise point positioning of the LEOs, because the new model has a lower noise and feasibility of the fixed ambiguity estimation for both L_1 and L_2. The analysis process has to enable to estimate the ambiguity parameter of the new ionosphere-free combination (see Gao and Shen 2002).

2.7.4 Multi-path Effect

This effect is well described by its name: a signal emitted from the satellite arrives at the receiver along more than one path. Multi-path is mainly caused either by reflections at surfaces nearby the receiver, or by

reflections at the satellite during the signal transmission (e.g. in case of LEOs). The (indirect) multi-path GPS signals are caused by the offset in the carrier phase and by variations in the amplitudes relative to the (direct) GPS signal. The amplitude variation and phase offset are dependent on the conditions of the environment of the GPS satellite and the receiver as well as by the geometric constellation of these elements. The influence of the multi-path, however, can be estimated by using a combination of L_1 and L_2 code pseudo-range and carrier phase measurements. This holds because the troposphere, the clock error and the relativistic effects influence the code and carrier phases by the same amount. This is not the case for the ionospheric correction which is frequency dependent. By using the ionosphere-free code pseudo ranges (P_3) and carrier phases (Φ_3), and forming differences between P_3 and Φ_3 all mentioned effects except for the multi-path are canceled. The remaining part reflects the multi-path effect, apart from the noise (Hofmann-Wellenhof et al. 2001). Because of the geometrical constellation, it is obvious that signals received from low satellites are more susceptible to multi-path than those at high altitudes. Note also that code pseudo-ranges are more affected by multi-path than carrier phases (Hofmann-Wellenhof et al. 2001). Comparing single epochs, the multi-path effect may amount up to $10 - 20cm$ for code pseudo-ranges (Wells et al. 1987). On the carrier phases for relative positioning with short baseline this effect will not be greater than $1cm$ under good satellite geometry constellation and long observation intervals (Hofmann-Wellenhof et al. 2001). To reduce or estimate the multi-path effects, various methods are available which can be classified as follows,

- Antenna based mitigation,
- Improved receiver technology and
- Signal processing methods.

In the case of a LEO's data processing, high-low GPS-SST observations at low elevations are not corrupted by tropospheric refraction but multi-path effects may be an important source of degradation of low-elevation data. This is important particular for a LEO which may be tracked at zenith angles well above 90° up to 105° – 110°. A possibility to minimize the impact of multi-path is by using an elevation-dependent weighting scheme. Using all observations with properly selected weights, this procedure promises a gain of observation information for the kinematic solution (Bock 2003). For the processing of ground station observations, the weight function can be introduced as follows (Hugentobler et al. 2001),

$$w(z) = \cos^2(z), \tag{2.49}$$

where z is the zenith distance of the GPS satellite observed from the ground station. To analyse the GPS-SST data under the horizon of LEOs, the question arises whether these measurements help to improve the precise orbit determination in case of an appropriate weighting or whether they even reduce the accuracy of the solution. A simple modification of the weighting function in Eq. (2.49) is the introduction of a stretching factor, i.e. α (see Bock 2003),

$$w(z) = \cos^2(\alpha z). \tag{2.50}$$

Based on the results of Bock (Bock 2003) the stretching factor for CHAMP should read $\alpha = 1$ and the zenith cut-off angle 90° to improve the accuracy.

There are another methods, i.e. correction of multi-path effects in GPS observations with SNR data. The SNR data are available in CHAMP GPS-SST data from GFZ-ISDC in the standard RINEX format.

2.7.5 Antenna-Mass Center Offset Correction

The geometrical distance between the GPS satellite at the signal emission time and the receiver at the signal reception time is the distance of the phase centers of the two antennas. However, the orbit determination results, which describe the positions of the GPS satellite are referred to the mass center of the satellite. Therefore, a mass center correction has to be applied to the coordinates of the satellite position for precise

applications, especially for precise orbit determinations of the LEOs. A satellite fixed coordinate system shall be set up for describing the antenna phase center offset referring to the mass center of the satellite or vice versa. The origin of this coordinate system coincides with the mass center of the satellite (GPS satellite or LEO) and the z-axis is parallel to the direction antenna-Earth direction, the $y-$axis is parallel to the solar-panel axis, and the $x-$axis is selected to complete a right-hand coordinate system. A solar vector is a vector from the satellite mass center pointing to the Sun. During the motion of a GPS satellite, the z-axis

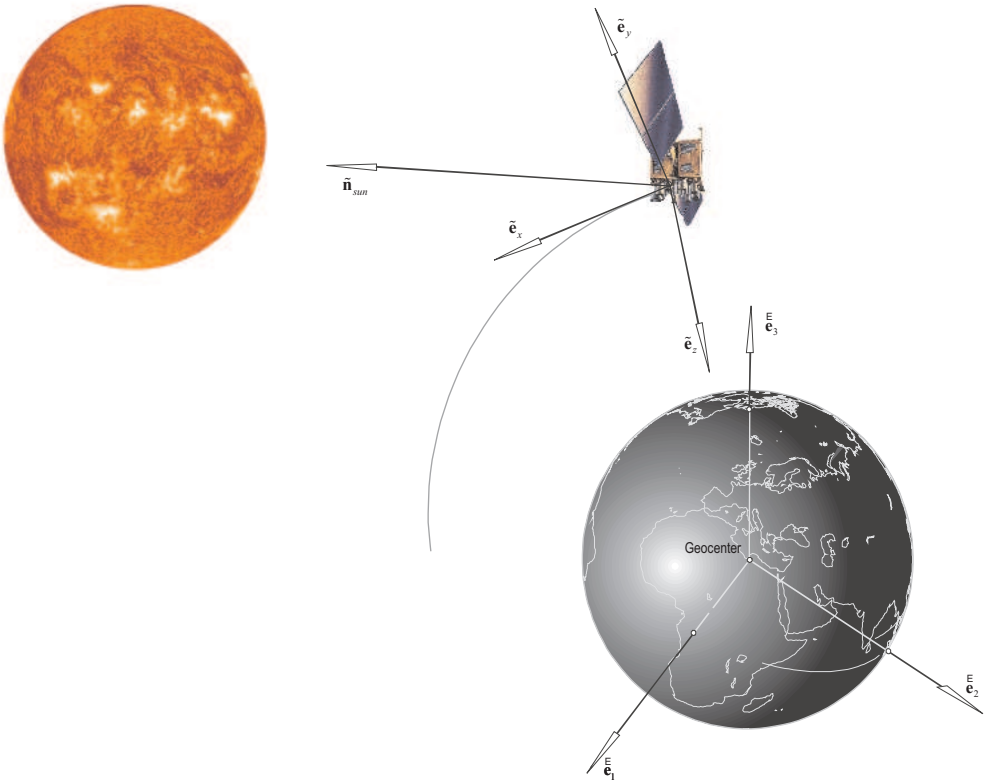

Figure 2.3: GPS satellite body coordinate system

is always pointing to the Earth, and the y-axis (solar panel axis) shall be kept perpendicular to the solar vector. In other words, the $y-$axis is always perpendicular to the plane, which is formed by the Sun, the Earth and the GPS satellite (see Fig. 2.3). The solar panel can be rotated around its axis to keep the solar panel perpendicular to the ray of the Sun. This is important to collect the solar energy in an optimal way. This definition of the satellite fixed coordinate system becomes meaningless when the Sun, the GPS satellite and the Earth are collinear. In this case and when the satellite is in the Earth's shadow, the satellite attitude cannot be modeled in such an easy way. Denoting the three unit vectors of the satellite fixed coordinate system as $(\tilde{\mathbf{e}}_x, \tilde{\mathbf{e}}_y, \tilde{\mathbf{e}}_z)$, then the vector of the geocenter to the GPS satellite and to the Sun reads $\mathbf{r}^s$ and $\mathbf{r}_S$, respectively. The vector $\mathbf{r}^s$ is obtained from the final GPS orbit products (in SP3 format) and $\mathbf{r}_S$ is calculated from the JPL planetary ephemeris (e.g. DE 405, Development Ephemeris 405). The unit vector $\tilde{\mathbf{e}}_z$ can be written (Xu 2007),

$$\tilde{\mathbf{e}}_z = -\frac{\mathbf{r}^s}{\left\|\mathbf{r}^s\right\|}, \tag{2.51}$$

and the solar vector can be derived from,

$$\tilde{\mathbf{n}}_{sun} = \frac{\mathbf{r}_S - \mathbf{r}^s}{\left\|\mathbf{r}_S - \mathbf{r}^s\right\|}, \tag{2.52}$$

then it holds for the unit vector $\tilde{\mathbf{e}}_y$ according to the above definition,

$$\tilde{\mathbf{e}}_y = \frac{\tilde{\mathbf{e}}_z \times \tilde{\mathbf{n}}_{sun}}{\left\|\tilde{\mathbf{e}}_z \times \tilde{\mathbf{n}}_{sun}\right\|}, \tag{2.53}$$

and for the unit vector $\tilde{\mathbf{e}}_x$ holds finally,

$$\tilde{\mathbf{e}}_x = \tilde{\mathbf{e}}_y \times \tilde{\mathbf{e}}_z. \tag{2.54}$$

If $\tilde{\mathbf{r}}_o$ denotes the GPS antenna phase offset referring to the GPS satellite system then the correction of the GPS position, $\Delta\tilde{\mathbf{r}}_o$, can be written as,

$$\Delta\tilde{\mathbf{r}}_o = \mathbf{E}\tilde{\mathbf{r}}_o, \quad \mathbf{E} = (\tilde{\mathbf{e}}_x, \tilde{\mathbf{e}}_y, \tilde{\mathbf{e}}_z)\,. \tag{2.55}$$

This term may be added to the GPS satellite position vector $\mathbf{r}^s$ to calculate the position of the GPS antenna center, which is necessary to calculate the geometrical distance between the phase centers of the GPS satellite antenna and the receiver antenna.

2.7.6 LEO Antenna-Mass Center Correction

The geometrical distance between the phase centers of the antennas of the GPS satellite transmitter at the signal emission time and of the GPS receiver on-board LEO at the reception time can be determined from the satellite positions. To transform the position of the antenna phase center of the LEO to its center of mass, the offset of both centers must be given. This requires the LEO geometry and the LEO fixed reference coordinate system as well as the satellite orientation (satellite attitude). The location of the LEO antenna is known from the assembly of the satellite. However, the location of the antenna phase center of the LEO with respect to the center of mass of the spacecraft is also required. The position vector can be assumed to be constant in the body-fixed coordinate system of the spacecraft, but a correction is necessary to refer it to the center of mass of the satellite. The ephemerides of the GPS satellites are usually referred to its center of mass, but the position of the phase center of the LEO-antenna must be referred to its center of mass based on attitude information of the LEO, derived by a calibration procedure. In case of CHAMP, the effect of the antenna - mass center offset can be calculated either approximately from the satellite position and velocity data or more precisely based on the real attitude data, given in form of quaternions of the LEO measured by its star camera (if such equipment is available as in case of CHAMP and GRACE). The real attitude and antenna - mass offset data of the LEOs are available from the star camera and the calibration data.

2.7.6.1 Mass Center Correction with the Position and Velocity

If the position ($\mathbf{r}$) and the velocity ($\dot{\mathbf{r}}$) of the LEO-antenna are available, then the unit vector of the body reference coordinate system of the LEO can be represented by,

$$\mathbf{E} = (\mathbf{e}_x, \mathbf{e}_y, \mathbf{e}_z)^{\mathrm{T}}, \quad \mathbf{e}_z = -\frac{\mathbf{r}}{\left\|\mathbf{r}\right\|}, \quad \mathbf{e}_y = -\frac{\mathbf{r} \times \dot{\mathbf{r}}}{\left\|\mathbf{r} \times \dot{\mathbf{r}}\right\|}, \quad \mathbf{e}_z = \mathbf{e}_y \times \mathbf{e}_z. \tag{2.56}$$

The position of the mass center of the LEO can be approximately determined from the offset antenna - mass centers $\mathbf{r}_o$ as,

$$\mathbf{r}_c = \mathbf{r} - \mathbf{E}\mathbf{r}_o. \tag{2.57}$$

2.7.6.2 Mass Center Correction with the Quaternions

Quaternions are quadruples of real numbers, for which a special multiplication is defined. The quaternions can be represented by a column vector of four elements,

$$\mathbf{q} = \begin{pmatrix} q_0 & q_1 & q_2 & q_3 \end{pmatrix}^{\mathrm{T}}. \tag{2.58}$$

If we assume that $\boldsymbol{\Delta}$ is the rotational axis and δ the rotation angle, respectively, then the elements of the quaternions can be determined by the relations,

$$q_0 := \cos(\delta/2), \quad q_1 := \frac{\delta_x}{\delta}\sin(\delta/2), \quad q_2 := \frac{\delta_y}{\delta}\sin(\delta/2), \quad q_3 := \frac{\delta_z}{\delta}\sin(\delta/2), \tag{2.59}$$

with the coordinates δ_x, δ_y, δ_z of the rotational vector

$$\mathbf{e} = \frac{1}{\delta}\begin{pmatrix} \delta_x & \delta_y & \delta_z \end{pmatrix}^{\mathrm{T}}, \quad \delta = \|\mathbf{e}\|.$$

To control the LEOs attitude and to transform the LEO observations (e.g. acceleration data) to an inertial coordinate frame, the Star Camera Assembly (SCA) on-board the LEOs plays an important role. The digital images from the CCD cameras on-board the LEOs are processed to achieve the orientation of the LEOs as time series of the quaternion values. The inertial orientation of the spacecraft is modeled using tabular input data quaternions (derived from the LEO CCD cameras). The same data (with appropriate definitions) are used for rotating the accelerometer data to the inertial frame prior to the numerical integration, for the corrections of the range observations due to the offset of the satellite center of mass and the GPS antenna location on-board LEO, as well as for computing the non-gravitational forces (if necessary). At the epochs, where the LEOs quaternions are not available, a linear interpolation between adjacent values is used. If $\mathbf{r}_{\mathrm{ICRF}}$, $\mathbf{r}_c$ are the GPS antenna absolute position on-board LEO in the ICRF and the LEO mass center positions in the spacecraft fixed system and the GPS receiver on-board LEO has the offset $\mathbf{r}_o$ from the LEO mass center then LEO mass center position can be written as,

$$\mathbf{r}_c = \mathbf{r}_{\mathrm{ICRF}} - \mathbf{Q}\mathbf{r}_o, \quad \mathbf{c}_{\mathrm{ICRF}} := \mathbf{Q}\mathbf{r}_o, \tag{2.60}$$

with the transformation matrix $\mathbf{Q}$ from the spacecraft fixed coordinate system to the international celestial reference frame,

$$\mathbf{Q} = \begin{pmatrix} q_1^2 - q_2^2 - q_3^2 + q_0^2 & 2(q_1q_2 + q_3q_0) & 2(q_1q_3 - q_2q_0) \\ 2(q_1q_2 - q_3q_0) & -q_1^2 + q_2^2 - q_3^2 + q_0^2 & 2(q_2q_3 + q_1q_0) \\ 2(q_1q_3 + q_2q_0) & 2(q_2q_3 - q_1q_0) & -q_1^2 - q_2^2 + q_3^2 + q_0^2 \end{pmatrix}. \tag{2.61}$$

In the case of CHAMP, the GPS receiver antenna-mass center offset with respect to the LEO body reference frame by the vector $\mathbf{r}_o$ is available at every epoch as well as the attitude of the satellite with respect to the international celestial reference frame (ICRF) by quaternions derived from accelerometer data. The rotation matrix to transform the mass center offset to the inertial coordinate system can be performed with the quaternion values. In a first step, the LEO antenna position in the ITRF frame has to be transformed to the position based on the ICRF frame. Then the correction vector ($\mathbf{c}_{ICRF}$) in the ICRF frame may be added to the position referenced to the ICRF to determine the position of the mass center. If desired, the ICRF mass center coordinates can be transformed to the ITRF coordinates based on the IERS conventions.

2.7.7 Receiver Antenna Phase Center Correction and its Variation

It is assumed that the phase centers of both carrier frequencies L_1 and L_2 of the sender antenna are the same and its location remains constant during the lifetime of the GPS satellites. There is some evidence that the phase center of the GPS receiver antenna depends on the direction where the signal comes from. It is considered constant because of missing information. The angle between the wave front and the GPS

satellite's nadir may reach up to 14° (at low elevation) and they have to be corrected (Rothacher et al. 1996). In the case of GPS receiver antenna, the situation is more complicated because the GPS signals come from different direction (from the different GPS satellites to receiver) and the position of the antenna phase center depends on the incoming GPS signal direction. This directional dependency is called antenna phase center variation. In the case of GPS receiver, we also have to take into account that the antenna phase center positions and the antenna phase center variations are not identical for L_1 and L_2 carriers and they are antenna-type-dependent. We use the following antenna phase center total correction (phase center correction and variation) as (Rothacher et al. 1996),

$$PCT(\alpha, z) = \Delta\mathbf{r}.\mathbf{e} + PCV(\alpha, z), \tag{2.62}$$

where,

$PCT(\alpha, z)$	total phase center correction (phase center correction and its variation),
α	azimuth angle of GPS satellite from the receiver,
z	zenith distance of GPS satellite from receiver,
$\Delta\mathbf{r}$	definition of the position of the mean receiver antenna phase center w.r.t. antenna reference point. Antenna reference points and mean antenna phase center offset are defined for differ--ent antenna types in ANTEX format,
$\mathbf{e}$	unit vector in the directional GPS receiver antenna to GPS satellite and
$PCV(\alpha, z)$	model of azimuth and zenith dependent phase center variation.

The total correction, $PCT(\alpha, z)$, are added to the geometrical distance in the code pseudo-range or carrier phase equations.

2.7.8 Relativistic Correction

The relativistic effects on the GPS observations can be divided into two parts: a constant term and a periodic effect. In the GPS system, the fundamental frequency f_0 is selected to 10.23 *MHz*. All clocks on the GPS satellites and receivers are based on the fundamental frequency. If all the GPS satellites are working simply on the fundamental frequency f_0 on the geoid, then we will view a frequency f at the altitude of the GPS satellites and f is not the same as f_0 due to relativistic effects. In order to be able to view the fundamental frequency, the working frequency f of the GPS satellites can be computed as,

$$-\frac{f_0 - f}{f} = \frac{1}{2}\left(\frac{\|\dot{\mathbf{r}}\|}{c}\right)^2 + \frac{\Delta U}{c^2}, \tag{2.63}$$

where $\|\dot{\mathbf{r}}\|$ is the velocity of the satellite and ΔU is the difference of the Earth's gravitational potential between the satellite and the geoid. The difference between the fundamental clock frequency and set frequency is called the satellite clock frequency offset. Such an offset of the relativistic effects has been implemented in the GPS satellite clock settings, therefore users do not need to consider the offset (Xu 2007).

When the GPS satellites are orbiting around the Earth, the GPS satellites are affected under the periodically changing influence of the Earth's gravitational potential because of the orbit ellipticity. As a consequence, the rate of the clocks on-board the GPS satellites is subject to periodic changes due to the special relativistic effect. This periodic effect can be represented as a correction to the satellite clock error or as correction to the GPS observation equation for high-low GPS-SST measurements as (Ashby 2003):

$$d_R^r - d_R^s = \frac{2}{c}\left(\mathbf{r}.\dot{\mathbf{r}} - \mathbf{r}^s.\dot{\mathbf{r}}^s\right), \tag{2.64}$$

$\mathbf{r}$, $\dot{\mathbf{r}}$ are the position and velocity of the LEO satellite or tracking stations respectively, and $\mathbf{r}^s$, $\dot{\mathbf{r}}^s$ are the position and velocity of the GPS satellite s. Before the precise orbit determination, there are only approximate information about the position and velocity of the LEO. Therefore, we have to start the computation

by neglecting the special relativistic effects of the receiver of the LEO and consider the following correction to the GPS observation equations:

$$d_R^s = -\frac{2}{c}\left(\mathbf{r}^s.\dot{\mathbf{r}}^s\right). \tag{2.65}$$

After the initial estimation of the LEO position without applying the periodic special relativistic effect, the velocity can be estimated from the positions in the specified intervals by interpolation. Then with the help of Eq. (2.64), the special relativistic effect of the GPS satellites and the LEO can be taken into account in the subsequent computation step.

2.7.9 Receiver Noise

GPS measurements cannot be performed without errors. There is always a certain level of noise in the observations. The most basic kind of noise is that produced by the movement of electrons in any substance that has a temperature above absolute zero (Kleusberg and Teunissen 1998). The receiver noise depends on the type and structure of the receiver (analogue or digital). With improved technologies, un-modeled effects in the GPS observations are minimized, so that the receiver noise can be treated as random error. This error is minimized in the least squares adjustment.

3. Pre-processing of GPS-SST Code Pseudo-range and Carrier Phase Observations

3.1 GPS-SST Data Pre-screening Methods

3.1.1 Introduction

For all applications of GPS, an efficient pre-processing and data screening of the GPS observations is necessary. It is in particular an important issue for the processing of the GPS-SST observations of space-borne receivers of LEOs and of the determination of the LEO absolute positions. The procedure to determine the outliers of the code pseudo-range SST observations is divided into two main steps (Bock 2003),

1. The data are pre-screened based on a-priori information of the absolute positions of the space-borne GPS receiver combined with a 'majority voting' algorithm. The observations which are flagged as outliers in this step are excluded from the following processing.
2. The least squares adjustment step includes an iterative procedure where bad observations may be detected and can be excluded from the main processing.

In the following, these processing steps will be described in more detail.

3.1.2 Majority Voting Technique to Detect Outliers

Majority voting is based on an epoch wise processing of the GPS-SST observations. In a first step, the code pseudo-range observations are processed for each epoch and the receiver clock offset is synchronized with the GPS time. In a second step, the carrier phase differences between subsequent epochs can be processed to determine outliers (cycle slip) of the carrier phase observations (Bock et al. 2002). Let us have a look at the code pseudo-range GPS-SST observations of the receiver for a particular epoch. The unknowns in the code observation equations of one epoch are the three coordinates and a clock offset of the GPS receiver on-board LEO. For the processing of the GPS-SST observations with the majority voting algorithm not only precise GPS orbits and clock corrections are required, but also the a-priori information of the absolute positions of the GPS receiver. If this reliable and accurate information is available, only the receiver clock offset remains as unknown in the code observation equations for every tracked GPS satellite. The receiver clock offset should be within the accuracy of code pseudo-ranges of one epoch. It is the key assumption for the data screening procedure (Bock et al. 2002). This procedure is robust in case of only one unknown receiver clock offset. From the statistical point of view normally distributed observations with a standard deviation of σ_c deviate from the expected value by $3\sigma_c$ with a probability of 99.73%. This means that the difference between two clock offsets derived from the code pseudo-range observations to GPS satellites i and j, respectively, should lie within $3\sqrt{2}\sigma_c$, where σ_c is the standard deviation of the ionosphere-free linear combination of the code pseudo-range observations. The majority voting algorithm is set up in the following way (Bock et al. 2002),

1. receiver absolute positions and clock offsets are estimated from the ionosphere-free linear combination of code pseudo-range observations without applying a pre-screening algorithm,
2. with the receiver absolute position, estimated in step 1, and ionosphere-free code observation equations for every tracked GPS satellite, the receiver clock offset can be estimated for every GPS satellite,
3. all possible differences are formed between the receiver clock offsets for n_s tracked GPS satellites, i.e. $\gamma_i = c\delta t_i, i = 1, ..., n_s$,

4. a check is performed whether the absolute value of each difference is smaller than $3\sqrt{2}\sigma_c$; $\Delta\gamma_{ij} = |\gamma_j - \gamma_i| \leq 3\sqrt{2}\sigma_c \quad , i = 1, ..., n_s - 1; j = i + 1, ..., n_s$, where all γ_j, meeting the above condition with a particular γ_i, are assigned to the same group as γ_i. We may influence the size of the group by changing the value of $3\sqrt{2}\sigma_c$,

5. the clock offset values with the largest members ('majority voting') are used to compute a mean value ($\bar{\gamma}$) and a standard deviation (σ_γ) of the clock correction at every observation epoch,

6. each receiver clock offset γ_i, of the processed epoch is compared to the mean values of the groups, computed in step 5, $\Delta\gamma_i = |\gamma_i - \bar{\gamma}|$,

$$\Delta\gamma_i = \begin{cases} \Delta\gamma_i \leq \beta\sigma_\gamma & case\ (a) \\ \Delta\gamma_i > \beta\sigma_\gamma & case\ (b) \end{cases} \tag{3.1}$$

In case (a), the code pseudo-range observation is accepted but has to be checked within the following iterative least squares adjustment step. In case (b), the code pseudo-range observation is considered as outlier and is excluded from the epoch wise LEO precise point positioning procedure. β is a parameter defined for the majority voting algorithm. If the observations do not have systematic errors, all differences $\Delta\gamma_i$ are within $3\sigma_\gamma$ with a probability of 99.73%. Since we cannot completely avoid systematic errors in the data (e.g. insufficient a-priori information, biased GPS satellite clocks, etc.), this assumption usually is not met. That is why we provide the possibility to select a value for β manually. If we would choose a too large value for β (e.g. $\beta = 30$) then the pre-screening will only detect extreme outliers in the code pseudo-range observations and the other bad observations remaining in the data have to be found in the second step, the iterative least squares adjustment step. The performance of the majority voting algorithm may be influenced by modifying the following input parameters (Bock et al. 2002),

1. the standard deviation of the code pseudo-range observations σ_c for the arrangement of observations into groups (depending on the code observation quality),

2. the standard deviation for setting the rejection threshold (it may be derived from the code observations or specified as fixed),

3. the factor β.

The same pre-screening algorithm can be applied to the subsequent time differenced carrier phase observations where σ_c (code pseudo-range observation accuracy) is replaced by $\sqrt{2}\sigma_p$ (carrier phase observation accuracy), while the receiver clock offset difference of subsequent epochs, $\gamma_i(t_1, t_2) = \gamma_i(t_2) - \gamma_i(t_1)$, derived from the carrier phase observations to the GPS satellite i. The key factor limiting the performance of the pre-screening approach of the carrier phase observations is the quality of the prior information (i.e. LEO absolute position). For the point positioning by code pseudo-range observations, this is not a serious problem, but for the cleaning of the carrier phase observations from cycle slips (outliers), the quality of a-prior information is a critical issue. To be sure that this does not happen, the rejection threshold should be set not too small. This implies that a second screening step has to follow in order to find all observation deteriorating the solution (Bock 2003).

3.1.3 Iterative Least Squares Method to Detect Outliers

The second data screening step is included in the least squares adjustment of the observations. It follows the same scheme for the code pseudo-range as for the carrier phase difference processing (Bock 2003):

1. The code pseudo-range observations of the processed epoch which have been accepted by the pre-processing procedure are used to generate an absolute position estimate. No solution can be computed for a particular epoch if the number n_s of GPS satellites per epoch is less than four (i.e. $n_s < 4$).

2. The solution is checked whether the RMS error of the absolute position estimates is smaller than an externally specified threshold. If yes, the solution is accepted. If not, a series of n_{ss} solutions with different geometrical combinations of the tracked GPS satellites is computed (n_{ss} is the optimal number of observations in the data processing),

3. The solution with the smallest RMS error of LEO absolute positions is selected and the code pseudo-range observations which were excluded for this solution are marked as outliers.

It is clear that, this second data screening step is not as robust as the first pre-screening step. There are four unknowns, i.e. the GPS receiver on-board LEO absolute position and the clock offset, and between four and twelve GPS-SST observations depending on the number of tracked GPS satellites. This means that the degree of freedom of the adjustment is small and the identification of outliers is difficult (Bock et al. 2002).

3.2 Cycle Slips

3.2.1 Introduction

Any orbit determination procedure by high-low GPS-SST pseudo-range and carrier phase observations depends crucially on the ability to identify and remove invalid and degraded measurements from the estimation process. In order to attain high precision positioning and navigation results with GPS, cycle slips in the carrier phase observations must be correctly repaired at the pre-processing stage. A slip of only a few cycles can influence the measurements such that a centimeter-level positioning can not be achieved. Cycle slips are caused by an integer number of cycle jumps in the carrier phase observables. Reason is the loss of lock of the receiver phase lock loops (Leick 1995). The loss may be due to internal receiver tracking problems or by an interruption in the ability of the antenna to receive the satellite signals (Seeber 2003). A loss of lock may be shorter than the time interval between two adjacent data collection epochs or as long as the time interval between many epochs, in which case the term data gap may be in order. The process of cycle slip correction involves the detection of slips estimating the exact number of L_1 and L_2 frequency cycles that comprise the slip, and actually correcting the carrier phase measurements by these integer estimates.

Over the past decade, a number of methods have been developed to detect, identify and repair cycle slips. The majority of approaches involve forming cycle slip sensitive linear combinations of the available observables (pseudo-range and/or carrier phase observations). Many algorithms have been designed to detect, determine and repair these cycle slips by fitting functions to the linear combinations and observed differences between the functions and the date combinations. These methods require user information of problematic cycle slips in portions of the data, the tuning of input parameters of the available observations, or the introduction of additional carrier phase ambiguity resolution parameters as new additional unknowns of the main data processing, where the pre-processing of cycle slip determination has failed. A method has been developed from various existing techniques that provides a fully automatic cycle slip correction at the data pre-processing stage. The algorithms utilize two dual frequency carrier phase and pseudo range geometry free linear combinations. These combinations are filtered to allow a high resolution cycle slip detection and then compared with the determination of filtered Chebyschev polynomials (Bisnath 2004).

The next sub-section describes the development of a cycle slip detection and correction technique designed to detect and correct cycle slips in dual frequency carrier phase measurements of LEOs in a post-processing environment.

3.2.2 Methods of Detecting and Determining Cycle Slips

The techniques used in the detection and determination of cycle slips have not changed drastically since the first methods were proposed in the early 1980s. The focus has always been on attempting to develop a reliable,

somewhat automatic detection and repair procedure. All methods have the common premise that to detect a slip at least. One smooth (i.e. low noise) quantity derived from the observations must be tested in some manner for discontinuities that may represent cycle slips (Hofmann-Wellenhof et al. 2001). The derived quantities usually consist of linear combinations of the un-differenced or double differenced L_1 and L_2 of the carrier phases and possibly pseudo ranges. Examples of combinations useful for kinematic data (e.g. in the case of LEOs) are the ionosphere carrier phase residuals (i.e. geometry free carrier phase combination)(Goad 1988, Bastos and Landau 1988, Blewitt 1990, Gao and Li 1999) and the ionosphere pseudo-range residuals (Bastos and Landau 1988) as well as wide-lane carrier phases minus narrow-lane pseudo ranges (i.e. Melbourne-Wübbena combination) (Blewitt 1990, Gao and Li 1999). Once the time series for the derived quantities have been produced, the cycle slip detection process (that is, the detection of discontinuities in the time series) can be initiated. Of the various methods available, only four methods will be discussed in this section. The most straightforward method is to compute higher order differences of the time series of the carrier phase, which accentuate any discontinuities. The main disadvantages of this method are that data specific tolerance values have to be set manually (time difference values that are greater than the tolerances indicating the presence of cycle slip), and that the geometry free linear combinations are required for kinematic GPS-SST data. Another method is to fit a low degree polynomial over the time series and conclude any large discrepancies (again, determined for the specific data set) between the polynomial and the time series representing a cycle slip (Hofmann-Wellenhof et al. 2001).

The method to be described here was developed by Blewitt (Blewitt 1990) and consists partially of applying a running average filter to a linear combination to improve the estimate of the combination's ambiguity term. Cycle slips are detected by determining two consecutive unfiltered data points which are outside the confidence interval of the running mean. This method has the advantage that it uses statistical information from the data detection process. After cycle slips have been detected, the actual number of L_1 and L_2 cycles that comprise each slip must be determined and then the carrier phase corrected. The latter is a simple task, but the determination can require additional information. If single frequency linear combinations resulting in integer ambiguity values are used (such as the single-frequency range residuals), then the integer number of cycles attributable to the slip can be directly estimated. If a dual-frequency combination is used, then this single combination consists of two unknowns, namely slip in L_1 and slip in L_2. Therefore, a second linear combination is needed to uniquely solve for the individual frequency slips. This can be accomplished by using one of the detection methods on a second linear combination, not to detect a slip, but rather to estimate the inter-frequency slip. With this additional information, the values of the L_1 and L_2 cycle slips can be uniquely determined. Various techniques can be used to fix the estimates to integers, ranging from simple rounding to searching for slip pairs that best fit the linear combinations in a least squares sense. If viable integer combinations cannot be determined, then the additional carrier phase ambiguity resolution parameters can be introduced in the main data processing (e.g., Seeber 2003).

3.2.3 GPS Observable Models

The mathematical models of the carrier phase and pseudo range GPS-SST data at the frequency of L_1 for GPS satellite s and the GPS receiver r on-board LEO are,

$$\Phi^s_{r,1} = \rho^s_r + c(\delta t_r - \delta t^s) + \lambda_1 A^s_{r,1} + d_{M,\Phi_1} + e^s_{r,\Phi_1} + \varepsilon^s_{r,\Phi_1}, \tag{3.2}$$

$$P^s_{r,1} = \rho^s_r + c(\delta t_r - \delta t^s) + d_{M,P_1} + e^s_{r,P_1} + \varepsilon^s_{r,P_1}, \tag{3.3}$$

and for the frequency of L_2,

$$\Phi^s_{r,2} = \rho^s_r + c(\delta t_r - \delta t^s) + \lambda_2 A^s_{r,2} + d_{M,\Phi_2} + e^s_{r,\Phi_2} + \varepsilon^s_{r,\Phi_2}, \tag{3.4}$$

$$P^s_{r,2} = \rho^s_r + c(\delta t_r - \delta t^s) + d_{M,P_2} + e^s_{r,P_2} + \varepsilon^s_{r,P_2}, \tag{3.5}$$

or in general, the carrier phase and code pseudo-range GPS-SST observations at frequency i read as,

$$\Phi^s_{r,i} = \rho^s_r + c(\delta t_r - \delta t^s) + \lambda_i A^s_{r,i} + d_{M,\Phi_i} + e^s_{r,\Phi_i} + \varepsilon^s_{r,\Phi_i}, \tag{3.6}$$

$$P^s_{r,i} = \rho^s_r + c(\delta t_r - \delta t^s) + d_{M,P_i} + e^s_{r,P_i} + \varepsilon^s_{r,P_i}, \tag{3.7}$$

where

$\Phi^s_{r,i}$, $P^s_{r,i}$	are the measured carrier phase and pseudo-range between GPS satellite s and the receiver r (in units of length) at frequency i,
λ_i	the carrier wavelength at frequency i,
c	the vacuum speed of light,
ρ^s_r	the geometrical range from the GPS receiver r on-board LEO to GPS satellite s,
δt_r, δt^s	the clock offsets of the receiver r and GPS satellite s from GPS time, respectively,
$A^s_{r,i}$	the number of cycles by which the initial phase are undetermined,
d_{M,Φ_i}, d_{M,P_i}	the effect of the multi-path on the carrier phases and code pseudo-ranges at frequency i,
e^s_{r,Φ_i}, e^s_{r,P_i}	the errors summarization of the carrier phase and code pseudo-range observations at freq--uency i and
ε^s_{r,Φ_i}, ε^s_{r,P_i}	the effect of the receiver noise on the carrier phases and code pseudo-ranges at frequency i.

GPS satellite and receiver hardware delays and other small effects have been ignored as they have negligible effects on the data processing.

3.2.4 GPS Observables to Detect Cycle Slips

Two observables were chosen so that they do not contain any absolute position of the GPS satellites and the receiver and provided so that they contain minimum measurement noise. Therefore, the two linear combinations produce time series which are relatively invariant with respect to the receiver time, to the receiver-satellite position and to the receiver motion mode (static or kinematic positioning). Obviously, these two observables are within the limits of ionosphere residuals, multi-path and receiver noises, respectively. The chosen combinations are the geometry-free carrier phases and Melbourne-Wübbena combinations. The code pseudo-range ionosphere residuals were not used, as the measurement noise of these observables is larger than the Melbourne-Wübbena combination (Bock et al. 2002). In the next sections, two observation models will be described in more detail.

3.2.4.1 Geometry-free Carrier Phase Observations

The most important observable to detect cycle slips in the GPS-SST carrier phase observations is the geometry-free carrier phase combination as,

$$\Phi^s_{r,GF} = \Phi^s_{r,1} - \Phi^s_{r,2} = \lambda_1 A^s_{r,1} - \lambda_2 A^s_{r,2} + d_{M,\Phi_1} - d_{M,\Phi_2} + e^s_{r,\Phi_1} - e^s_{r,\Phi_2} + \varepsilon^s_{r,\Phi_1} - \varepsilon^s_{r,\Phi_2}, \tag{3.8}$$

with the geometry-free combination $\Phi^s_{r,GF}$ in units of length. This combination contains of ionospheric difference effects $(I^s_{r,2} - I^s_{r,1})$ and differences of carrier phase multi-path effects at the bands L_1 and L_2 as well as the GPS ambiguities , carrier phase noise and GPS receiver noise on-board LEO. If a cycle slip at the following epoch occurred, then this combination would result in the ambiguities term being replaced by

$$\lambda_1(N^s_{r,1} + n_1) - \lambda_2(N^s_{r,2} + n_2), \tag{3.9}$$

where n_1 and n_2 are the integer cycle slips on the L_1 and L_2 frequencies in terms of cycles.

3.2.4.2 Melbourne-Wübbenna Combination

The second observable to detect cycle slips is the Melbourne-Wübbenna combination, which is build from the wide-lane carrier phases minus the narrow-lane code pseudo-range observables (Blewitt 1990, Gao and Li 1999),

$$\Phi^s_{r,MW} = \lambda_4(\Phi^s_{r,1} - \Phi^s_{r,2}) - \lambda_5(\frac{P^s_{r,1}}{\lambda_1} + \frac{P^s_{r,2}}{\lambda_2}) = \lambda_4(A^s_{r,1} - A^s_{r,2}) + \lambda_4(e^s_{r,\Phi_1} - e^s_{r,\Phi_2}) + \\ + \lambda_4(\frac{d_{M,\Phi_1}}{\lambda_1} - \frac{d_{M,\Phi_2}}{\lambda_2}) - \lambda_5(\frac{d_{M,P_1}}{\lambda_1} + \frac{d_{M,P_2}}{\lambda_2}) + \lambda_4(\frac{\varepsilon^s_{r,\Phi_1}}{\lambda_1} - \frac{\varepsilon^s_{r,\Phi_2}}{\lambda_2}) - \lambda_5(\frac{\varepsilon^s_{r,P_1}}{\lambda_1} + \frac{\varepsilon^s_{r,P_2}}{\lambda_2}), \quad (3.10)$$

with

$$\lambda_4 = \frac{c}{f_1 - f_2} = 86.2cm, \quad \lambda_5 = \frac{c}{f_1 + f_2} = 10.7cm,$$

where

$\Phi^s_{r,MW}$	the Melbourne-Wübbenna combination (in units of length),
λ_4	the wide-lane wavelength and
λ_5	the narrow-lane wavelength.

This combination consists of the wide-lane ambiguity, a residual multi-path term and a residual receiver noise term. It is remarkable that this combination has not any effect of the ionosphere delay. Since the multi-path and noise terms of the code pseudo-range measurements are much larger than those of the carrier phase measurements. The fluctuations in this combination are mainly due to the code pseudo-range multi-path and pseudo-range measurement noise. The former of these error terms can cause variations of many meters. A cycle slip on the occurred epoch would result in the ambiguities term as,

$$\lambda_4[(N^s_{r,1} + n_1) - (N^s_{r,2} + n_2)]. \quad (3.11)$$

The noise of this observable makes a high resolution cycle slip detection unlikely. However, Blewitt (Blewitt 1990) proposed a simple running average filter to make this observable more useful. This strategy is quite intuitive, since over time one would expect that the residual multi-path and the noise terms average down to nearly constant values. The filter is an expanding-memory low pass filter, whose output is identical to the recursive mean,

$$\bar{x}_t = \bar{x}_{t-1} + \frac{1}{t}(x_t - \bar{x}_{t-1}). \quad (3.12)$$

The standard deviation of the recursive mean at epoch t with respect to epoch $t-1$ is computed (Blewitt 1990) as,

$$\sigma^2_t = \sigma^2_{t-1} + \frac{1}{t}\left[(x_t - \bar{x}_{t-1})^2 - \sigma^2_{t-1}\right], \quad (3.13)$$

where x is the observation, $\bar{x}$ is the mean value of the observation x and $t, t-1$ represent the current and previous epoch counts, respectively, and finally σ_t, σ_{t-1} are the standard deviations of the observations at the epoch counts t, $t-1$ (Bisnath 2000).

3.3 Weighting of the GPS-SST Observations

3.3.1 Introduction

In the post processing of LEO GPS-SST data, several errors in the high-low GPS-SST observations have to be considered. These error sources can be classified in three main groups, namely sender, signal transmitter

medium and receiver errors. The GPS satellite specific errors are the GPS satellite orbit error, the satellite clock error and the GPS geometrical constellation. Signal transmitting medium errors in the LEO GPS-SST data are the ionospheric effect. As errors related to the signal delay in the receiver, the receiver clock error, the receiver hardware error and the receiver environmental errors (e.g. multi-path effect on GPS signals) can be mentioned. The GPS satellite clock error can either be eliminated by the use of an appropriate data processing strategy (e.g. single differencing (SD) technique between two GPS receivers) or they can be minimized by the use of GPS clock corrections from the IGS centers.

Because GPS satellite orbit information can be obtained more precisely (i.e. with an accuracy of about 5 cm) by means of several permanent GPS stations in recent years from the IGS analysis centers. Therefore, GPS satellite orbit errors can be neglected in the LEO data processing. The receiver errors are reduced in course of the technological progress and by the improvements related to the GPS satellite constellation and with the operation of new GPS satellite types. The signal transmitter medium effects the high-low GPS-SST data by the ionosphere. The main part of the ionospheric effect can be reduced by the ionosphere-free linear combination of GPS observations at the frequencies of L_1 and L_2. Therefore, the most important remaining errors in LEO GPS-SST measurements are the multi-path effects and the un-modeled errors on LEO observations. Obviously, the multi-path error is taking place when the GPS electro-magnetic signals reflect at the reflecting environment around the LEOs antenna. The LEO multi-path effect increases as the GPS satellite elevation decreases (Bock 2003). Therefore, the elevation mask of at least $10° - 20°$ is used in the GPS data processing to determine the geometrical LEO orbit. The observed GPS satellite signals are distorted by the multi-path delay effect, which are not completely taken into account in the functional model of the GPS data processing. Subsequently, the use of elevation mapping functions to weight LEO code pseudo-range and carrier phase SST observations is an important issue. Of course, in case of atmosphere sounding with the LEOs (e.g. CHAMP and twin GRACE satellites), the low elevation tracked GPS satellites have to be used.

One way of improving the accuracy of LEO geometrical point positioning is to increase the number of GPS-SST observations in the data processing procedure. This is possible by observations with low elevation together with an appropriate weighting strategy. Furthermore, studies show that the inclusion of low elevated GPS satellites in the data processing also improve the accuracy of the height component. Normally, the accuracy of the heights determined by GPS techniques on the Earth are three times worse than the accuracy of the horizontal components because of the multi-path effects of the GPS signals and because of the tropospheric delay (Herring 1992).

In general, there are three possible weighting schemes that can be used in the GPS code pseudo-range and carrier phase observation adjustment procedure which enable us to process even low elevated GPS observations, namely,

- Equally weighting of the observations in the adjustment procedure,
- Signal to Noise Ratio (SNR) weighting,
- Zenith distance weighting (or elevation weighting algorithm).

3.3.2 Equally Weighting

The observation weights, which are arranged in a weight matrix for the least squares estimation procedure, allow in which way individual GPS observations should contribute to the overall solution. For instance, it is necessary to give lower weights to the noisy observations and higher weights to the less noisy observations (Teunissen et al. 1998). In order to specify the weight matrix adequately, one needs to know the stochastic properties of the actual GPS data (Tiberius et al. 1999). The random noise affects both, GPS pseudo-range and carrier phase observations, therefore, the random behaviour of the noise effect should be taken into account in the stochastic modelling of GPS observations (Tiberius et al. 1999). In recent years, some weighting algorithms have been developed. Most of the models are based either on signal quality

measures (sigma-ε model weighting or SNR weighting) or on the zenith distance of the tracked GPS satellite. Conventionally GPS observations are equally weighted in the GPS data processing procedure as,

$$w_{\phi_i} = \frac{1}{\sigma^2_{\phi_i}}, \tag{3.14}$$

where w_{ϕ_i} is the weight of the carrier phase observation ϕ_i and σ_{ϕ_i} is the a-priori known standard deviation of the GPS observations. In the stochastic model of Eq. (3.14), it is assumed that all one-way code pseudo-range or carrier phase observations have the same variance and are statistically independent. The equally weighting is a simple model but in most cases not realistic.

3.3.3 Signal to Noise Ratio (SNR) Weighting

A more realistic weighting function can be derived directly from the quality of each carrier phase measurement. The most common signal quality measures that can be used for weighting are the Signal to Noise Ratio (SNR) and the Carrier to Noise power density ratio (C/N_0). The SNR is the ratio of the amplitude of the desired signal to the amplitude of noise at a given point in time. The SNR can be expressed as 20 times the logarithm of the signal-noise amplitude ratio, or 10 times the logarithm of the signal-noise power ratio (Collins and Langley 1999). The SNR is usually represented in terms of the carrier to noise power density ratio, C/N_0. This is the ratio of the power level of the signal carrier to the noise power in a one Hertz bandwidth. A typical value is 45 dB-Hz, although actual values will vary due to multi-path, the receiver antenna gain pattern, the GPS satellite transmission level differences and the atmospheric attenuation effects (Collins and Langley 1999). The use of the SNR information for weighting the GPS observations can be seen as an intermediate step between simple functional models, e.g. mapping functions and the more complicated stochastic methods which require as much information as possible about the stochastic quantities of the observables to construct a fully populated variance-covariance matrix (Tiberius et al. 1999). The SNR value is generally used as a measure of the noise level that can contaminate a GPS observation. The SNR values can be recovered from the LEO space-borne GPS receiver. The equation of approximating the error of the carrier phase observations ϕ_i based on the GPS signal power at frequency i has been given by (see Langley 1997 and Braasch and Dierendonck 1999),

$$\sigma_{\phi_i} = \sqrt{\frac{B}{(c/n_0)_i}}\frac{\lambda_i}{2\pi}, \tag{3.15}$$

with the carrier phase tracking loop bandwidth B in units of Hz, the carrier phase wavelength λ_i and the carrier to noise density $(c/n_0)_i$ expressed as a ratio $10^{\frac{C/N_0}{10}}$, whose C/N_0 is expressed in dB-Hz. This equation gives a nominal value for the L_1 carrier phase noise of $0.2mm$ for a $2Hz$ bandwidth and a C/N_0 value of $45dB\text{-}Hz$ (Collins and Langley 1999).

3.3.4 Sigma-ε Model Weighting

The signal to noise ratio can be used directly for weighting the carrier phase observations in the GPS data processing. From Eq. (3.15), the carrier phase variance for the carrier phase ϕ_i can be rewritten as a function of the measured C/N_0 as,

$$\sigma^2_{\phi_i} = \alpha_{\phi_i} 10^{-(\frac{C/N_0}{10})}, \tag{3.16}$$

α_{ϕ_i} is a measure determined from the GPS signal structure and receiver properties. The sigma-ε model is based on Eq. (3.16) expressing the estimation of the carrier phase variance. The weights of the carrier phase observations ϕ_i can be determined as,

$$w_{\phi_i} = \frac{1}{\sigma^2_{\phi_i}}. \tag{3.17}$$

Through the sigma-ε model, the measured C/N_0 values are used for the calculation of the GPS carrier phase weights in the GPS data processing. Obviously, from the sigma-ε model, the carrier phase observations are weighted corresponding to the measured signal strength and is more realistic than the equally weighting.

3.3.5 Zenith Distance Weighting

Zenith distance weighting is one of the frequently used weighting procedures in the GPS data processing. It is only based on the geometrical strength of the tracked GPS satellites. Obviously, the sigma-ε weighting was based on the physical strength of the received GPS signals, namely on th C/N_0 values. Among the remaining un-modeled errors in the GPS data processing are the multi-path delay effects, which increases when the Line Of Sight(LOS) approaches the horizon. In other words, the larger the GPS satellite zenith angle is the higher is the carrier phase noise. Therefore, a relation between the GPS observations and the zenith distance angle can be formulated. The zenith-distance weighting, as introduced by Rothacher (Rothacher et al. 1998) for processing data of ground GPS stations can be written (see Hugentobler et al. 2001),

$$w(z^{s_i}) = \cos^2(z^{s_i}), \tag{3.18}$$

where z^{s_i} is the zenith distance of the tracked GPS satellite s_i with respect to the local vertical of the GPS receiver on-board LEO. The zenith distance weighting can be used simply in the GPS data weighting. The zenith weighting strategy is useful in case of lack of signal quality measures (i.e. SNR data). LEO GPS-SST observations at low elevation angles are not corrupted by the troposphere refraction but multi-path effects can be the main reason to degrade the GPS-SST observations with low elevations. Specially, the space-borne receiver on-board LEO can track the GPS satellites under the LEO local horizon ($z \geq 90°$). To process the observations under the LEO horizon in the orbit determination procedure, an appropriate weighting function has to be used. A simple modification of the zenith weighting (Eq. (3.18)) has been proposed by Bock (Bock 2003),

$$w(z^{s_i}) = \cos^2(\alpha z^{s_i}), \tag{3.19}$$

with α as a zenith distance factor of the high-low GPS-SST observations above the LEO local horizon (i.e. $z \geq 90°$). The estimated geometrical LEO absolute positions by Bock (Bock 2003) show the best results for the case of the CHAMP satellite with $\alpha = 1$ and a cut-off angle 0° and for the case of the SAC-C satellite with $\alpha = \frac{3}{4}$ and a cut-off angle 0°.

4. Zero Difference Geometrical Precise Point Positioning of a LEO

4.1 Introduction

The International GNSS Service (IGS) provides GNSS orbit products to the scientific community with increasing precision and temporal resolution. Many users have adopted the IGS precise orbits to achieve cm - accuracy and long-term stability of the reference frame. Differential positioning approaches (SD, DD or TD) require the combination of observations from a minimum of two GPS receivers (or one GPS receiver at two sub-sequential epochs) with at least one station with known coordinates. The station positions of single points (terrestrial stations or GPS satellite-receiver locations), baseline endpoints or network points can then be estimated relative to one or more multiple reference stations using differenced carrier phase observations. Baseline or network processing is an effective way to cancel out common satellite/receiver errors and to connect the user position to the coordinates of the reference stations while the precise orbit virtually eliminates the errors introduced by the GPS space segment. This mode of GPS data processing has been proved to be very effective, has received widespread acceptance and has been used in many GPS data processing software packages (e.g. Bernese, GAMIT/GLOBK, etc.). One drawback is the practical constraint imposed by the requirement that simultaneous observations have to be made at the reference stations. An attractive alternative to differential positioning is a single station positioning utilizing GPS precise orbits, clock offsets and un-differenced observations as zero difference or un-differenced positioning mode. Single station positioning (IGS station or LEO) with fixed (without variance-covariance) or not-fixed (with variance-covariance) precise orbit solutions and Doppler satellite observations were first introduced in the early 1970s by *R.R. Anderle*, who named the method "precise point positioning (PPP or 3P)" (Kouba and Heroux 2001).

The interest in a precise orbit determination of Low Earth Orbiters (LEOs) especially in pure geometrical mode using GPS observations has been grown rapidly as already pointed out. Conventional GPS-based strategies rely on the GPS observations from a terrestrial network of ground receivers (IGS network) as well as the GPS receiver on-board LEO in double difference (DD) or in triple difference (TD) data processing modes. This is a complex and time-consuming estimation procedure. At first, it is necessary to describe the concept of geometrical precise point positioning. Conventional Standard Point Positioning (SPP) is based on the processing of un-differenced GPS observations and is subject to the influence of all error sources. Major error sources include those introduced by broadcast (not-precise) GPS orbits and clocks as sender errors, as well as atmospheric and ionospheric effects as medium errors, multi-path influences as receiver environment errors and the technical incompleteness of the receiver as receiver errors. Since SPP is only able to provide an accuracy of several meters in the positioning, it is not suitable for applications that require a high position accuracy such as for precise orbit determinations of LEO. With the advent of precise orbit and clock products at centimeter level accuracy provided by the IGS centers, the two errors associated with broadcast orbits and clocks can be significantly reduced. Once these errors are removed from the observations, higher positioning accuracy can be expected even when only a single GPS receiver is used (zero difference mode). The method that allows to determine highly precise solutions by processing of un-differenced carrier phase observations from a single GPS receiver supplemented by precise orbit and clock products is called Precise Point Positioning (PPP). The word 'precise' is used to distinguish it from the conventional standard point positioning method (SPP). If this procedure is applied to the LEO GPS-SST observations, it is denoted as LEO Geometrical Precise Orbit Determination (GPOD)(see Fig. 4.1). To determine the geometrical point wise LEO orbit, the code pseudo-range SST observations play an important role. Obviously, the code pseudo-range observations are very noisy; subsequently the determined LEO absolute point positions have a poor accuracy. The determination of absolute positions based on only carrier phase ambiguous-range observations has the disadvantage that the ambiguity term must be determined in addition, but the advantage with respect to the positioning accuracy is significant. Generally, the accuracy of all geometrical point positioning methods relies on the geometry status (configuration, DOPs) of the GPS satellites and on the number

of tracked GPS satellites as well as on the GPS measurement strength (observation accuracy in the data processing). Therefore, on the one hand, the approximate absolute positions and the clock offset of a LEO can be determined epoch-wise based on the unambiguous code pseudo-range GPS-SST observations. On the other hand, the absolute positions of the LEOs can be improved with the accurate screened carrier phase GPS-SST observations. Obviously, the subsequent time differenced carrier phase observations are free from ambiguity terms (if no cycle slips or outliers between two sub-sequent carrier phase observations exist) and therefore the sub-sequent time differenced carrier phase observations can be used to screen the carrier phase observations for cycle slips and outliers or to estimate absolute position differences (or absolute positions) between two sub-sequent epochs with high accuracy. In case of the estimation of absolute positions, the absolute positions and clock offsets of a LEO from the code pseudo-range observations have to be combined with the absolute position and clock offset differences from the sub-sequent time differenced carrier phase observations.

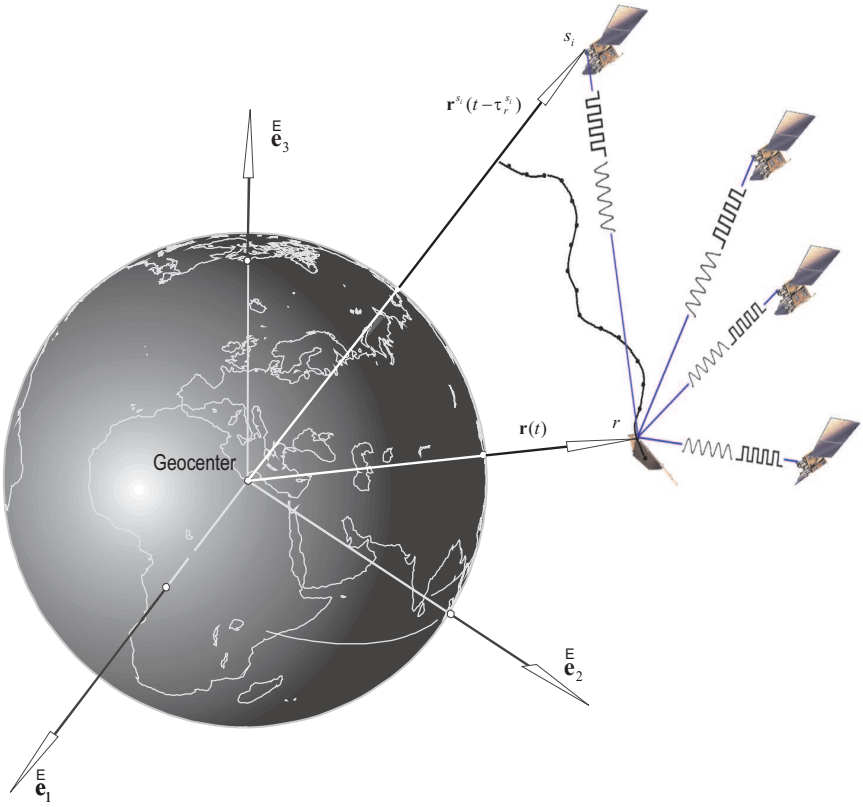

Figure 4.1: Zero difference mode of a LEO precise orbit determination procedure.

4.2 Zero Difference Absolute Point Positioning with Code Pseudo-range Observations

4.2.1 Methodology

The determination of geometrical LEO absolute position with the code pseudo-range GPS-SST observations is a sub-process of GPS data processing, which is needed to initialize the LEO precise point positioning with the carrier phase observation or sub-sequential time differenced carrier phase observations. The LEO absolute positions can be derived with an accuracy of meters, depending on the geometrical configuration

of tracked GPS satellites and the receiver environment error with the code pseudo-range observations. The observations used for the code geometrical point positioning model are the ionosphere-free code pseudo ranges, GPS precise orbits and clock offsets from the IGS center with the high-rate interval and an additional modeling of systematic errors of the GPS-SST observation. Examples are the systematic errors on GPS-SST observations, special relativistic effects on the GPS satellites and LEO and antenna-mass center offsets on the GPS satellites and LEOs can be mentioned.

4.2.2 Model of the Code Pseudo-range Observable

GPS code pseudo-range observations at time t for LEOs can be modeled as:

$$P^s_{r,i}(t) = \rho^s_r(t) + c[\delta t_r(t) - \delta t^s(t - \tau^s_r)] + I^r_i(t) + d^s_O(t) + d^r_R(t) - d^s_R(t) + \\ + d^r_{C,i}(t) + d^r_{V,i}(t) + d_{M,P_i}(t) + \varepsilon^s_{r,P_i}, \tag{4.1}$$

or in more details,

$$P^s_{r,i}(t) = \left\| \mathbf{R}_z(\omega_e \tau^s_r)\mathbf{r}^s(t - \tau^s_r) - \mathbf{r}(t) \right\| + c[\delta t_r(t) - \delta t^s(t - \tau^s_r)] + I^r_i(t) + d^s_O(t) + \\ + d^r_R(t) - d^s_R(t) + d^r_{C,i}(t) + d^r_{V,i}(t) + d_{M,P_i}(t) + \varepsilon^s_{r,P_i}, \tag{4.2}$$

where

s, r, i	GPS satellite (sender), LEO (receiver) and frequency identifiers, respectively,
τ^s_r	travel time of the signal from the GPS satellite to a LEO,
t, $t - \tau^s_r$	GPS signal reception time in the receiver and GPS signal sending time from GPS satellite,
$P^s_{r,i}(t)$	code pseudo-range observation in units of length at frequency i,
$\rho^s_r(t)$	true geometrical distance between the GPS satellite (sender) at emission time and the LEO (receiver) at reception time,
$\mathbf{r}^s(t - \tau^s_r)$	position vector of the GPS satellite at emission time $t - \tau^s_r$,
$\delta t^s(t - \tau^s_r)$	GPS clock offset at $t - \tau^s_r$,
$\mathbf{r}(t)$	position vector of a LEO at reception time t,
$\delta t_r(t)$	LEO clock offset at time t,
c	speed of light in vacuum,
ω_e	rotation rate of the Earth,
$\mathbf{R}_z(\omega_e \tau^s_r)$	rotation matrix of the ITRF around the z axis by the angle $\omega_e \tau^s_r$,
$I^r_i(t)$	ionosphere effect on the GPS observations at frequency i,
$d^s_O(t)$	orbital error of s^{th} GPS satellite at time t,
$d^r_R(t)$	periodic special relativistic effect on a LEO at time t,
$d^s_R(t)$	periodic special relativistic effect on the GPS satellite s at time t,
$d^r_{C,i}(t)$	LEO phase center offset correction for the frequency i at time t,
$d^r_{V,i}(t)$	LEO phase center offset variation for the frequency i at time t,
$d_{M,P_i}(t)$	multi-path effect on the code pseudo range measurements at frequency i at time t,
ε^s_{r,P_i}	noise of code observation (receiver noise and remaining errors).

If the error effects are summarized as follows,

$$e^s_{r,P_i}(t) = -c\delta t^s(t - \tau^s_r) + I^r_i(t) + d^s_O(t) + d^r_{Tr}(t) + d^r_{Ti}(t) + d^r_R(t) - d^s_R(t) + \\ + d^r_{C,i}(t) + d^r_{V,i}(t), \tag{4.3}$$

then the code pseudo-range observation between the GPS satellite s and the GPS receiver r on-board LEO at frequency i according to Eq. (4.3) reads,

$$P^s_{r,i}(t) = \left\| \mathbf{R}_z(\omega_e \tau^s_r)\mathbf{r}^s(t - \tau^s_r) - \mathbf{r}(t) \right\| + c\delta t_r(t) + d_{M,P_i}(t) + e^s_{r,P_i}(t) + \varepsilon^s_{r,P_i}. \tag{4.4}$$

At first, the rotation matrix around the z-axis is necessary when using vectors referred to an Earth fixed coordinate system, located in its center of mass, i.e. ITRF (Strang and Borre 1997). Because of the dependency of the ionosphere effect on the frequency of the GPS signal, in a first approximation, the ionosphere effect can be eliminated with a linear combination of the GPS signals at two frequencies, namely f_1 and f_2. In other words, if P_1 and ϕ_1 are the code pseudo-range and carrier phase observations in the band L_1 and P_2 and ϕ_2 are the code pseudo-range and carrier phase observations in the band L_2, then the ionosphere-free code pseudo-range observation, P_3, and the ionosphere-free carrier phase observation, Φ_3, can be written according to Eq. (2.45) as:

$$P_3 = n_1 P_1 + n_2 P_2, \quad \Phi_3 = n_1 \lambda_1 \phi_1 + n_2 \lambda_2 \phi_2, \quad n_1 = \frac{f_1^2}{f_1^2 - f_2^2}, \quad n_2 = -\frac{f_2^2}{f_1^2 - f_2^2},$$

Therefore, in all GPS-SST observation equations, the ionospheric effect with sufficient accuracy has been eliminated with the ionosphere-free linear combination (Xu 2007). With the advent of the GPS precise orbit and clock offset products, the GPS satellite orbital error, i.e. $d_O^s(t)$, can be neglected in the observation equations. The multi-path effect of code pseudo-range observations, i.e. $d_{M,P_i}(t)$, can be neglected too. In case of carrier phase GPS-SST observation, the multi-path effect can be mitigated with taking into account the observation weights with respect to the GPS satellite (sender) zenith distance from the LEOs (observer)(see Bock et al. 2002). It is noticeable that all ionosphere-free observations with sub-script 3 ($i = 3$) have been indexed, and ϕ_i, Φ_i are the carrier phase observations at frequency i in units of cycles and length respectively.

4.2.3 Absolute Point Positioning with the Code Pseudo-range Observations

After linearization of Eq. (4.4) for ionosphere-free code pseudo-range observation between the GPS satellite s and the GPS receiver r at time t follows:

$$P_{r,3}^s(t) - \left(\rho_r^s(t) + c\delta t_r(t) + d_{M,P_3}(t) + e_{r,P_3}^s(t)\right)\Big|_{\mathbf{x}(t)=\mathbf{x}_0(t)} = \mathbf{a}_{\mathbf{x}}^s(t)\Big|_{\mathbf{x}(t)=\mathbf{x}_0(t)} [\mathbf{x}(t) - \mathbf{x}_0(t)] + \varepsilon_{r,P_3}^s, \quad (4.5)$$

where

$\mathbf{x}_0(t) = \begin{pmatrix} x_{r,0}(t) & y_{r,0}(t) & z_{r,0}(t) & c\delta t_{r,0}(t) \end{pmatrix}^{\mathrm{T}}$ initial absolute position vector and initial clock offset of a LEO receiver in the units of length at reception time t,

$\mathbf{x}(t) = \begin{pmatrix} x_r(t) & y_r(t) & z_r(t) & c\delta t_r(t) \end{pmatrix}^{\mathrm{T}}$ final absolute position vector and clock offset of a LEO receiver in the units of length at reception time t,

$\delta\mathbf{x}(t) = \mathbf{x}(t) - \mathbf{x}_0(t)$ absolute position and clock offset difference vector betw--een the final and the initial values at time t,

$\mathbf{a}_{\mathbf{x}}^s(t)$ row of the design matrix (1×4) for the GPS satellite s at time t.

The Gauss-Markov Model (GMM) with the observation equation Eq. (4.5) for the GPS satellite s can be written as,

$$\Delta l^s(t) = \mathbf{a}_{\mathbf{x}}^s(t)\delta\mathbf{x}(t), \quad w_{r,P_3}^s(t) = \frac{\sigma_0^2}{\sigma_{P_{r,3}^s(t)}^2} \cos^2(z_r^s(t)), \quad (4.6)$$

with the initial standard deviation σ_0, the standard deviation of the ionosphere-free code pseudo-range observation $\sigma_{P_{r,3}^s(t)}$, and the zenith distance $z_r^s(\tau)$ from the GPS receiver r on-board LEO to the GPS satellite s at time t. $w_{r,P_3}^s(t)$ is the weight of the ionosphere-free code pseudo-range observation. The calculated ionosphere-free code pseudo-range observation, $P_C(t)$, with the initial given values can be built as,

$$P_{r,C}^s(t) = \left(\rho_r^s(t) + c\delta t_r(t) + d_{M,P_3}(t) + e_{r,P_3}^s(t)\right)\Big|_{\mathbf{x}(t)=\mathbf{x}_0(t)}. \quad (4.7)$$

The quantity $\Delta l^s(t)$ is one element of the residual vector (in the sense observed minus calculated) for the GPS satellite s as follow,

$$\Delta l^s(t) = P^s_{r,3}(t) - P^s_{r,C}(t), \tag{4.8}$$

$\mathbf{a}^s_{\mathbf{x}}(t)$, $\mathbf{a}^s_{\mathbf{x}}(t)\Big|_{\mathbf{x}(t)=\mathbf{x}_0(t)}$ are the design matrices of the code pseudo-range observation in general form and with the initial position and clock offset of a LEO at time t inserted, respectively,

$$\mathbf{a}^s_{\mathbf{x}}(t) = \Big(\frac{x_r(t) - x^s(t-\tau^s_r)}{\rho^s_r(t)}, \frac{y_r(t) - y^s(t-\tau^s_r)}{\rho^s_r(t)}, \frac{z_r(t) - z^s(t-\tau^s_r)}{\rho^s_r(t)}, 1\Big), \tag{4.9}$$

$$\mathbf{a}^s_{\mathbf{x}}(t)\Big|_{\mathbf{x}(t)=\mathbf{x}_0(t)} = \Big(\frac{x_0(t) - x^s(t-\tau^s_r)}{\rho^s_{r,0}(t)}, \frac{y_0(t) - y^s(t-\tau^s_r)}{\rho^s_{r,0}(t)}, \frac{z_0(t) - z^s(t-\tau^s_r)}{\rho^s_{r,0}(t)}, 1\Big). \tag{4.10}$$

The vectors $\mathbf{x}_0(t)$, $\mathbf{x}(t)$ and $\delta\mathbf{x}(t)$ are the initial and the final values of the position vector and the clock offset of the LEO as well as the difference between them at time t, respectively. In case of $n\,(n \geq 4)$ code pseudo-range observations from the GPS receiver r on-board LEO to the GPS satellites $s_1, \ldots, s_n$ at time t, the design matrix for all the GPS satellites can be built as follows:

$$\mathbf{A}(t) = (\ \mathbf{a}^{s_1}_{\mathbf{x}} \ldots \mathbf{a}^{s_j}_{\mathbf{x}} \ldots \mathbf{a}^{s_n}_{\mathbf{x}}\ )^{\mathrm{T}}. \tag{4.11}$$

The residual vector of all observations at t reads:

$$\Delta\mathbf{l}(t) = (\ \Delta l^{s_1}(t), \quad \ldots \quad \Delta l^{s_j}(t), \quad \ldots \quad \Delta l^{s_n}(t)\ )^{\mathrm{T}}, \tag{4.12}$$

and the initial and the final values of the unknowns,

$$\mathbf{x}_0(t) = \begin{pmatrix} x_{r,0}(t) \\ y_{r,0}(t) \\ z_{r,0}(t) \\ c\delta t_{r,0}(t) \end{pmatrix}, \quad \mathbf{x}(t) = \begin{pmatrix} x_r(t) \\ y_r(t) \\ z_r(t) \\ c\delta t_r(t) \end{pmatrix}, \delta\mathbf{x}(t) = \mathbf{x}(t) - \mathbf{x}_0(t). \tag{4.13}$$

Finally, the observation equations of the Gauss-Markov model can be written at time t in the form,

$$\Delta\mathbf{l}(t) = \mathbf{A}(t)\delta\mathbf{x}(t), \quad \mathbf{W}_l(t) = \begin{pmatrix} w^{s_1}_{r,P_3}(t) & \ldots & 0 & \ldots & 0 \\ \vdots & \ddots & \vdots & \ddots & \vdots \\ 0 & \ldots & w^{s_j}_{r,P_3}(t) & \ldots & 0 \\ \vdots & \ddots & \vdots & \ddots & \vdots \\ 0 & \ldots & 0 & \ldots & w^{s_n}_{r,P_3}(t) \end{pmatrix}. \tag{4.14}$$

After solving the least squares adjustment problem, the solution for every observation time t can be written as follow,

$$\delta\hat{\mathbf{x}}(t) = \left(\mathbf{A}^{\mathrm{T}}(t)\mathbf{W}_l(t)\mathbf{A}(t)\right)^{-1}\mathbf{A}^{\mathrm{T}}(t)\mathbf{W}_l(t)\Delta\mathbf{l}(t), \quad \mathbf{C}_{\delta\hat{\mathbf{x}}(t)} = \left(\mathbf{A}^{\mathrm{T}}(t)\mathbf{W}_l(t)\mathbf{A}(t)\right)^{-1}. \tag{4.15}$$

$\mathbf{W}_l(t)$ is the weight matrix of the observations (inverse to the variance-covariance matrix of the ionosphere-free code pseudo-range observations, see Sec. 3.3). In case of code pseudo-range observations, it is frequently diagonal, with the diagonal elements derived from the variance of the ionosphere-free code pseudo-range observations.

The estimated unknowns in Eq. (4.15) are the corrections to the initial LEO absolute position and initial LEO clock offset at time t. The LEO absolute position and clock offset at time t read,

$$\mathbf{x}(t) = \mathbf{x}_0(t) + \delta\hat{\mathbf{x}}(t), \quad \mathbf{C}_{\hat{\mathbf{x}}(t)} = \mathbf{C}_{\delta\hat{\mathbf{x}}(t)}. \tag{4.16}$$

The residual vector of the ionosphere-free code pseudo-range observations at epoch t can be estimated as,

$$\hat{\mathbf{v}}(t) = \mathbf{A}(t)\hat{\mathbf{x}}(t) - \mathbf{l}(t). \tag{4.17}$$

The variance factor reads with the redundancy number df as follows,

$$\hat{\sigma}_0^2 = \frac{\hat{\mathbf{v}}^{\mathrm{T}}(t)\mathbf{W}_l(t)\hat{\mathbf{v}}(t)}{df}, \tag{4.18}$$

and the a-posteriori variance-covariance matrix reads,

$$\hat{\mathbf{C}}_{\hat{\mathbf{x}}(t)} = \hat{\sigma}_0^2 \left(\mathbf{A}^{\mathrm{T}}(t)\mathbf{W}_l(t)\mathbf{A}(t)\right)^{-1}. \tag{4.19}$$

It is remarkable that the unknowns of the code pseudo-range normal equations are computed using the initialized parameters, but the initial parameters are usually not (exactly) known; therefore, an iterative process has to be carried out to solve for the geometrical LEO point positions. For the given initial vector, a modified one can be obtained by solving the above problem; the modified initial vector can be used in turn as the initial vector to form the code pseudo-range GPS-SST observation normal equation, and the unknowns can be solved again until the process converges. The estimated unknown parameters in Eq. (4.15), $\delta\hat{\mathbf{x}}(t)$, are the corrections to the LEO absolute position and the initial LEO clock offset. Because of the non linearized observation model, an iteration procedure is necessary. The convergence of the unknowns can be achieved after a few iterations (i.e. i),

$$\hat{\mathbf{x}}(t)_{(i)} = \hat{\mathbf{x}}(t)_{(i-1)} + \delta\hat{\mathbf{x}}(t)_{(i)} = \hat{\mathbf{x}}(t)_{(i-1)} + \left(\mathbf{A}_{(i)}^{\mathrm{T}}(t)\mathbf{W}_l(t)\mathbf{A}_{(i)}(t)\right)^{-1}\mathbf{A}_{(i)}^{\mathrm{T}}(t)\mathbf{W}_l(t)\boldsymbol{\Delta}\mathbf{l}_{(i)}(t). \tag{4.20}$$

There are four unknowns in the code pseudo-range observation equation, therefore in the point-wise geometrical LEO positioning, at least four observables from LEO to GPS satellites are needed to make the problem solvable. In other words, as soon as four or more GPS satellites are tracked, single point positioning of LEO at the observed epoch is possible.

4.3 Zero Difference Carrier Phase Absolute Point Positioning

4.3.1 Introduction

The carrier phase is the phase of the received satellite signal relative to the carrier phase, generated in the receiver at the reception time. The measurement is realized by shifting the receiver-generated carrier phase to the received GPS carrier phase. The number of full carrier waves between the receiver and the satellite cannot be accounted for the initial signal acquisition. Therefore, measuring the carrier phase means to measure the fractional phase and to keep track of changes in the cycles. The carrier phase is indeed an accumulated carrier phase observation. The fractional carrier phase can be measured with a precision better than 1% of the carrier phase wavelength, which corresponds to millimeter precision in the positions. This is the reason why the use of carrier phases lead to more precise results than the use of code pseudo-range observations (Xu 2007).

4.3.2 Establishment of Carrier Phase Observation Equation

The observation equation for GPS carrier phase observation at frequency i between the GPS satellite s and the LEO receiver r according to Eq. (2.31) at reception time t can be written as:

$$\begin{aligned}\Phi_{r,i}^s(t) = \lambda_i\phi_{r,i}^s(t) = \rho_r^s(t,t^s) + c[\delta t_r(t) - \delta t^s(t-\tau_r^s)] + \lambda_i A_{r,i}^s - I_i^r(t) + d_{C,i}^r(t) + d_{V,i}^r(t) + \\ + d_R^r(t) - d_R^s(t) + d_{M,\Phi_i}(t) + \varepsilon_{r,\Phi_i}^s,\end{aligned} \tag{4.21}$$

or in more details,

$$\Phi^s_{r,i}(t) = \left\| \mathbf{R}_z(\omega_e \tau^s_r)\mathbf{r}^s(t-\tau^s_r) - \mathbf{r}(t) \right\| + c[\delta t_r(t) - \delta t^s(t-\tau^s_r)] + \lambda_i A^s_{r,i} - I^r_i(t) + d^r_{C,i}(t) + \\ + d^r_{V,i}(t) + d^r_R(t) - d^s_R(t) + d_{M,\Phi_i}(t) + \varepsilon^s_{r,\Phi_i}, \tag{4.22}$$

with the quantities

$\Phi^s_{r,i}(t), \phi^s_{r,i}(t)$	observed carrier phase in units of length and in units of cycles for the frequency i, re--spectively,
$d_{M,\phi_i}(t)$	multi-path effect on the carrier phase measurements for the frequency i at time t,
ε^s_{r,Φ_i}	noise of carrier phase observation (receiver noise and remaining errors).

If we assume that all error effects of the receiver and the GPS satellite have been considered, either by specified models or by elimination through the data combination procedures (e.g. ionosphere-free linear data combination), then the error effects can be summarized at the reception time t according to Eq. (2.32) as follows,

$$e^s_{r,\Phi_i}(t) = -c\delta t^s(t-\tau^s_r) - I^r_i(t) + d^s_O(t) + d^r_R(t) - d^s_R(t) + d^r_{C,i}(t) + d^r_{V,i}(t). \tag{4.23}$$

The geometrical distance between the GPS satellite s and the GPS receiver r on-board LEO at frequency i reads,

$$\rho^s_{r,i}(t) = \left\| \mathbf{R}_z(\omega_e \tau^s_r)\mathbf{r}^s(t-\tau^s_r) - \mathbf{r}(t) \right\|, \tag{4.24}$$

or in more details,

$$\mathbf{R}_z(\omega_e \tau^s_r)\mathbf{r}^s(t-\tau^s_r) = \mathbf{r}^s_m(t-\tau^s_r) = \begin{pmatrix} x^s(t-\tau^s_r) & y^s(t-\tau^s_r) & z^s(t-\tau^s_r) \end{pmatrix}^{\mathrm{T}}, \\ \mathbf{r}(t) = \begin{pmatrix} x_r(t) & y_r(t) & z_r(t) \end{pmatrix}^{\mathrm{T}}, \tag{4.25}$$

with

$$\rho^s_{r,i}(t) = \left\| \mathbf{r}^s_m(t) - \mathbf{r}(t) \right\| = \left([x^s(t-\tau^s_r) - x_r(t)]^2 + [y^s(t-\tau^s_r) - y_r(t)]^2 + [z^s(t-\tau^s_r) - z_r(t)]^2 \right)^{1/2}. \tag{4.26}$$

The observation equation can be written at time t with the error term from Eq. (4.23) and the geometrical distance from Eq. (4.26) inserted into Eq. (4.22),

$$\Phi^s_{r,i}(t) = \left\| \mathbf{r}^s_m(t) - \mathbf{r}(t) \right\| + c\delta t_r(t) + \lambda_i A^s_{r,i} + d_{M,\Phi_i}(t) + e^s_{r,\Phi_i}(t) + \varepsilon^s_{r,\Phi_i}. \tag{4.27}$$

Obviously, the observation equation Eq. (4.27) for the carrier phase GPS-SST observation with respect to the LEO clock offset and the GPS ambiguity term is linear but it is non-linear with respect to the GPS receiver position on-board LEO. It has to be linearized with respect to the GPS-receiver position $\mathbf{r}(t)$ on-board LEO. The linearized carrier phase observation equation for the GPS satellite s and the GPS receiver r at frequency i can be written as follows,

$$\Phi^s_{r,i}(t) = \Phi^s_{r,i,0}(t) + \left. \frac{\partial \Phi^s_{r,i}(t)}{\partial \mathbf{x}} \right|_{\mathbf{x}=\mathbf{x}_0} (\mathbf{x} - \mathbf{x}_0), \tag{4.28}$$

$$\Delta\Phi^s_{r,i}(t) = \mathbf{a}^s_{\mathbf{x}}(t)\Delta\mathbf{x}, \quad w^s_{r,\Phi_i}(t) = \frac{\sigma^2_0}{\sigma^2_{\Phi^s_{r,i}(t)}} \cos^2(z^s_r(t)), \tag{4.29}$$

where,

$$\mathbf{a}^s_{\mathbf{x}}(t) = \frac{\partial \Phi^s_{r,i}(t)}{\partial \mathbf{x}}, \quad \Delta\Phi^s_{r,i}(t) = \Phi^s_{r,i}(t) - \Phi^s_{r,i,0}(t), \quad \Delta\mathbf{x} = \mathbf{x} - \mathbf{x}_0, \tag{4.30}$$

with the initial standard deviation σ_0, the carrier phase observation standard deviation $\sigma_{\Phi^s_{r,i}(t)}$ and the zenith distance $z^s_r(t)$, observed by the GPS receiver r to the GPS satellite s at time t. The term $w^s_{r,\Phi_i}(t)$ is the weight of the carrier phase observations and $\mathbf{x}$ summarizes the final unknown parameters, namely the LEO receiver position, the clock offset and the GPS satellites ambiguity terms. Only the corrections to the initial absolute position, the LEO clock offset and the GPS ambiguity parameters are estimated by solving the Gauss-Markov problem by an iterative procedure. The linearized observation equation for the carrier phase of the GPS satellite s with respect to the LEO receiver position, can be formulated based on Eq. (4.27) as follows,

$$\mathbf{a}^s_{\mathbf{r}}(t) = \frac{\partial \Phi^s_{r,i}(t)}{\partial \mathbf{r}(t)} = \begin{pmatrix} e^s_{r,x}(t) & e^s_{r,y}(t) & e^s_{r,z}(t) \end{pmatrix}, \tag{4.31}$$

with

$$e^s_{r,x}(t) = \frac{x_r(t) - x^s(t-\tau^s_r)}{\rho^s_r(t)}, \quad e^s_{r,y}(t) = \frac{y_r(t) - y^s(t-\tau^s_r)}{\rho^s_r(t)}, \quad e^s_{r,z}(t) = \frac{z_r(t) - z^s(t-\tau^s_r)}{\rho^s_r(t)}.$$

To establish all ionosphere-free carrier phase observation equations, we assume that the GPS receiver r at the first epoch is tracked for example by the GPS satellites s_1, s_2, s_3, s_4, s_5 and s_6. Then the Gauss-Markov model of all observed GPS satellites reads,

$$\begin{pmatrix} \Delta\Phi^{s_1}_{r,3}(t) \\ \Delta\Phi^{s_2}_{r,3}(t) \\ \Delta\Phi^{s_3}_{r,3}(t) \\ \Delta\Phi^{s_4}_{r,3}(t) \\ \Delta\Phi^{s_5}_{r,3}(t) \\ \Delta\Phi^{s_6}_{r,3}(t) \end{pmatrix} = \begin{pmatrix} e^{s_1}_{x,r}(t) & e^{s_1}_{y,r}(t) & e^{s_1}_{z,r}(t) & 1 & 1 & 0 & 0 & 0 & 0 & 0 \\ e^{s_2}_{x,r}(t) & e^{s_2}_{y,r}(t) & e^{s_2}_{z,r}(t) & 1 & 0 & 1 & 0 & 0 & 0 & 0 \\ e^{s_3}_{x,r}(t) & e^{s_2}_{y,r}(t) & e^{s_3}_{z,r}(t) & 1 & 0 & 0 & 1 & 0 & 0 & 0 \\ e^{s_4}_{x,r}(t) & e^{s_4}_{y,r}(t) & e^{s_4}_{z,r}(t) & 1 & 0 & 0 & 0 & 1 & 0 & 0 \\ e^{s_5}_{x,r}(t) & e^{s_5}_{y,r}(t) & e^{s_5}_{z,r}(t) & 1 & 0 & 0 & 0 & 0 & 1 & 0 \\ e^{s_6}_{x,r}(t) & e^{s_6}_{y,r}(t) & e^{s_6}_{z,r}(t) & 1 & 0 & 0 & 0 & 0 & 0 & 1 \end{pmatrix} \begin{pmatrix} \Delta x_r(t) \\ \Delta y_r(t) \\ \Delta z_r(t) \\ \Delta c\delta t_r(t) \\ \Delta\lambda_3 A^{s_1} \\ \Delta\lambda_3 A^{s_2} \\ \Delta\lambda_3 A^{s_3} \\ \Delta\lambda_3 A^{s_4} \\ \Delta\lambda_3 A^{s_5} \\ \Delta\lambda_3 A^{s_6} \end{pmatrix}, \tag{4.32}$$

with the weight matrix of all ionosphere-free carrier phase GPS-SST observations at the epoch t (inverse to the variance-covariance matrix of the ionosphere-free carrier phase observations, see Sec. 3.3),

$$\mathbf{W}_{\mathrm{l}}(t) = \begin{pmatrix} w^{s_1}_{r,\Phi_3}(t) & \dots & 0 & \dots & 0 \\ \vdots & \ddots & \vdots & \ddots & \vdots \\ 0 & \dots & w^{s_j}_{r,\Phi_3}(t) & \dots & 0 \\ \vdots & \ddots & \vdots & \ddots & \vdots \\ 0 & \dots & 0 & \dots & w^{s_6}_{r,\Phi_3}(t) \end{pmatrix}. \tag{4.33}$$

If the number of observations is smaller than the number of unknowns, (e.g. in present case the number of observations is 6 and the number of unknown parameters is 10), then the carrier phase single point positioning problem is not solvable after the first few epochs or within an epoch-wise single epoch point positioning procedure. To solve this problem, the carrier phase observations at more epochs have to be summed up and solved within a batch processing procedure for all desired epochs, either in static mode or in the kinematic mode of the geometrical precise point positioning.

4.3.3 Static Mode of Geometrical Precise Point Positioning Procedure

To show the observation equations in the static mode, we assume that the GPS satellites s_1, s_2, s_3, s_4, s_5 and s_6 have been tracked at two sequential epochs, then the number of observations is 12 and the number of

unknowns is 11, respectively (three coordinates and two clock offset parameters and 6 ambiguity parameters for 6 observed GPS satellites). The Gauss-Markov model reads,

$$\begin{pmatrix} \Delta\Phi_{r,3}^{s_1}(t_1) \\ \Delta\Phi_{r,3}^{s_2}(t_1) \\ \Delta\Phi_{r,3}^{s_3}(t_1) \\ \Delta\Phi_{r,3}^{s_4}(t_1) \\ \Delta\Phi_{r,3}^{s_5}(t_1) \\ \Delta\Phi_{r,3}^{s_6}(t_1) \\ \Delta\Phi_{r,3}^{s_1}(t_2) \\ \Delta\Phi_{r,3}^{s_2}(t_2) \\ \Delta\Phi_{r,3}^{s_3}(t_2) \\ \Delta\Phi_{r,3}^{s_4}(t_2) \\ \Delta\Phi_{r,3}^{s_5}(t_2) \\ \Delta\Phi_{r,3}^{s_6}(t_2) \end{pmatrix} = \begin{pmatrix} e_{x,r}^{s_1}(t_1) & e_{y,r}^{s_1}(t_1) & e_{z,r}^{s_1}(t_1) & 1 & 0 & 1 & 0 & 0 & 0 & 0 & 0 \\ e_{x,r}^{s_2}(t_1) & e_{y,r}^{s_2}(t_1) & e_{z,r}^{s_2}(t_1) & 1 & 0 & 0 & 1 & 0 & 0 & 0 & 0 \\ e_{x,r}^{s_3}(t_1) & e_{y,r}^{s_2}(t_1) & e_{z,r}^{s_3}(t_1) & 1 & 0 & 0 & 0 & 1 & 0 & 0 & 0 \\ e_{x,r}^{s_4}(t_1) & e_{y,r}^{s_4}(t_1) & e_{z,r}^{s_4}(t_1) & 1 & 0 & 0 & 0 & 0 & 1 & 0 & 0 \\ e_{x,r}^{s_5}(t_1) & e_{y,r}^{s_5}(t_1) & e_{z,r}^{s_5}(t_1) & 1 & 0 & 0 & 0 & 0 & 0 & 1 & 0 \\ e_{x,r}^{s_6}(t_1) & e_{y,r}^{s_6}(t_1) & e_{z,r}^{s_6}(t_1) & 1 & 0 & 0 & 0 & 0 & 0 & 0 & 1 \\ e_{x,r}^{s_1}(t_2) & e_{y,r}^{s_1}(t_2) & e_{z,r}^{s_1}(t_2) & 0 & 1 & 1 & 0 & 0 & 0 & 0 & 0 \\ e_{x,r}^{s_2}(t_2) & e_{y,r}^{s_2}(t_2) & e_{z,r}^{s_2}(t_2) & 0 & 1 & 0 & 1 & 0 & 0 & 0 & 0 \\ e_{x,r}^{s_3}(t_2) & e_{y,r}^{s_2}(t_2) & e_{z,r}^{s_3}(t_2) & 0 & 1 & 0 & 0 & 1 & 0 & 0 & 0 \\ e_{x,r}^{s_4}(t_2) & e_{y,r}^{s_4}(t_2) & e_{z,r}^{s_4}(t_2) & 0 & 1 & 0 & 0 & 0 & 1 & 0 & 0 \\ e_{x,r}^{s_5}(t_2) & e_{y,r}^{s_5}(t_2) & e_{z,r}^{s_5}(t_2) & 0 & 1 & 0 & 0 & 0 & 0 & 1 & 0 \\ e_{x,r}^{s_6}(t_2) & e_{y,r}^{s_6}(t_2) & e_{z,r}^{s_6}(t_2) & 0 & 1 & 0 & 0 & 0 & 0 & 0 & 1 \end{pmatrix} \begin{pmatrix} \Delta x_r(t_1) \\ \Delta y_r(t_1) \\ \Delta z_r(t_1) \\ \Delta c\delta t_r(t_1) \\ \Delta c\delta t_r(t_2) \\ \Delta\lambda_3 A^{s_1} \\ \Delta\lambda_3 A^{s_2} \\ \Delta\lambda_3 A^{s_3} \\ \Delta\lambda_3 A^{s_4} \\ \Delta\lambda_3 A^{s_5} \\ \Delta\lambda_3 A^{s_6} \end{pmatrix}, \quad (4.34)$$

or in matrix form,

$$\Delta\mathbf{l} = \mathbf{A}\mathbf{x}, \quad \mathbf{W}_l, \quad (4.35)$$

with the weight matrix of all ionosphere-free carrier phase GPS-SST observations at the epochs t_1 and t_2 as (inverse to the variance-covariance matrix of the ionosphere-free carrier phase observations, see Sec.(3)),

$$\mathbf{W}_l = \begin{pmatrix} \mathbf{W}_l(t_1) & \mathbf{0} \\ \mathbf{0} & \mathbf{W}_l(t_2) \end{pmatrix}. \quad (4.36)$$

The carrier phase observation equations can be solved by a least squares adjustment,

$$\Delta\hat{\mathbf{x}} = \left(\mathbf{A}^{\mathrm{T}}\mathbf{W}_l\mathbf{A}\right)^{-1}\mathbf{A}^{\mathrm{T}}\mathbf{W}_l\Delta\mathbf{l}, \quad \mathbf{C}_{\Delta\hat{\mathbf{x}}} = \left(\mathbf{A}^{\mathrm{T}}\mathbf{W}_l\mathbf{A}\right)^{-1}. \quad (4.37)$$

If we assume that n_s different GPS satellites are observed at every epoch and the total number of epochs is n_e then the total number of observations is $n_s \times n_e$. In this case, there are n_s ambiguity parameters, three coordinates and one clock offset at every epoch as unknown parameters, i.e. $n_s + n_e + 3$. If it holds $n_s \times n_e \geq n_s + n_e + 3$ then the Gauss-Markov model in the static case can be solved by a least squares minimization of the observation residuals.

The estimated unknown parameters in Eq. (4.37), $\Delta\hat{\mathbf{x}}$, are the corrections to the LEO absolute position, the initial LEO clock offsets and the initial ambiguities of all observed GPS satellites from the GPS receiver r on-board LEO. Because of the non linearized observation model, an iteration procedure is necessary. The convergence of the unknowns can be achieved after a few iterations (i.e. i),

$$\hat{\mathbf{x}}_{(i)} = \hat{\mathbf{x}}_{(i-1)} + \Delta\hat{\mathbf{x}}_{(i)} = \hat{\mathbf{x}}_{(i-1)} + \left(\mathbf{A}_{(i)}^{\mathrm{T}}\mathbf{W}_l\mathbf{A}_{(i)}\right)^{-1}\mathbf{A}_{(i)}^{\mathrm{T}}\mathbf{W}_l\Delta\mathbf{l}_{(i)}. \quad (4.38)$$

4.3.4 Non-static Mode of Geometrical Precise Point Positioning Procedure

In the kinematical mode, we assume that the receiver is moving and the absolute positions and clock offsets at every epoch are changing. This has to be considered in the establishment of the system of observation equations. In the static positioning mode, we assume that the GPS satellites s_1, s_2, s_3, s_4, s_5 and s_6 have been tracked at two subsequent epochs. In the present case, the numbers of observations and unknown parameters are 12 and 14 (six coordinates and two clock offset parameters and 6 ambiguity parameters for 6 observed GPS satellites) for the subsequent observations epochs. Obviously, the number of the carrier phase observations is less than the number of unknown parameters and the problem is underdetermined. To solve this problem, a sufficient number of carrier phase observations has to be added to the system of observation equations to arrive at a uniquely solvable regular normal matrix. The Gauss-Markov model in the kinematical mode for two subsequent epochs, t_1 and t_2, can be established as follows,

$$\begin{pmatrix} \Delta\Phi_{r,3}^{s_1}(t_1) \\ \Delta\Phi_{r,3}^{s_2}(t_1) \\ \Delta\Phi_{r,3}^{s_3}(t_1) \\ \Delta\Phi_{r,3}^{s_4}(t_1) \\ \Delta\Phi_{r,3}^{s_5}(t_1) \\ \Delta\Phi_{r,3}^{s_6}(t_1) \\ \Delta\Phi_{r,3}^{s_1}(t_2) \\ \Delta\Phi_{r,3}^{s_2}(t_2) \\ \Delta\Phi_{r,3}^{s_3}(t_2) \\ \Delta\Phi_{r,3}^{s_4}(t_2) \\ \Delta\Phi_{r,3}^{s_5}(t_2) \\ \Delta\Phi_{r,3}^{s_6}(t_2) \end{pmatrix} =$$

$$\begin{pmatrix} e_{x,r}^{s_1}(t_1) & e_{y,r}^{s_1}(t_1) & e_{z,r}^{s_1}(t_1) & 1 & 0 & 0 & 0 & 0 & 1 & 0 & 0 & 0 & 0 & 0 \\ e_{x,r}^{s_2}(t_1) & e_{y,r}^{s_2}(t_1) & e_{z,r}^{s_2}(t_1) & 1 & 0 & 0 & 0 & 0 & 0 & 1 & 0 & 0 & 0 & 0 \\ e_{x,r}^{s_3}(t_1) & e_{y,r}^{s_3}(t_1) & e_{z,r}^{s_3}(t_1) & 1 & 0 & 0 & 0 & 0 & 0 & 0 & 1 & 0 & 0 & 0 \\ e_{x,r}^{s_4}(t_1) & e_{y,r}^{s_4}(t_1) & e_{z,r}^{s_4}(t_1) & 1 & 0 & 0 & 0 & 0 & 0 & 0 & 0 & 1 & 0 & 0 \\ e_{x,r}^{s_5}(t_1) & e_{y,r}^{s_5}(t_1) & e_{z,r}^{s_5}(t_1) & 1 & 0 & 0 & 0 & 0 & 0 & 0 & 0 & 0 & 1 & 0 \\ e_{x,r}^{s_6}(t_1) & e_{y,r}^{s_6}(t_1) & e_{z,r}^{s_6}(t_1) & 1 & 0 & 0 & 0 & 0 & 0 & 0 & 0 & 0 & 0 & 1 \\ 0 & 0 & 0 & 0 & e_{x,r}^{s_1}(t_2) & e_{y,r}^{s_1}(t_2) & e_{z,r}^{s_1}(t_2) & 1 & 1 & 0 & 0 & 0 & 0 & 0 \\ 0 & 0 & 0 & 0 & e_{x,r}^{s_2}(t_2) & e_{y,r}^{s_2}(t_2) & e_{z,r}^{s_2}(t_2) & 1 & 0 & 1 & 0 & 0 & 0 & 0 \\ 0 & 0 & 0 & 0 & e_{x,r}^{s_3}(t_2) & e_{y,r}^{s_3}(t_2) & e_{z,r}^{s_3}(t_2) & 1 & 0 & 0 & 1 & 0 & 0 & 0 \\ 0 & 0 & 0 & 0 & e_{x,r}^{s_4}(t_2) & e_{y,r}^{s_4}(t_2) & e_{z,r}^{s_4}(t_2) & 1 & 0 & 0 & 0 & 1 & 0 & 0 \\ 0 & 0 & 0 & 0 & e_{x,r}^{s_5}(t_2) & e_{y,r}^{s_5}(t_2) & e_{z,r}^{s_5}(t_2) & 1 & 0 & 0 & 0 & 0 & 1 & 0 \\ 0 & 0 & 0 & 0 & e_{x,r}^{s_6}(t_2) & e_{y,r}^{s_6}(t_2) & e_{z,r}^{s_6}(t_2) & 1 & 0 & 0 & 0 & 0 & 0 & 1 \end{pmatrix} \begin{pmatrix} \Delta x_r(t_1) \\ \Delta y_r(t_1) \\ \Delta z_r(t_1) \\ \Delta c\delta t_r(t_1) \\ \Delta x_r(t_2) \\ \Delta y_r(t_2) \\ \Delta z_r(t_2) \\ \Delta c\delta t_r(t_2) \\ \Delta\lambda_3 A^{s_1} \\ \Delta\lambda_3 A^{s_2} \\ \Delta\lambda_3 A^{s_3} \\ \Delta\lambda_3 A^{s_4} \\ \Delta\lambda_3 A^{s_5} \\ \Delta\lambda_3 A^{s_6} \end{pmatrix}, \tag{4.39}$$

or in matrix notation,

$$\Delta\mathbf{l} = \mathbf{A}\Delta\mathbf{x}, \quad \mathbf{W}_l, \tag{4.40}$$

with the weight matrix at the sub-sequent epochs t_1 and t_2 as,

$$\mathbf{W}_l = \begin{pmatrix} \mathbf{W}_1(t_1) & \mathbf{0} \\ \mathbf{0} & \mathbf{W}_1(t_2) \end{pmatrix}. \tag{4.41}$$

If the number of the carrier phase observations is more than the number of the unknowns, then the carrier phase observation equations can be solved in the batch processing mode,

$$\Delta\hat{\mathbf{x}} = \left(\mathbf{A}^{\mathrm{T}}\mathbf{W}_l\mathbf{A}\right)^{-1}\mathbf{A}^{\mathrm{T}}\mathbf{W}_l\Delta\mathbf{l}, \quad \mathbf{C}_{\Delta\hat{\mathbf{x}}} = \left(\mathbf{A}^{\mathrm{T}}\mathbf{W}_l\mathbf{A}\right)^{-1}. \tag{4.42}$$

The estimated unknown parameters in Eq. (4.42), $\Delta\hat{\mathbf{x}}$, are the corrections to the LEO absolute positions, the initial LEO clock offsets and the initial ambiguities of all observed GPS satellites from the GPS receiver r on-board LEO. Because of the non linearized observation model, an iteration procedure is necessary. The convergence of the unknowns can be achieved after a few iterations (i.e. i),

$$\hat{\mathbf{x}}_{(i)} = \hat{\mathbf{x}}_{(i-1)} + \Delta\hat{\mathbf{x}}_{(i)} = \hat{\mathbf{x}}_{(i-1)} + \left(\mathbf{A}_{(i)}^{\mathrm{T}}\mathbf{W}_l\mathbf{A}_{(i)}\right)^{-1}\mathbf{A}_{(i)}^{\mathrm{T}}\mathbf{W}_l\Delta\mathbf{l}_{(i)}. \tag{4.43}$$

If the normal equation is solvable, then it is clear that the float ambiguities only can be solved from the least squares method without any pre-conditions. In the case of geometrical precise point positioning of a GPS receiver on-board LEO with zero difference ionosphere-free carrier phase observations, the float ambiguity solving mode has to be used.

4.3.5 Rank Defect of the Carrier Phase Observation Equation

The rank of the design matrix $\mathbf{A}$ is the number of its linear independent columns, $r = \text{rank}(\mathbf{A})$. If this is not the case, then the matrix is column-singular. The singular system of equations becomes regular if a parameter corresponding to a linearly dependent column is fixed. This can be arrived such that the column is transferred to the left side of the system of observation equations to become part of the observation vector. This transfer reduces the columns of the design matrix by the number of rank deficiencies (Hofmann-Wellenhof et al. 2001). Mathematically speaking, if $\mathbf{A}_{\text{m}\times\text{n}}$ is the design matrix of zero difference carrier phase observations, $\mathbf{A}$ has a rank defect if

$$\mathbf{Av} = 0, \quad \exists\, \mathbf{v} \neq \mathbf{0}. \tag{4.44}$$

If there exists an $n \times 1$ vector $\mathbf{v} \neq \mathbf{0}$ so that it holds $\mathbf{Av} = \mathbf{0}$, then the system has a rank defect. The design matrix of zero difference carrier phase observations for two first subsequent epochs of the GPS satellites s_1, s_2, s_3, s_4, s_5 and s_6 in static mode can be written as described in Eq. (4.34). If we choose the $\mathbf{v} \neq \mathbf{0}$, e.g.,

$$\mathbf{v} = \begin{pmatrix} 0 & 0 & 0 & -1 & -1 & 1 & 1 & 1 & 1 & 1 & 1 \end{pmatrix}^{\text{T}}, \tag{4.45}$$

then it yields $\mathbf{Av} = \mathbf{0}$. The rank-defect corresponds to the kinematical mode of geometrical precise point positioning solution, although the vector $\mathbf{v} \neq \mathbf{0}$ is slightly different, because of the different positions of the unknown parameters in the design matrix. For example, in case of three sequential epochs in the kinematic mode of geometrical precise point positioning mode, the vector $\mathbf{v}$ can be chosen as (for $\mathbf{A}$ refer to Eq. (4.39)),

$$\mathbf{v} = \begin{pmatrix} 0 & 0 & 0 & -1 & 0 & 0 & 0 & -1 & 0 & 0 & 0 & -1 & 1 & 1 & 1 & 1 & 1 & 1 \end{pmatrix}^{\text{T}}, \tag{4.46}$$

then if follows as in the static mode, $\mathbf{Av} = \mathbf{0}$. The rank defect affects only the ambiguity and clock parameters. The position vector is not affected by the rank defect, because the elements of the vector $\mathbf{v} \neq 0$, which correspond to the positions are zero. A common solution for solving the rank defect in case of zero difference carrier phase observation equations is to fix one of the ambiguity or clock parameters to its a-priori values. However, in the case of this kind of rank defect, it does not matter what we choose, the position parameters (or baseline parameters) which have been estimated will not be changed by it (Van der Marel 2003). If the geometric configuration of the GPS satellites for the observer has been sufficiently changed, e.g. for GPS satellite s_1 at two sub-sequent epochs $e^{s_1}_{x..z,r}(t_2) \neq e^{s_1}_{x..z,r}(t_1)$, then this is only the rank defect in the Gauss-Markov model, i.e. the rank defect of the zero difference carrier phase observation equation is one. But if the GPS satellites geometry configuration for the observer has not been sufficiently changed, i.e. for GPS satellites s_1, s_2, s_3, s_4, s_5 and s_6 at two sub-sequent epochs in the static mode of geometrical positioning, $e^{s_1}_{x...z,r}(t_2) = e^{s_1}_{x...z,r}(t_1) = e^{s_2}_{x...z,r}(t_2) = e^{s_6}_{x...z,r}(t_2)$, and if we choose the vector as,

$$\mathbf{v} = \begin{pmatrix} -1 & 0 & 0 & 0 & 0 & 0 & e^{s_1}_{x,r}(t_1) & e^{s_1}_{x,r}(t_1) & e^{s_1}_{x,r}(t_1) & e^{s_1}_{x,r}(t_1) & e^{s_1}_{x,r}(t_1) \end{pmatrix}^{\text{T}}, \tag{4.47}$$

then $\mathbf{Av} = \mathbf{0}$. The rank-defect of the design matrix is three. The rank defects in case of the kinematical and the static modes of geometrical positioning is identical. In case of GPS solutions based on carrier phase observations, it is necessary to have a sufficient number of intervals in between two subsequent epochs, in order to avoid the rank defects.

5. Representation of Short Arcs

5.1 Introduction

The ephemerides of point-wise satellite positions can be derived by GNSS analysis techniques as discussed in chapter 4. The different precise point positioning techniques will be designated as geometric orbit determination methods. There is no connection between subsequent positions, and consequently, no information about the velocity or even the acceleration of the satellite is available. To describe the time dependency of the motion of a satellite, it is necessary to provide a properly constructed function which consistently connects analytically positions, velocities and accelerations. In many applications such a continuous function is provided by a properly selected linear interpolation or an approximation function derived from a table of positions by a least squares adjustment process. From these position functions, velocities and accelerations can be derived consistently by numerical or analytical differentiation. With such a function the kinematics of the satellite's motion is given as result of a kinematic orbit determination process. It should be pointed out that no dynamic force model at all is used for this kind of orbit determination. The kinematical orbit is represented by a sufficient number of approximation parameters, including the initial or boundary values of the arc. These parameters are determined such that the observations are approximated in the best possible way with respect to a properly selected norm.
The approach presented in this thesis is based on approximation parameters, which have also a clearly defined relation to the dynamical model of the satellite's motion. To realize this, the kinematical orbit is not only a continuous approximation of the orbit as it is observed by GNSS observations, it is also a solution of Newton's equation of motion of the satellite. If the kinematical parameters are determined by a best fitting process based on the observations, then we perform a pure kinematical orbit determination, which will be discussed in Sec. 6.1. If the parameters are determined by a model of the forces acting on the satellites, then a dynamic orbit determination is realized. These aspects will be treated in Sec. 6.2. In addition, there is also the possibility to use certain constraints based on the dynamical force function model. In this case, we carry out a reduced kinematical orbit determination of a specific level, depending on the strength of the dynamical restrictions; the various possibilities will be discussed in this section. It will be demonstrated, that this formulation of the orbit determination problem allows a smooth transition from a kinematical orbit determination to a dynamical orbit determination. At the one end, the orbit parameters are determined without any force function information at all, and at the other extreme end, all parameters are functions of the force function model.
The flexibility of this orbit determination procedure is achieved by formulating a boundary value problem to Newton-Euler's equation of motion in form of an integral equation of Fredholm type. The solution of this integral equation can be formulated in a semi-analytical form, either as a series of Fourier coefficients as outlined in Sec. 5.2, or as a series of Euler and Bernoulli polynomials as discussed in Sec. 5.3. These approximations represent kinematical models of residual orbits based on reference motions of the satellites to minimize the numerical problems. This reference motion can be formulated either as a linear combination of the boundary position vectors, either a straight line (Sec. 5.2.1) or an ellipse connecting the end points of the arc (Sec. 5.2.2) or as a reference orbit derived by any dynamic orbit determination procedure (Sec. 5.2.3). The interpretation of the difference function as a Fourier series based on the reference orbit (Sec. 5.2.4) and the transformation to a series of Euler and Bernoulli polynomials (Sec. 5.3) builds the basis for the integrated flexible kinematical, dynamical and reduced kinematical orbit determination approach.

5.2 Boundary Value Problem for the Equation of Motion as Integral Equation of Fredholm Type

5.2.1 Equation of Motion Based on the Simple Newton Operator

The idea as outlined in the following was proposed as a general method for orbit determination by Schneider in 1967 (Schneider 1968). This orbit determination technique has been further developed and modified

to various applications in Satellite Geodesy and Celestial Mechanics (Schneider 1997, Schneider 1992, Schneider 1993, Schneider 2002a and Schneider 2002b, Schneider 1984). A first application to determine preliminary orbits of artificial satellites was performed by Ilk (Ilk 1972). First tests for a dynamic orbit determination based on direction and distance measurements are reported in (Ilk 1973) and a technique for the numerical solution of a two-point boundary value problem of Newton-Euler's equation of motion as well as of Lagrange's equation of motion based on Schneider's proposal has been developed by Ilk (Ilk 1976). This technique was modified for gravity field determination by Reigber (Reigber 1969), and successfully applied subsequently, especially as additional observation equations for zonal and resonant potential coefficients, in a series of gravity field models (e.g., Balmino et al. 1976). In the following, the idea has been applied to the Satellite-to-Satellite Tracking (SST) problem by Ilk (Ilk 1983a) and later to the Satellite Gravity Gradiometry (SGG) analysis. After that, the method has been developed and tested based on various simulation scenarios, e.g. see Ilk et al. 1995 and Ilk et al. 2003. The recovery procedure can be applied in the space domain or in the spectral domain, for POD analysis, high-low GPS-SST or low-low-SST. So far, this technique has been applied very successfully for gravity field determinations but was not yet applied to kinematical orbit determination as an independent product. The reason was that the observation types of the past were not the proper ones needed for this solution method. The success of GNSS changed the situation dramatically and it seems that Schneider's proposal is especially tailored to the in-situ gravity field determination technique which is based on very precisely determined short arcs. In the following, we will present the theoretical foundation of the integrated kinematical-dynamical orbit determination approach (Fig. 5.1). The mathematical-physical model for densely tracked orbits is based on the formulation of the

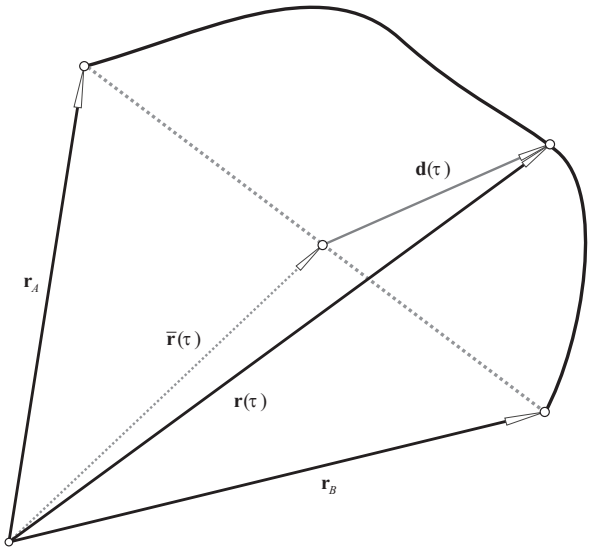

Figure 5.1: Representation of the orbit in the straight line mode.

equation of motion with the self-adjoint differential operator L,

$$L\left(\mathbf{r}(\tau)\right) = \mathbf{a}(\tau'; \mathbf{r}, \dot{\mathbf{r}}), \tag{5.1}$$

as a boundary value problem,

$$\mathbf{r}(\tau) = \bar{\mathbf{r}}(\tau) - T^2 \int_{\tau'=0}^{1} K\left(\tau, \tau'\right) \mathbf{a}(\tau'; \mathbf{r}, \dot{\mathbf{r}})\, d\tau', \tag{5.2}$$

with the force function $\mathbf{a}(\tau'; \mathbf{r}, \dot{\mathbf{r}})$, the integral kernel $K\left(\tau, \tau'\right)$ and the normalized time variable,

$$\tau = \frac{t - t_A}{T} \quad \text{with} \quad T = t_B - t_A, \;\; t \in [t_A, t_B]. \tag{5.3}$$

The function $\bar{\mathbf{r}}(t)$ corresponds to the solution of the homogeneous differential equation

$$L\left(\bar{\mathbf{r}}(t)\right) = 0, \tag{5.4}$$

which satisfies the boundary values

$$\mathbf{r}_A := \mathbf{r}(t_A), \quad \mathbf{r}_B := \mathbf{r}(t_B), \quad t_A < t_B. \tag{5.5}$$

If L is the simple Newton operator,

$$L := L_N = \frac{d}{dt}\dot{\mathbf{r}}(t), \tag{5.6}$$

then the boundary value problem is equivalent to the integral equation,

$$\mathbf{r}(\tau) = \bar{\mathbf{r}}(\tau) - T^2 \int_{\tau'=0}^{1} K^I\left(\tau, \tau'\right) \mathbf{a}(\tau'; \mathbf{r}, \dot{\mathbf{r}})\, d\tau', \tag{5.7}$$

with the integral kernel

$$K^I\left(\tau, \tau'\right) = \begin{cases} \tau'(1-\tau), & \tau' \leq \tau \\ \tau(1-\tau'), & \tau \leq \tau' \end{cases}. \tag{5.8}$$

The solution of the boundary value problem reads

$$\mathbf{r}(\tau) = \bar{\mathbf{r}}(\tau) + \mathbf{d}(\tau) = \bar{\mathbf{r}}(\tau) + \sum_{\nu=1}^{\infty} \mathbf{c}_\nu \sin(\nu\pi\tau), \tag{5.9}$$

with

$$\bar{\mathbf{r}}(\tau) = (1-\tau)\,\mathbf{r}_A + \tau \mathbf{r}_B, \tag{5.10}$$

the orthonormal eigenfunctions $\sqrt{2}\sin(\nu\pi\tau)$ and the eigen values $\nu^2\pi^2$ of the integral kernel,

$$K^I\left(\tau, \tau'\right) = 2\sum_{\nu=1}^{\infty} \frac{\sin(\nu\pi\tau)\sin(\nu\pi\tau')}{\nu^2\pi^2}. \tag{5.11}$$

The coefficients can be derived by inserting Eq. (5.9) and Eq. (5.11) in Eq. (5.7) and comparison of the coefficients with the same eigen functions,

$$\sum_{\nu=1}^{\infty} \mathbf{c}_\nu \sin(\nu\pi\tau) = -\sum_{\nu=1}^{\infty} \sin(\nu\pi\tau) \frac{2T^2}{\nu^2\pi^2} \int_{\tau'=0}^{1} \sin(\nu\pi\tau')\, \mathbf{a}(\tau'; \mathbf{r}, \dot{\mathbf{r}})\, d\tau', \tag{5.12}$$

resulting in the integrals,

$$\mathbf{c}_\nu = -\frac{2T^2}{\nu^2\pi^2} \int_{\tau'=0}^{1} \sin(\nu\pi\tau')\, \mathbf{a}(\tau'; \mathbf{r}, \dot{\mathbf{r}})\, d\tau'. \tag{5.13}$$

5.2.2 Equation of Motion Based on the Linear Extended Newton Operator

If L is the linear extended Newton operator,

$$L := L_E = L_N + \mu^2 \mathbf{r}(t), \tag{5.14}$$

with

$$\mu = \sqrt{\frac{GM}{a^3}}T, \tag{5.15}$$

and a properly selected coefficient a which approximates the major semi axis of the orbit, then the boundary value problem is equivalent to the integral equation,

$$\mathbf{r}(\tau) = \bar{\mathbf{r}}(\tau) - \frac{T^2}{m}\int_{\tau'=0}^{1} K^{II}(\tau,\tau')\,\mathbf{a}^{II}(\tau';\mathbf{r},\dot{\mathbf{r}})\,d\tau', \tag{5.16}$$

with the integral kernel

$$K^{II}(\tau,\tau') = \begin{cases} \dfrac{1}{\mu}\dfrac{\sin\mu(1-\tau)\sin\mu\tau'}{\sin\mu}, & \tau' \le \tau \\ \\ \dfrac{1}{\mu}\dfrac{\sin\mu(1-\tau')\sin\mu\tau}{\sin\mu}, & \tau \le \tau' \end{cases}, \tag{5.17}$$

and the reduced force function (Fig. 5.2),

$$\mathbf{a}^{II}(\tau;\mathbf{r},\dot{\mathbf{r}}) = \mathbf{a}(\tau;\mathbf{r},\dot{\mathbf{r}}) - \frac{\mu^2}{T^2}\mathbf{r}(\tau) = \mathbf{a}(\tau;\mathbf{r},\dot{\mathbf{r}}) - \frac{GM}{a^3}\mathbf{r}(\tau). \tag{5.18}$$

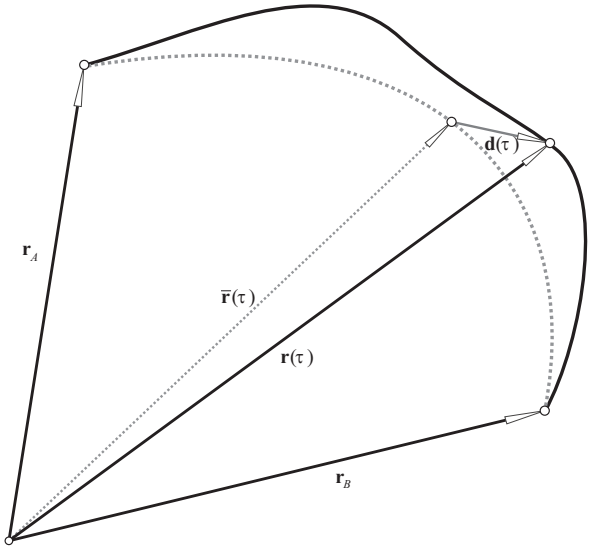

Figure 5.2: Representation of the orbit in the ellipse mode.

The solution of the boundary value problem reads again

$$\mathbf{r}(\tau) = \bar{\mathbf{r}}(\tau) + \mathbf{d}(\tau) = \bar{\mathbf{r}}(\tau) + \sum_{\nu=1}^{\infty}\mathbf{c}_\nu \sin(\nu\pi\tau), \tag{5.19}$$

with

$$\bar{\mathbf{r}}(\tau) = \frac{\sin\mu(1-\tau)}{\sin\mu}\mathbf{r}_A + \frac{\sin\mu\tau}{\sin\mu}\mathbf{r}_B. \tag{5.20}$$

The integral kernel $K^{II}(\tau,\tau')$ can be expressed by its eigen values and its eigen functions,

$$K^{II}(\tau,\tau') = 2\sum_{\nu=1}^{\infty}\frac{\sin(\nu\pi\tau)\sin(\nu\pi\tau')}{\nu^2\pi^2-\mu^2}, \tag{5.21}$$

and the coefficients can be derived by inserting Eq. (5.19) and Eq. (5.21) in Eq. (5.16) and comparison of the coefficients with the same eigen functions,

$$\sum_{\nu=1}^{\infty}\mathbf{c}_\nu\sin(\nu\pi\tau) = -\sum_{\nu=1}^{\infty}\sin(\nu\pi\tau)\frac{2T^2}{\nu^2\pi^2-\mu^2}\int_{\tau'=0}^{1}\sin(\nu\pi\tau')\,\mathbf{a}^{II}(\tau;\mathbf{r},\dot{\mathbf{r}})\,d\tau'. \tag{5.22}$$

Then the coefficients read,

$$\mathbf{c}_\nu = -\frac{2T^2}{\nu^2\pi^2-\mu^2}\int_{\tau'=0}^{1}\sin(\nu\pi\tau')\,\mathbf{a}^{II}(\tau;\mathbf{r},\dot{\mathbf{r}})\,d\tau'. \tag{5.23}$$

5.2.3 Solution of the Equation of Motion as Correction to a Reference Orbit

If the force function $\tilde{\mathbf{a}}(\tau';\tilde{\mathbf{r}},\dot{\tilde{\mathbf{r}}}) := \mathbf{a}(\tau';\tilde{\mathbf{r}},\dot{\tilde{\mathbf{r}}})$ in Eq. (5.1) is well-known, then the satellite arc can be determined in the dynamic orbit determination mode. In this case the orbit can be represented in a semi-analytical way by Eq. (5.9)

$$\tilde{\mathbf{r}}(\tau) = \bar{\tilde{\mathbf{r}}}(\tau) + \sum_{\nu=1}^{\infty}\tilde{\mathbf{c}}_\nu\sin(\nu\pi\tau) = \bar{\tilde{\mathbf{r}}}(\tau) + \tilde{\mathbf{d}}(\tau) \tag{5.24}$$

with (Eq. (5.10))

$$\bar{\tilde{\mathbf{r}}}(\tau) = (1-\tau)\,\tilde{\mathbf{r}}_A + \tau\,\tilde{\mathbf{r}}_B, \tag{5.25}$$

and the coefficients (Eq. (5.13))

$$\tilde{\mathbf{c}}_\nu = -\frac{2T^2}{\nu^2\pi^2}\int_{\tau'=0}^{1}\sin(\nu\pi\tau')\,\tilde{\mathbf{a}}(\tau';\tilde{\mathbf{r}},\dot{\tilde{\mathbf{r}}})\,d\tau'. \tag{5.26}$$

Instead of Eq. (5.10) also Eq. (5.20) in case of the linear extended Newton operator could be selected alternatively,

$$\bar{\tilde{\mathbf{r}}}(\tau) = \frac{\sin\mu(1-\tau)}{\sin\mu}\tilde{\mathbf{r}}_A + \frac{\sin\mu\tau}{\sin\mu}\tilde{\mathbf{r}}_B. \tag{5.27}$$

Based on the dynamical reference orbit $\tilde{\mathbf{r}}(\tau)$, following the force function model $\tilde{\mathbf{a}}(\tau';\tilde{\mathbf{r}},\dot{\tilde{\mathbf{r}}})$, the dynamical orbit for an improved force function model

$$\mathbf{a}(\tau';\mathbf{r},\dot{\mathbf{r}}) = \tilde{\mathbf{a}}(\tau';\tilde{\mathbf{r}},\dot{\tilde{\mathbf{r}}}) + \Delta\mathbf{a}(\tau';\tilde{\mathbf{r}}+\mathbf{x},\dot{\tilde{\mathbf{r}}}+\dot{\mathbf{x}}), \tag{5.28}$$

can be formulated as difference motion,

$$\mathbf{r}(\tau) = \mathbf{x}(\tau) + \tilde{\mathbf{r}}(\tau). \tag{5.29}$$

Based on the simple Newton operator L,

$$L := L_N = \frac{d}{dt}\dot{\mathbf{x}}(t), \tag{5.30}$$

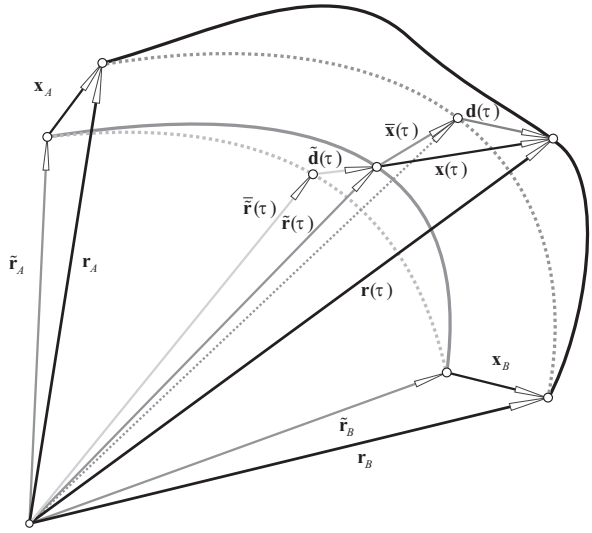

Figure 5.3: Representation of the orbit in the reference orbit orbit.

the equation of motion for the difference motion $\mathbf{x}(\tau)$ reads (Fig. 5.3),

$$\frac{d}{dt}\dot{\mathbf{x}}(t) = \mathbf{a}(\tau';\mathbf{r},\dot{\mathbf{r}}) - \tilde{\mathbf{a}}(\tau';\tilde{\mathbf{r}},\dot{\tilde{\mathbf{r}}}) = \Delta\mathbf{a}(\tau';\tilde{\mathbf{r}}+\mathbf{x},\dot{\tilde{\mathbf{r}}}+\dot{\mathbf{x}}). \tag{5.31}$$

The solution of the boundary value problem with the corrections $\bar{\mathbf{x}}_A,\ \bar{\mathbf{x}}_B$ to the boundary values $\mathbf{r}_A,\ \mathbf{r}_B$ reads

$$\mathbf{x}(\tau) = \bar{\mathbf{x}}(\tau) + \mathbf{d}(\tau) = \bar{\mathbf{x}}(\tau) + \sum_{\nu=1}^{\infty} \mathbf{x}_\nu \sin(\nu\pi\tau), \tag{5.32}$$

with

$$\bar{\mathbf{x}}(\tau) = (1-\tau)\,\mathbf{x}_A + \tau\,\mathbf{x}_B, \tag{5.33}$$

and the corrections to the coefficients $\mathbf{c}_\nu$ of Eq. (5.13) or Eq. (5.23),

$$\mathbf{x}_\nu = -\frac{2T^2}{\nu^2\pi^2} \int_{\tau'=0}^{1} \sin(\nu\pi\tau')\ \Delta\mathbf{a}(\tau';\tilde{\mathbf{r}}+\mathbf{x},\dot{\tilde{\mathbf{r}}}+\dot{\mathbf{x}})\ d\tau', \tag{5.34}$$

derived analogously to Eq. (5.13) or Eq. (5.23). The final solution can be written as follows

$$\mathbf{r}(\tau) = \big(\bar{\tilde{\mathbf{r}}}(\tau) + \bar{\mathbf{x}}(\tau)\big) + \sum_{\nu=1}^{\infty} (\tilde{\mathbf{c}}_\nu + \mathbf{x}_\nu)\sin(\nu\pi\tau), \tag{5.35}$$

corresponding to Eq. (5.9) or Eq. (5.19),

$$\mathbf{r}(\tau) = \bar{\mathbf{r}}(\tau) + \sum_{\nu=1}^{\infty} \mathbf{x}_\nu \sin(\nu\pi\tau) = \bar{\mathbf{r}}(\tau) + \mathbf{d}(\tau), \tag{5.36}$$

with

$$\bar{\mathbf{r}}(\tau) := \tilde{\mathbf{r}}(\tau) + \bar{\mathbf{x}}(\tau) = \bar{\tilde{\mathbf{r}}}(\tau) + \bar{\mathbf{x}}(\tau) + \tilde{\mathbf{d}}(\tau), \tag{5.37}$$

and

$$\mathbf{c}_\nu := \tilde{\mathbf{c}}_\nu + \mathbf{x}_\nu. \tag{5.38}$$

5.2.4 Interpretation of the Solution of Fredholm's Integral Equation as Fourier Series

It can be shown (Ilk 1976), that the solution series Eq. (5.9) or Eq. (5.19) contain Fourier series of the difference function,

$$\mathbf{d}(\tau) := \mathbf{r}(\tau) - \bar{\mathbf{r}}(\tau) = \sum_{\nu=1}^{\infty} \mathbf{d}_\nu \sin(\nu\pi\tau) =: \mathbf{d}_F^{\infty}(\tau), \tag{5.39}$$

with the coefficients $\mathbf{d}_\nu$ derived from the difference function,

$$\mathbf{d}_\nu = 2 \int_{\tau'=0}^{1} \mathbf{d}(\tau)\ \sin(\nu\pi\tau')\ d\tau'. \tag{5.40}$$

It should be pointed out that the reference motion $\bar{\mathbf{r}}(\tau)$ can be also of the type of Eq. (5.37),

$$\bar{\mathbf{r}}(\tau) = \tilde{\mathbf{r}}(\tau) + \bar{\mathbf{x}}(\tau). \tag{5.41}$$

Because of the uniqueness of both series in Eqs.(5.9), (5.19) and (5.39), it holds

$$\mathbf{d}_\nu = \mathbf{c}_\nu \quad \text{for} \quad \nu = 1.....\infty. \tag{5.42}$$

If the function $\mathbf{d}(\tau)$ is continued to an odd periodic function with the period $2T$ or normalized to the interval $[-1, 1]$, then it holds

$$\mathbf{d}(-\tau) = -\mathbf{d}(\tau), \tag{5.43}$$

and all cosine terms become zero. Some important facts result from the theory of Fourier series and hold also for the solution of the boundary value problem as well:

- Because of the fact that the function $\mathbf{d}(\tau)$ is continuous in $[-1, 1]$ together with its first derivatives, the series $\mathbf{D}_\infty(\tau)$ converges absolutely and uniformly and therefore represents the function $\mathbf{d}(\tau)$; the coefficients $d_{\nu,i}$ for $i = 1, 2, 3$ build a zero sequence:

$$\lim_{\nu\to\infty} d_{\nu,i} = 0, \tag{5.44}$$

- Because of the fact that the functions $d_i(\tau)$ are continuous within [-1,1], the Fourier coefficients fulfill Parseval's equation,

$$\sum_{\nu=1}^{\infty} d_{\nu,i}^2 = 2 \int_{0}^{1} d_i^2(\tau)\ d\tau, \tag{5.45}$$

- The asymptotic behavior of the coefficients depends on the order of differentiability of the function $\mathbf{d}(\tau)$. Because of the specific characteristics of this function, it holds:

$$|d_{\nu,i}| \leq \frac{c}{\nu^3}, \tag{5.46}$$

  with a constant $c > 0$.

- The limitation of the series $\mathbf{D}_\infty(\tau)$ at a finite index n,

$$\mathbf{D}_n(\tau) = \sum_{\nu=1}^{n} \mathbf{d}_\nu \sin(\nu\pi\tau), \tag{5.47}$$

is the best mean approximation of the function $\mathbf{d}(\tau)$ in the interval $\tau \in [-1, 1]$.

The minimal quadratic error for the coordinates reads

$$\int_0^1 (d_i(\tau) - D_{n,i}(\tau))^2 d\tau = \int_0^1 (d_i(\tau))^2 d\tau - \frac{1}{2}\sum_{\nu=1}^{n} d_{\nu,i}^2, \tag{5.48}$$

and it holds for the residual terms of the series

$$\lim_{n\to\infty} \int_0^1 (d_i(\tau) - D_{n,i}(\tau))\, d\tau = 0. \tag{5.49}$$

The Fourier coefficients $\mathbf{d}_\nu$ of the function $\mathbf{d}(\tau)$,

$$\mathbf{d}_\nu = 2 \int_{\tau'=0}^{1} \mathbf{d}(\tau)\ \sin(\nu\pi\tau')\, d\tau', \tag{5.50}$$

can be determined approximately by

$$\mathbf{d}_\nu \approx \frac{2}{K+1} \sum_{k=1}^{K} \mathbf{d}(\tau_k)\ \sin\left(\frac{\nu\pi k}{K+1}\right), \tag{5.51}$$

if the function $\mathbf{d}(\tau)$ is given discrete at a regular sampling rate of τ_i,

$$\mathbf{d}(\tau_k) \quad \text{with} \quad \tau_k = \frac{k}{K+1}, \quad k = 1, 2, 3, ..., K, \quad \tau_k \in \,]\, 0, 1\, [. \tag{5.52}$$

This equidistant ephemeris of satellite positions $\mathbf{d}(\tau)$ can be considered to be given, derived by a geometrical orbit determination procedure based on carrier phase GPS-SST measurements.

$$\mathbf{d}(\tau_k) := \mathbf{r}(\tau_k) - \bar{\mathbf{r}}(\tau_k) \quad \rightarrow \quad \begin{pmatrix} d_{k,1} \\ d_{k,2} \\ d_{k,3} \end{pmatrix} = \begin{pmatrix} x_r(\tau_k) \\ y_r(\tau_k) \\ z_r(\tau_k) \end{pmatrix} - \begin{pmatrix} \bar{x}_r(\tau_k) \\ \bar{y}_r(\tau_k) \\ \bar{z}_r(\tau_k) \end{pmatrix}. \tag{5.53}$$

The arc is divided by these points in $K+1$ equal parts of the arc. If the force function is known then the coefficients fulfill the Eq. (5.23) with the reduced force Eq. (5.18).

5.3 Series of Euler–and Bernoulli Polynomials

5.3.1 Continuous Position Function

5.3.1.1 From Fourier Series to Series of Euler and Bernoulli Polynomials

The orbit of a satellite can be represented in a semi-analytical way by one of the Eqs. (5.9), (5.19) or (5.36),

$$\mathbf{r}(\tau) = \bar{\mathbf{r}}(\tau) + \sum_{\nu=1}^{\infty} \mathbf{c}_\nu \sin(\nu\pi\tau). \tag{5.54}$$

An alternative representation of the orbit can be derived starting from the Eq. (5.39) with the Fourier coefficients of Eq. (5.40). As already outlined, Eq. (5.39) can be written as

$$\mathbf{d}(\tau) := \mathbf{r}(\tau) - \bar{\mathbf{r}}(\tau) = \sum_{\nu=1}^{\infty} \mathbf{d}_\nu \sin(\nu\pi\tau) = \sum_{\nu=1}^{\infty} \mathbf{c}_\nu \sin(\nu\pi\tau), \tag{5.55}$$

so that it holds

$$\mathbf{c}_\nu \stackrel{\wedge}{=} \mathbf{d}_\nu = 2 \int_{\tau'=0}^{1} \mathbf{d}(\tau') \, \sin(\nu\pi\tau') \, d\tau'. \tag{5.56}$$

If we apply a first integration by parts to this equation then we can write:

$$\mathbf{d}_\nu = 2 \int_{\tau'=0}^{1} \mathbf{d}(\tau') \, \sin(\nu\pi\tau') \, d\tau' = -2\mathbf{d}(\tau')\frac{1}{\nu\pi}\cos(\nu\pi\tau')\Big|_{\tau'=0}^{1} + 2\frac{1}{\nu\pi}\int_{\tau'=0}^{1} \mathbf{d}^{[1]}(\tau') \, \cos(\nu\pi\tau') \, d\tau', \tag{5.57}$$

and by inserting the limits and considering $\mathbf{d}(\tau'=0) = \mathbf{d}(\tau'=1) = \mathbf{0}$,

$$\mathbf{d}_\nu = 2 \int_{\tau'=0}^{1} \mathbf{d}(\tau') \, \sin(\nu\pi\tau') \, d\tau' = 2\frac{1}{\nu\pi}\int_{\tau'=0}^{1} \mathbf{d}^{[1]}(\tau') \, \cos(\nu\pi\tau') \, d\tau', \tag{5.58}$$

with the first derivative of the orbit $\mathbf{d}^{[1]}(\tau)$ with respect to the normalized time τ. A second integration by parts results in

$$\mathbf{d}_\nu = 2\frac{1}{\nu\pi}\int_{\tau'=0}^{1} \mathbf{d}^{[1]}(\tau') \, \cos(\nu\pi\tau') \, d\tau' = -2\frac{1}{(\nu\pi)^2}\int_{\tau'=0}^{1} \mathbf{d}^{[2]}(\tau') \, \sin(\nu\pi\tau') \, d\tau'. \tag{5.59}$$

A third integration by parts gives

$$\begin{aligned}\mathbf{d}_\nu &= -2\frac{1}{(\nu\pi)^2}\int_{\tau'=0}^{1} \mathbf{d}^{[2]}(\tau') \, \sin(\nu\pi\tau') \, d\tau' = \\ &= 2\,\mathbf{d}^{[2]}(\tau')\frac{1}{(\nu\pi)^3}\cos(\nu\pi\tau')\Big|_{\tau'=0}^{1} - 2\frac{1}{(\nu\pi)^3}\int_{\tau'=0}^{1} \mathbf{d}^{[3]}(\tau') \, \cos(\nu\pi\tau') \, d\tau',\end{aligned} \tag{5.60}$$

and a fourth integration by parts,

$$\mathbf{d}_\nu = 2\,\mathbf{d}^{[2]}(\tau')\frac{1}{(\nu\pi)^3}\cos(\nu\pi\tau')\Big|_{\tau'=0}^{1} + 2\frac{1}{(\nu\pi)^4}\int_{\tau'=0}^{1} \mathbf{d}^{[4]}(\tau') \, \sin(\nu\pi\tau') \, d\tau'. \tag{5.61}$$

The general expression reads after $2J+2$ integrations by parts (Klose 1985),

$$\mathbf{d}_\nu = \sum_{j=1}^{J} \mathbf{d}^{[2j]}(\tau')\frac{2(-1)^{j+1}}{(\nu\pi)^{2j+1}}\cos(\nu\pi\tau')\Big|_{\tau'=0}^{1} + \beta\frac{2}{(\nu\pi)^{2J+2}}\int_{\tau'=0}^{1} \mathbf{d}^{[2J+2]}(\tau') \, \sin(\nu\pi\tau') \, d\tau', \tag{5.62}$$

with

$$\beta = \begin{cases} +1 & J = 1,4,5,8,9,12,13,\cdots \\ -1 & J = 2,3,6,7,10,11,\cdots \end{cases}, \tag{5.63}$$

and with the integration limits in the first term,

$$\mathbf{d}_\nu = \sum_{j=1}^{J} \frac{2(-1)^{j+1}}{(\nu\pi)^{2j+1}}\left((-1)^\nu \mathbf{d}^{[2j]}(1) - \mathbf{d}^{[2j]}(0)\right) + \beta\frac{2}{(\nu\pi)^{2J+2}}\int_{\tau'=0}^{1} \mathbf{d}^{[2J+2]}(\tau') \, \sin(\nu\pi\tau') \, d\tau'. \tag{5.64}$$

Inserting Eq. (5.64) in Eq. (5.39) gives

$$\mathbf{d}(\tau) := \mathbf{r}(\tau) - \bar{\mathbf{r}}(\tau) = \sum_{\nu=1}^{\infty} \mathbf{d}_\nu \sin(\nu\pi\tau) = \tag{5.65}$$
$$= \sum_{\nu=1}^{\infty} \left(\sum_{j=1}^{J} \frac{2(-1)^{j+1}}{(\nu\pi)^{2j+1}} \left((-1)^\nu \mathbf{d}^{[2j]}(1) - \mathbf{d}^{[2j]}(0) \right) + \beta \frac{2}{(\nu\pi)^{2J+2}} \int_{\tau'=0}^{1} \mathbf{d}^{[2J+2]}(\tau') \, \sin(\nu\pi\tau') \, d\tau' \right) \sin(\nu\pi\tau).$$

The sine coefficients read in this case as follows:

$$\mathbf{d}_\nu = \sum_{j=1}^{J} \frac{2(-1)^{j+1}}{(\nu\pi)^{2j+1}} \left((-1)^\nu \mathbf{d}^{[2j]}(1) - \mathbf{d}^{[2j]}(0) \right) + \beta \frac{2}{(\nu\pi)^{2J+2}} \int_{\tau'=0}^{1} \mathbf{d}^{[2J+2]}(\tau') \, \sin(\nu\pi\tau') d\tau'. \tag{5.66}$$

If we separate the inner sum of Eq. (5.65) in terms of even and odd indices ν,

$$\begin{aligned} \mathbf{d}(\tau) :&= \mathbf{r}(\tau) - \bar{\mathbf{r}}(\tau) = \sum_{\nu=1}^{\infty} \mathbf{d}_\nu \sin(\nu\pi\tau) = \\ &= \sum_{j=1}^{J} \frac{2(-1)^{j+1}}{(2\pi)^{2j+1}} \left(\mathbf{d}^{[2j]}(1) - \mathbf{d}^{[2j]}(0) \right) \sum_{\nu=1}^{\infty} \frac{\sin(2\nu\pi\tau)}{\nu^{2j+1}} + \\ &+ \sum_{j=1}^{J} \frac{2(-1)^{j}}{\pi^{2j+1}} \left(\mathbf{d}^{[2j]}(1) + \mathbf{d}^{[2j]}(0) \right) \sum_{\nu=1}^{\infty} \frac{\sin(2\nu-1)\pi\tau}{(2\nu-1)^{2j+1}} + \\ &+ \beta \frac{2}{\pi^{2J+2}} \sum_{\nu=1}^{\infty} \left(\frac{1}{\nu^{2J+2}} \int_{\tau'=0}^{1} \mathbf{d}^{[2J+2]}(\tau') \, \sin(\nu\pi\tau') \, d\tau' \sin(\nu\pi\tau) \right), \end{aligned} \tag{5.67}$$

so that it holds for the coefficients according to Eq. (5.66) here for even coefficients,

$$\mathbf{d}_{2\nu} = \sum_{j=1}^{J} \frac{2(-1)^{j+1}}{(2\nu\pi)^{2j+1}} \left(\mathbf{d}^{[2j]}(1) - \mathbf{d}^{[2j]}(0) \right) + \beta \frac{2}{(2\nu\pi)^{2J+2}} \int_{\tau'=0}^{1} \mathbf{d}^{[2J+2]}(\tau') \, \sin 2\nu\pi\tau' \, d\tau', \tag{5.68}$$

and for odd coefficients

$$\mathbf{d}_{2\nu-1} = \sum_{j=1}^{J} \frac{2(-1)^{j}}{(2\nu-1)^{2j+1}\pi^{2j+1}} \left(\mathbf{d}^{[2j]}(1) + \mathbf{d}^{[2j]}(0) \right) + \beta \frac{2}{(2\nu-1)^{2J+2}\pi^{2J+2}} \int_{\tau'=0}^{1} \mathbf{d}^{[2J+2]}(\tau') \, \sin(2\nu-1)\pi\tau' \, d\tau'. \tag{5.69}$$

The terms in Eq. (5.67) can be replaced by the absolutely and uniformly continuous series expansions of the Euler polynomials (Abramowitz and Stegun 1972),

$$E_{2j}(\tau) = \frac{4(-1)^j (2j)!}{\pi^{2j+1}} \sum_{\nu=1}^{\infty} \frac{\sin(2\nu-1)\pi\tau}{(2\nu-1)^{2j+1}}, \tag{5.70}$$

and the Bernoulli polynomials

$$B_{2j+1}(\tau) = \frac{2(-1)^{j+1}(2j+1)!}{(2\pi)^{2j+1}} \sum_{\nu=1}^{\infty} \frac{\sin(2\nu\pi\tau)}{\nu^{2j+1}}. \tag{5.71}$$

The Euler polynomials of even degree can be represented also as polynomials of the normalized time τ as follows, e.g. for $j = 1, 2, 3, 4, 5, 6$ (Abramowitz and Stegun 1972):

$$\begin{aligned}
E_2(\tau) &= -\tau + \tau^2, \\
E_4(\tau) &= \tau - 2\tau^3 + \tau^4, \\
E_6(\tau) &= -3\tau + 5\tau^3 - 3\tau^5 + \tau^6, \\
E_8(\tau) &= 17\tau - 28\tau^3 + 14\tau^5 - 4\tau^7 + \tau^8, \\
E_{10}(\tau) &= -155\tau + 255\tau^3 - 126\tau^5 + 30\tau^7 - 5\tau^9 + \tau^{10}, \\
E_{12}(\tau) &= 2073\tau - 3410\tau^3 + 1683\tau^5 - 396\tau^7 + 55\tau^9 - 6\tau^{11} + \tau^{12},
\end{aligned} \tag{5.72}$$

and the Bernoulli polynomials for odd degrees read for the indices $j = 1, 2, 3, 4, 5, 6$:

$$\begin{aligned}
B_3(\tau) &= \frac{1}{2}\tau - \frac{3}{2}\tau^2 + \tau^3, \\
B_5(\tau) &= -\frac{1}{6}\tau + \frac{5}{3}\tau^3 - \frac{5}{2}\tau^4 + \tau^5, \\
B_7(\tau) &= \frac{1}{6}\tau - \frac{7}{6}\tau^3 + \frac{7}{2}\tau^5 - \frac{7}{2}\tau^6 + \tau^7, \\
B_9(\tau) &= -\frac{3}{10}\tau + 2\tau^3 - \frac{21}{5}\tau^5 + 6\tau^7 - \frac{9}{2}\tau^8 + \tau^9, \\
B_{11}(\tau) &= \frac{5}{6}\tau - \frac{11}{2}\tau^3 + 11\tau^5 - 11\tau^7 + \frac{55}{6}\tau^9 - \frac{11}{2}\tau^{10} + \tau^{11}, \\
B_{13}(\tau) &= -\frac{691}{210}\tau + \frac{65}{3}\tau^3 - \frac{429}{10}\tau^5 + \frac{286}{7}\tau^7 - \frac{143}{6}\tau^9 + 13\tau^{11} - \frac{13}{2}\tau^{12} + \tau^{13}.
\end{aligned} \tag{5.73}$$

If the Eq. (5.70) and Eq. (5.71) are inserted in Eq. (5.67) then it holds:

$$\begin{aligned}
\mathbf{d}(\tau) := \mathbf{r}(\tau) - \bar{\mathbf{r}}(\tau) = \sum_{\nu=1}^{\infty} \mathbf{d}_\nu \sin(\nu\pi\tau) = \sum_{j=1}^{J} \mathbf{e}_{2j} E_{2j}(\tau) + \sum_{j=1}^{J} \mathbf{b}_{2j+1} B_{2j+1}(\tau) + \\
+ \beta \frac{2}{\pi^{2J+2}} \sum_{\nu=1}^{\infty} \left(\frac{1}{\nu^{2J+2}} \int_{\tau'=0}^{1} \mathbf{d}^{[2J+2]}(\tau') \, \sin(\nu\pi\tau') \, d\tau' \sin(\nu\pi\tau) \right),
\end{aligned} \tag{5.74}$$

with the coefficients of the Euler polynomials,

$$\mathbf{e}_{2j} := \frac{1}{2(2j)!} \left(\mathbf{d}^{[2j]}(1) + \mathbf{d}^{[2j]}(0) \right), \tag{5.75}$$

and the coefficients of the Bernoulli polynomials,

$$\mathbf{b}_{2j+1} := \frac{1}{(2j+1)!} \left(\mathbf{d}^{[2j]}(1) - \mathbf{d}^{[2j]}(0) \right). \tag{5.76}$$

The partial integration refers to the normalized time variable τ. If the real time t is used then it holds $d\tau/dt = 1/T$ with the arc length $T = t_B - t_A$ and the relation $\tau = (t - t_A)/T$ with $t \in [t_A, t_B]$,

$$\mathbf{d}^{(2j)} = \frac{d^{2j}\mathbf{d}(t)}{dt^{2j}} = \frac{d^{2j}\mathbf{d}(\tau)}{d\tau^{2j}} \left(\frac{d\tau}{dt} \right)^{2j} = \mathbf{d}^{[2j]} \frac{1}{T^{2j}}, \tag{5.77}$$

and the coefficients of the Euler polynomials read

$$\mathbf{e}_{2j} := \frac{1}{2(2j)!} \left(\mathbf{d}^{[2j]}(1) + \mathbf{d}^{[2j]}(0) \right) = \frac{T^{2j}}{2(2j)!} \left(\mathbf{d}^{(2j)}(t_B) + \mathbf{d}^{(2j)}(t_A) \right) = T^{2j} \tilde{\mathbf{e}}_{2j}, \tag{5.78}$$

with $\tilde{\mathbf{e}}_{2j}$ as

$$\tilde{\mathbf{e}}_{2j} := \frac{1}{2(2j)!} \left(\mathbf{d}^{(2j)}(t_B) + \mathbf{d}^{(2j)}(t_A) \right), \tag{5.79}$$

and analogously the coefficients of the Bernoulli polynomials

$$\mathbf{b}_{2j+1} = \frac{1}{(2j+1)!}\left(\mathbf{d}^{[2j]}(1) - \mathbf{d}^{[2j]}(0)\right) = \frac{T^{2j}}{(2j+1)!}\left(\mathbf{d}^{(2j)}(t_B) - \mathbf{d}^{(2j)}(t_A)\right) = T^{2j}\tilde{\mathbf{b}}_{2j+1}, \tag{5.80}$$

with $\tilde{\mathbf{b}}_{2j+1}$ as

$$\tilde{\mathbf{b}}_{2j+1} = \frac{1}{(2j+1)!}\left(\mathbf{d}^{(2j)}(t_B) - \mathbf{d}^{(2j)}(t_A)\right). \tag{5.81}$$

The factors are given according to Eqs. (5.75) and (5.76) with J_{max}=6 as follows:

$$\begin{aligned}
\mathbf{b}_3 &= \frac{1}{6}\left(\mathbf{d}^{[2]}(1) - \mathbf{d}^{[2]}(0)\right) = \frac{T^2}{6}\left(\mathbf{d}^{(2)}(1) - \mathbf{d}^{(2)}(0)\right), \\
\mathbf{b}_5 &= \frac{1}{120}\left(\mathbf{d}^{[4]}(1) - \mathbf{d}^{[4]}(0)\right) = \frac{T^4}{120}\left(\mathbf{d}^{(4)}(1) - \mathbf{d}^{(4)}(0)\right), \\
\mathbf{b}_7 &= \frac{1}{5040}\left(\mathbf{d}^{[6]}(1) - \mathbf{d}^{[6]}(0)\right) = \frac{T^6}{5040}\left(\mathbf{d}^{(6)}(1) - \mathbf{d}^{(6)}(0)\right), \\
\mathbf{b}_9 &= \frac{1}{362880}\left(\mathbf{d}^{[8]}(1) - \mathbf{d}^{[8]}(0)\right) = \frac{T^8}{362880}\left(\mathbf{d}^{(8)}(1) - \mathbf{d}^{(8)}(0)\right), \\
\mathbf{b}_{11} &= \frac{1}{39916800}\left(\mathbf{d}^{[10]}(1) - \mathbf{d}^{[10]}(0)\right) = \frac{T^{10}}{39916800}\left(\mathbf{d}^{(10)}(1) - \mathbf{d}^{(10)}(0)\right), \\
\mathbf{b}_{13} &= \frac{1}{6227020800}\left(\mathbf{d}^{[12]}(1) - \mathbf{d}^{[12]}(0)\right) = \frac{T^{12}}{6227020800}\left(\mathbf{d}^{(12)}(1) - \mathbf{d}^{(12)}(0)\right),
\end{aligned} \tag{5.82}$$

and

$$\begin{aligned}
\mathbf{e}_2 &= \frac{1}{4}\left(\mathbf{d}^{[2]}(1) + \mathbf{d}^{[2]}(0)\right) = \frac{T^2}{4}\left(\mathbf{d}^{(2)}(1) + \mathbf{d}^{(2)}(0)\right), \\
\mathbf{e}_4 &= \frac{1}{48}\left(\mathbf{d}^{[4]}(1) + \mathbf{d}^{[4]}(0)\right) = \frac{T^4}{48}\left(\mathbf{d}^{(4)}(1) + \mathbf{d}^{(4)}(0)\right), \\
\mathbf{e}_6 &= \frac{1}{1440}\left(\mathbf{d}^{[6]}(1) + \mathbf{d}^{[6]}(0)\right) = \frac{T^6}{1440}\left(\mathbf{d}^{(6)}(1) + \mathbf{d}^{(6)}(0)\right), \\
\mathbf{e}_8 &= \frac{1}{80640}\left(\mathbf{d}^{[8]}(1) + \mathbf{d}^{[8]}(0)\right) = \frac{T^8}{80640}\left(\mathbf{d}^{(8)}(1) + \mathbf{d}^{(8)}(0)\right), \\
\mathbf{e}_{10} &= \frac{1}{7257600}\left(\mathbf{d}^{[10]}(1) + \mathbf{d}^{[10]}(0)\right) = \frac{T^{10}}{7257600}\left(\mathbf{d}^{(10)}(1) + \mathbf{d}^{(10)}(0)\right), \\
\mathbf{e}_{12} &= \frac{1}{958003200}\left(\mathbf{d}^{[12]}(1) + \mathbf{d}^{[12]}(0)\right) = \frac{T^{12}}{958003200}\left(\mathbf{d}^{(12)}(1) + \mathbf{d}^{(12)}(0)\right).
\end{aligned} \tag{5.83}$$

The Eqs. (5.78) and (5.80) can be used to derive the time derivatives of the difference function $\mathbf{d}(\tau)$ with respect to the time t at the boundary epochs t_A and t_B of the arc,

$$\mathbf{d}^{(2j)}(t_A) = \frac{2(2j)!\tilde{\mathbf{e}}_{2j} - (2j+1)!\tilde{\mathbf{b}}_{2j+1}}{2} = \frac{2(2j)!\mathbf{e}_{2j} - (2j+1)!\mathbf{b}_{2j+1}}{2T^{2j}} = \frac{1}{T^{2j}}\mathbf{d}^{[2j]}(\tau = 0), \tag{5.84}$$

and

$$\mathbf{d}^{(2j)}(t_B) = \frac{2(2j)!\tilde{\mathbf{e}}_{2j} + (2j+1)!\tilde{\mathbf{b}}_{2j+1}}{2} = \frac{2(2j)!\mathbf{e}_{2j} + (2j+1)!\mathbf{b}_{2j+1}}{2T^{2j}} = \frac{1}{T^{2j}}\mathbf{d}^{[2j]}(\tau = 1). \tag{5.85}$$

In the following, we will use both time variables; the differences can be seen from the functional dependencies either on t or τ and from the boundary epochs t_A, t_B or $\tau = 0,\ \tau = 1$, used. The Euler polynomial coefficients are written $\tilde{\mathbf{e}}_{2j}$ or $\mathbf{e}_{2j}$ and $\tilde{\mathbf{b}}_{2j+1}$ or $\mathbf{b}_{2j+1}$, whether they refer to the real time or the normalized one. The derivatives of the difference function $\mathbf{d}$ with respect to the real time is written as $\mathbf{d}^{(2j)}$ and with respect to the normalized time as $\mathbf{d}^{[2j]}$.

The sine coefficients can be written as

$$\mathbf{d}_{2\nu} = \sum_{j=1}^{J} \frac{2(-1)^{j+1}(2j+1)!}{(2\nu\pi)^{2j+1}} \mathbf{b}_{2j+1} + \beta \frac{2}{(2\nu\pi)^{2J+2}} \int_{\tau'=0}^{1} \mathbf{d}^{[2J+2]}(\tau') \, \sin 2\nu\pi\tau' \, d\tau', \tag{5.86}$$

and

$$\mathbf{d}_{2\nu-1} = \sum_{j=1}^{J} \frac{4(-1)^{j}(2j)!}{(2\nu-1)^{2j+1}\pi^{2j+1}} \mathbf{e}_{2j} + \beta \frac{2}{(2\nu-1)^{2J+2}\pi^{2J+2}} \int_{\tau'=0}^{1} \mathbf{d}^{[2J+2]}(\tau') \, \sin(2\nu-1)\pi\tau' d\tau'. \tag{5.87}$$

If we consider the asymptotic behaviors of the integrals in the Eqs. (5.74), (5.86) and (5.87),

$$\left| \frac{2}{(\nu\pi)^{2J+2}} \int_{\tau'=0}^{1} d_i^{[2J+2]}(\tau') \, \sin \nu\pi\tau' \, d\tau' \right| = O\left(\frac{1}{\nu^{J+1}} \right), \tag{5.88}$$

then it holds for a sufficient large $\nu \geq N$

$$\left| \frac{2}{(\nu\pi)^{2J+2}} \int_{\tau'=0}^{1} d_i^{[2J+2]}(\tau') \, \sin \nu\pi\tau' \, d\tau' \right| < \delta, \tag{5.89}$$

with an error δ for the coefficients $d_{\nu,i}$ with $i = 1, 2, 3$.

5.3.1.2 Finite Series and Remainder Terms

If the series in Eq. (5.55) and in Eq. (5.74) are summed up to infinity then we can write:

$$\mathbf{r}(\tau) = \bar{\mathbf{r}}(\tau) + \mathbf{d}_F^{\infty}(\tau) = \bar{\mathbf{r}}(\tau) + \mathbf{d}_P^{\infty}(\tau), \tag{5.90}$$

or

$$\mathbf{d}_F^{\infty}(\tau) = \mathbf{d}_P^{\infty}(\tau), \tag{5.91}$$

with

$$\mathbf{d}_F^{\infty}(\tau) := \sum_{\nu=1}^{n\to\infty} \mathbf{d}_\nu \sin(\nu\pi\tau), \tag{5.92}$$

and

$$\mathbf{d}_P^{\infty}(\tau) := \sum_{j=1}^{J\to\infty} \mathbf{e}_{2j} E_{2j}(\tau) + \sum_{j=1}^{J\to\infty} \mathbf{b}_{2j+1} B_{2j+1}(\tau). \tag{5.93}$$

If we restrict the upper summation indices to final numbers then we have to take into account remainder functions as follows,

$$\mathbf{d}_F^{\infty}(\tau) = \mathbf{d}_F^{n}(\tau) + \mathbf{R}_F(\tau) = \mathbf{r}(\tau) - \bar{\mathbf{r}}(\tau) = \mathbf{d}_P^{J}(\tau) + \mathbf{R}_P(\tau) = \mathbf{d}_P^{\infty}(\tau). \tag{5.94}$$

The remainder term $\mathbf{R}_F(\tau)$ is simply the rest of the Fourier series from index $n+1$ to infinity,

$$\mathbf{R}_F(\tau) = \sum_{\nu=n+1}^{\infty} \mathbf{d}_\nu \sin(\nu\pi\tau), \tag{5.95}$$

while the remainder term $\mathbf{R}_P(\tau)$ contains the Euler and Bernoulli polynomials from index $J+1$ to infinity or high order derivatives of the orbit at the boundaries according to Eq. (5.74),

$$\begin{aligned}\mathbf{R}_P(\tau) &= \sum_{j=J+1}^{\infty} \mathbf{e}_{2j} E_{2j}(\tau) + \sum_{j=J+1}^{\infty} \mathbf{b}_{2j+1} B_{2j+1}(\tau) \\ &= \beta \frac{2}{\pi^{2J+2}} \sum_{\nu=1}^{\infty} \left(\frac{1}{\nu^{2J+2}} \int_{\tau'=0}^{1} \mathbf{d}^{[2J+2]}(\tau') \, \sin(\nu\pi\tau') \, d\tau' \sin(\nu\pi\tau) \right).\end{aligned} \tag{5.96}$$

The Fourier series coefficients, here the sine coefficients $\mathbf{d}_{2\nu}$ with even indices ($\nu = 1, 2, 3, ...$) can be expressed by the coefficients of the Bernoulli polynomials,

$$\mathbf{d}_{2\nu} = \sum_{j=1}^{\infty} \frac{2(-1)^{j+1}(2j+1)!}{(2\nu\pi)^{2j+1}} \mathbf{b}_{2j+1}, \tag{5.97}$$

and the coefficients $\mathbf{d}_{2\nu-1}$with odd indices ($\nu = 1, 2, 3, ...$) by the coefficients of the Euler polynomials,

$$\mathbf{d}_{2\nu-1} = \sum_{j=1}^{\infty} \frac{4(-1)^{j}(2j)!}{(2\nu-1)^{2j+1}\pi^{2j+1}} \mathbf{e}_{2j}. \tag{5.98}$$

If these series are restricted by an upper index J then the remainder terms $\mathbf{R}_{2\nu}$ and $\mathbf{R}_{2\nu-1}$ of the series

$$\mathbf{d}_{2\nu} = \sum_{j=1}^{J} \frac{2(-1)^{j+1}(2j+1)!}{(2\nu\pi)^{2j+1}} \mathbf{b}_{2j+1} + \mathbf{R}_{2\nu}, \tag{5.99}$$

and

$$\mathbf{d}_{2\nu-1} = \sum_{j=1}^{J} \frac{4(-1)^{j}(2j)!}{(2\nu-1)^{2j+1}\pi^{2j+1}} \mathbf{e}_{2j} + \mathbf{R}_{2\nu-1}. \tag{5.100}$$

can be written according to Eq. (5.86),

$$\mathbf{R}_{2\nu} = \sum_{j=J+1}^{\infty} \frac{2(-1)^{j+1}(2j+1)!}{(2\nu\pi)^{2j+1}} \mathbf{b}_{2j+1} = \beta \frac{2}{(2\nu\pi)^{2J+2}} \int_{\tau'=0}^{1} \mathbf{d}^{[2J+2]}(\tau') \, \sin 2\nu\pi\tau' \, d\tau', \tag{5.101}$$

and Eq. (5.87), respectively,

$$\mathbf{R}_{2\nu-1} = \sum_{j=J+1}^{\infty} \frac{4(-1)^{j}(2j)!}{(2\nu-1)^{2j+1}\pi^{2j+1}} \mathbf{e}_{2j} = \beta \frac{2}{(2\nu-1)^{2J+2}\pi^{2J+2}} \int_{\tau'=0}^{1} \mathbf{d}^{[2J+2]}(\tau') \, \sin(2\nu-1)\pi\tau' d\tau'. \tag{5.102}$$

Because of the fact that there exists a functional dependency between the coefficients $\mathbf{d}_\nu$ of the Fourier series and the coefficients $\mathbf{e}_{2j}$ and $\mathbf{b}_{2j+1}$ of the Euler- and Bernoulli polynomials the latter ones can be restricted also by the dynamical model, because the Fourier coefficients must fulfil the conditions either according to Eq. (5.13),

$$\mathbf{d}_\nu \equiv \mathbf{c}_\nu = -\frac{2T^2}{\nu^2\pi^2} \int_{\tau'=0}^{1} \sin(\nu\pi\tau') \, \mathbf{a}(\tau'; \mathbf{r}, \dot{\mathbf{r}}) \, d\tau',$$

or to Eq. (5.23)

$$\mathbf{d}_\nu \equiv \mathbf{c}_\nu = -\frac{2T^2}{\nu^2\pi^2 - \mu^2} \int_{\tau'=0}^{1} \sin(\nu\pi\tau') \, \mathbf{a}^{II}(\tau; \mathbf{r}, \dot{\mathbf{r}}) \, d\tau'.$$

or according to Eq. (5.38), respectively,

$$\mathbf{d}_\nu \equiv \mathbf{c}_\nu = \tilde{\mathbf{c}}_\nu + \mathbf{x}_\nu,$$

with Eq. (5.26)

$$\tilde{\mathbf{c}}_\nu = -\frac{2T^2}{\nu^2\pi^2} \int_{\tau'=0}^{1} \sin(\nu\pi\tau')\ \tilde{\mathbf{a}}(\tau'; \tilde{\mathbf{r}}, \dot{\tilde{\mathbf{r}}})\ d\tau',$$

and Eq. (5.34)

$$\mathbf{x}_\nu = -\frac{2T^2}{\nu^2\pi^2} \int_{\tau'=0}^{1} \sin(\nu\pi\tau')\ \Delta\mathbf{a}(\tau'; \tilde{\mathbf{r}} + \mathbf{x}, \dot{\tilde{\mathbf{r}}} + \dot{\mathbf{x}})\ d\tau'.$$

Besides this functional dependency of the Fourier coefficients on the dynamical force model, the coefficients of the Euler polynomials are also connected to the dynamical model by the temporal derivatives of the orbit at the boundaries according to Eq. (5.78),

$$\mathbf{e}_{2j} := \frac{T^{2j}}{2(2j)!} \left(\mathbf{d}^{(2j)}(t_B) + \mathbf{d}^{(2j)}(t_A) \right),$$

and the coefficients of the Bernoulli polynomials according to Eq. (5.80),

$$\mathbf{b}_{2j+1} := \frac{T^{2j}}{(2j+1)!} \left(\mathbf{d}^{(2j)}(t_B) - \mathbf{d}^{(2j)}(t_A) \right).$$

Therefore, both representations of the satellite's orbit, either in form of the Fourier series or as a series in terms of Euler- and Bernoulli polynomials can be interpreted as a kinematical approximation for the orbit or as solution to the boundary value problem realizing the basis for a dynamical orbit determination.

5.3.2 Determination of the Euler and Bernoulli Polynomial Coefficients

5.3.2.1 Space Domain Representation of the Euler and Bernoulli Polynomial Coefficients

The approximation of the satellite's arc based on Euler and Bernoulli polynomials reads according to Eq. (5.74) by disregarding the remainder term $\mathbf{R}_P(\tau)$ according to Eq. (5.96),

$$\mathbf{d}(\tau) = \sum_{\nu=1}^{\infty} \mathbf{d}_\nu \sin(\nu\pi\tau) \approx \sum_{j=1}^{J} \mathbf{e}_{2j} E_{2j}(\tau) + \sum_{j=1}^{J} \mathbf{b}_{2j+1} B_{2j+1}(\tau). \tag{5.103}$$

In the following, we will write the two sums at the right hand side in matrix notation,

$$\mathbf{d}(\tau) \approx \sum_{j=1}^{J} \mathbf{e}_{2j} E_{2j}(\tau) + \sum_{j=1}^{J} \mathbf{b}_{2j+1} B_{2j+1}(\tau) = \mathbf{e}^{\mathsf{T}}\,\mathbf{E} + \mathbf{b}^{\mathsf{T}}\,\mathbf{B}. \tag{5.104}$$

The matrices $\mathbf{E}$ and $\mathbf{B}$ are composed by the polynomials according to Eqs. (5.72) and (5.73), if we select the upper index $J_{max} = 6$, resulting in an upper polynomial degree of 13 without restricting the generality. An upper polynomial degree of 13 means more precisely, degree 12 for the Euler polynomials and degree 13 for the Bernoulli polynomials. The matrices will be labelled accordingly; because of the fact that an Euler polynomial of degree $2j$ and a Bernoulli polynomial of degree $2j+1$ belong together as a pair, we will select the upper most degree of such a pair of polynomials as $\mathbf{E}^{13}$ and $\mathbf{B}^{13}$. Furthermore, these polynomials are

written as matrix products of the coefficients and the increasing powers of the basic (normalized) time as shown in the following.

$$\mathbf{E}^{13} = \mathbf{E}_c^{13}\,\mathbf{t}^{13} = \begin{pmatrix} -1 & 1 & 0 & 0 & 0 & 0 & 0 & 0 & 0 & 0 & 0 & 0 & 0 \\ 1 & 0 & -2 & 1 & 0 & 0 & 0 & 0 & 0 & 0 & 0 & 0 & 0 \\ -3 & 0 & 5 & 0 & -3 & 1 & 0 & 0 & 0 & 0 & 0 & 0 & 0 \\ 17 & 0 & -28 & 0 & 14 & 0 & -4 & 1 & 0 & 0 & 0 & 0 & 0 \\ -155 & 0 & 255 & 0 & -126 & 0 & 30 & 0 & -5 & 1 & 0 & 0 & 0 \\ 2073 & 0 & -3410 & 0 & 1683 & 0 & -396 & 0 & 55 & 0 & -6 & 1 & 0 \end{pmatrix} \begin{pmatrix} \tau \\ \tau^2 \\ \tau^3 \\ \tau^4 \\ \tau^5 \\ \tau^6 \\ \tau^7 \\ \tau^8 \\ \tau^9 \\ \tau^{10} \\ \tau^{11} \\ \tau^{12} \\ \tau^{13} \end{pmatrix}, \quad (5.105)$$

and

$$\mathbf{B}^{13} = \mathbf{B}_c^{13}\,\mathbf{t}^{13} = \begin{pmatrix} \frac{1}{2} & -\frac{3}{2} & 1 & 0 & 0 & 0 & 0 & 0 & 0 & 0 & 0 & 0 & 0 \\ -\frac{1}{6} & 0 & \frac{5}{3} & -\frac{5}{2} & 1 & 0 & 0 & 0 & 0 & 0 & 0 & 0 & 0 \\ \frac{1}{6} & 0 & -\frac{7}{6} & 0 & \frac{7}{2} & -\frac{7}{2} & 1 & 0 & 0 & 0 & 0 & 0 & 0 \\ -\frac{3}{10} & 0 & 2 & 0 & -\frac{21}{5} & 0 & 6 & -\frac{9}{2} & 1 & 0 & 0 & 0 & 0 \\ \frac{5}{6} & 0 & -\frac{11}{2} & 0 & 11 & 0 & -11 & 0 & \frac{55}{6} & -\frac{11}{2} & 1 & 0 & 0 \\ -\frac{691}{210} & 0 & \frac{65}{3} & 0 & -\frac{429}{10} & 0 & \frac{286}{7} & 0 & -\frac{143}{6} & 0 & 13 & -\frac{13}{2} & 1 \end{pmatrix} \begin{pmatrix} \tau \\ \tau^2 \\ \tau^3 \\ \tau^4 \\ \tau^5 \\ \tau^6 \\ \tau^7 \\ \tau^8 \\ \tau^9 \\ \tau^{10} \\ \tau^{11} \\ \tau^{12} \\ \tau^{13} \end{pmatrix}. \quad (5.106)$$

The matrix of the coefficients of the Euler polynomials reads

$$\mathbf{e}_{12}^{\mathsf{T}} = (\ \mathbf{e}_2 \quad \mathbf{e}_4 \quad \mathbf{e}_6 \quad \mathbf{e}_8 \quad \mathbf{e}_{10} \quad \mathbf{e}_{12}\ ), \quad (5.107)$$

and the matrix of the coefficients of the Bernoulli polynomials, respectively

$$\mathbf{b}_{13}^{\mathsf{T}} = (\ \mathbf{b}_3 \quad \mathbf{b}_5 \quad \mathbf{b}_7 \quad \mathbf{b}_9 \quad \mathbf{b}_{11} \quad \mathbf{b}_{13}\ ), \quad (5.108)$$

so that Eq. (5.103) reads with the upper summation index J_{max}=6

$$\mathbf{d}(\tau) \approx \sum_{j=1}^{J_{max}=6} \mathbf{e}_{2j} E_{2j}(\tau) + \sum_{j=1}^{J_{max}=6} \mathbf{b}_{2j+1} B_{2j+1}(\tau) = \mathbf{e}_{12}^{\mathsf{T}}\,\mathbf{E}^{13} + \mathbf{b}_{13}^{\mathsf{T}}\,\mathbf{B}^{13}, \quad (5.109)$$

or in rearranged form

$$\mathbf{d}(\tau) \approx \sum_{j=1}^{J_{max}=6} \mathbf{e}_{2j} E_{2j}(\tau) + \sum_{j=1}^{J_{max}=6} \mathbf{b}_{2j+1} B_{2j+1}(\tau) = \left(\mathbf{e}_{12}^{\mathsf{T}}\,\mathbf{E}_c^{13} + \mathbf{b}_{13}^{\mathsf{T}}\,\mathbf{B}_c^{13}\right)\,\mathbf{t}^{13} = (\ \mathbf{e}_{12}^{\mathsf{T}} \quad \mathbf{b}_{13}^{\mathsf{T}}\ ) \begin{pmatrix} \mathbf{E}_c^{13} \\ \mathbf{B}_c^{13} \end{pmatrix} \mathbf{t}^{13}. \quad (5.110)$$

If we skip the maximal index of the Euler-Bernoulli polynomials and write Eq. (5.110) as follows,

$$\mathbf{d}(\tau) \approx \mathbf{p}^{\mathsf{T}}\mathbf{P}\,\mathbf{t} = \mathbf{t}^{\mathsf{T}}\mathbf{P}^{\mathsf{T}}\mathbf{p}, \quad (5.111)$$

with

$$\mathbf{p} := \begin{pmatrix} \mathbf{e}_{12} \\ \mathbf{b}_{13} \end{pmatrix}, \qquad \mathbf{P} := \begin{pmatrix} \mathbf{E}_c^{13} \\ \mathbf{B}_c^{13} \end{pmatrix}, \qquad \mathbf{t} \equiv \mathbf{t}^{13} = \begin{pmatrix} \tau \\ \vdots \\ \tau^{13} \end{pmatrix}. \tag{5.112}$$

If the observational functionals $\mathbf{d}(\tau_k)$ are available at a sufficient number K of epochs τ_k,

$$\mathbf{d} := \begin{pmatrix} \mathbf{d}(\tau_1) \\ \vdots \\ \mathbf{d}(\tau_K) \end{pmatrix}, \tag{5.113}$$

then the system of linear observation equations reads,

$$\mathbf{d} = \mathbf{T}^\mathsf{T}\mathbf{P}^\mathsf{T}\mathbf{p}, \tag{5.114}$$

with the matrix of epochs

$$\mathbf{T} = \begin{pmatrix} \mathbf{t}_1 & \cdots & \mathbf{t}_K \end{pmatrix} = \begin{pmatrix} \tau_1 & \cdots & \tau_K \\ \vdots & \ldots & \vdots \\ \tau_1^{13} & \cdots & \tau_K^{13} \end{pmatrix}, \tag{5.115}$$

or in detail,

$$\begin{pmatrix} \mathbf{d}(\tau_1) \\ \vdots \\ \mathbf{d}(\tau_K) \end{pmatrix} \approx \begin{pmatrix} \tau_1 & \cdots & \tau_1^{13} \\ \vdots & \ldots & \vdots \\ \tau_K & \cdots & \tau_K^{13} \end{pmatrix} \begin{pmatrix} (\mathbf{E}_c^{13})^\mathsf{T} & (\mathbf{B}_c^{13})^\mathsf{T} \end{pmatrix} \begin{pmatrix} \mathbf{e}_{12} \\ \mathbf{b}_{13} \end{pmatrix}. \tag{5.116}$$

The coefficients of the Euler and Bernoulli polynomials can be determined by a least squares solution as follows,

$$\mathbf{p} = \left(\mathbf{P}\,\mathbf{T}\,\mathbf{T}^\mathsf{T}\mathbf{P}^\mathsf{T}\right)^{-1}\mathbf{P}\,\mathbf{T}\,\mathbf{d}, \tag{5.117}$$

with the matrix

$$\mathbf{T}\,\mathbf{T}^\mathsf{T} = \begin{pmatrix} \sum_{k=1}^{K} (\tau_k)^2 & \cdots & \sum_{k=1}^{K} \tau_k \tau_k^{13} \\ \vdots & \cdots & \vdots \\ \sum_{k=1}^{K} \tau_k^{13} \tau_k & \cdots & \sum_{k=1}^{K} (\tau_k^{13})^2 \end{pmatrix}, \tag{5.118}$$

and in detail, respectively,

$$\begin{aligned} \begin{pmatrix} \mathbf{e}_{12} \\ \mathbf{b}_{13} \end{pmatrix} = \Bigg(& \begin{pmatrix} \mathbf{E}_c^{13} \\ \mathbf{B}_c^{13} \end{pmatrix} \begin{pmatrix} \sum_{k=1}^{K} (\tau_k)^2 & \cdots & \sum_{k=1}^{K} \tau_k \tau_k^{13} \\ \vdots & \cdots & \vdots \\ \sum_{k=1}^{K} \tau_k^{13} \tau_k & \cdots & \sum_{k=1}^{K} (\tau_k^{13})^2 \end{pmatrix} \begin{pmatrix} (\mathbf{E}_c^{13})^\mathsf{T} & (\mathbf{B}_c^{13})^\mathsf{T} \end{pmatrix} \Bigg)^{-1} \\ & \begin{pmatrix} \mathbf{E}_c^{13} \\ \mathbf{B}_c^{13} \end{pmatrix} \begin{pmatrix} \tau_1 & \cdots & \tau_K \\ \vdots & \cdots & \vdots \\ \tau_1^{13} & \cdots & \tau_K^{13} \end{pmatrix} \begin{pmatrix} \mathbf{d}(\tau_1) \\ \vdots \\ \mathbf{d}(\tau_K) \end{pmatrix}. \end{aligned} \tag{5.119}$$

5.3.2.2 Spectral Domain Representation of the Euler and Bernoulli Polynomial Coefficients

If the polynomial coefficients are determined within a least squares adjustment process of the GNSS observations, then the sine coefficients can be computed based on Eq. (5.40),

$$\mathbf{d}_\nu = 2 \int_{\tau'=0}^{1} \mathbf{d}(\tau)\ \sin(\nu\pi\tau')\ d\tau',$$

and because of the identity, Eq. (5.42), we can write by inserting e.g. for the case given by Eq. (5.13),

$$\mathbf{d}_\nu \equiv \mathbf{c}_\nu = -\frac{2T^2}{\nu^2\pi^2} \int_{\tau'=0}^{1} \sin(\nu\pi\tau')\ \mathbf{a}(\tau';\mathbf{r},\dot{\mathbf{r}})\ d\tau', \tag{5.120}$$

which interprets these coefficients directly in dependency of the force function model $\mathbf{a}(\tau';\mathbf{r},\dot{\mathbf{r}})$. On the other hand, the coefficients $\mathbf{d}_\nu$ can be determined by the approximate orbit representation, Eq. (5.109),

$$\mathbf{d}_\nu \approx 2 \int_{\tau'=0}^{1} \left(\sum_{j=1}^{J_{max}=6} \mathbf{e}_{2j} E_{2j}(\tau) + \sum_{j=1}^{J_{max}=6} \mathbf{b}_{2j+1} B_{2j+1}(\tau) \right) \sin(\nu\pi\tau')\ d\tau'. \tag{5.121}$$

This equation can be written in matrix form with Eq. (5.110) as following

$$\mathbf{d}_\nu \approx 2 \int_{\tau'=0}^{1} \left(\mathbf{e}_{12}^{\mathsf{T}}\ \mathbf{E}_c^{13} + \mathbf{b}_{13}^{\mathsf{T}}\ \mathbf{B}_c^{13}\right)\ \mathbf{t}^{13}\ \sin(\nu\pi\tau')\ d\tau' = \left(\mathbf{e}_{12}^{\mathsf{T}}\ \mathbf{E}_c^{13} + \mathbf{b}_{13}^{\mathsf{T}}\ \mathbf{B}_c^{13}\right)\ \mathbf{l}_\nu^{13}. \tag{5.122}$$

The coefficients can be determined by the matrix relation,

$$\mathbf{d}_n^{\mathsf{T}} \approx \left(\mathbf{e}_{12}^{\mathsf{T}}\ \mathbf{E}_c^{13} + \mathbf{b}_{13}^{\mathsf{T}}\ \mathbf{B}_c^{13}\right)\ \mathbf{N}_n^{13}, \tag{5.123}$$

with

$$\mathbf{d}_n^{\mathsf{T}} = \begin{pmatrix} \mathbf{d}_1 & \cdots & \mathbf{d}_\nu & \cdots & \mathbf{d}_n \end{pmatrix}, \tag{5.124}$$

and

$$\mathbf{N}_n^{13} = \begin{pmatrix} \mathbf{l}_1^{13} & \cdots & \mathbf{l}_\nu^{13} & \cdots & \mathbf{l}_n^{13} \end{pmatrix} = \begin{pmatrix} I_1^1 & \cdots & I_\nu^1 & \cdots & I_n^1 \\ \vdots & \vdots & \vdots & \vdots & \vdots \\ I_1^k & \cdots & I_\nu^k & \cdots & I_n^k \\ \vdots & \vdots & \vdots & \vdots & \vdots \\ I_1^{13} & \cdots & I_\nu^{13} & \cdots & I_n^{13} \end{pmatrix}, \tag{5.125}$$

with the integrals

$$I_\nu^k := 2 \int_{\tau'=0}^{1} \tau'^k \sin(\nu\pi\tau')\ d\tau'. \tag{5.126}$$

The formula,

$$\mathbf{d}_n^{\mathsf{T}} \approx \left(\mathbf{e}_{12}^{\mathsf{T}}\ \mathbf{E}_c^{13} + \mathbf{b}_{13}^{\mathsf{T}}\ \mathbf{B}_c^{13}\right)\ \mathbf{N}_n^{13} = \begin{pmatrix} \mathbf{e}_{12}^{\mathsf{T}} & \mathbf{b}_{13}^{\mathsf{T}} \end{pmatrix} \begin{pmatrix} \mathbf{E}_c^{13} \\ \mathbf{B}_c^{13} \end{pmatrix} \mathbf{N}_n^{13}, \tag{5.127}$$

represents conditions for the Euler polynomials coefficients $\mathbf{e}$ and the Bernoulli polynomial coefficients $\mathbf{b}$ to satisfy the force function $\mathbf{a}(\tau';\mathbf{r},\dot{\mathbf{r}})$ contained in $\mathbf{d}_n$.

To show the structure of these condition equations, we will give an example with the upper limit 5 (J=2) instead of 13. In this case the equation reads as follows:

$$\begin{aligned}
&\left(\begin{array}{cccccc} \mathbf{d}_1 & \cdots & \mathbf{d}_\nu & \cdots & \mathbf{d}_n \end{array} \right) \approx \\
&= \left(\left(\begin{array}{cc} \mathbf{e}_2 & \mathbf{e}_4 \end{array} \right) \left(\begin{array}{ccccc} -1 & 1 & 0 & 0 & 0 \\ 1 & 0 & -2 & 1 & 0 \end{array} \right) + \left(\begin{array}{cc} \mathbf{b}_3 & \mathbf{b}_5 \end{array} \right) \left(\begin{array}{ccccc} \frac{1}{2} & -\frac{3}{2} & 1 & 0 & 0 \\ -\frac{1}{6} & 0 & \frac{5}{3} & -\frac{5}{2} & 1 \end{array} \right) \right) \cdot \\
&\cdot \left(\begin{array}{ccccc} I_1^1 & \cdots & I_\nu^1 & \cdots & I_n^1 \\ I_1^2 & & I_\nu^2 & & I_n^2 \\ I_1^3 & \cdots & I_\nu^3 & \cdots & I_n^3 \\ I_1^4 & & I_\nu^4 & & I_n^4 \\ I_1^5 & \cdots & I_\nu^5 & \cdots & I_n^5 \end{array} \right).
\end{aligned} \tag{5.128}$$

It reads for the sine coefficients $\mathbf{d}_\nu$, $\nu = 1, \cdots, n$,

$$\begin{aligned}
\mathbf{d}_\nu = &-\mathbf{e}_2 I_\nu^1 + \mathbf{e}_4 I_\nu^1 + \mathbf{e}_2 I_\nu^2 - 2\mathbf{e}_4 I_\nu^3 + \mathbf{e}_4 I_\nu^4 + \\
&+ \tfrac{1}{2}\mathbf{b}_3 I_\nu^1 - \tfrac{1}{6}\mathbf{b}_5 I_\nu^1 - \tfrac{3}{2}\mathbf{b}_3 I_\nu^2 + \mathbf{b}_3 I_\nu^3 + \tfrac{5}{3}\mathbf{b}_5 I_\nu^3 - \tfrac{5}{2}\mathbf{b}_5 I_\nu^4 + \mathbf{b}_5 I_\nu^5.
\end{aligned} \tag{5.129}$$

If sufficient condition equations according to e.g. Eq. (5.120) are introduced into the observation equations to derive the Euler polynomials coefficients $\mathbf{e}$ and the Bernoulli polynomial coefficients $\mathbf{b}$ then a purely dynamic orbit will result. If only selected conditions with specific indices ν are introduced then the orbit will be of reduced-kinematical character with a dynamic information.

The Eq. (5.127) can be written in a compact form if we skip the maximal indices of the Euler-Bernoulli polynomials and the matrix of integrals $\mathbf{N}$ as follows,

$$\mathbf{d}_n \approx \mathbf{p}^\mathsf{T}\mathbf{P}\,\mathbf{N} = \mathbf{N}^\mathsf{T}\mathbf{P}^\mathsf{T}\mathbf{p}, \tag{5.130}$$

with

$$\mathbf{p} := \left(\begin{array}{c} \mathbf{e}_{12} \\ \mathbf{b}_{13} \end{array} \right), \qquad \mathbf{P} := \left(\begin{array}{c} \mathbf{E}_c^{13} \\ \mathbf{B}_c^{13} \end{array} \right), \qquad \mathbf{N} \equiv \mathbf{N}_n^{13}. \tag{5.131}$$

Eq. (5.130) reads in detail,

$$\left(\begin{array}{c} \mathbf{d}_1 \\ \vdots \\ \mathbf{d}_n \end{array} \right) \approx \left(\begin{array}{ccc} I_1^1 & \cdots & I_1^{13} \\ \vdots & \ldots & \vdots \\ I_n^1 & \cdots & I_n^{13} \end{array} \right) \left(\begin{array}{cc} (\mathbf{E}_c^{13})^\mathsf{T} & (\mathbf{B}_c^{13})^\mathsf{T} \end{array} \right) \left(\begin{array}{c} \mathbf{e}_{12} \\ \mathbf{b}_{13} \end{array} \right). \tag{5.132}$$

It should be pointed out that the approximate sign "≈" holds for the sine coefficients of the real orbit as given by Eq. (5.66) or Eqs. (5.68) and (5.69). They could be determined by Eqs. (5.97) and (5.98) or by Eqs. (5.99) and (5.100). The sign "≈" has to be replaced by the equals sign "=" in Eq. (5.132), if the sine coefficients $\mathbf{d}_\nu$ are understood as the coefficients of the Fourier series of the Euler-Bernoulli polynomials $\mathbf{d}_P^J(\tau)$, in the present case for J_{max}=6. These coefficients can be computed rigorously by Eq. (5.132) or numerically by a discrete Fourier analysis procedure as given, e.g. in Sec. 5.2.4, (see also Sec. 5.4.2.2).

The coefficients of the Euler and Bernoulli polynomials can be determined by a least squares approximation in case of $n \geq p$ as follows,

$$\mathbf{p} = \left(\mathbf{P}\,\mathbf{N}\,\mathbf{N}^\mathsf{T}\mathbf{P}^\mathsf{T}\right)^{-1}\mathbf{P}\,\mathbf{N}\,\mathbf{d}_n, \tag{5.133}$$

with the matrices

$$\mathbf{N} = \left(\begin{array}{ccc} I_1^1 & \cdots & I_n^1 \\ \vdots & \ldots & \vdots \\ I_1^{13} & \cdots & I_n^{13} \end{array} \right), \qquad \mathbf{N}\,\mathbf{N}^\mathsf{T} = \left(\begin{array}{ccc} \sum\limits_{\nu=1}^{n} (I_1^1)^2 & \cdots & \sum\limits_{\nu=1}^{n} I_1^1 I_\nu^{13} \\ \vdots & \ldots & \vdots \\ \sum\limits_{\nu=1}^{n} I_\nu^{13} I_1^1 & \cdots & \sum\limits_{\nu=1}^{n} (I_\nu^{13})^2 \end{array} \right), \tag{5.134}$$

and in detail, respectively,

$$\begin{pmatrix} \mathbf{e}_{12} \\ \mathbf{b}_{13} \end{pmatrix} = \left(\begin{pmatrix} \mathbf{E}_c^{13} \\ \mathbf{B}_c^{13} \end{pmatrix} \begin{pmatrix} \sum_{\nu=1}^{n} (I_1^1)^2 & \cdots & \sum_{\nu=1}^{n} I_1^1 I_\nu^{13} \\ \vdots & \cdots & \vdots \\ \sum_{\nu=1}^{n} I_\nu^{13} I_1^1 & \cdots & \sum_{\nu=1}^{n} (I_\nu^{13})^2 \end{pmatrix} \begin{pmatrix} (\mathbf{E}_c^{13})^{\mathsf{T}} & (\mathbf{B}_c^{13})^{\mathsf{T}} \end{pmatrix} \right)^{-1}$$
$$\begin{pmatrix} \mathbf{E}_c^{13} \\ \mathbf{B}_c^{13} \end{pmatrix} \begin{pmatrix} I_1^1 & \cdots & I_n^1 \\ \vdots & \cdots & \vdots \\ I_1^{13} & \cdots & I_n^{13} \end{pmatrix} \begin{pmatrix} \mathbf{d}_1 \\ \vdots \\ \mathbf{d}_n \end{pmatrix}. \tag{5.135}$$

It shall be pointed out that the coefficients $\mathbf{d}_\nu$ can be determined either by Eq. (5.40) or by Eq. (5.120). For numerical tests refer to Sec. 5.4.

5.3.2.3 Numerical Quadrature

For the determination of the integrals

$$I_\nu^k := 2S_\nu^k = 2 \int_{\tau=0}^{1} \tau^k \sin(\nu\pi\tau)\, d\tau, \tag{5.136}$$

we apply a recursion formula similarly to that which has been proposed in (Ilk 1976). It can be derived easily by applying a partial integration to Eq. (5.136):

$$S_\nu^k = \int_{\tau=0}^{1} \tau^k \sin(\nu\pi\tau)\, d\tau = -\frac{\tau^k}{\nu\pi} \cos(\nu\pi\tau)\Big|_{\tau=0}^{1} + \frac{k}{\nu\pi} \int_{\tau=0}^{1} \tau^{k-1} \cos(\nu\pi\tau)\, d\tau. \tag{5.137}$$

If we insert the following abbreviations into Eq. (5.137),

$$C_\nu^k := \int_{\tau=0}^{1} \tau^k \cos(\nu\pi\tau)\, d\tau, \tag{5.138}$$

then the integrals S_ν^k can be determine as follows

$$S_\nu^k = -\frac{(-1)^\nu}{\nu\pi} + \frac{k}{\nu\pi} C_\nu^{k-1}. \tag{5.139}$$

A similar relation can be derived for the integrals C_ν^k,

$$C_\nu^k = \int_{\tau=0}^{1} \tau^k \cos(\nu\pi\tau)\, d\tau = \frac{\tau^k}{\nu\pi} \sin(\nu\pi\tau)\Big|_{\tau=0}^{1} - \frac{k}{\nu\pi} \int_{\tau=0}^{1} \tau^{k-1} \sin(\nu\pi\tau)\, d\tau = -\frac{k}{\nu\pi} S_\nu^{k-1}. \tag{5.140}$$

The recursion formula will be applied for a fixed index ν and the set of powers of τ^k with $k = 0, ..., J+1$. The initial functionals are simply

$$C_\nu^0 = C_\nu^{k=0} = \int_{\tau=0}^{1} \tau^0 \cos(\nu\pi\tau)\, d\tau = 0, \tag{5.141}$$

and

$$S_\nu^0 = S_\nu^{k=0} = \int_{\tau=0}^{1} \tau^0 \sin(\nu\pi\tau)\, d\tau = -\frac{1}{\nu\pi} \cos(\nu\pi\tau)\Big|_{\tau=0}^{1} = \frac{1}{\nu\pi} \left(1 - (-1)^\nu\right), \tag{5.142}$$

so that the following recursion scheme follows,

$$S_\nu^k = -\frac{(-1)^\nu}{\nu\pi} + \frac{k}{\nu\pi} C_\nu^{k-1}, \qquad C_\nu^k = -\frac{k}{\nu\pi} S_\nu^{k-1}. \tag{5.143}$$

The final results can be derived by a multiplication by the factor 2,

$$I_\nu^k := 2S_\nu^k. \tag{5.144}$$

It should be pointed out that this integrals can be determined once for all and can be used for all orbit determination cases.

Unfortunately, these simple and fast formula show a very critical numerical behavior for high indices k and small indices ν. This can be seen if the Eq. (5.139) are written in closed form,

$$C_\nu^k = \sin\nu\pi\ F_1^k + \cos\nu\pi\ F_2^k + F_3^k, \tag{5.145}$$

and

$$S_\nu^k = \sin\nu\pi\ F_2^k - \cos\nu\pi\ F_1^k + F_4^k, \tag{5.146}$$

with

$$F_1^k = \sum_{i=0}^{[k/2]} (-1)^i \frac{1}{(\nu\pi)^{2i+1}} \frac{k!}{(k-2i)!}, \tag{5.147}$$

$$F_2^k = \sum_{i=0}^{[k-1/2]} (-1)^i \frac{1}{(\nu\pi)^{2(2+1)}} \frac{k!}{(k-2i-1)!}, \tag{5.148}$$

$$F_3^k = \frac{1-(-1)^k}{2} (-1)^{\frac{k+1}{2}} \frac{k!}{(\nu\pi)^{k+1}}, \tag{5.149}$$

$$F_4^k = \frac{(-1)^k+1}{2} (-1)^{\frac{k}{2}} \frac{k!}{(\nu\pi)^{k+1}}. \tag{5.150}$$

These functions contain very large terms with alternating signs with the consequence that leading numbers cancel, because the absolute values of the integrals are small, fulfilling the inequalities,

$$\left|C_\nu^k\right| \le \frac{1}{k+1}, \qquad \left|S_\nu^k\right| \le \frac{1}{k+1}. \tag{5.151}$$

The integrals S_ν^k can be determined alternatively by a series expansion of the sine function and a subsequent analytical integration and an insertion of the integration limits

$$S_\nu^k = I_\nu^k = \int_{\tau=0}^{1} \tau^k \sin(\nu\pi\tau)\ d\tau = \sum_{i=0}^{\infty} (-1)^i \frac{(\nu\pi)^{2i+1}}{(2i+1)!(2i+2+k)}. \tag{5.152}$$

These series show a fast convergence with small index ν and large index k.

5.3.3 Temporal Derivatives of the Orbit Function

5.3.3.1 Velocity

In the following, we will use the hybrid version of the orbit representation, that means, we will represent the orbit by three terms, a first one represents a reference motion $\overline{\mathbf{r}}(\tau)$, a second one represents the Euler-Bernoulli polynomials $\mathbf{d}_P^J(\tau)$ and a third one the Fourier series $\mathbf{d}_F^n(\tau)$. The last two difference orbit representations

can be used alternatively or as combination representation. If we set one of the indices J or n zero then we get the specific alternatives as discussed in the last sections. The velocities along the orbit can be derived by a differentiation of the orbit function, Eq. (5.90),

$$\mathbf{r}(t) = \mathbf{r}(\tau) \approx \bar{\mathbf{r}}(\tau) + \mathbf{d}_P^J(\tau) + \mathbf{d}_F^n(\tau) + \mathbf{R}_{\mathrm{PF}}(\tau) \approx \bar{\mathbf{r}}(\tau) + \mathbf{d}_P^J(\tau) + \mathbf{d}_F^n(\tau), \tag{5.153}$$

where the normalized time τ is related to the real time t according to Eq. (5.3),

$$\tau = \frac{t - t_A}{T} \quad \text{with} \quad T = t_B - t_A, \;\; t \in [t_A, t_B],$$

with respect to the time

$$\frac{d\mathbf{r}(\tau)}{dt} = \frac{d\bar{\mathbf{r}}(\tau)}{dt} + \frac{d\mathbf{d}_P^J(\tau)}{dt} + \frac{d\mathbf{d}_F^n(\tau)}{dt}, \tag{5.154}$$

and with μ according to Eq. (5.15),

$$\frac{d\bar{\mathbf{r}}(\tau)}{dt} = \frac{\mu}{T \sin\mu} \left(-\cos\mu(1-\tau)\mathbf{r}_A + \cos\mu\tau\mathbf{r}_B \right), \tag{5.155}$$

and the terms

$$\frac{d\mathbf{d}_P^J(\tau)}{dt} = \frac{1}{T} \left(\sum_{j=1}^{J} 2j\mathbf{e}_{2j} E_{2j-1}(\tau) + \sum_{j=1}^{J} (2j+1)\mathbf{b}_{2j+1} B_{2j}(\tau) \right), \tag{5.156}$$

$$\frac{d\mathbf{d}_F^n(\tau)}{dt} = \frac{1}{T} \sum_{\nu=1}^{n} \mathbf{d}_\nu \nu\pi \cos(\nu\pi\tau). \tag{5.157}$$

Then the velocities can be determined by the function

$$\begin{aligned} \frac{d\mathbf{r}(\tau)}{dt} = {} & \frac{\mu}{T \sin\mu} \left(-\cos\mu(1-\tau)\mathbf{r}_A + \cos\mu\tau\mathbf{r}_B \right) + \\ & + \frac{1}{T} \left(\sum_{j=1}^{J} 2j\mathbf{e}_{2j} E_{2j-1}(\tau) + \sum_{j=1}^{J} (2j+1)\mathbf{b}_{2j+1} B_{2j}(\tau) \right) + \frac{1}{T} \sum_{\nu=1}^{n} \mathbf{d}_\nu \nu\pi \cos(\nu\pi\tau). \end{aligned} \tag{5.158}$$

If the upper index n is not sufficiently high then Gibbs' effects can cause errors especially at the boundaries of the arcs. If the force function $\mathbf{a}(\tau')$ is available, then it is preferable to determine first the velocity at the time t_A according to (Ilk 1976),

$$\dot{\mathbf{r}}_A = \frac{1}{T} (\mathbf{r}_B - \mathbf{r}_A) - T \int_{\tau'=0}^{1} (1 - \tau') \, \mathbf{a}(\tau') \, d\tau', \tag{5.159}$$

and then the velocity at an arbitrary time instant t by an integration as follows,

$$\dot{\mathbf{r}}(t) = \dot{\mathbf{r}}_A + (t - t_A) \int_{\tau'=0}^{1} \mathbf{a}(\tau') \, d\tau', \tag{5.160}$$

with

$$\tau' = \frac{t' - t_A}{t - t_A} \in [0, 1] \;, \qquad t, t' \in [t_A, t_B], \tag{5.161}$$

or, by transformation of the integration interval,

$$\dot{\mathbf{r}}(\tau) = \dot{\mathbf{r}}_A + T \int_{\tau'=0}^{\tau} \mathbf{a}(\tau') \, d\tau', \tag{5.162}$$

with

$$\tau' = \frac{t' - t_A}{T} \in [0, 1] \,, \quad \tau = \frac{t - t_A}{T} \in [0, 1] \,. \tag{5.163}$$

5.3.3.2 Acceleration

The force function corresponds to the second derivative of the orbit with respect to the time according to Eq. (5.1) with Eq. (5.6)

$$L\left(\mathbf{r}(t)\right) = \frac{d}{dt}\dot{\mathbf{r}}(t) = \mathbf{a}(\tau). \tag{5.164}$$

It holds for the second derivatives

$$\frac{d\dot{\mathbf{r}}(\tau)}{dt} = \frac{d\dot{\tilde{\mathbf{r}}}(\tau)}{dt} + \frac{d\dot{\mathbf{d}}_P^J(\tau)}{dt} + \frac{d\dot{\mathbf{d}}_F^n(\tau)}{dt}, \tag{5.165}$$

with

$$\frac{d\dot{\tilde{\mathbf{r}}}(\tau)}{dt} = \frac{\mu^2}{T^2 \sin\mu}\left(-\sin\mu(1-\tau)\mathbf{r}_A - \sin\mu\tau\mathbf{r}_B\right), \tag{5.166}$$

$$\frac{d\dot{\mathbf{d}}_P^J(\tau)}{dt} = \frac{1}{T^2}\left(\sum_{j=1}^{J} 2j(2j-1)\mathbf{e}_{2j}E_{2j-2}(\tau) + \sum_{j=1}^{J} 2j(2j+1)\mathbf{b}_{2j+1}B_{2j-1}(\tau)\right), \tag{5.167}$$

$$\frac{d\dot{\mathbf{d}}_F^n(\tau)}{dt} = -\frac{1}{T^2}\sum_{\nu=1}^{n}\mathbf{d}_\nu\left(\nu\pi\right)^2\sin(\nu\pi\tau). \tag{5.168}$$

The accelerations can be determined by

$$\begin{aligned}\frac{d\dot{\mathbf{r}}(\tau)}{dt} = {} & \frac{\mu^2}{T^2 \sin\mu}\left(-\sin\mu(1-\tau)\mathbf{r}_A - \sin\mu\tau\mathbf{r}_B\right) + \\ & + \frac{1}{T^2}\left(\sum_{j=1}^{J} 2j(2j-1)\mathbf{e}_{2j}E_{2j-2}(\tau) + \sum_{j=1}^{J} 2j(2j+1)\mathbf{b}_{2j+1}B_{2j-1}(\tau)\right) - \frac{1}{T^2}\sum_{\nu=1}^{n}\mathbf{d}_\nu\left(\nu\pi\right)^2\sin(\nu\pi\tau),\end{aligned} \tag{5.169}$$

which corresponds to the force function $\mathbf{a}(\tau)$.

5.3.3.3 Check

If this formula is inserted into Eq. (5.159) instead of the force function $\ddot{\mathbf{r}}(\tau) = \mathbf{a}(\tau)$ and with it in (5.160) then we arrive again at Eq. (5.158). This shall be demonstrated for the velocity at the time t_A. It holds

$$\dot{\mathbf{r}}_A = \frac{1}{T}\left(\mathbf{r}_B - \mathbf{r}_A\right) - T\int_{\tau'=0}^{1}(1-\tau')\left(\frac{d\dot{\tilde{\mathbf{r}}}(\tau')}{dt} + \frac{d\dot{\mathbf{d}}_P^J(\tau')}{dt} + \frac{d\dot{\mathbf{d}}_F^n(\tau')}{dt}\right)d\tau', \tag{5.170}$$

with the integrals

$$\begin{aligned}&\int_{\tau'=0}^{1}(1-\tau')\,\frac{d\dot{\tilde{\mathbf{r}}}(\tau')}{dt}\,d\tau' = \\ &= -\frac{\mu^2}{T^2\sin\mu}\left(\mathbf{r}_A\int_{\tau'=0}^{1}(1-\tau')\,\sin\mu(1-\tau')\,d\tau' + \mathbf{r}_B\int_{\tau'=0}^{1}(1-\tau')\,\sin\mu\tau'\,d\tau'\right) = \\ &= -\frac{1}{T^2\sin\mu}\left(\mathbf{r}_A\left(\sin\mu - \mu\cos\mu\right) + \mathbf{r}_B\left(\mu - \sin\mu\right)\right),\end{aligned} \tag{5.171}$$

and

$$\int_{\tau'=0}^{1} (1-\tau')\,\frac{d\dot{\mathbf{d}}_P^J(\tau')}{dt}\,d\tau' =$$

$$= \frac{1}{T^2}\int_{\tau'=0}^{1}\left(\sum_{j=1}^{J} 2j(2j-1)\mathbf{e}_{2j}E_{2j-2}(\tau') + \sum_{j=1}^{J} 2j(2j+1)\mathbf{b}_{2j+1}B_{2j-1}(\tau')\right)(1-\tau')\,d\tau' \tag{5.172}$$

$$= \frac{1}{T^2}\left(\sum_{j=1}^{J} 2j(2j-1)\mathbf{e}_{2j}\int_{\tau'=0}^{1}(1-\tau')\,E_{2j-2}(\tau')\,d\tau' + \sum_{j=1}^{J} 2j(2j+1)\mathbf{b}_{2j+1}\int_{\tau'=0}^{1}(1-\tau')\,B_{2j-1}(\tau')d\tau'\right)$$

$$= -\frac{1}{T^2}\left(\sum_{j=1}^{J}\left(E_{2j}(\tau'=0) - E_{2j}(\tau'=1) + 2jE_{2j-1}(\tau'=0)\right)\mathbf{e}_{2j} + \sum_{j=1}^{J}(2j+1)B_{2j}(\tau'=1)\mathbf{b}_{2j+1}\right),$$

as well as with

$$\int_{\tau'=0}^{1}(1-\tau')\,\frac{d\dot{\mathbf{d}}_F^n(\tau')}{dt}\,d\tau' = -\frac{1}{T^2}\sum_{\nu=1}^{n}\mathbf{d}_\nu\,(\nu\pi)^2\int_{\tau'=0}^{1}(1-\tau')\,\sin(\nu\pi\tau')\,d\tau'$$

$$= -\frac{1}{T^2}\sum_{\nu=1}^{n}\mathbf{d}_\nu\,(\nu\pi - \sin(\nu\pi)). \tag{5.173}$$

The velocity at the starting point can be determined by the formula,

$$\dot{\mathbf{r}}_A = \frac{\mu}{T\sin\mu}\,(-\cos\mu\mathbf{r}_A + \mathbf{r}_B) + \tag{5.174}$$

$$+ \frac{1}{T}\left(\sum_{j=1}^{J} 2jE_{2j-1}(\tau=0)\mathbf{e}_{2j} + \sum_{j=1}^{J}(2j+1)B_{2j}(\tau=0)\mathbf{b}_{2j+1}\right) + \frac{1}{T}\sum_{\nu=1}^{n}\mathbf{d}_\nu\nu\pi.$$

This equation coincides with Eq. (5.158) for the time $\tau = 0$.

5.4 Numerical Verifications

In this section, various numerical tests are performed which shall demonstrate the approximation characteristics and the numerical properties of the formulae derived so far. Furthermore, these tests shall be helpful for the subsequent developments to construct procedures for the kinematical and reduced kinematical orbit determination. The computations are performed based on noise-free simulated data sets; details will be given in the different sub-sections. In a first subsection, the approximation properties of the Fourier series, the series in terms of Euler and Bernoulli polynomials as well as combinations of them are tested. The latter modification is the most promising and will be used later on for the construction of a proper orbit determination technique. In a second subsection, the dynamical restrictions on the various parameters, which model the kinematical orbits are tested. This is important in so far as these restrictions force some kinematical orbit parameters to fulfill a selected dynamical model. Selected dynamical restrictions will be used to construct "reduced" kinematical orbit determination modifications.

5.4.1 Approximation Tests

5.4.1.1 The Approximation by a Finite Fourier Series

If the sine series is limited by a finite upper index n according to Eq. (5.94), then it holds,

$$\mathbf{r}(\tau) = \bar{\mathbf{r}}(\tau) + \mathbf{d}_F^\infty(\tau) = \bar{\mathbf{r}}(\tau) + \mathbf{d}_F^n(\tau) + \mathbf{R}_F(\tau), \tag{5.175}$$

with the approximation function

$$\mathbf{d}_F^n(\tau) = \sum_{\nu=1}^{n} \mathbf{d}_\nu \sin(\nu\pi\tau), \tag{5.176}$$

and the remainder term $\mathbf{R}_F(\tau)$,

$$\mathbf{R}_F(\tau) = \sum_{\nu=n+1}^{\infty} \mathbf{d}_\nu \sin(\nu\pi\tau). \tag{5.177}$$

The function $\mathbf{d}_F^n(\tau)$ itself as well as the remainder function $\mathbf{R}_F(\tau)$ depend on the reference motions $\bar{\mathbf{r}}(\tau)$. It can be modelled by $\bar{\mathbf{r}}(\tau)$ either according to Eq. (5.10) as a *straight line* (Fig. 5.1),

$$\bar{\mathbf{r}}(\tau) = (1-\tau)\,\mathbf{r}_A + \tau\mathbf{r}_B,$$

or according to Eq. (5.20) as an *ellipse* with the center at the origin of the reference system (Fig. 5.2),

$$\bar{\mathbf{r}}(\tau) = \frac{\sin\mu(1-\tau)}{\sin\mu}\mathbf{r}_A + \frac{\sin\mu\tau}{\sin\mu}\mathbf{r}_B,$$

or according to Eq. (5.37),

$$\bar{\mathbf{r}}(\tau) := \tilde{\mathbf{r}}(\tau) + \bar{\mathbf{x}}(\tau),$$

as a dynamical *reference orbit* $\tilde{\mathbf{r}}(\tau)$ until to a specified degree of the gravity field model in addition to a linear combination of the boundary values of the difference function $\bar{\mathbf{x}}(\tau)$, according to Eq. (5.33) (Fig. 5.3),

$$\bar{\mathbf{x}}(\tau) = (1-\tau)\,\mathbf{x}_A + \tau\,\mathbf{x}_B.$$

To show the approximation characteristics in case of the various choices of reference motions, a 30 minute arc has been simulated based on a gravity field model up to a maximal spherical harmonic degree of N_F =300. In case of a *reference orbit* as reference motion a gravity field model up to a spherical harmonic degree of N_R =30 has been selected. The remainder functions will depend on the approximation functions and the various modes of the reference motions $\bar{\mathbf{r}}(\tau)$. They are shown for different maximal upper indices of the Fourier series. If the maximal index n is too small then a pronounced Gibb's effect will occur. The Figs. 5.4, 5.6 and 5.8 show the spectra of the various reference motions divided in various spectral bounds for a better visibility and Figs. 5.5, 5.7 and 5.9 the corresponding remainder functions for different upper series indices n.

It becomes clear that the kind of reference motion $\bar{\mathbf{r}}(\tau)$ is important for the size of the amplitudes but also for the size of the remainder functions. A reference motion based on a gravity field of a maximal upper degree and order of N_R =30 models the (pseudo) real orbit with an accuracy of less than a meter. If, in addition, the sine series is restricted by an upper index of 50 then the remainder function deviates from the real orbit by less than a *mm*. In summary, we can state that the accuracy becomes much better by using as reference motion a dynamically determined arc than a straight line or an elliptic motion. On the other hand, one has to keep in mind that the determination of a dynamical reference arc is more costly than the use of an elliptic reference. Therefore, the latter one might be an acceptable compromise.

5.4.1.2 The Approximation by a Finite Series of Euler and Bernoulli Polynomials

If the solution series in terms of Euler and Bernoulli polynomials are limited by a finite upper index J according to Eq. (5.94), then it holds

$$\mathbf{r}(\tau) = \bar{\mathbf{r}}(\tau) + \mathbf{d}_P^\infty(\tau) = \bar{\mathbf{r}}(\tau) + \mathbf{d}_P^J(\tau) + \mathbf{R}_P(\tau), \tag{5.178}$$

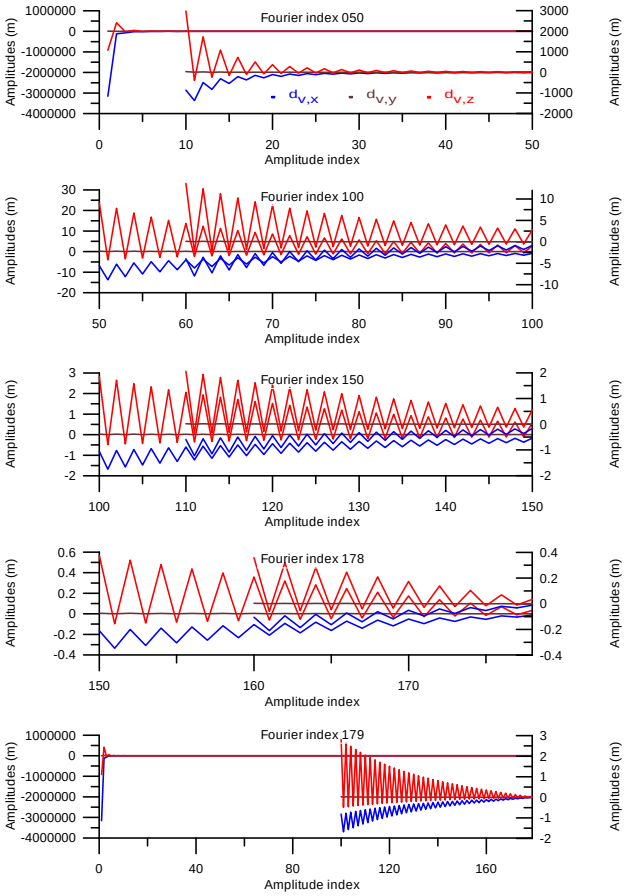

Figure 5.4: Spectrum of $\mathbf{d}_F^n(\tau)$ based on $\bar{\mathbf{r}}(\tau)$ selected as reference motion in the *straight line* mode for an Earth gravity field model up to degree and order N_F =300.

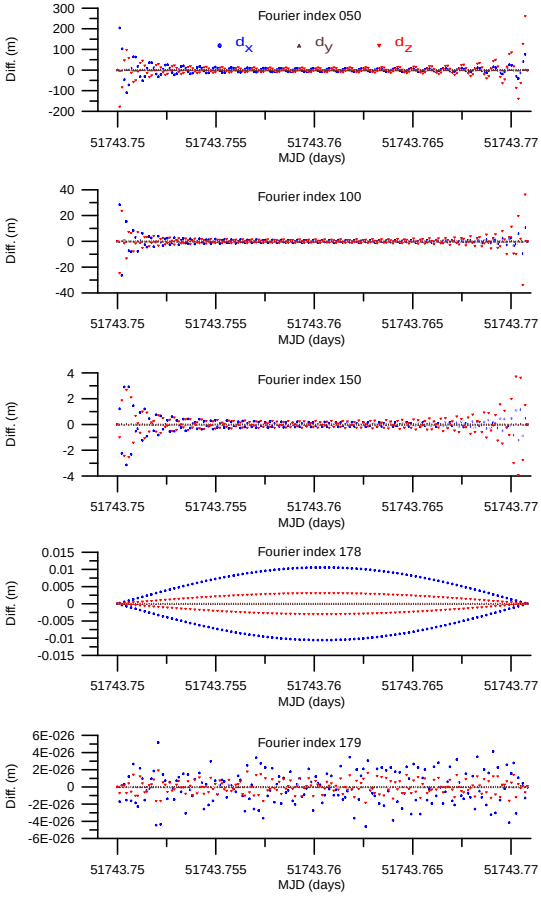

Figure 5.5: Remainder function $\mathbf{R}_F(\tau)$ based on $\bar{\mathbf{r}}(\tau)$ selected as reference motion in the *straight line* mode for different Fourier indices n for an Earth gravity field model up to degree and order N_F =300.

with the approximation function

$$\mathbf{d}_P^J(\tau) = \sum_{j=1}^{J} \mathbf{e}_{2j} E_{2j}(\tau) + \sum_{j=1}^{J} \mathbf{b}_{2j+1} B_{2j+1}(\tau), \tag{5.179}$$

and the remainder term $\mathbf{R}_P(\tau)$,

$$\mathbf{R}_P(\tau) = \sum_{j=J+1}^{\infty} \mathbf{e}_{2j} E_{2j}(\tau) + \sum_{j=J+1}^{\infty} \mathbf{b}_{2j+1} B_{2j+1}(\tau). \tag{5.180}$$

Analogously to the last section, the function $\mathbf{d}_P^J(\tau)$ itself as well as the remainder function $\mathbf{R}_P(\tau)$ depend on the reference motion $\bar{\mathbf{r}}(\tau)$, either according to Eq. (5.10) as a *straight line*, according to Eq. (5.20) as an *ellipse* or according to Eq. (5.37) as a dynamical *reference orbit* $\tilde{\mathbf{r}}(\tau)$.

To show the approximation characteristics in case of the various choices of reference motions, again a 30 minute arc has been simulated based on a gravity field model up to a maximal spherical harmonic degree of N_F =300. In case of a *reference orbit* as reference motion a gravity field model up to a spherical harmonic degree of N_R =30 has been selected. The remainder functions will depend on the approximation functions and the various modes of the reference motion $\bar{\mathbf{r}}(\tau)$. In the following, they are shown for different maximal

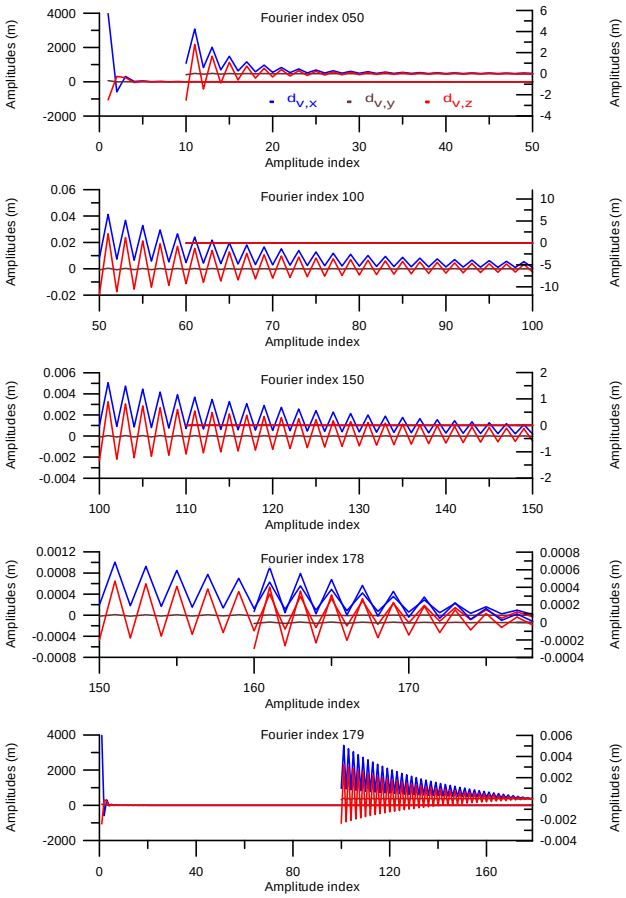

Figure 5.6: Spectrum of $\mathbf{d}_F^n(\tau)$ based on $\bar{\mathbf{r}}(\tau)$ selected as reference motion in the *ellipse* mode for an Earth gravity field model up to degree and order N_F =300.

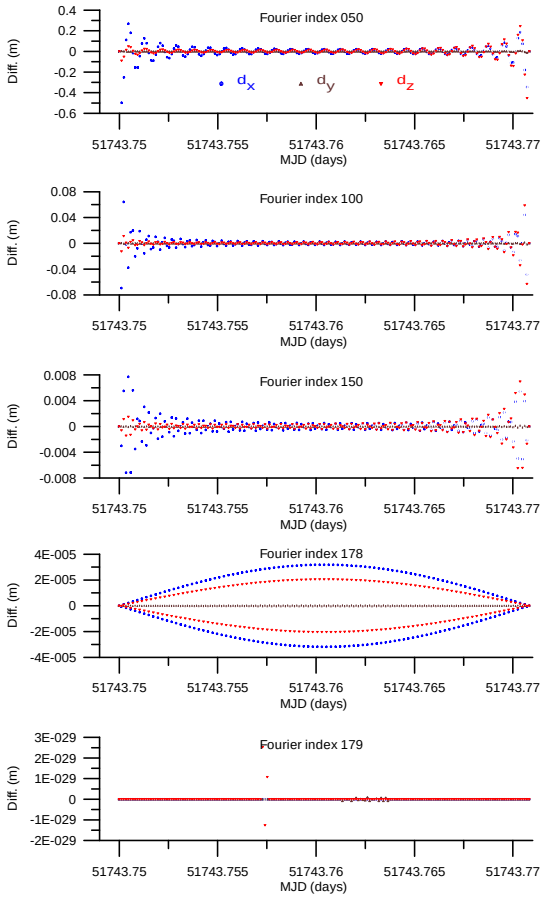

Figure 5.7: Remainder function $\mathbf{R}_F(\tau)$ based on $\bar{\mathbf{r}}(\tau)$ selected as reference motion in the *ellipse* mode for different Fourier indices n for an Earth gravity field model up to degree and order N_F =300.

upper indices of the series in terms of Euler-Bernoulli polynomials. It became clear in Sec. 5.3 that the Euler polynomials of degree $2j$ and the Bernoulli polynomials of degree $2j+1$ belong together for a specific index j. Figs. 5.11, 5.13 and 5.15 show the remainder functions for various maximal series indices $J = 1, 2, 3, 4, 5$ based on the reference motions (i.e. straight line, ellipse and reference orbit degree and order 30 modes) as discussed before. Figs. 5.10, 5.12 and 5.14 show the series contributions for the indices $j = 1, 2, 3, 4, 5$ of an Euler-Bernoulli polynomial approximation with a maximal index $J_{max} = 5$ for the different reference motions. It is interesting to note that the approximation quality increases with increasing upper index J. Nevertheless, the series contributions of the separate polynomial degrees J=1,2,3,4 and 5 to the series $\mathbf{d}_P^{J_{max}=5}(\tau)$ do not become smaller. The reason is not completely clear; it seems that the convergence of the Euler-Bernoulli polynomials require a large upper index J until the convergence can be directly seen.

5.4.1.3 The Approximation by a Combination of Fourier Series and Series of Euler-Bernoulli Polynomials

In the last section, it is demonstrated that the upper index J of the series in terms of Euler-Bernoulli polynomials should be very high to achieve an approximation accuracy at the sub millimeter level. But it should be pointed out once again that a pure representation by a series of Euler-Bernoulli polynomials is not in the focus of this approach. Rather a fit of a series in terms of Euler-Bernoulli polynomials to the geometrically determined arc at a reasonable upper degree (e.g. J_{max}=4) should guarantee a sufficient

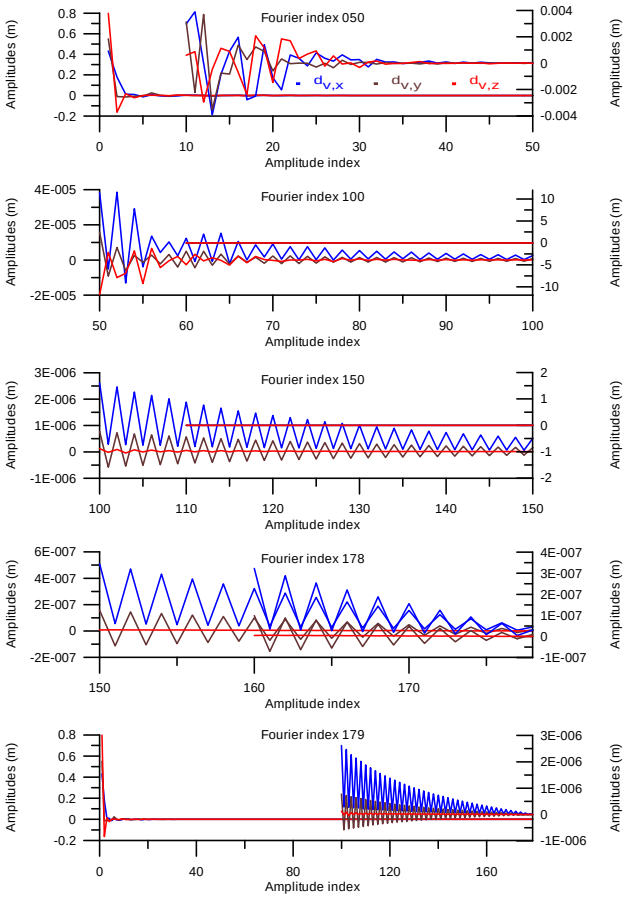

Figure 5.8: Spectrum of $\mathbf{d}_F^n(\tau)$ based on $\bar{\mathbf{r}}(\tau)$ selected as reference motion in the *reference orbit up to degree and order 30* mode for an Earth gravity field model up to degree and order N_F =300.

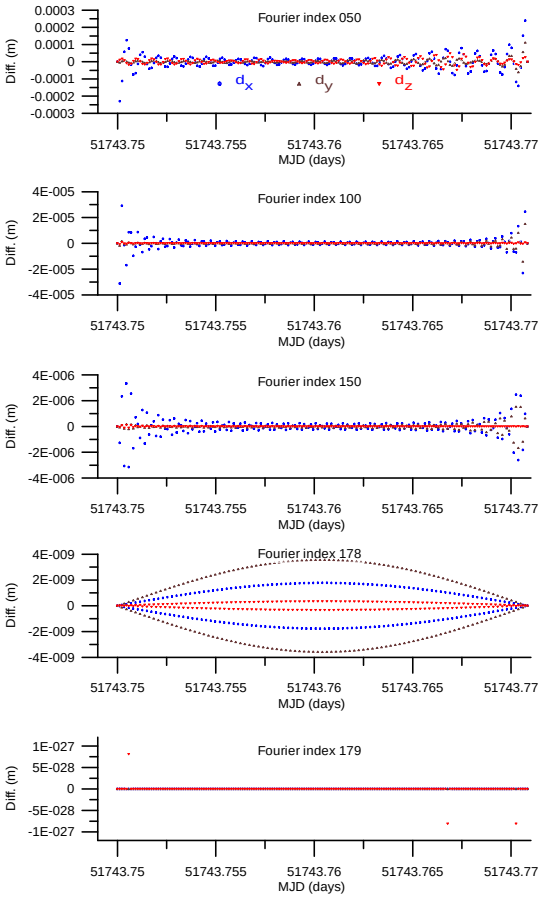

Figure 5.9: Remainder function $\mathbf{R}_F(\tau)$ based on $\bar{\mathbf{r}}(\tau)$ selected as reference motion in the *reference orbit up to degree and order 30* mode for different Fourier indices n for an Earth gravity field model up to degree and order N_F =300.

confident determination of the Euler-Bernoulli coefficients, corresponding to sufficiently precise arc derivatives at the arc boundary epochs. In that case, the residual sine series should show a fast convergence and low residuals of the combined series when compared to the true ephemerides. Detailed investigations to this facts are performed in Sec. 5.4.2.2. To demonstrate the numerical characteristics of the combined series the simulation cases as used in the above section have been considered in the straight line, elliptic and reference orbit mode. Then a series of Euler-Bernoulli polynomials up to degree J_{max}=4 has been fitted to the difference function $\mathbf{d}(\tau)$ and subsequently a sine series has been determined for the Euler-Bernoulli remainder function. Fig. 5.16 shows the various spectral bands of the amplitudes for the "straight line" mode. Fig. 5.17 shows the residuals of the combined series "Euler-Bernoulli polynomials" plus "sine series" up to different upper summation limits. The figure shows from top to bottom the residuals of the approximation cases, where the sine series are limited by the upper indices 20, 30, 50, 70, 90, 100, 150 and 178 and finally by the index 179 which represents the interpolation case; the residuals are very small and caused only by rounding errors. Similar cases are shown in Figs. 5.18 and 5.19 for the "elliptic mode" and Figs. 5.20 and 5.21 for the "reference orbit mode". The combination of a series in terms of Euler-Bernoulli polynomials up to degree J_{max}=4 and a series of sine functions shows a very good approximation quality for all modes of reference motions. This is especially the case for the straight line mode but also for the ellipse mode. This is a consequence of the similar convergence charactistics of the spectra of the real orbit and the approximation by Euler-Bernoulli polynomials (refer to Sec. 5.4.2.2). The case of a dynamical reference orbit up to degree

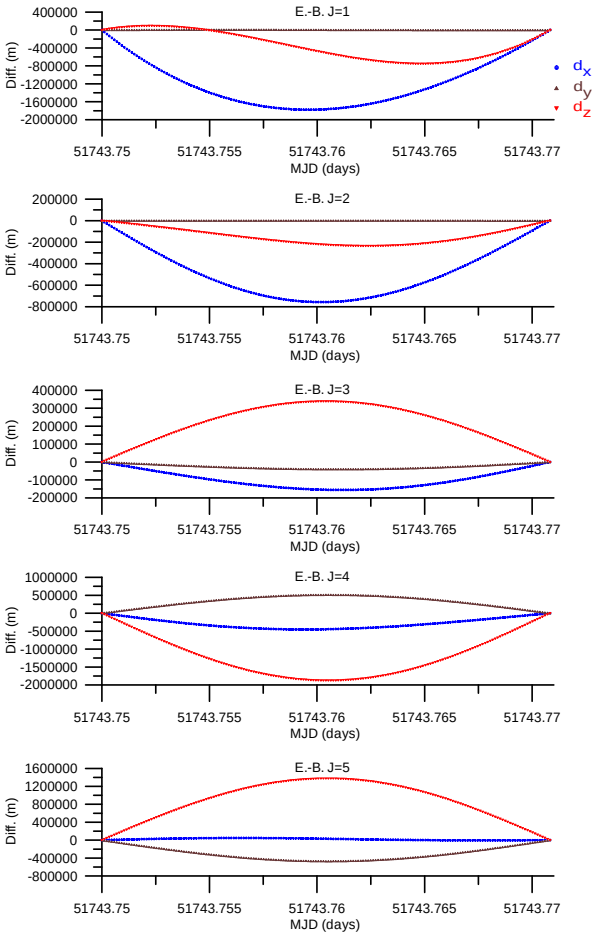

Figure 5.10: Series contributions of the separate degrees j=1,2,3,4 and 5 to the sum $\mathbf{d}_P^J(\tau)$ based on $\bar{\mathbf{r}}(\tau)$ (reference motion: *straight line* mode) for an Earth gravity field model up to degree and order N_F =300.

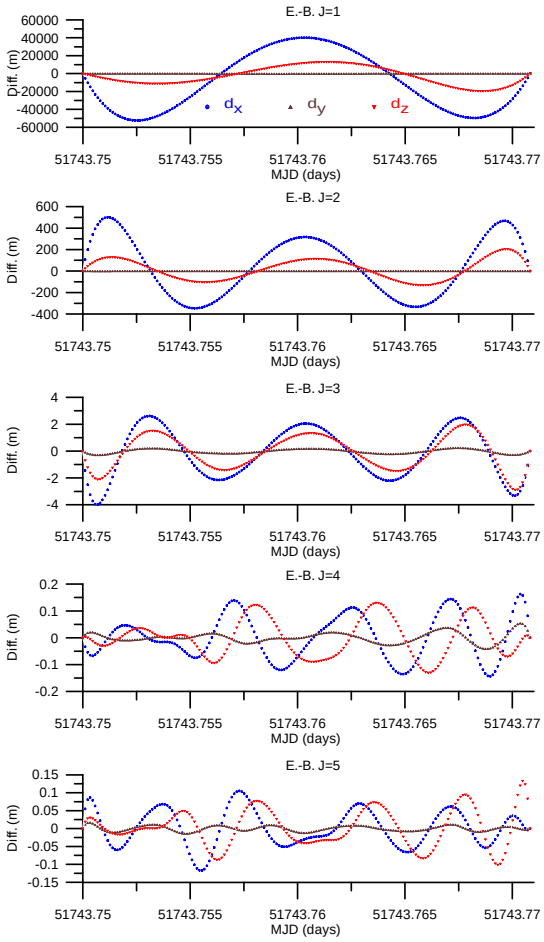

Figure 5.11: Remainder function $\mathbf{R}_P(\tau)$ based on $\bar{\mathbf{r}}(\tau)$ (reference motion: *straight line* mode) for least squares fits of $\mathbf{d}_P^J(\tau)$ with indices J=1,2,3,4,5 for an Earth gravity field model up to degree and order N_F =300.

N_R =30 shows similar results as in the case of a pure sine series approximation. In that case, the reference orbit obviously shows a similar approximation quality as the Euler-Bernoulli polynomial series up to degree J_{max} =4 so that the approximation of the remainder function in terms of sine series is approximately identical. Because of the fact that the computation of the dynamical reference orbit is much more costly than the use of an ellipse as reference motion the latter one should be preferred.

5.4.2 Dynamical Restrictions on the Kinematical Orbit Parameters

5.4.2.1 Euler and Bernoulli Polynomial Coefficients and the Derivatives of the Position Function at the Orbit Boundaries

As outlined in sections 5.2 and 5.3, there is a functional dependency between the coefficients of the Euler and Bernoulli polynomials and the derivatives of the difference function $\mathbf{d}(t)$ at the boundaries of a satellite arc. This is a first dynamical restriction on the coefficients of the Euler-Bernoulli polynomials if these derivatives are derived from the force function acting on the satellite. This is obvious for the second derivatives which

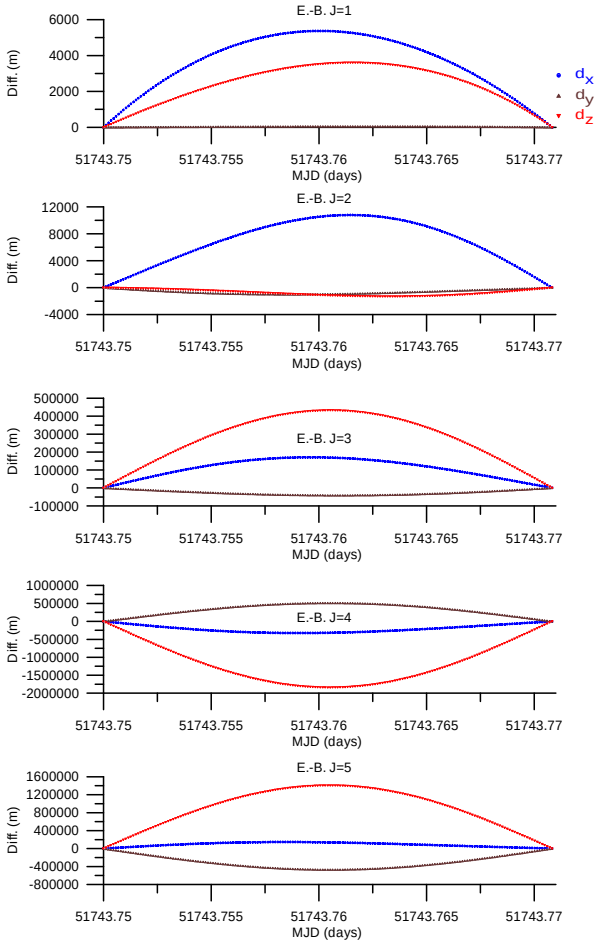

Figure 5.12: Series contributions of the separate degrees j=1,2,3,4 and 5 to the sum $\mathbf{d}_P^J(\tau)$ based on $\bar{\mathbf{r}}(\tau)$ (reference motion: *ellipse* mode) for an Earth gravity field model up to degree and order N_F =300.

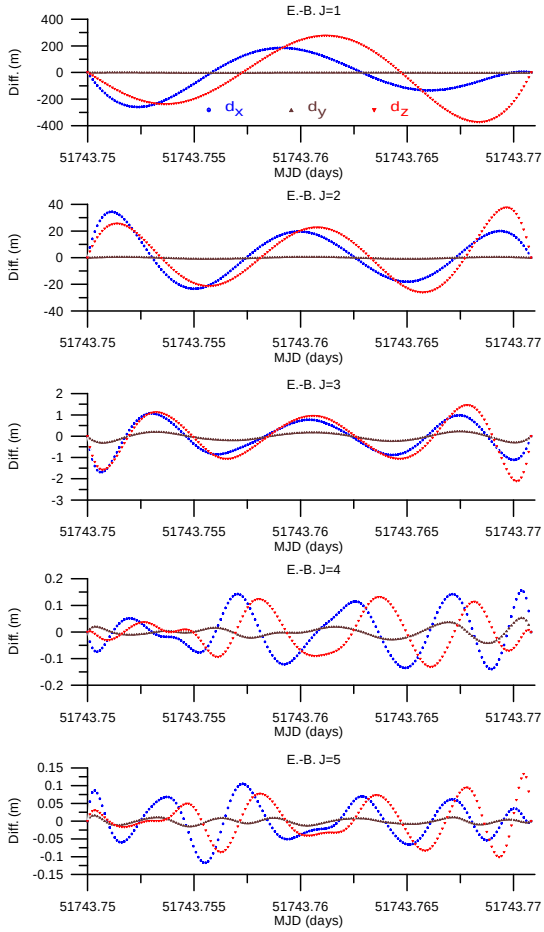

Figure 5.13: Remainder function $\mathbf{R}_P(\tau)$ based on $\bar{\mathbf{r}}(\tau)$ (reference motion: *ellipse* mode) for least squares fits of $\mathbf{d}_P^J(\tau)$ with indices J=1,2,3,4,5 for an Earth gravity field model up to degree and order N_F =300.

correspond to the force functions at the boundaries. Higher derivatives can be derived from the force function model as well. The relations are given by Eq. (5.75) for the coefficients of the Euler polynomials,

$$\mathbf{e}_{2j} = \frac{1}{2(2j)!}\left(\mathbf{d}^{[2j]}(1) + \mathbf{d}^{[2j]}(0)\right),$$

and by Eq. (5.76) for the coefficients of the Bernoulli polynomials,

$$\mathbf{b}_{2j+1} = \frac{1}{(2j+1)!}\left(\mathbf{d}^{[2j]}(1) - \mathbf{d}^{[2j]}(0)\right).$$

From these formulae it is easy to derive the derivatives of $\mathbf{d}(t)$, $\mathbf{d}^{(2j)}(t)$ with $j = 1, 2, 3, 4, ...$, at t_A of the arc, Eq. (5.84),

$$\mathbf{d}^{(2j)}(t_A) = \frac{2(2j)!\mathbf{e}_{2j} - (2j+1)!\mathbf{b}_{2j+1}}{2T^{2j}},$$

and at t_B, Eq. (5.85),

$$\mathbf{d}^{(2j)}(t_B) = \frac{2(2j)!\mathbf{e}_{2j} + (2j+1)!\mathbf{b}_{2j+1}}{2T^{2j}}.$$

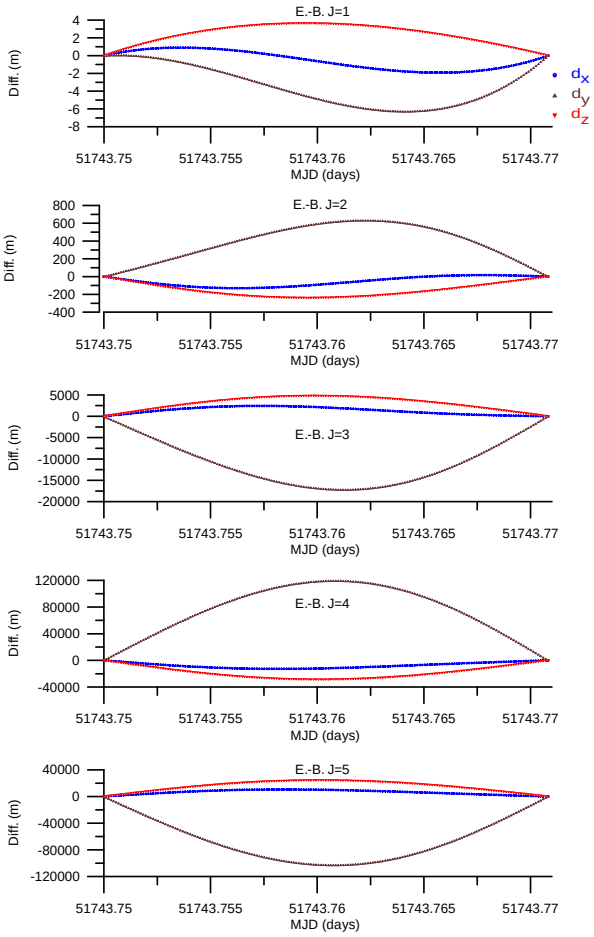

Figure 5.14: Series contributions of the separate degrees j=1,2,3,4 and 5 to the sum $\mathbf{d}_P^J(\tau)$ based on $\bar{\mathbf{r}}(\tau)$ (reference motion: *reference orbit* N_R=*30* mode) for an Earth gravity field model up to degree and order N_F =300.

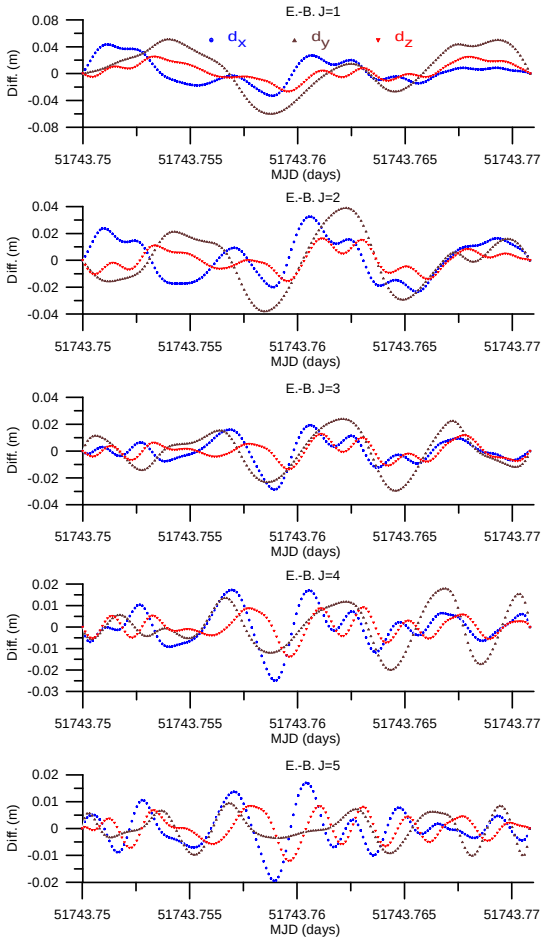

Figure 5.15: Remainder function $\mathbf{R}_P(\tau)$ based on $\bar{\mathbf{r}}(\tau)$ (reference motion: *dynamical reference orbit* N_R=*30* mode) for least squares fits of $\mathbf{d}_P^J(\tau)$ with indices J=1,2,3,4,5 for an Earth gravity field model up to degree and order N_F =300.

The Euler and Bernoulli polynomials of degree $2j$ and $2j+1$, respectively, are closely related to the time derivatives of the orbit function at the boundaries of the arc. This is the reason that these polynomials have to be considered together and should be characterized by the index j. Unfortunately, it is not easy to determine analytically higher derivatives in a simple straight forward way, except as mentioned in the case of the first derivatives, which correspond to the velocity and in the case of the second derivatives, the accelerations, which coincide with the specific force function at the arc boundaries. Numerically, one could approximate the differential quotients by the difference quotients. Because of subtractive cancellation and the resulting loss of significance the computations require a very high number of digits. Here the computations are performed by Martin Ettl (Fundamental Station Wettzell) who developed a computer code based on the LiDIA library with 200 digits after the comma (personal communication). This is certainly no possibility in real case applications but a way to check the numerical characteristics in this research. Therefore, in the following, we will determine the coefficients $\mathbf{e}_{2j}$ and $\mathbf{b}_{2j+1}$ by a least squares fit of the Euler-Bernoulli polynomials to a specific orbit limited by an upper index $J_{max} = 6$ according to Eq. (5.109),

$$\mathbf{d}_P^6(\tau) := \sum_{j=1}^{6} \mathbf{e}_{2j} E_{2j}(\tau) + \sum_{j=1}^{6} \mathbf{b}_{2j+1} B_{2j+1}(\tau) \approx \mathbf{r}(\tau) - \bar{\mathbf{r}}(\tau). \tag{5.181}$$

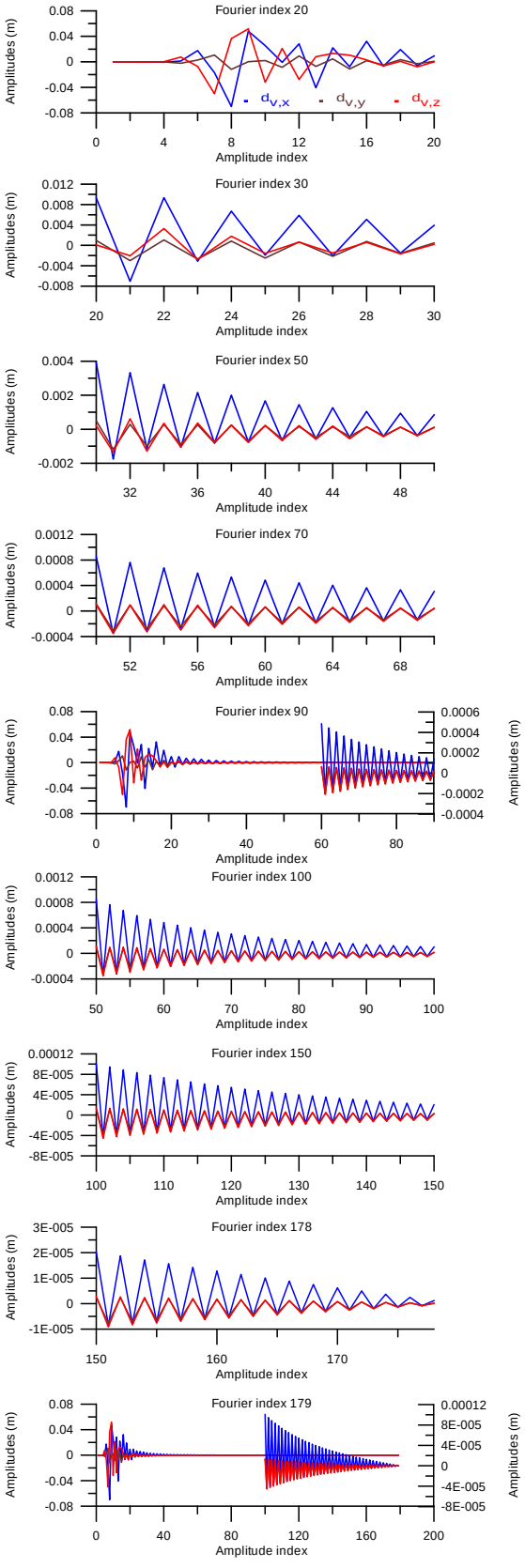

Figure 5.16: Spectrum of the Euler Bernoulli remainder function (reference motion: *straight line* mode, $J_{max} = 4$).

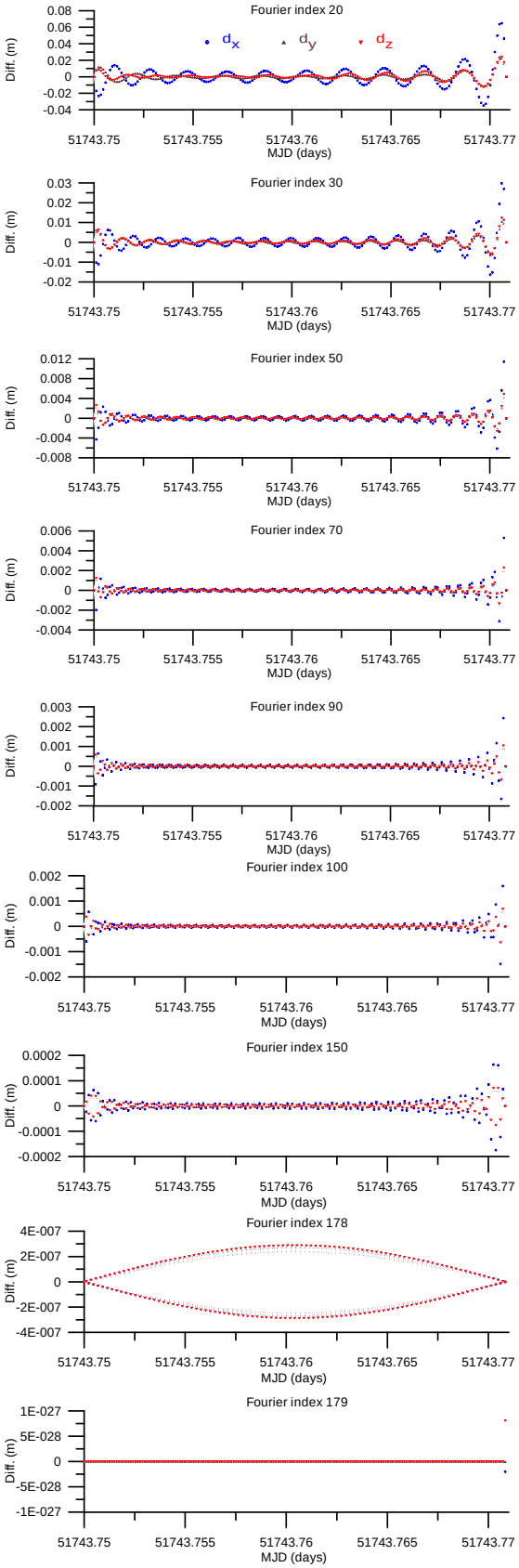

Figure 5.17: Residuals for the combined series Euler Bernoulli polynomials and sine series with various upper limits (reference motion: *straight line* mode, $J_{max} = 4$).

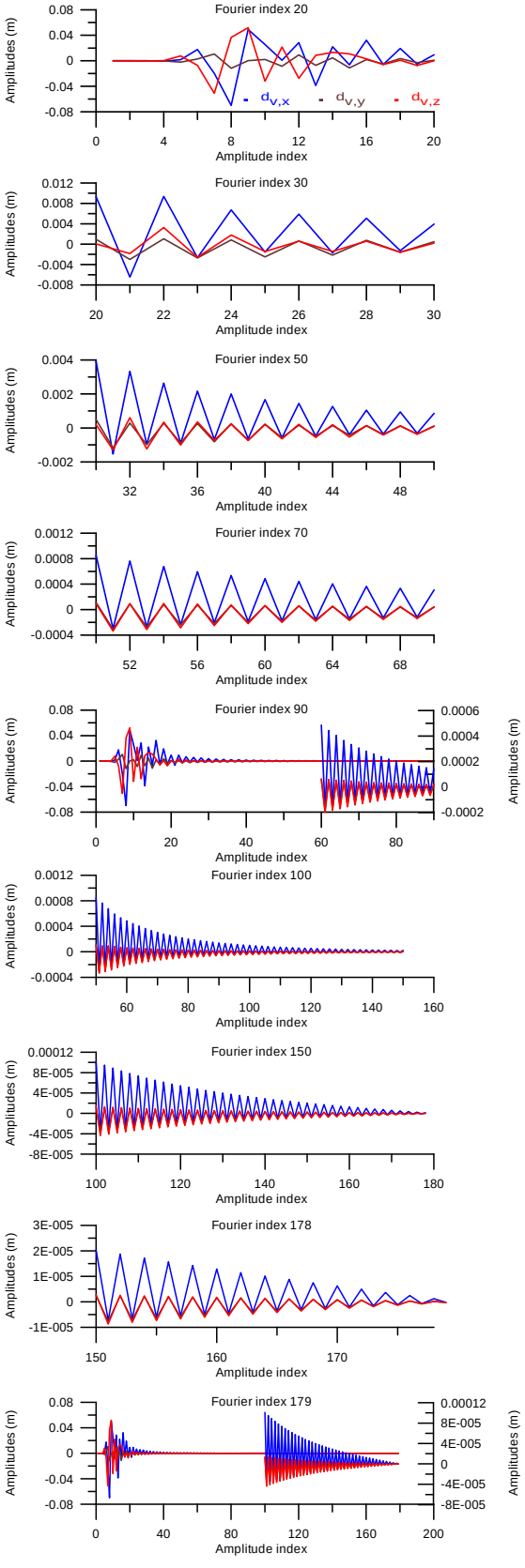

Figure 5.18: Spectrum of the Euler Bernoulli remainder function (reference motion: *ellipse* mode, $J_{max} = 4$).

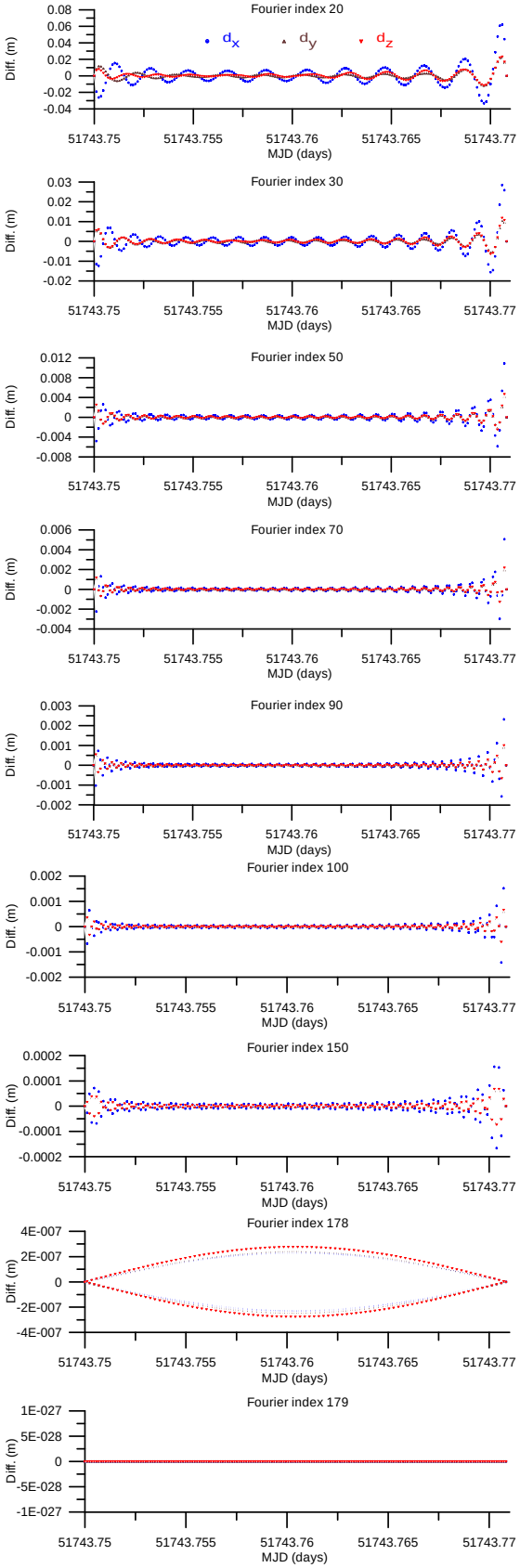

Figure 5.19: Residuals for the combined series Euler Bernoulli polynomials and sine series with various upper limits (reference motion: *ellipse* mode, $J_{max} = 4$).

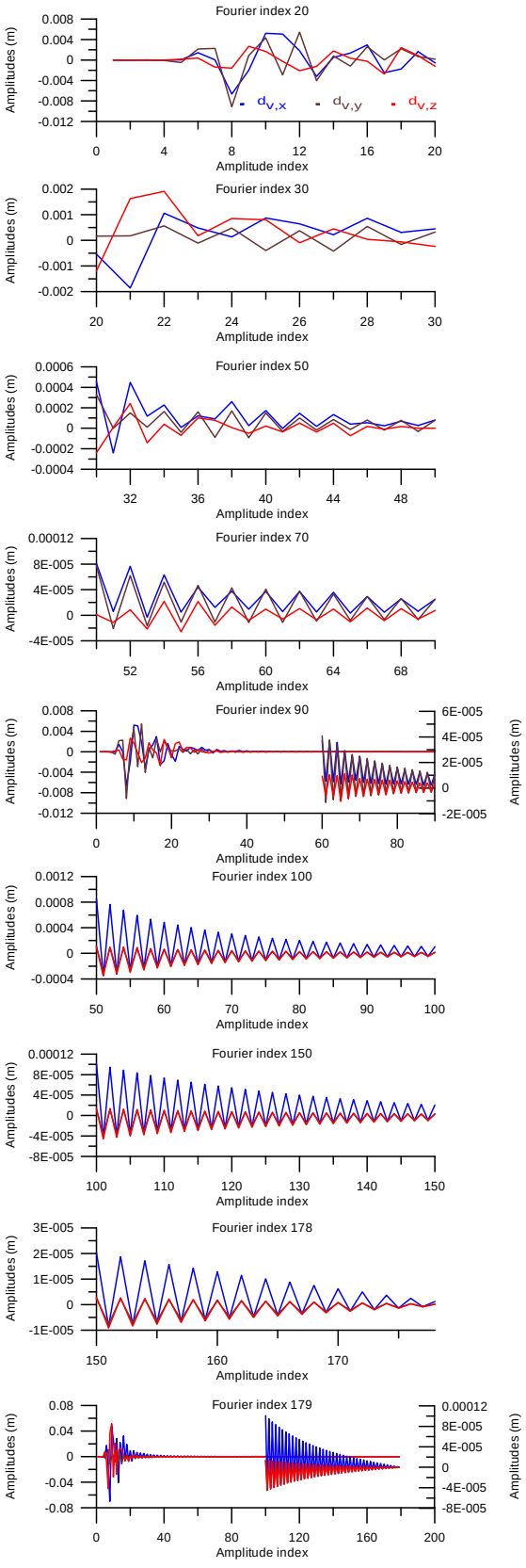

Figure 5.20: Spectrum of the Euler Bernoulli remainder function (reference motion: *dynamical reference orbit up to degree and order 30 (N_R=30)*, $J_{max} = 4$).

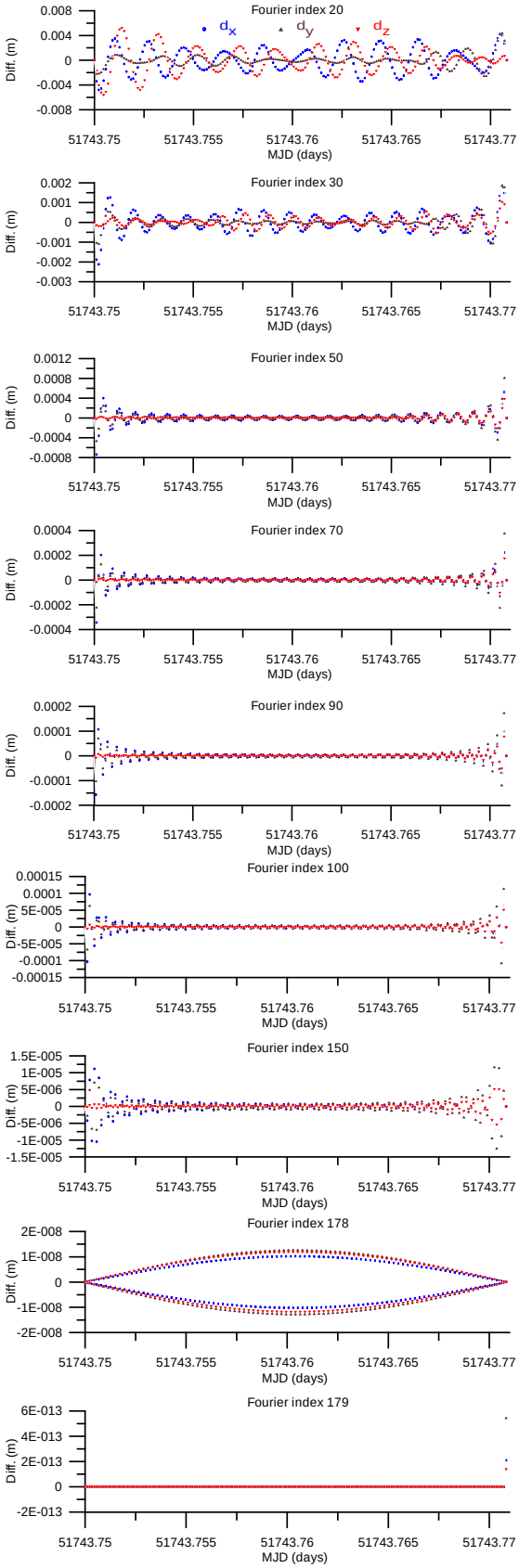

Figure 5.21: Residuals for the combined series Euler Bernoulli polynomials and sine series with various upper limits (reference motion: *dynamical reference orbit up to degree and order 30 (N_R=30)*, $J_{max} = 4$).

Then the derivatives $\mathbf{d}^{(2j)}(t)$ at t_A and t_B up to the 12^{th} order are determined from the Eqs. (5.84) and (5.85) and compared to the analytically or numerically precisely determined derivatives $\mathbf{d}^{(2j)}(t_A)$ and $\mathbf{d}^{(2j)}(t_B)$.

A simple first example of an orbit is a ***circular orbit***. In this case, the derivatives can be derived analytically and, therefore, the numerical values can be considered as error free "true" values. Here, a circular orbit with radius r=6774383.56175931 m and an arc length of 30 minute has been selected. The arc is located in the $y-z-$ plane. To derive the arc derivatives from the coefficients of the Euler and Bernoulli polynomials, the 30 minute arc is approximated by an Euler-Bernoulli polynomial with a maximum index $J_{max} = 6$, $\mathbf{d}_P^6(\tau)$. As reference motion, the "straight line" modification has been selected. The approximation quality of the circular arc by the Euler-Bernoulli polynomials is shown in Fig. 5.22(a). The residuals show an oscillating structure as expected but the mean deviations are very small and, therefore, the polynomial coefficients (Table 5.1) can be considered as reliable. The derivatives $\mathbf{d}^{(2j)}(t_A)$ and $\mathbf{d}^{(2j)}(t_B)$ are given in Table 5.2. This table shows that the derivatives become not acceptable from the index $j = 6$ upwards. Because of the fact that the "true" values are error-free, in this case the deviations are caused by the restricted numerical accuracy of the determination of the Euler-Bernoulli polynomial coefficients derived from the least squares fit.

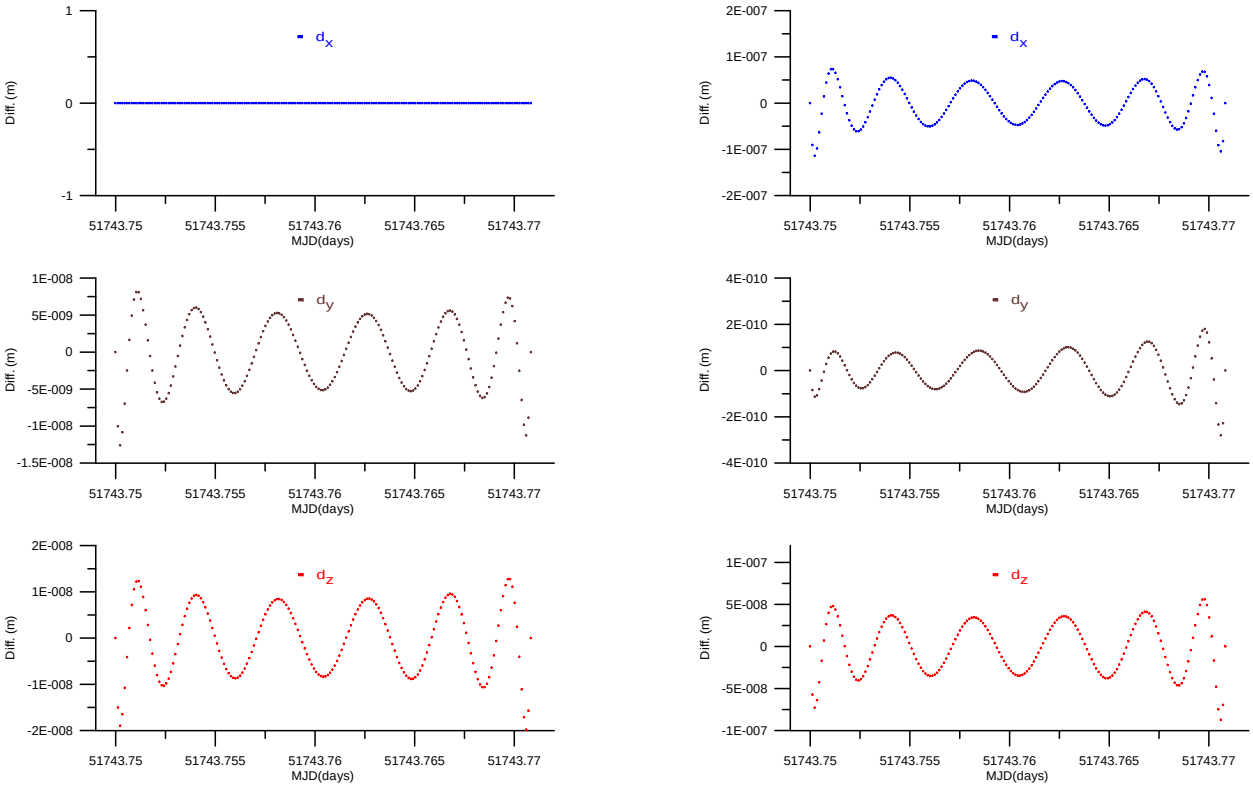

Figure 5.22: (a) Differences between the circular orbit and the approximations by a series in terms of Euler-Bernoulli polynomials, limited by an upper degree J_{max}=6, $\mathbf{d}_P^6(\tau)$ (reference motion: *straight line* mode) (b)Differences between the Keplerian orbit and the approximations by a series in terms of Euler-Bernoulli polynomial $\mathbf{d}_P^6(\tau)$ (reference motion: *ellipse* mode).

Another example is a ***Keplerian orbit***. In this case, the derivatives can be derived only numerically but with a very high reliability as mentioned above and, therefore, the numerical values can be considered also as error free "true" values, compared to the derivatives derived from the polynomial coefficients. Again, a 30 minute arc of the (nearly circular) Keplerian orbit has been selected. To determine the derivatives from the coefficients of the Euler and Bernoulli polynomials, the 30 minute arc is again approximated by an Euler-Bernoulli polynomial with a maximum index $J_{max} = 6$, $\mathbf{d}_P^6(\tau)$. The approximation quality of the Keplerian

Table 5.1: Coefficients of the Euler and Bernoulli polynomials for the circular orbit (reference motion: *straight line*).

j	$\mathbf{e}_{2j}$			$\mathbf{b}_{2j+1}$		
	x	y	z	x	y	z
1	0.000000E+00	-0.386570E+07	-0.628086E+07	0.000000E+00	0.680327E+07	-0.418724E+07
2	0.000000E+00	0.133820E+07	0.217425E+07	0.000000E+00	-0.141306E+07	0.869703E+06
3	0.000000E+00	-0.185296E+06	-0.301063E+06	0.000000E+00	0.139760E+06	-0.860191E+05
4	0.000000E+00	0.137653E+05	0.223653E+05	0.000000E+00	-0.806437E+04	0.496341E+04
5	0.000000E+00	-0.593884E+03	-0.964921E+03	0.000000E+00	0.302395E+03	-0.186116E+03
6	0.000000E+00	0.373499E+02	0.606847E+02	0.000000E+00	-0.952765E+01	0.586402E+01

Table 5.2: Derivatives of a circular arc at the arc boundaries: derived from the Euler-Bernoulli polynomial coefficients and the analytically derived values (reference motion: *straight line*).

j	$\mathbf{r}^{(2j)}(t_A)$ derived			$\mathbf{r}^{(2j)}(t_B)$ derived		
	x	y	z	x	y	z
1	0.000000E+00	-0.868556E+01	0.171679E-09	0.000000E+00	0.391308E+01	-0.775414E+01
2	0.000000E+00	0.111359E-04	0.209661E-12	0.000000E+00	-0.501704E-05	0.994174E-05
3	0.000000E+00	-0.142775E-10	0.769952E-16	0.000000E+00	0.643249E-11	-0.127464E-10
4	0.000000E+00	0.183142E-16	0.109670E-19	0.000000E+00	-0.824126E-17	0.163551E-16
5	0.000000E+00	-0.229393E-22	0.596783E-24	0.000000E+00	0.108675E-22	-0.202105E-22
6	0.000000E+00	0.411080E-28	0.934484E-29	0.000000E+00	-0.101776E-28	0.409098E-28
j	$\mathbf{r}^{(2j)}(t_A)$ true			$\mathbf{r}^{(2j)}(t_B)$ true		
1	0.000000E+00	-0.868556E+01	0.000000E+00	0.000000E+00	0.391308E+01	-0.775414E+01
2	0.000000E+00	0.111359E-04	0.000000E+00	0.000000E+00	-0.501704E-05	0.994174E-05
3	0.000000E+00	-0.142775E-10	0.000000E+00	0.000000E+00	0.643244E-11	-0.127464E-10
4	0.000000E+00	0.183055E-16	0.000000E+00	0.000000E+00	-0.824716E-17	0.163425E-16
5	0.000000E+00	-0.234699E-22	0.000000E+00	0.000000E+00	0.105738E-22	-0.209530E-22
6	0.000000E+00	0.300912E-28	0.000000E+00	0.000000E+00	-0.135569E-28	0.268643E-28

Table 5.3: Coefficients of the Euler and Bernoulli polynomials for the Keplerian orbit (reference motion: *ellipse* mode).

j	$\mathbf{e}_{2j}$			$\mathbf{b}_{2j+1}$		
	x	y	z	x	y	z
1	-0.122329E+05	0.128078E+03	0.837430E+04	0.735920E+04	-0.106743E+03	-0.846907E+04
2	-0.466065E+04	-0.704263E+02	-0.105860E+05	-0.765793E+04	0.111088E+03	0.881414E+04
3	0.558174E+04	0.238045E+02	0.568256E+04	0.318583E+04	-0.462239E+02	-0.366791E+04
4	-0.167750E+04	-0.530766E+01	-0.149444E+04	-0.750597E+03	0.109150E+02	0.867000E+03
5	0.693424E+03	0.153336E+01	0.541414E+03	0.979518E+02	-0.138269E+01	-0.108324E+03
6	0.900661E+02	0.221174E+00	0.728656E+02	-0.216322E+02	0.338186E+00	0.277158E+02

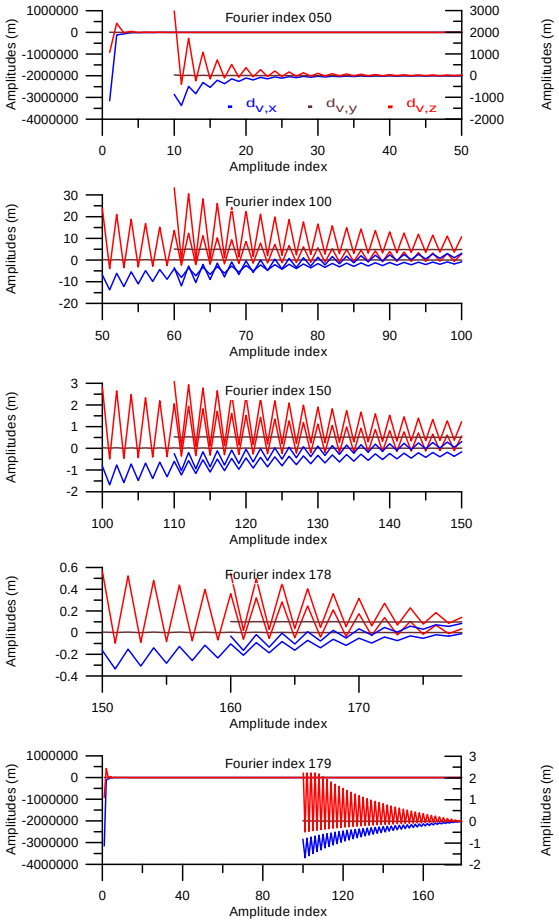

Figure 5.23: Spectrum of the Euler Bernoulli orbit based on the discrete Fourier analysis (reference motion: *straight line* mode, J_{max}=6).

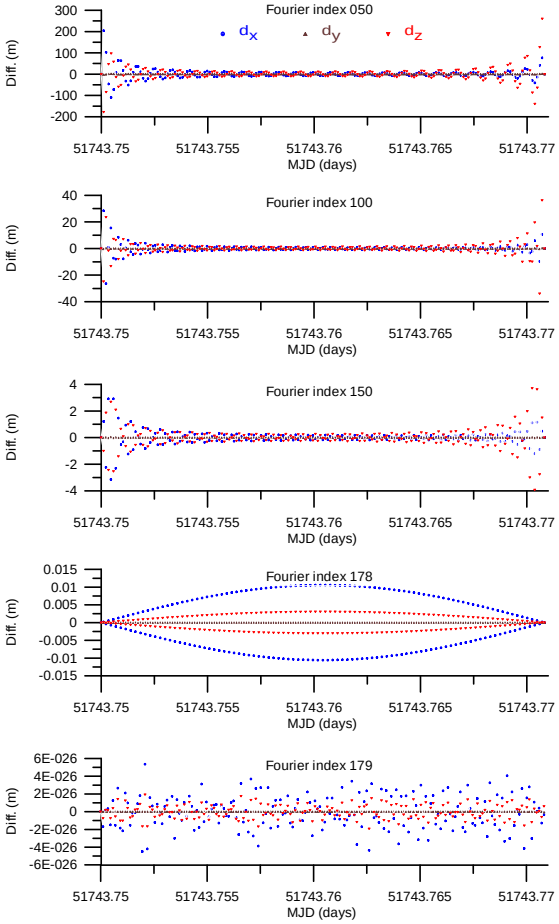

Figure 5.24: Residuals of the Euler Bernoulli orbit analyzed by the discrete Fourier (reference motion: *straight line* mode, J_{max}=6).

Table 5.4: Derivatives of the Keplerian orbit at the arc boundaries: derived from the Euler-Bernoulli polynomial coefficients and the "true" values (reference motion: *ellipse* mode).

j	$\mathbf{r}^{(2j)}(t_A)$ derived			$\mathbf{r}^{(2j)}(t_B)$ derived		
	x	y	z	x	y	z
1	0.643729E+01	-0.797184E-01	-0.583043E+01	0.231242E+01	0.620382E-01	0.838333E+01
2	-0.825714E-05	0.101869E-06	0.743413E-05	-0.302679E-05	-0.792694E-07	-0.107496E-04
3	0.105349E-10	-0.127994E-12	-0.925649E-11	0.417364E-11	0.995477E-13	0.136952E-10
4	-0.130665E-16	0.149604E-18	0.104239E-16	-0.675750E-17	-0.115640E-18	-0.169121E-16
5	0.191618E-22	-0.124952E-24	-0.437365E-23	0.188294E-22	0.107486E-24	0.223108E-22
6	0.729120E-28	-0.538715E-30	-0.239522E-28	-0.290320E-28	0.784369E-30	0.753867E-28
j	$\mathbf{r}^{(2j)}(t_A)$ true			$\mathbf{r}^{(2j)}(t_B)$ true		
1	0.643734E+01	-0.797181E-01	-0.583038E+01	0.231226E+01	0.620393E-01	0.838337E+01
2	-0.825720E-05	0.101868E-06	0.743405E-05	-0.302658E-05	-0.792709E-07	-0.107497E-04
3	0.105345E-10	-0.127993E-12	-0.925664E-11	0.417294E-11	0.995482E-13	0.136949E-10
4	-0.131410E-16	0.149651E-18	0.103901E-16	-0.681237E-17	-0.115932E-18	-0.169746E-16
5	0.147863E-22	-0.117499E-24	-0.581068E-23	0.161046E-22	0.862902E-25	0.184302E-22
6	-0.747261E-29	-0.217763E-30	-0.290883E-28	-0.572537E-28	0.223415E-30	-0.425683E-29

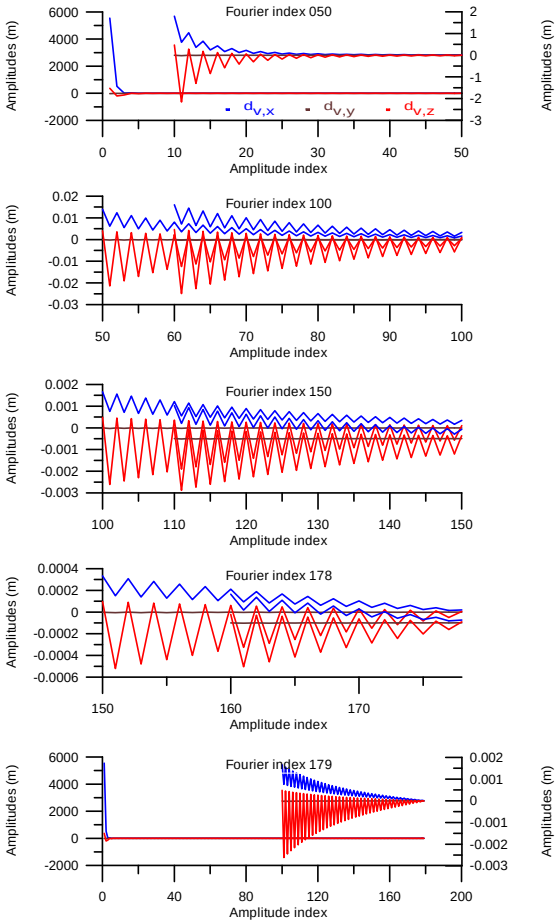

Figure 5.25: Spectrum of the Euler Bernoulli orbit based on the discrete Fourier analysis (reference motion: *ellipse* mode, J_{max}=6).

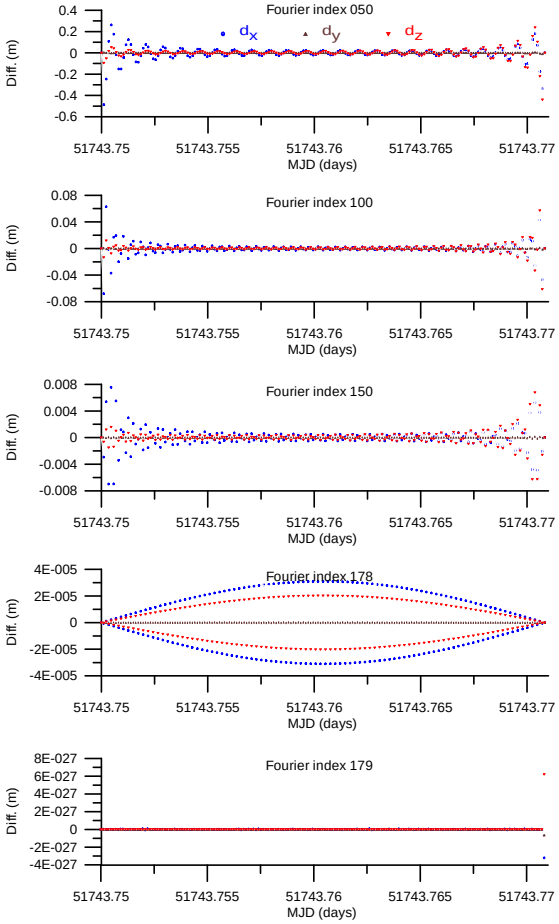

Figure 5.26: Residuals of the Euler Bernoulli orbit analyzed by the discrete Fourier (reference motion: *ellipse* mode, J_{max}=6).

Table 5.5: Coefficients of the Euler and Bernoulli polynomials for the orbit for a gravity field complete up to degree and order 20 (reference motion: *ellipse* mode).

j	$\mathbf{e}_{2j}$			$\mathbf{b}_{2j+1}$		
	x	y	z	x	y	z
1	-0.207985E+05	-0.222995E+03	-0.134916E+05	0.261890E+04	-0.304429E+03	-0.608830E+04
2	0.155647E+06	-0.837390E+04	0.121316E+06	-0.130295E+05	-0.960638E+04	0.572999E+05
3	0.235208E+07	-0.823831E+05	0.191847E+07	-0.574036E+06	-0.254568E+06	0.136351E+07
4	0.955080E+07	-0.370319E+06	0.820270E+07	-0.346470E+07	-0.133560E+07	0.666286E+07
5	0.669390E+07	-0.307651E+06	0.579023E+07	-0.402014E+07	-0.148441E+07	0.716359E+07
6	0.425513E+06	-0.200816E+05	0.368384E+06	-0.729290E+06	-0.266599E+06	0.127179E+07

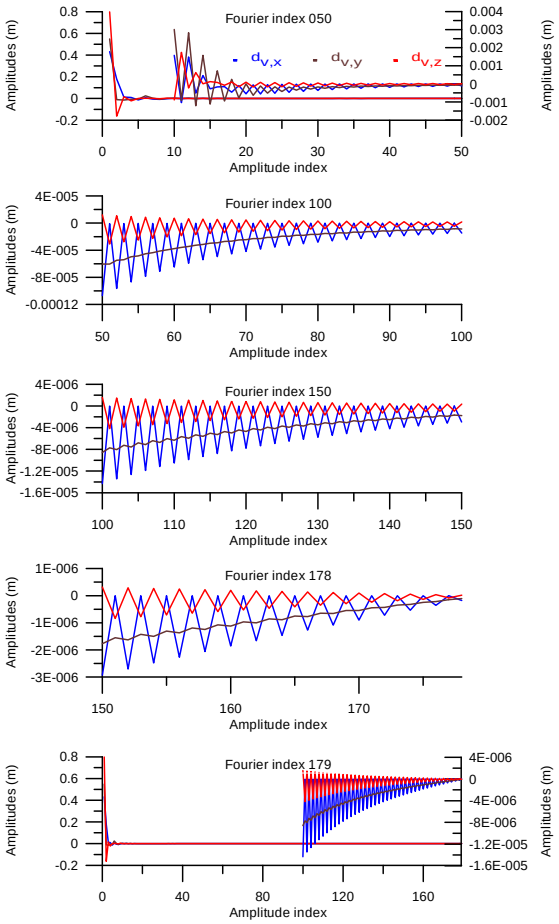

Figure 5.27: Spectrum of the Euler Bernoulli orbit based on the discrete Fourier analysis (reference motion: *dynamical reference orbit* N_R=*30* mode, J_{max}=6).

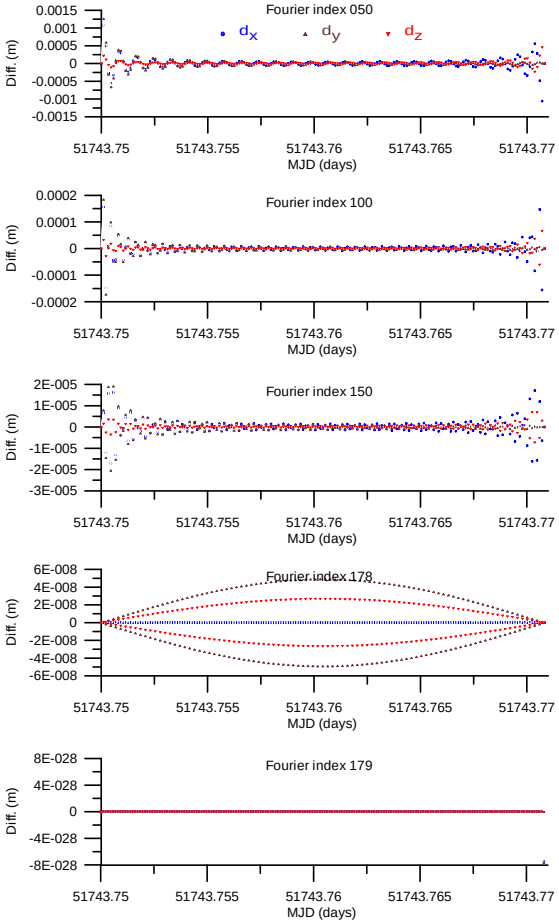

Figure 5.28: Residuals of the Euler Bernoulli orbit analyzed by the discrete Fourier (reference motion: *dynamical reference orbit* N_R=*30* mode, J_{max}=6).

Table 5.6: Derivatives of the orbit for a gravitational field complete up to degree and order 20 at the arc boundaries: derived from the Euler-Bernoulli polynomial coefficients and the "true" values (*ellipse* mode).

j	$\mathbf{r}^{(2j)}(t_A)$ derived			$\mathbf{r}^{(2j)}(t_B)$ derived		
	x	y	z	x	y	z
1	0.642626E+01	-0.796266E-01	-0.583696E+01	0.229820E+01	0.616869E-01	0.836091E+01
2	-0.783392E-05	0.138104E-06	0.743500E-05	-0.268048E-05	-0.153731E-06	-0.101398E-04
3	0.102924E-09	0.169859E-10	-0.700151E-10	0.110598E-10	-0.205029E-10	0.155421E-09
4	0.918537E-14	0.206370E-14	-0.795665E-14	-0.221492E-14	-0.233465E-14	0.139537E-13
5	0.292770E-18	0.798495E-19	-0.341602E-18	-0.156681E-18	-0.861031E-19	0.459305E-18
6	0.213899E-23	0.709214E-24	-0.327035E-23	-0.178664E-23	-0.725844E-24	0.357541E-23
j	$\mathbf{r}^{(2j)}(t_A)$ true			$\mathbf{r}^{(2j)}(t_B)$ true		
1	0.642595E+01	-0.796355E-01	-0.583684E+01	0.229793E+01	0.617670E-01	0.836053E+01
2	-0.815142E-05	0.102101E-06	0.759544E-05	-0.284848E-05	-0.782383E-07	-0.106185E-04
3	0.100836E-10	-0.313140E-12	-0.124344E-10	0.248519E-11	-0.315073E-12	0.136226E-10
4	0.626784E-16	0.583655E-16	0.365874E-15	-0.157287E-15	0.117856E-15	-0.115508E-14
5	-0.163904E-18	-0.146297E-19	-0.679462E-19	0.103142E-18	-0.271902E-19	0.760713E-18
6	0.139661E-21	0.272801E-23	0.316305E-24	-0.493618E-22	0.434053E-23	-0.450464E-21

arc by the Euler-Bernoulli polynomials is shown in Fig. 5.22(b) (ellipse mode). The mean deviations are very small and, therefore, the polynomial coefficients can be considered as reliable. The deviations show an oscillating character as expected, and are more or less identical for the straight line mode and the ellipse mode of the reference motion. The Euler-Bernoulli coefficients and the derivatives $\mathbf{r}^{(2j)}(t_A)$, $\mathbf{r}^{(2j)}(t_B)$ are shown in Tables 5.3 and 5.4. These tables show that the derivatives become not acceptable already from the index $j = 5$ upwards. The reason might be the same as above.

If the degree of the gravitational field is increased, resulting in a "rough" orbit then the least squares fit of the series in terms of Euler-Bernoulli polynomials becomes increasingly worse. In these cases, the derivatives of the arc at the boundary epochs do not coincide well with the derivatives based on a very precise numerical differentiation. This can be observed already in case of the "Main problem". Here the Euler-Bernoulli polynomial fit is still sufficient (Fig. 5.36), but the derivatives differ already for J_{max}=4 in contrast to the Keplerian orbit. In case of an orbit example determined for a gravitational field complete up to a spherical harmonic degree 20, the situation does not change very much. The derivatives differ again for an index J_{max} =4 and upwards. The results are given in Tables 5.5 and 5.6 for the ellipse mode of the reference motion. Fig. 5.37 demonstrates that the approximation quality of the series in terms of the Euler-Bernoulli polynomials up to degree J_{max} =6 is not better than a couple of centimeters.

5.4.2.2 Comparisons of Fourier Series Computations

The coefficients of the Fourier series convey directly a relation to the force function model, see e.g. Eq. (5.13). A similar relation is important also for the representation of the orbit in terms of Euler and Bernoulli polynomials. In Sec. 5.3.2.2, it is shown that the Fourier coefficients can be expressed in terms of the coefficients of the Euler and Bernoulli polynomials, e.g. theoretically by Eqs. (5.99) and (5.100), and as an example by Eq. (5.129) for an upper polynomial degree 5 (i.e. $J_{max} = 2$), and finally for the general case in Eq. (5.132). It should be pointed out already here, that the series in terms of Euler-Bernoulli polynomials can be represented by an infinite series of sine coefficients. The approximation quality of this sine series to represent the real orbit is certainly limited by the approximation quality of the Euler-Bernoulli polynomials. In the following, the numerical properties of the direct Fourier analysis and the procedure based on a prior determination of the Euler-Bernoulli polynomial coefficients will be investigated.

Sine analysis of the difference function: According to Eq. (5.39), the solution series Eq. (5.9) or Eq. (5.19) represents a Fourier series of the difference function,

$$\mathbf{d}(\tau) = \mathbf{r}(\tau) - \bar{\mathbf{r}}(\tau) = \sum_{\nu=1}^{\infty} \mathbf{d}_\nu \sin(\nu\pi\tau) = \mathbf{d}_F^{\infty}(\tau).$$

The Fourier coefficients $\mathbf{d}_\nu$ of the function $\mathbf{d}(\tau)$,

$$\mathbf{d}_\nu = 2 \int_{\tau'=0}^{1} \mathbf{d}(\tau)\ \sin(\nu\pi\tau')\ d\tau',$$

can be directly determined by a Fourier analysis according to Eq. (5.51)

$$\mathbf{d}_\nu \approx \frac{2}{K+1} \sum_{k=1}^{K} \mathbf{d}(\tau_k)\ \sin\left(\frac{\nu\pi k}{K+1}\right),$$

if the function $\mathbf{d}(\tau)$ is given discrete at a regular sampling rate of τ_k (see Eq. (5.52)),

$$\mathbf{d}(\tau_k) \quad \text{with} \quad \tau_k = \frac{k}{K+1}, \quad k = 1, 2, 3, ..., K, \quad \tau_k \in]\,0, 1\,[.$$

Because of the orthogonality relation of the discretized sine functions as basis functions, the coefficients $\mathbf{d}_\nu$ up to an upper index of $n = K$ can be determined rigorously in case of a regular equidistant sampling. In case of an upper summation index n and a remainder term $\mathbf{R}_F(\tau)$, we can write according to Eq. (5.94),

$$\mathbf{d}(\tau) = \mathbf{r}(\tau) - \bar{\mathbf{r}}(\tau) = \mathbf{d}_F^{n}(\tau) + \mathbf{R}_F(\tau) = \mathbf{d}_F^{\infty}(\tau),$$

with the remainder term $\mathbf{R}_F(\tau)$ according to Eq. (5.95),

$$\mathbf{R}_F(\tau) = \sum_{\nu=n+1}^{\infty} \mathbf{d}_\nu \sin(\nu\pi\tau).$$

The minimal quadratic error for the coordinates reads in this case according to Eq. (5.48),

$$\int_0^1 \left(d_i(\tau) - d^n_{F,i}(\tau)\right)^2 d\tau = \int_0^1 R^2_{F,i} d\tau = \int_0^1 \left(d_i(\tau)\right)^2 d\tau - \frac{1}{2}\sum_{\nu=1}^{n} d^2_{\nu,i}. \tag{5.182}$$

It should be pointed out that the sine coefficients derived from an "error free" orbit model corresponding to a gravitational field model are rigorous because of the orthogonality properties of the (discrete) sine functions. This means, they fulfill also the Eq. (5.13) etc. and can be considered as "true" reference values for the following considerations.

Spectral representation of Euler and Bernoulli polynomials: If the coefficients of the Euler and Bernoulli polynomials are determined, e.g. by an approximation procedure according to Eq. (5.119), then the Fourier coefficients can be determined according to Eqs. (5.99) and (5.100), respectively,

$$\mathbf{d}_{2\nu} = \sum_{j=1}^{J} \frac{2(-1)^{j+1}(2j+1)!}{(2\nu\pi)^{2j+1}} \mathbf{b}_{2j+1} + \mathbf{R}_{2\nu},$$

and

$$\mathbf{d}_{2\nu-1} = \sum_{j=1}^{J} \frac{4(-1)^{j}(2j)!}{(2\nu-1)^{2j+1}\pi^{2j+1}} \mathbf{e}_{2j} + \mathbf{R}_{2\nu-1},$$

with the remainder terms $\mathbf{R}_{2\nu}$ and $\mathbf{R}_{2\nu-1}$. In practical applications, one has to disregard these remainder terms. The coefficients up to index J_{max}=6 can be written for even indices 2ν:

$$\begin{aligned} \mathbf{d}_{2\nu} &\approx \sum_{j=1}^{6} \frac{2(-1)^{j+1}(2j+1)!}{(2\nu\pi)^{2j+1}} \mathbf{b}_{2j+1} = \\ &= \frac{3}{2(\nu\pi)^3}\mathbf{b}_3 - \frac{15}{2(\nu\pi)^5}\mathbf{b}_5 + \frac{315}{4(\nu\pi)^7}\mathbf{b}_7 - \frac{2835}{2(\nu\pi)^9}\mathbf{b}_9 + \frac{155925}{4(\nu\pi)^{11}}\mathbf{b}_{11} - \frac{6081075}{4(\nu\pi)^{13}}\mathbf{b}_{13}, \end{aligned} \tag{5.183}$$

and for coefficients with odd indices $2\nu - 1$,

$$\begin{aligned} \mathbf{d}_{2\nu-1} &\approx \sum_{j=1}^{6} \frac{4(-1)^{j}(2j)!}{(2\nu-1)^{2j+1}\pi^{2j+1}} \mathbf{e}_{2j} = \\ &= -\frac{8}{(2\nu-1)^3\pi^3}\mathbf{e}_2 + \frac{96}{(2\nu-1)^5\pi^5}\mathbf{e}_4 - \frac{2880}{(2\nu-1)^7\pi^7}\mathbf{e}_6 + \\ &+ \frac{161280}{(2\nu-1)^9\pi^9}\mathbf{e}_8 - \frac{14515200}{(2\nu-1)^{11}\pi^{11}}\mathbf{e}_{10} + \frac{1916006400}{(2\nu-1)^{13}\pi^{13}}\mathbf{e}_{12}. \end{aligned} \tag{5.184}$$

Because of the fact that the remainder terms of the direct Fourier analysis, Eq. (5.95),

$$\mathbf{R}_F(\tau) = \sum_{\nu=n+1}^{\infty} \mathbf{d}_\nu \sin(\nu\pi\tau), \tag{5.185}$$

and those of the spectra of the Euler-Bernoulli polynomials, Eq. (5.101), for J_{max} =6

$$\mathbf{R}_{2\nu} = \sum_{j=7}^{\infty} \frac{2(-1)^{j+1}(2j+1)!}{(2\nu\pi)^{2j+1}} \mathbf{b}_{2j+1} = \beta \frac{2}{(2\nu\pi)^{14}} \int_{\tau'=0}^{1} \mathbf{d}^{[14]}(\tau') \, \sin 2\nu\pi\tau' d\tau', \tag{5.186}$$

and Eq. (5.102), respectively, for J_{max}=6

$$\mathbf{R}_{2\nu-1} = \sum_{j=7}^{\infty} \frac{4(-1)^j(2j)!}{(2\nu-1)^{2j+1}\pi^{2j+1}}\mathbf{e}_{2j} = \beta\frac{2}{(2\nu-1)^{14}\pi^{14}} \int_{\tau'=0}^{1} \mathbf{d}^{[14]}(\tau')\ \sin(2\nu-1)\pi\tau' d\tau', \tag{5.187}$$

are different, we cannot expect identical results as derived from either the force function or by a sine analysis, Eq. (5.185).

Before we discuss the "real orbit" simulations, we will investigate the error of a simplified determination of the coefficients $\mathbf{d}_{2\nu}$ and $\mathbf{d}_{2\nu-1}$ according to the Eqs. (5.183) and (5.184). As already mentioned in Sec. 5.3.2.2, the coefficients of the Fourier series up to index n can be determined from the coefficients of the Euler-Bernoulli, e.g. up to degree $J_{max} = 6$ according to Eq. (5.132)

$$\begin{pmatrix} \mathbf{d}_1 \\ \vdots \\ \mathbf{d}_n \end{pmatrix} = \begin{pmatrix} I_1^1 & \cdots & I_1^{13} \\ \vdots & \ldots & \vdots \\ I_n^1 & \cdots & I_n^{13} \end{pmatrix} \begin{pmatrix} (\mathbf{E}_c^{13})^T & (\mathbf{B}_c^{13})^T \end{pmatrix} \begin{pmatrix} \mathbf{e}_{12} \\ \mathbf{b}_{13} \end{pmatrix},$$

in principle, up to an arbitrarily chosen upper index n. The same results can be achieved by determining the coefficients $\mathbf{d}_\nu$ numerically by a discrete Fourier analysis according to Eq. (5.51). In the following, a 30 minute arc has been simulated based on a gravity field model up to a maximal spherical harmonic degree of N_F =300. As reference motions, the straight line, the ellipse mode and a dynamical reference arc based on a gravity field up to degree N_R=30 has been selected. To these three cases, an Euler-Bernoulli polynomial with J_{max} =6 has been fitted by a least squares adjustment procedure. Then only the Euler-Bernoulli function has been developed in a Fourier series. This has been performed first by the analytical determination according to Eqs. (5.183) and (5.184) and then directly. The direct Fourier analysis has been performed, based on a sampling rate of 10 seconds. For the present example, the interpolation case has been applied, so that $n = K = 179$ nodal points (except the boundary values) are available according to Eq. (5.52),

$$\mathbf{d}(\tau_k) \quad \text{with} \quad \tau_k = \frac{k}{K+1}, \quad k = 1, 2, 3, ..., K, \quad \tau_k \in]\ 0, 1\ [,$$

resulting in 179 amplitudes according to Eq. (5.51),

$$\mathbf{d}_\nu \approx \frac{2}{K+1}\sum_{k=1}^{K} \mathbf{d}(\tau_k)\ \sin\left(\frac{\nu\pi k}{K+1}\right).$$

The differences for the straight line mode, the ellipse mode and the dynamical reference orbit mode are shown in Figs. 5.29(a), 5.29(b) and 5.29(c). The figures clearly show increasing differences with increasing index ν. The absolute differences depend also on the size of the amplitudes. But it is interesting to note that the relation between the approximated coefficients, derived according to Eqs. (5.183) and (5.184), $\mathbf{d}^a_{\nu,i}(i = 1, 2, 3)$ and derived numerically by discrete Fourier analysis, $\mathbf{d}^c_{\nu,i}(i = 1, 2, 3)$,

$$\frac{\mathbf{d}^a_{\nu,i}}{\mathbf{d}^c_{\nu,i}} = f(\nu), \tag{5.188}$$

follows the same error characteristic $f(\nu)$, independent of the coordinates and the mode of the reference motion and also independent of the coefficient, whether it is odd or even (Figs. 5.30 to 5.35). This result corresponds approximately with the functional dependency of the remainder functions Eqs. (5.186) and (5.187).

The convergence behavior of the Fourier series should be similar to the convergence of the simulated orbit. To demonstrate this, the differences are shown between the amplitudes of the orbit, determined on the one hand by discrete Fourier analysis according to Eq. (5.51) and on the other hand from the discrete Fourier analysis of the Euler-Bernoulli orbit (J_{max} =6). Fig. 5.38 shows the case for the straight line mode and Fig. 5.39 for the ellipse mode. The differences start with zero and become slightly larger with increasing

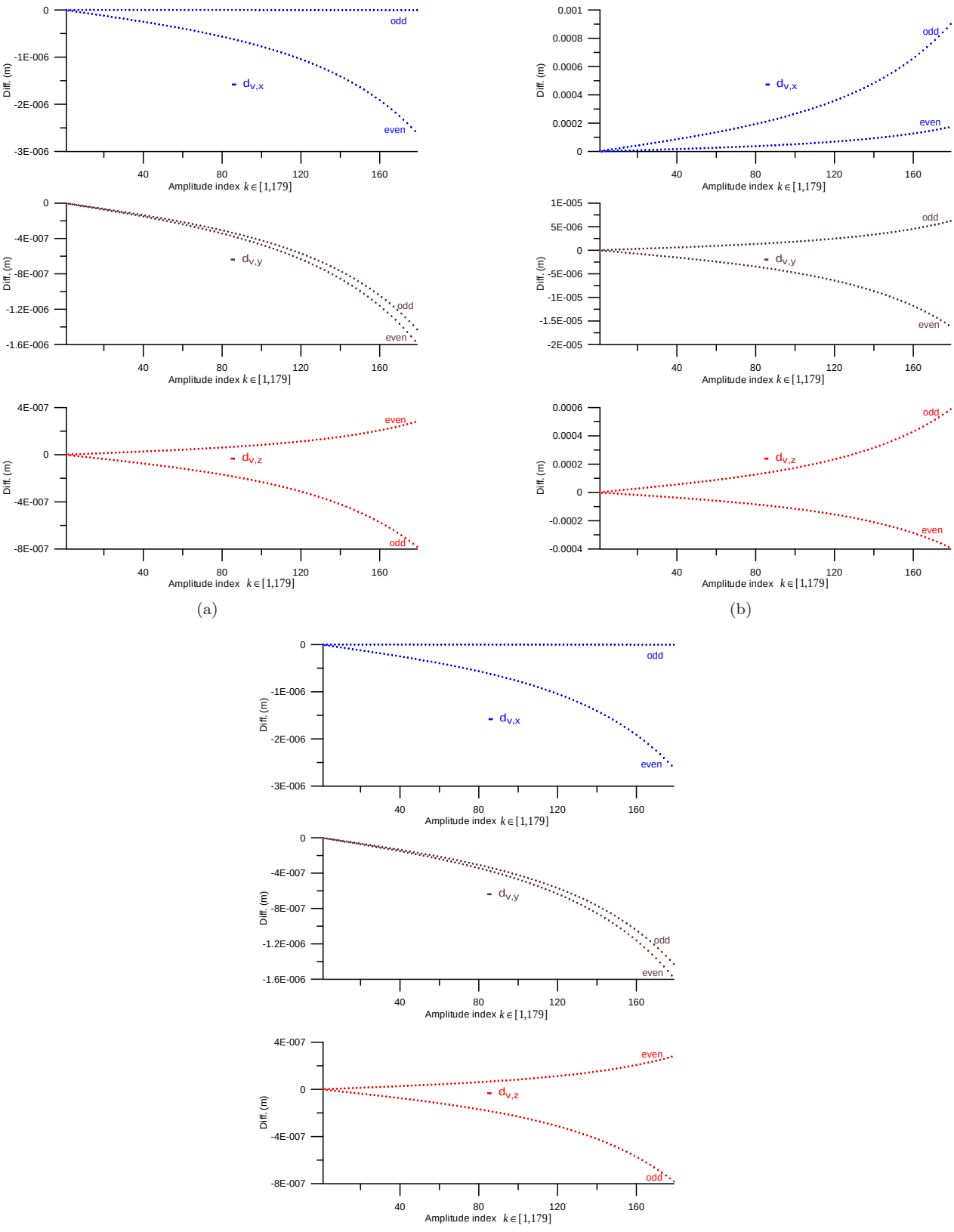

Figure 5.29: Effects of the remainder terms Eqs. (5.186) and (5.187): Differences of the spectra of an Euler-Bernoulli polynomial of degree J_{max}=6, determined by Eqs. (5.183) and (5.184) on the one hand and by discrete Fourier analysis according to Eq. (5.51) on the other hand ((a) for *straight line* mode (b) for *ellipse* mode (c) for *dynamical reference orbit* N_R=*30* mode).

index of the Fourier series. The residuals in the space domain derived by a Fourier synthesis are shown in Fig. 5.40; the upper index is selected in this case to $n = 179$. The residuals are rather large up to 2cm at the boundaries of the arc in accordance with the fact that the amplitudes differ especially in the high frequency part of the spectrum. If the limit of the Fourier series is extended to $n = 400$, then the residuals become smaller by one order as shown in Fig. 5.41. The residuals in these figures reflect the remainder term of the Fourier series (Eq. (5.94)). The test computations demonstrate the possibility to derive the Fourier spectrum based on the Euler-Bernoulli polynomial coefficients, in principle, up to an arbitrary degree.
On the other hand the inverse procedure can be used to determine also the coefficients of the Euler and Bernoulli polynomials according to Eq. (5.135) based on the spectrum of the satellite's arc in terms of directly derived Fourier amplitudes according to Eq. (5.51). This is an over-determined problem, because only $3 \cdot 12 = 24$ coefficients in case of an upper limit of $J_{max} = 6$ have to be determined by $3 \cdot 179$ amplitudes. The results are shown in the Tables 5.7 and 5.8 together with the (true) polynomial coefficients derived by a numerically very precise technique for the straight line and ellipse modes as explained in Sec. 5.4.2.1. If the Euler-Bernoulli polynomials are used to determine the ephemerides of the arc, then the result will slightly differ from the original positions as shown in Figs. 5.43 and 5.45 for the straight line and an ellipse modes, respectively.

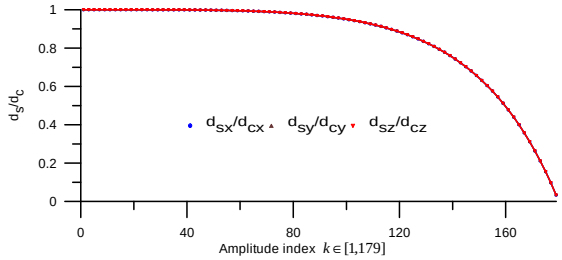

Figure 5.30: Error characteristic $f(\nu)$ of odd amplitudes (reference motion: *straight line* mode, J_{max}=6, N_F =300).

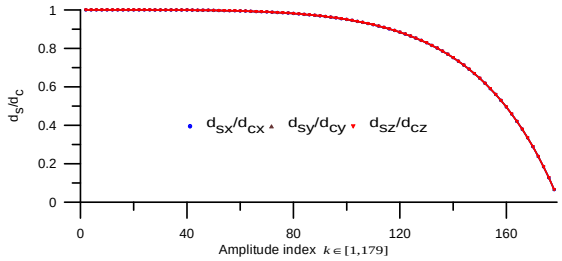

Figure 5.31: Error characteristic $f(\nu)$ of even amplitudes (reference motion: *straight line* mode, J_{max}=6, N_F =300).

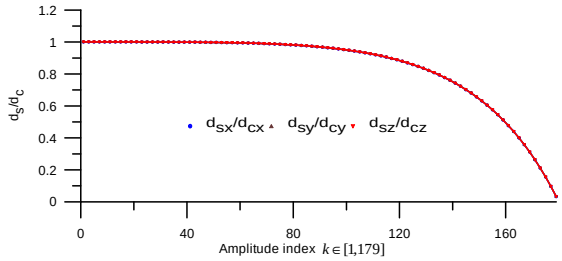

Figure 5.32: Error characteristic $f(\nu)$ of odd amplitudes (reference motion: *ellipse* mode, J_{max}=6, N_F =300).

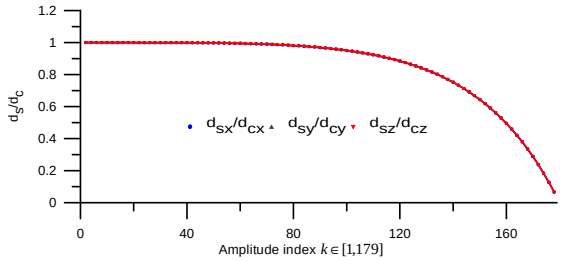

Figure 5.33: Error characteristic $f(\nu)$ of even amplitudes (reference motion: *ellipse* mode, J_{max}=6, N_F =300).

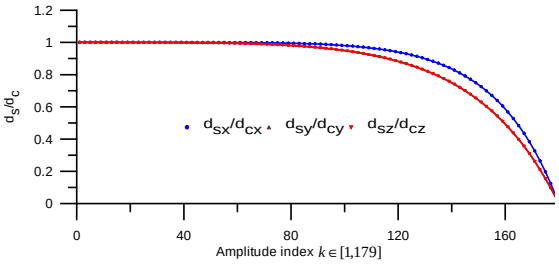

Figure 5.34: Error characteristic $f(\nu)$ of odd amplitudes (reference motion: *dynamical reference orbit* mode N_R=30, J_{max}=6, N_F =300).

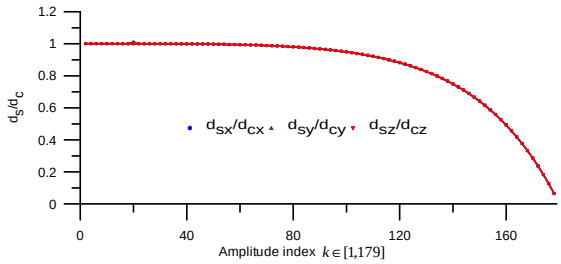

Figure 5.35: Error characteristic $f(\nu)$ of even amplitudes (reference motion: *reference orbit N_R=30 mode*, J_{max}=6, N_F =300).

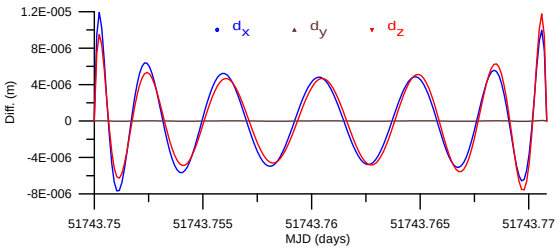

Figure 5.36: Differences between the orbit for a gravitational field complete up to degree 2 order 0 and the approximations by a series in terms of Euler-Bernoulli polynomial $\mathbf{d}_P^6(\tau)$ (reference motion: *ellipse* mode).

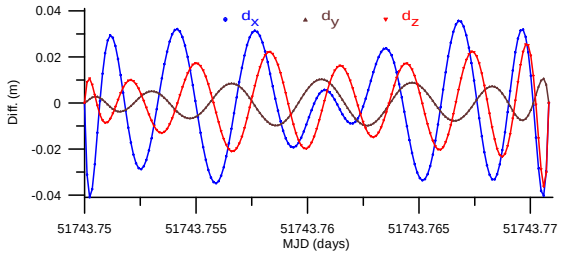

Figure 5.37: Differences between the orbit for a gravitational field complete up to degree and order 20 and the approximations by a series in terms of Euler-Bernoulli polynomial $\mathbf{d}_P^6(\tau)$ (reference motion: *ellipse* mode).

Table 5.7: Coefficients of the Euler-Bernoulli polynomials either determined by a least squares fit based on the (error free) ephemerides and derived from the sine coefficient according to Eq. (5.135) (reference motion: *straight line* mode, J_{max}=6, N_F=300).

j	$\mathbf{e}_{(2j)}$ (derived)			$\mathbf{b}_{(2j+1)}$ (derived)		
	x	y	z	x	y	z
1	0.706691E+07	-0.144490E+05	0.204437E+07	-0.222914E+07	0.763672E+05	0.766694E+07
2	-0.228500E+07	0.170542E+05	-0.589279E+06	0.455433E+06	-0.186582E+05	-0.152528E+07
3	0.290107E+07	0.347438E+06	0.220624E+07	-0.575009E+06	-0.119336E+06	0.175057E+07
4	0.101018E+08	0.122968E+07	0.917694E+07	-0.347575E+06	-0.727632E+06	0.756752E+07
5	0.703160E+07	0.793302E+06	0.654846E+07	-0.416333E+07	-0.844703E+06	0.803898E+07
6	0.446182E+06	0.497304E+05	0.417257E+06	-0.762230E+06	-0.153599E+06	0.142108E+07
j	$\mathbf{e}_{(2j)}$ (true)			$\mathbf{b}_{(2j+1)}$ (true)		
1	0.706576E+07	-0.144466E+05	0.204404E+07	-0.222849E+07	0.763449E+05	0.766471E+07
2	-0.245745E+07	0.174060E+05	-0.639163E+06	0.535126E+06	-0.213886E+05	-0.179938E+07
3	-0.296136E+06	0.353960E+06	0.128134E+07	0.929421E+06	-0.170880E+06	-0.342394E+07
4	-0.133528E+07	0.125301E+07	0.586838E+07	0.296407E+07	-0.948271E+06	-0.145824E+08
5	-0.741895E+06	0.809158E+06	0.429972E+07	0.234782E+07	-0.106779E+07	-0.143562E+08
6	-0.458014E+05	0.507340E+05	0.274934E+06	0.371884E+06	-0.192455E+06	-0.247972E+07

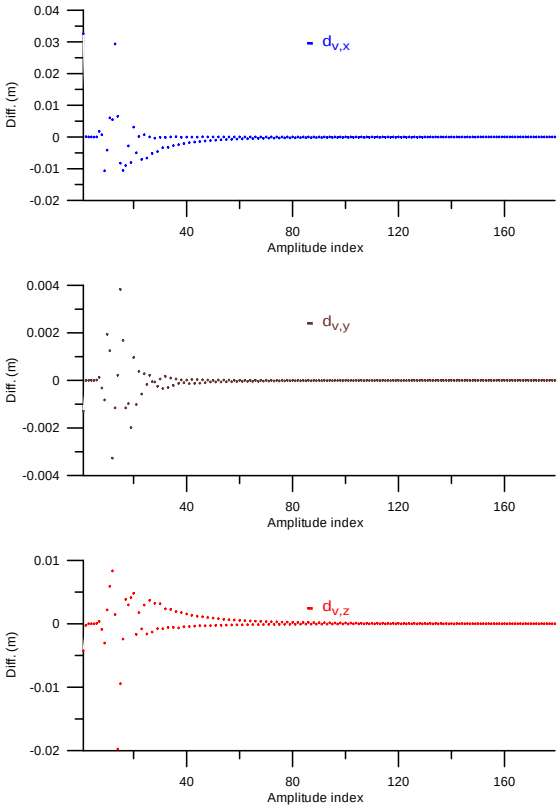

Figure 5.38: Differences between the amplitudes of the orbit, determined on the one hand by direct Fourier analysis according to Eq. (5.51) and on the other hand from the discrete Fourier analysis of the Euler-Bernoulli orbit (reference motion: *straight line* mode, $J_{max} = 6$, gravitational field degree N_F =300).

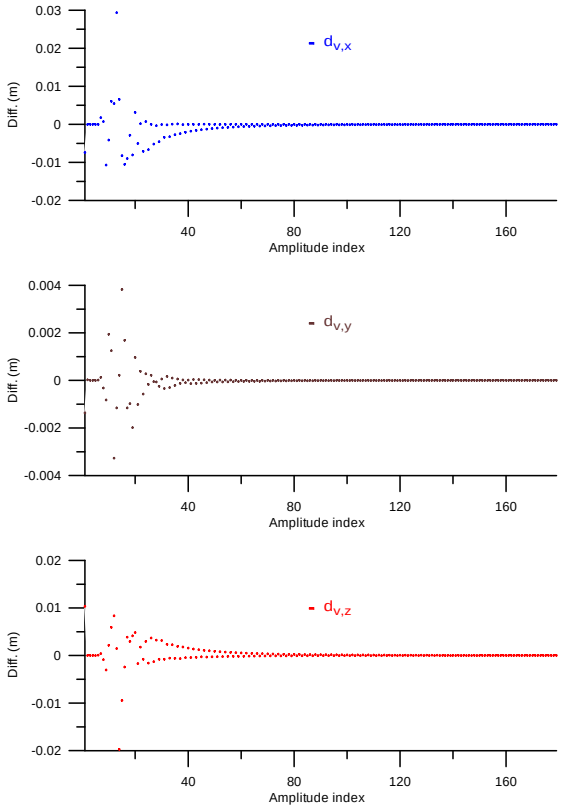

Figure 5.39: Differences between the amplitudes of the orbit, determined on the one hand by direct Fourier analysis according to Eq. (5.51) and on the other hand from the discrete Fourier analysis of the Euler-Bernoulli orbit (reference motion: *ellipse* mode, $J_{max} = 6$, gravitational field degree N_F =300).

Table 5.8: Coefficients of the Euler-Bernoulli polynomials either determined by a least squares fit based on the (error free) ephemerides and derived from the sine coefficient according to Eq. (5.135) (reference motion: *ellipse* mode, J_{max}=6, N_F=300).

j	$\mathbf{e}_{(2j)}$ (derived)			$\mathbf{b}_{(2j+1)}$ (derived)		
	x	y	z	x	y	z
1	-0.206947E+05	-0.141918E+03	-0.135193E+05	0.265025E+04	-0.247473E+03	-0.600679E+04
2	0.170146E+06	0.120982E+05	0.123577E+06	-0.842299E+04	-0.273456E+04	0.694690E+05
3	0.256089E+07	0.348125E+06	0.210747E+07	-0.529101E+06	-0.120912E+06	0.159274E+07
4	0.101271E+08	0.122963E+07	0.918428E+07	-0.347840E+07	-0.727541E+06	0.757663E+07
5	0.703051E+07	0.793304E+06	0.654814E+07	-0.416323E+07	-0.844707E+06	0.803864E+07
6	0.446251E+06	0.497303E+05	0.417277E+06	-0.762233E+06	-0.153598E+06	0.142109E+07
j	$\mathbf{e}_{(2j)}$ (true)			$\mathbf{b}_{(2j+1)}$ (true)		
1	-0.206914E+05	-0.141900E+03	-0.135171E+05	0.264948E+04	-0.247403E+03	-0.600510E+04
2	0.170640E+06	0.121009E+05	0.123904E+06	-0.851752E+04	-0.272596E+04	0.696755E+05
3	0.257006E+07	0.348175E+06	0.211354E+07	-0.530885E+06	-0.120749E+06	0.159663E+07
4	0.101599E+08	0.122980E+07	0.920601E+07	-0.348604E+07	-0.726847E+06	0.759328E+07
5	0.705278E+07	0.793424E+06	0.656291E+07	-0.417095E+07	-0.844005E+06	0.805547E+07
6	0.447660E+06	0.497379E+05	0.418211E+06	-0.763578E+06	-0.153476E+06	0.142402E+07

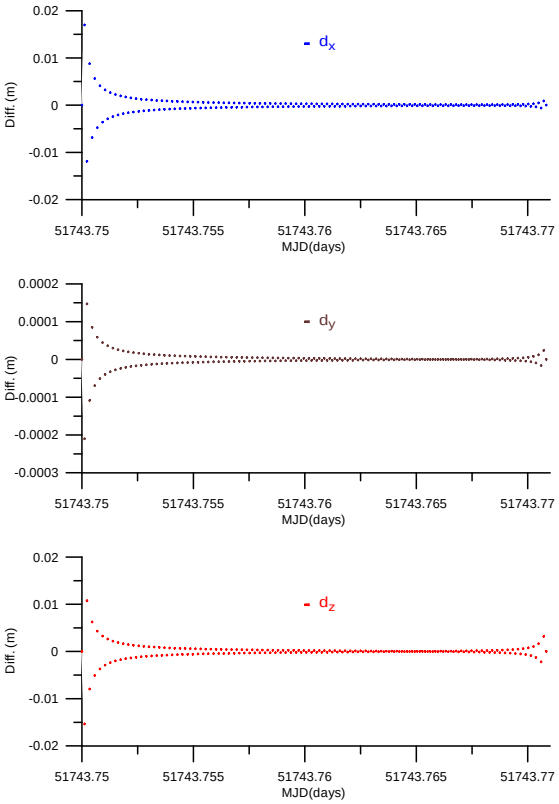

Figure 5.40: Residuals of the Fourier series with an upper summation limit of n=179 in space domain based on Eq. (5.132) with a maximal Euler-Bernoulli index $J_{max} = 6$ (reference motion: *ellipse* mode).

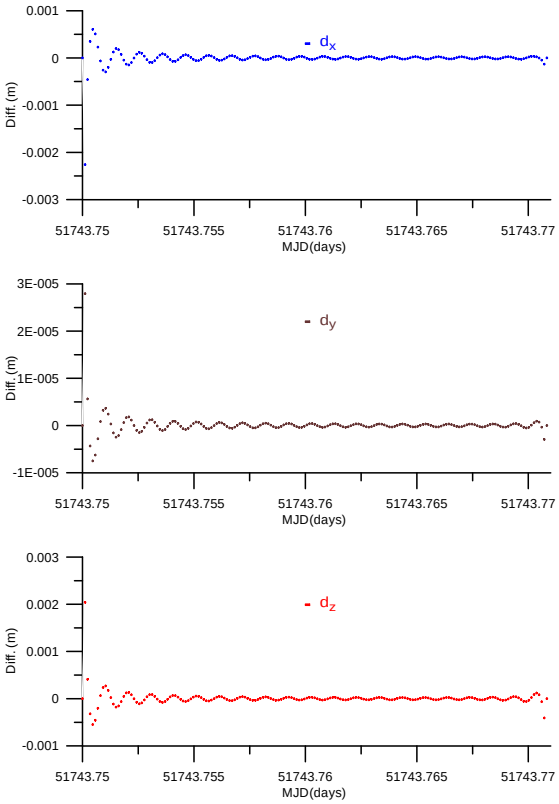

Figure 5.41: Residuals of the Fourier series with an upper summation limit of n=400 in space domain based on Eq. (5.132) with a maximal Euler-Bernoulli index $J_{max} = 6$ (reference motion: *ellipse* mode).

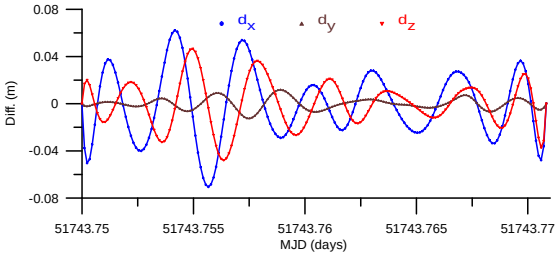

Figure 5.42: Residuals based on the least squares fit: observed orbit-E.B. polynomials (reference motion: *straight line* mode, J_{max}=6, N_F=300).

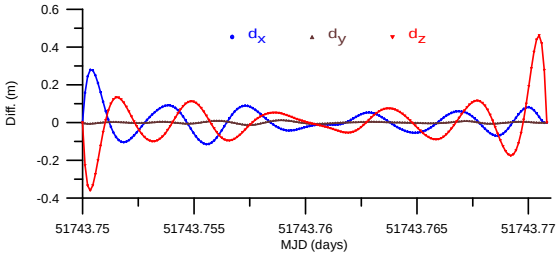

Figure 5.43: Residuals: observed orbit-E.B. polynomials based on Eq. (5.135)(reference motion: *straight line* mode, J_{max}=6, N_F=300).

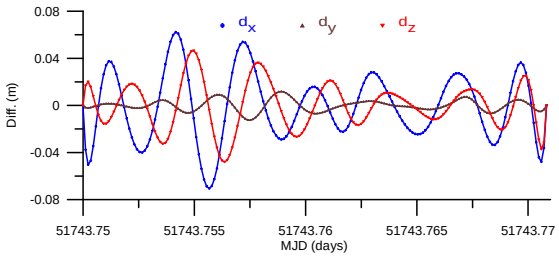

Figure 5.44: Residuals based on the least squares fit: observed orbit-E.B. polynomials (reference motion: *ellipse* mode, J_{max}=6, N_F=300).

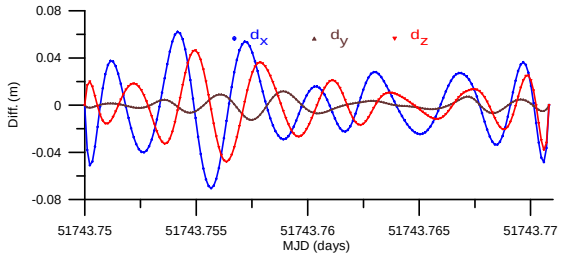

Figure 5.45: Residuals: observed orbit-E.B. polynomial based on Eq. (5.135)(reference motion: *ellipse* mode, J_{max}=6, N_F=300).

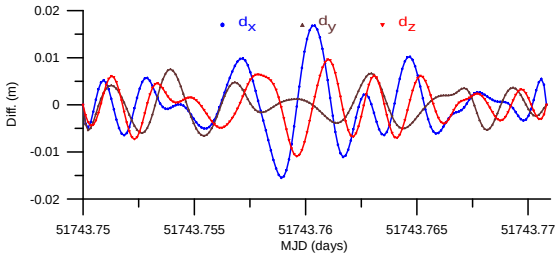

Figure 5.46: Position residuals of the ephemerides derived from the Euler-Bernoulli polynomials based on the least squares fit (reference motion: *dynamical reference orbit* N_R=*30*, J_{max}=6, N_F=300).

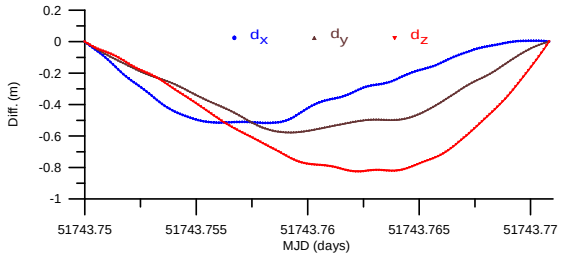

Figure 5.47: Position residuals of the ephemerides derived from the Euler-Bernoulli polynomials based on Eq. (5.135) (reference motion: *dynamical reference orbit* N_R=*30*, J_{max}=6, N_F=300).

Table 5.9: Coefficients of the Euler-Bernoulli polynomials either determined by a least squares fit based on the (error free) ephemerides and derived from the sine coefficient according to Eq. (5.135) (reference motion: *dynamical reference orbit* N_R=*30* mode, J_{max}=6, N_F=300).

j	$\mathbf{e}_{(2j)}$ (derived)			$\mathbf{b}_{(2j+1)}$ (derived)		
	x	y	z	x	y	z
1	0.359618E-01	0.330090E+02	0.181584E+02	-0.405017E+02	-0.246965E+02	0.434717E+01
2	-0.808657E+03	0.417723E+04	0.502471E+04	-0.752098E+04	-0.659277E+04	0.508468E+03
3	-0.130014E+05	0.629410E+05	0.111405E+06	-0.182863E+06	-0.175187E+06	0.430465E+04
4	-0.425381E+05	0.189597E+06	0.427631E+06	-0.897313E+06	-0.901560E+06	-0.800662E+03
5	-0.280497E+05	0.117783E+06	0.298447E+06	-0.967525E+06	-0.994583E+06	-0.122277E+05
6	-0.176688E+04	0.734101E+04	0.189671E+05	-0.172109E+06	-0.178230E+06	-0.283041E+04
j	$\mathbf{e}_{(2j)}$ (true)			$\mathbf{b}_{(2j+1)}$ (true)		
1	0.360998E-01	0.329994E+02	0.181520E+02	-0.404794E+02	-0.246847E+02	0.434584E+01
2	-0.808635E+03	0.417576E+04	0.502371E+04	-0.751816E+04	-0.659128E+04	0.508304E+03
3	-0.130010E+05	0.629134E+05	0.111387E+06	-0.182809E+06	-0.175159E+06	0.430155E+04
4	-0.425366E+05	0.189498E+06	0.427564E+06	-0.897080E+06	-0.901438E+06	-0.813930E+03
5	-0.280487E+05	0.117716E+06	0.298401E+06	-0.967289E+06	-0.994459E+06	-0.122411E+05
6	-0.176682E+04	0.733673E+04	0.189641E+05	-0.172068E+06	-0.178209E+06	-0.283275E+04

6. Integrated Kinematic-Dynamic Orbit Determination

6.1 Kinematical Orbit Determination

In the preceding sections, the theoretical foundation of the integrated kinematical-dynamical orbit determination procedure is presented. Some additional more application oriented aspects but important as pre-requisite for the following developments are discussed as well. The proposed orbit determination approach is characterized by the fact that the semi-analytical representation of the satellite's arc can be considered as solution to Newton's equation of motion on the one hand or by an empirical approximation of the satellite's arc on the other hand. In the former case, the boundary vectors are computed by a least squares fitting process to the (pseudo) observations while the orbit parameters have to fulfill the restrictions caused by the force function acting on the satellite. In the latter case, the orbit parameters are determined together with the boundary vectors of the specific arc by an adjustment process, where the parameters are determined such that the square sum of the residuals is minimized. As outlined in detail, the satellite's arc can be represented by a sine series on the one hand and by a combination of Euler and Bernoulli polynomials on the other hand. Preferable is a combinations between both representations, which allow to take advantage by the specific features of these two semi-analytical orbit representations. There are various modes of the orbit representation and different alternatives of a kinematical orbit determination, which shall be discussed in the following. First of all, an overview is given which repeats some essential facts from the preceding sections of this thesis.

The satellite's arc is represented by the function:

$$\mathbf{r}(\tau) = \bar{\mathbf{r}}(\tau) + \mathbf{d}(\tau), \tag{6.1}$$

where the reference motion can be modeled by $\bar{\mathbf{r}}(\tau)$ either according to Eq. (5.10),

$$\bar{\mathbf{r}}(\tau) = (1-\tau)\,\mathbf{r}_A + \tau \mathbf{r}_B,$$

or according to Eq. (5.20),

$$\bar{\mathbf{r}}(\tau) = \frac{\sin\mu(1-\tau)}{\sin\mu}\mathbf{r}_A + \frac{\sin\mu\tau}{\sin\mu}\mathbf{r}_B,$$

or according to Eq. (5.37),

$$\bar{\mathbf{r}}(\tau) = \tilde{\mathbf{r}}(\tau) + \bar{\mathbf{x}}(\tau). \tag{6.2}$$

The difference function $\mathbf{d}(\tau)$ can be formulated as solution to the respective boundary value problem as treated in Sec. 5.2, based on Eqs. (5.9), (5.19) or (5.32) and interpreted as Fourier series or sine series, respectively, according to Eq. (5.39),

$$\mathbf{d}(\tau) \equiv \mathbf{d}_F^{\infty}(\tau) = \sum_{\nu=1}^{\infty} \mathbf{d}_\nu \sin(\nu\pi\tau) \approx \sum_{\nu=1}^{n} \mathbf{d}_\nu \sin(\nu\pi\tau) = \mathbf{d}_F^{n}(\tau). \tag{6.3}$$

This series can be used as pure kinematical orbit representation with the kinematical orbit parameters $\mathbf{d}_\nu$ as treated in detail in Sec. 6.1.1.

In Sec. 5.3, we transformed this Fourier series into a series of Euler and Bernoulli polynomials,

$$\mathbf{d}(\tau) \equiv \mathbf{d}_F^{\infty}(\tau) = \mathbf{d}_P^{\infty}(\tau), \tag{6.4}$$

with

$$\mathbf{d}(\tau) \equiv \mathbf{d}_P^{\infty}(\tau) = \sum_{j=1}^{\infty} \mathbf{e}_{2j} E_{2j}(\tau) + \sum_{j=1}^{\infty} \mathbf{b}_{2j+1} B_{2j+1}(\tau) \quad \approx \sum_{j=1}^{J} \mathbf{e}_{2j} E_{2j}(\tau) + \sum_{j=1}^{J} \mathbf{b}_{2j+1} B_{2j+1}(\tau) = \mathbf{d}_P^{J}(\tau). \tag{6.5}$$

Here, the coefficients of the Euler and Bernoulli polynomials, $\mathbf{e}_{2j}$ and $\mathbf{b}_{2j+1}$, can be used as kinematical parameters of the orbit representation but they can be related also to the force function acting on the satellite. The different possibilities are discussed in Sec. 6.1.2.

Besides these two principle possibilities, another hybrid or combined version is possible where some specific advantageous features of these two representations can be exploited. The function $\mathbf{d}(\tau)$ and its corresponding series representation is split into a modified Fourier series $\bar{\mathbf{d}}_F^n(\tau)$ and a series $\mathbf{d}_P^J(\tau)$ in terms of Euler- and Bernoulli polynomials, Eq. (5.90), with properly selected upper indices n and J,

$$\mathbf{d}(\tau) \equiv \bar{\mathbf{d}}_F^n(\tau) + \mathbf{d}_P^J(\tau). \tag{6.6}$$

There are various possibilities to combine these two solution series as will be shown in Sec. 6.1.3.

If K positions at the discrete epochs $\tau_1, \cdots, \tau_K$ are available, derived from GNSS observations as treated in chapter 4, then we can use the following matrix notation,

$$\mathbf{r} = \bar{\mathbf{r}} + \mathbf{d}, \tag{6.7}$$

with the ephemerides of satellite positions at the observed epochs,

$$\mathbf{r} := \begin{pmatrix} \mathbf{r}(\tau_1) \\ \vdots \\ \mathbf{r}(\tau_K) \end{pmatrix}, \tag{6.8}$$

the contribution of the reference motion according to Eqs. (5.10), (5.20), or (5.37)

$$\bar{\mathbf{r}} := \begin{pmatrix} \bar{\mathbf{r}}(\tau_1) \\ \vdots \\ \bar{\mathbf{r}}(\tau_K) \end{pmatrix} = \begin{pmatrix} a(\tau_1) \\ \vdots \\ a(\tau_K) \end{pmatrix} \mathbf{r}(\tau_A) + \begin{pmatrix} b(\tau_1) \\ \vdots \\ b(\tau_K) \end{pmatrix} \mathbf{r}(\tau_B) =: \mathbf{a}\,\mathbf{r}(\tau_A) + \mathbf{b}\,\mathbf{r}(\tau_B), \tag{6.9}$$

and the linear factors $\mathbf{a}$ and $\mathbf{b}$ according to the reference motion terms and the discrete constituents of the difference function,

$$\mathbf{a} := \begin{pmatrix} a(\tau_1) \\ \vdots \\ a(\tau_K) \end{pmatrix}, \qquad \mathbf{b} := \begin{pmatrix} b(\tau_1) \\ \vdots \\ b(\tau_K) \end{pmatrix}, \qquad \mathbf{d} := \begin{pmatrix} \mathbf{d}(\tau_1) \\ \vdots \\ \mathbf{d}(\tau_K) \end{pmatrix}. \tag{6.10}$$

The latter matrix can be represented either by the sine coefficients or by the Euler and Bernoulli coefficients or by a combination of them, as discussed in the following.

6.1.1 Fourier Series

The difference function $\mathbf{d}(\tau)$ - in principle an infinite series - is approximated by a sine series with an upper limit n, $\mathbf{d}_F^n(\tau)$. The $3n$ series coefficients $\mathbf{d}_\nu$, together with the 6 coordinates of the boundary vectors $\mathbf{r}_A$ and $\mathbf{r}_B$ are the parameters, which have to be determined, based on the observations of the satellite's motion. These observations can be provided as ephemerides of positions as treated in chapter 5 or as direct GNSS observables as treated in chapter 4. The foundation of the observation equations are presented in chapter 5. If this is done without any additional dynamic information, then a continuous approximation function is available which is of pure kinematical character, because any further derivative with respect to the time can be determined as shown, at least theoretically, in Sec. 5.3.3 in a straight forward way.
The determination of the kinematical orbit parameters can be determined from positions, derived in a first preparation step by a geometrical orbit determination procedure (see chapter 4), or directly by the carrier phase GPS-SST observations, together with observation specific corrections. Both procedures are presented in the following.

6.1.1.1 Position Observations

The orbit of a satellite can be represented in a semi-analytical way by one of the Eqs. (5.9), (5.19) or (5.36),

$$\mathbf{r}(\tau) = \bar{\mathbf{r}}(\tau) + \sum_{\nu=1}^{\infty} \mathbf{c}_\nu \sin(\nu\pi\tau) = \bar{\mathbf{r}}(\tau) + \mathbf{d}(\tau) = \bar{\mathbf{r}}(\tau) + \mathbf{d}_F^\infty(\tau). \tag{6.11}$$

If the upper index ν is limited by a sufficient high number n, then the difference function reads,

$$\mathbf{d}(\tau) \equiv \mathbf{d}_F^\infty(\tau) = \sum_{\nu=1}^{\infty} \mathbf{d}_\nu \sin(\nu\pi\tau) \approx \sum_{\nu=1}^{n} \mathbf{d}_\nu \sin(\nu\pi\tau) = \mathbf{d}_F^n(\tau), \tag{6.12}$$

and the LEO orbit can be represented as,

$$\mathbf{r}(\tau) = \bar{\mathbf{r}}(\tau) + \sum_{\nu=1}^{n} \mathbf{d}_\nu \sin(\nu\pi\tau). \tag{6.13}$$

This formula can be considered as a linear approximation of the satellite's arc. If the absolute position of the LEO at the epoch τ is derived geometrically (see chapter 4) with its variance-covariance matrix, then the linear observation equation reads,

$$\mathbf{r}(\tau) = \bar{\mathbf{r}}(\tau) + \sum_{\nu=1}^{n} \mathbf{d}_\nu \sin(\nu\pi\tau), \quad \mathbf{C}(\tau) = \begin{pmatrix} \sigma_{x_r}^2 & \sigma_{x_r y_r} & \sigma_{x_r z_r} \\ & \sigma_{y_r}^2 & \sigma_{y_r z_r} \\ \text{Sym.} & & \sigma_{z_r}^2 \end{pmatrix}. \tag{6.14}$$

If the LEO positions are observed at the epochs $\tau_1, \ldots, \tau_K$, then the matrix of observation equations reads together with the a-priori variance-covariance matrix $\mathbf{C_r}$,

$$\mathbf{r} = \bar{\mathbf{r}} + \mathbf{d}, \quad \mathbf{C_r} = \begin{pmatrix} \mathbf{C}(\tau_1) & \cdots & \mathbf{0} \\ \vdots & \ddots & \vdots \\ \mathbf{0} & \cdots & \mathbf{C}(\tau_K) \end{pmatrix}, \tag{6.15}$$

with the contribution of the reference motion $\bar{\mathbf{r}}$, derived by an expression of the form of Eqs. (5.10), (5.20) or (5.37), and the discrete constituents of the difference function,

$$\mathbf{d} = \begin{pmatrix} \mathbf{d}(\tau_1) \\ \vdots \\ \mathbf{d}(\tau_K) \end{pmatrix} = \begin{pmatrix} \sin(\pi\tau_1) & \cdots & \sin(n\pi\tau_1) \\ \vdots & \vdots & \vdots \\ \sin(\pi\tau_K) & \cdots & \sin(n\pi\tau_K) \end{pmatrix} \begin{pmatrix} \mathbf{d}_1 \\ \vdots \\ \mathbf{d}_n \end{pmatrix} =: \mathbf{S}^{\mathrm{T}} \mathbf{d}_n, \tag{6.16}$$

so that it reads with Eqs. (6.9) and (6.10),

$$\mathbf{r} = \mathbf{a}\,\mathbf{r}(\tau_A) + \mathbf{b}\,\mathbf{r}(\tau_B) + \mathbf{S}^{\mathrm{T}} \mathbf{d}_n, \quad \mathbf{C_r}. \tag{6.17}$$

Gauss-Markov model for observed positions: In a pure kinematical orbit determination application, the boundary vectors $\mathbf{r}_A$ and $\mathbf{r}_B$ as well as the Fourier coefficients $\mathbf{d}_\nu$ are the unknown parameters so that the observation model reads,

$$\begin{pmatrix} \mathbf{r}(\tau_1) \\ \vdots \\ \mathbf{r}(\tau_K) \end{pmatrix} = \begin{pmatrix} \mathbf{a} & \mathbf{b} & \mathbf{S}^{\mathrm{T}} \end{pmatrix} \begin{pmatrix} \mathbf{r}_A \\ \mathbf{r}_B \\ \mathbf{d}_1 \\ \vdots \\ \mathbf{d}_n \end{pmatrix}, \quad \mathbf{C_r}, \tag{6.18}$$

or reformulated with the observation vector, the design matrix and the unknown parameters as,

$$\mathbf{l} = \begin{pmatrix} \mathbf{r}(\tau_1) \\ \vdots \\ \mathbf{r}(\tau_K) \end{pmatrix}, \quad \mathbf{A} = \begin{pmatrix} \mathbf{a} & \mathbf{b} & \mathbf{S}^{\mathrm{T}} \end{pmatrix}, \quad \mathbf{x} = \begin{pmatrix} \mathbf{r}_A \\ \mathbf{r}_B \\ \mathbf{d}_1 \\ \vdots \\ \mathbf{d}_n \end{pmatrix}, \tag{6.19}$$

or, respectively, with the dimensions $l = 3K$ and $u = 3n + 6$

$$\mathbf{l}_l = \mathbf{A}_{l\times u}\mathbf{x}_u, \quad \mathbf{C}_{\mathbf{r}}. \tag{6.20}$$

The unknown parameters and its a-posteriori variance-covariance matrix can be estimated directly as usual by,

$$\hat{\mathbf{x}} = \left(\mathbf{A}^{\mathrm{T}}\mathbf{C}_{\mathbf{r}}^{-1}\mathbf{A}\right)^{-1}\mathbf{A}^{\mathrm{T}}\mathbf{C}_{\mathbf{r}}^{-1}\mathbf{l}, \quad \mathbf{C}_{\hat{\mathbf{x}}} = \left(\mathbf{A}^{\mathrm{T}}\mathbf{C}_{\mathbf{r}}^{-1}\mathbf{A}\right)^{-1}. \tag{6.21}$$

Either in case of a kinematical orbit determination or in case of the dynamical orbit determination concept as discussed later, the upper index n has to be selected sufficiently high to avoid Gibbs' effects especially at the boundaries of the satellite's arcs. In Sec. 5.4.1.1, the approximation characteristics of the Fourier series based on different reference motions (straight line, ellipse, reference orbit) are discussed for the error free case. Usually, the number of observed three dimensional positions very often is not sufficient to provide a safe redundancy in the least squares adjustment of the orbit determination process. This is the reason that a modification to this approach is necessary.

6.1.1.2 SST Carrier Phase Observations

The Fourier amplitudes as well as the boundary positions of the satellite's arc can be directly estimated from the GPS-SST observations. The carrier phase observations at the frequency i between the GPS satellite s and the GPS receiver r on-board LEO at the normalized epoch τ can be formulated as (refer to chapter 4 for details),

$$\Phi^s_{r,i}(\tau) = \|\mathbf{r}^s_m(\tau) - \mathbf{r}(\tau)\| + c\delta t_r(\tau) + \lambda_i A^s_{r,i} + d_{M,\Phi_i}(\tau) + e^s_{r,\Phi_i}(\tau) + \varepsilon^s_{r,\Phi_i}, \tag{6.22}$$

If the LEO orbit representation Eq. (6.13) is inserted in the Eq. (6.22), then the carrier phase observation equation reads as follows

$$\Phi^s_{r,i}(\tau) = \left\|\mathbf{r}^s_m(\tau) - \bar{\mathbf{r}}(\tau) - \sum_{\nu=1}^{n}\mathbf{d}_\nu \sin(\nu\pi\tau)\right\| + c\delta t_r(\tau) + \lambda_i A^s_{r,i} + d_{M,\Phi_i}(\tau) + e^s_{r,\Phi_i}(\tau) + \varepsilon^s_{r,\Phi_i}. \tag{6.23}$$

The GPS-SST carrier phase observation equations are linear with respect to the LEO clock offsets and the GPS ambiguity parameters but are non-linear with respect to the LEO orbit representation parameters, namely the LEO boundary positions and the Fourier amplitudes. The carrier phase observation equation can be linearized with respect to the LEO orbit representation parameters at frequency i as,

$$\Phi^s_{r,i}(\tau) = \Phi^s_{r,i,0}(\tau) + \left.\frac{\partial\Phi^s_{r,i}(\tau)}{\partial\mathbf{x}}\right|_{\mathbf{x}=\mathbf{x}_0}(\mathbf{x} - \mathbf{x}_0), \tag{6.24}$$

with

$$\mathbf{x} := \begin{pmatrix} \mathbf{x}_r \\ \mathbf{x}_t \\ \mathbf{x}_A \end{pmatrix}, \quad \mathbf{x}_r := \begin{pmatrix} \mathbf{r}_A \\ \mathbf{r}_B \\ \mathbf{d}_1 \\ \vdots \\ \mathbf{d}_n \end{pmatrix}, \quad \mathbf{x}_t := \begin{pmatrix} c\delta t_r(\tau_1) \\ \vdots \\ c\delta t_r(\tau_K) \end{pmatrix}, \quad \mathbf{x}_A := \begin{pmatrix} \lambda_i A^{s_1} \\ \vdots \\ \lambda_i A^{s_m} \end{pmatrix}. \tag{6.25}$$

$\mathbf{x}$ contains the LEO boundary positions, the Fourier amplitudes up to the Fourier index n, the LEO clock offsets at every of the K observations and the GPS ambiguity parameters for m tracked GPS satellites. If the ionosphere-free carrier phase observations (index $i = 3$) are used in the procedure (see Sec. 2.7.3), then the multiplication of the design matrix by the corrections to the approximations of the unknowns reads

$$\frac{\partial \Phi^s_{r,3}(\tau)}{\partial \mathbf{x}}(\mathbf{x} - \mathbf{x}_0) = \left(\frac{\partial \Phi^s_{r,3}(\tau)}{\partial \mathbf{x}_r} \; \frac{\partial \Phi^s_{r,3}(\tau)}{\partial \mathbf{x}_t} \; \frac{\partial \Phi^s_{r,3}(\tau)}{\partial \mathbf{x}_A} \right) \begin{pmatrix} \mathbf{x}_r - \mathbf{x}_{r,0} \\ \mathbf{x}_t - \mathbf{x}_{t,0} \\ \mathbf{x}_A - \mathbf{x}_{A,0} \end{pmatrix}. \tag{6.26}$$

The partial derivatives of the ionosphere-free carrier phase GPS-SST observation $\Phi^s_{r,3}$ with respect to the non-linear parameters can be determined by applying the chain rule.

Partial derivatives of the carrier phase observations with respect to the LEO boundary positions and Fourier amplitudes: The partial derivatives of the ionosphere-free carrier phase GPS-SST observations with respect to the LEO boundary positions and the Fourier amplitudes, $\mathbf{x}_r$, can be written as follows,

$$\frac{\partial \Phi^s_{r,3}(\tau)}{\partial \mathbf{x}_r} = \frac{\partial \Phi^s_{r,3}(\tau)}{\partial \mathbf{r}(\tau)} \frac{\partial \mathbf{r}(\tau)}{\partial \mathbf{x}_r}, \tag{6.27}$$

or in matrix notation,

$$\mathbf{A}^s_{\mathbf{x}_r}(\tau) = \mathbf{a}^s_{\mathbf{r}}(\tau) \mathbf{A}^{\mathbf{r}}_{\mathbf{x}_r}(\tau). \tag{6.28}$$

according to Eqs. (4.25) and (4.31),

$$\mathbf{a}^s_{\mathbf{r}}(\tau) = \frac{\partial \Phi^s_{r,3}(\tau)}{\partial \mathbf{r}(\tau)} = \begin{pmatrix} e^s_{r,x}(\tau) & e^s_{r,y}(\tau) & e^s_{r,z}(\tau) \end{pmatrix},$$

$$e^s_{r,x}(\tau) = \frac{x_r(\tau) - x^s(\tau - \tau^s_r)}{\rho^s_r(\tau)}, \quad e^s_{r,y}(\tau) = \frac{y_r(\tau) - y^s(\tau - \tau^s_r)}{\rho^s_r(\tau)}, \quad e^s_{r,z}(\tau) = \frac{z_r(\tau) - z^s(\tau - \tau^s_r)}{\rho^s_r(\tau)},$$

with τ^s_r as the GPS signal travel time between the GPS satellite s and the GPS receiver r on-board LEO and with the factors $a(\tau)$ and $b(\tau)$ according to Eq. (6.9) and the sine coefficients in $\mathbf{H}^{\mathrm{T}}(\tau)$ according to Eq. (6.16),

$$\mathbf{A}^{\mathbf{r}}_{\mathbf{x}_r}(\tau) = \begin{pmatrix} \mathrm{a}(\tau)\mathbf{I} & \mathrm{b}(\tau)\mathbf{I} & \mathbf{H}^{\mathrm{T}}(\tau) \end{pmatrix}, \quad \mathbf{H}^{\mathrm{T}}(\tau) = \begin{pmatrix} \sin \pi\tau \mathbf{I} & \dots & \sin n\pi\tau \mathbf{I} \end{pmatrix}, \quad \mathbf{I} = \begin{pmatrix} 1 & 0 & 0 \\ 0 & 1 & 0 \\ 0 & 0 & 1 \end{pmatrix}. \tag{6.29}$$

Partial derivatives of the carrier phase observation with respect to the LEO clock offset: A carrier phase GPS-SST observation is linear with respect to the LEO clock offset. The partial derivatives of the ionosphere-free carrier phase observation with respect to the LEO clock offset reads for an observation epoch τ,

$$\frac{\partial \Phi^s_{r,3}(\tau)}{\partial \mathbf{x}_t} = \mathbf{a}^s_{\mathbf{x}_t}(\tau), \tag{6.30}$$

with

$$\mathbf{a}^s_{\mathbf{x}_t}(\tau) = \begin{pmatrix} 0 & \dots & 1 & \dots & 0 \end{pmatrix}. \tag{6.31}$$

Partial derivatives of the carrier phase observation with respect to the GPS ambiguity terms: A carrier phase GPS-SST observation is linear with respect to the GPS ambiguity term. Therefore, the partial derivative of the ionosphere-free carrier phase observation equation with respect to the ambiguity term of GPS satellite s at the observed epoch reads,

$$\frac{\partial \Phi^s_{r,3}(\tau)}{\partial \mathbf{x}_A} = \mathbf{a}^s_{\mathbf{x}_A}(\tau), \tag{6.32}$$

with

$$\mathbf{a}^s_{\mathbf{x}_A}(\tau) = \begin{pmatrix} 0 & \dots & 1 & \dots & 0 \end{pmatrix}. \tag{6.33}$$

Gauss-Markov model for SST carrier phase observations: A pure kinematical orbit determination from SST carrier phase observations requires the determination of the kinematical orbit parameters and additional observation specific corrections. The ionosphere-free observation equation for the GPS satellite s and the GPS receiver r on-board LEO reads for an epoch τ as follows,

$$\Delta\Phi^s_{r,3}(\tau) = \mathbf{a}^s_{\mathbf{r}}(\tau)\mathbf{A}^{\mathbf{r}}_{\mathbf{x}_r}(\tau)\big(\mathbf{x}_r - \mathbf{x}_{r,0}\big) + \mathbf{a}^s_{\mathbf{x}_t}(\tau)\big(\mathbf{x}_t - \mathbf{x}_{t,0}\big) + \mathbf{a}^s_A(\tau)\big(\mathbf{x}_A - \mathbf{x}_{A,0}\big), \quad w^s_{r,\Phi_3}(\tau) = \frac{\sigma_0^2}{\sigma^2_{\Phi^s_{r,3}(\tau)}}\cos^2(z^s_r(\tau)), \tag{6.34}$$

with the initial standard deviation σ_0, the standard deviation of the ionosphere-free carrier phase observation $\sigma_{\Phi^s_{r,3}(\tau)}$ and the zenith distance $z^s_r(\tau)$ from the GPS receiver r on-board LEO to the GPS satellite s at time τ. $w^s_{r,\Phi_3}(\tau)$ is the weight of the carrier phase observation $\Phi^s_{r,3}(\tau)$.

If m_τ is the total number of carrier phase observations at time τ from the GPS satellites $s_1, \dots, s_{m_\tau}$ to the GPS receiver r on-board LEO, the Gauss-Markov model for the three unknown groups can be summarized as follows,

$$\begin{pmatrix} \Delta\Phi^{s_1}_{r,3}(\tau) \\ \vdots \\ \Delta\Phi^{s_j}_{r,3}(\tau) \\ \vdots \\ \Delta\Phi^{s_{m_\tau}}_{r,3}(\tau) \end{pmatrix} = \begin{pmatrix} \mathbf{a}^{s_1}_{\mathbf{r}}(\tau)\mathbf{A}^{\mathbf{r}}_{\mathbf{x}_r}(\tau) \\ \vdots \\ \mathbf{a}^{s_j}_{\mathbf{r}}(\tau)\mathbf{A}^{\mathbf{r}}_{\mathbf{x}_r}(\tau) \\ \vdots \\ \mathbf{a}^{s_{m_\tau}}_{\mathbf{r}}(\tau)\mathbf{A}^{\mathbf{r}}_{\mathbf{x}_r}(\tau) \end{pmatrix} (\mathbf{x}_r - \mathbf{x}_{r,0}) + \begin{pmatrix} \mathbf{a}^{s_1}_{\mathbf{x}_t}(\tau) \\ \vdots \\ \mathbf{a}^{s_j}_{\mathbf{x}_t}(\tau) \\ \vdots \\ \mathbf{a}^{s_{m_\tau}}_{\mathbf{x}_t}(\tau) \end{pmatrix} (\mathbf{x}_t - \mathbf{x}_{t,0}) + \begin{pmatrix} \mathbf{a}^{s_1}_{\mathbf{x}_A}(\tau) \\ \vdots \\ \mathbf{a}^{s_j}_{\mathbf{x}_A}(\tau) \\ \vdots \\ \mathbf{a}^{s_{m_\tau}}_{\mathbf{x}_A}(\tau) \end{pmatrix} (\mathbf{x}_A - \mathbf{x}_{A,0}), \tag{6.35}$$

or in matrix notation at the epoch τ as,

$$\Delta\mathbf{l}(\tau) = \mathbf{A}(\tau)\Delta\mathbf{x}, \tag{6.36}$$

with the weight matrix of the carrier phase observation at the epoch τ (inverse of the variance-covariance matrix of the carrier phase observations, see Sec. 3.3),

$$\mathbf{W}(\tau) = \begin{pmatrix} w^{s_1}_{r,\Phi_3}(\tau) & \dots & 0 & \dots & 0 \\ \vdots & \ddots & \vdots & \ddots & \vdots \\ 0 & \dots & w^{s_j}_{r,\Phi_3}(\tau) & \dots & 0 \\ \vdots & \ddots & \vdots & \ddots & \vdots \\ 0 & \dots & 0 & \dots & w^{s_{m_\tau}}_{r,\Phi_3}(\tau) \end{pmatrix}. \tag{6.37}$$

If l and u ($l \geq u$) are the total numbers of the ionosphere-free carrier phase GPS-SST observations at epochs $\tau_1, \dots, \tau_K$ and the unknown parameters, respectively, then the Gauss-Markov model for all tracked GPS satellites and all observation epochs reads

$$\begin{pmatrix} \Delta\mathbf{l}(\tau_1) \\ \vdots \\ \Delta\mathbf{l}(\tau_K) \end{pmatrix} = \begin{pmatrix} \mathbf{A}(\tau_1) \\ \vdots \\ \mathbf{A}(\tau_K) \end{pmatrix} (\Delta\mathbf{x}), \tag{6.38}$$

or in matrix notation as,

$$\Delta \mathbf{l}_{(l)} = \mathbf{A}_{(l\times u)}\Delta \mathbf{x}_{(u)}, \quad \mathbf{W}_l = \begin{pmatrix} \mathbf{W}(\tau_1) & \cdots & \mathbf{0} \\ \vdots & \ddots & \vdots \\ \mathbf{0} & \cdots & \mathbf{W}(\tau_K) \end{pmatrix}, \tag{6.39}$$

with

- l the total number of carrier phase GPS-SST observations at epochs $\tau_1, \ldots, \tau_K$,
- u the total number of unknowns as $u = u_r + u_t + u_A$,
- u_r the number of LEO boundary position coordinates and the number of Fourier amplitudes for an upper index n ($u_r = 6 + 3n$),
- u_t the total number of the LEO clock offsets except the first epoch ($u_t = K - 1$),
- u_A the GPS ambiguity parameters.

The corrections to the approximate unknown parameters and its a-posteriori variance-covariance matrix can be determined according to

$$\Delta\hat{\mathbf{x}} = \left(\mathbf{A}^{\mathrm{T}}\mathbf{W}_l\mathbf{A}\right)^{-1}\mathbf{A}^{\mathrm{T}}\mathbf{W}_l\Delta\mathbf{l}, \quad \mathbf{C}_{\Delta\hat{\mathbf{x}}} = \left(\mathbf{A}^{\mathrm{T}}\mathbf{W}_l\mathbf{A}\right)^{-1}. \tag{6.40}$$

The estimated unknown parameters in Eq. (6.40), $\Delta\hat{\mathbf{x}}$, are the corrections to the initial LEO boundary positions, the Fourier amplitudes, the initial LEO clock offsets and the initial ambiguities of all observed GPS satellites from the GPS receiver r on-board LEO. Because of the non linearized observation model, an iteration procedure is necessary. The convergence of the unknowns can be achieved after a few iterations,

$$\hat{\mathbf{x}}_{(i)} = \hat{\mathbf{x}}_{(i-1)} + \Delta\hat{\mathbf{x}}_{(i)} = \hat{\mathbf{x}}_{(i-1)} + \left(\mathbf{A}^{\mathrm{T}}_{(i)}\mathbf{W}_l\mathbf{A}_{(i)}\right)^{-1}\mathbf{A}^{\mathrm{T}}_{(i)}\mathbf{W}_l\Delta\mathbf{l}_{(i)}. \tag{6.41}$$

6.1.2 Euler- and Bernoulli Polynomials

As shown in Eq. (5.74), the sine series can be transformed in a series of Euler- and Bernoulli polynomials. In case of an infinite series it holds

$$\mathbf{d}(\tau) := \mathbf{r}(\tau) - \bar{\mathbf{r}}(\tau) = \sum_{j=1}^{\infty}\mathbf{e}_{2j}E_{2j}(\tau) + \sum_{j=1}^{\infty}\mathbf{b}_{2j+1}B_{2j+1}(\tau) = \mathbf{d}_P^{\infty}(\tau). \tag{6.42}$$

If the upper index j is limited by a sufficient high number J, then the difference function reads,

$$\mathbf{d}(\tau) \equiv \mathbf{d}_P^{\infty}(\tau) = \sum_{j=1}^{\infty}\mathbf{e}_{2j}E_{2j}(\tau) + \sum_{j=1}^{\infty}\mathbf{b}_{2j+1}B_{2j+1}(\tau) \approx \sum_{j=1}^{J}\mathbf{e}_{2j}E_{2j}(\tau) + \sum_{j=1}^{J}\mathbf{b}_{2j+1}B_{2j+1}(\tau) = \mathbf{d}_P^{J}(\tau). \tag{6.43}$$

This formula can be considered as a linear approximation of the satellite's arc. In this case, the $6J$ coefficients $\mathbf{e}_{2j}$ and $\mathbf{b}_{2j+1}$, $j = 1, \ldots, J$, of the Euler- and Bernoulli polynomials together with the 6 coordinates of the boundary vectors $\mathbf{r}_A$ and $\mathbf{r}_B$ are the parameters to be determined based on the observations. In the following, again both cases of observation types for the kinematical orbit determination procedure are outlined.

6.1.2.1 Position Observations

If the observations are represented by absolute positions derived according to the geometrical orbit determination procedure as outlined in chapter 4, then the observation model reads

$$\mathbf{r}(\tau) = \bar{\mathbf{r}}(\tau) + \sum_{j=1}^{J}\mathbf{e}_{2j}E_{2j}(\tau) + \sum_{j=1}^{J}\mathbf{b}_{2j+1}B_{2j+1}(\tau), \tag{6.44}$$

with the variance-covariance matrix for the position coordinates

$$\mathbf{C}(\tau) = \begin{pmatrix} \sigma_{x_r}^2 & \sigma_{x_r y_r} & \sigma_{x_r z_r} \\ & \sigma_{y_r}^2 & \sigma_{y_r z_r} \\ \text{Sym.} & & \sigma_{z_r}^2 \end{pmatrix}. \tag{6.45}$$

The observation model for all observations at the epochs $\tau_1, \ldots, \tau_K$ reads in matrix notation,

$$\mathbf{r} = \overline{\mathbf{r}} + \mathbf{d}, \quad \mathbf{C_r} = \begin{pmatrix} \mathbf{C}(\tau_1) & \cdots & \mathbf{0} \\ \vdots & \ddots & \vdots \\ \mathbf{0} & \cdots & \mathbf{C}(\tau_K) \end{pmatrix}, \tag{6.46}$$

with the contribution of the reference motion $\overline{\mathbf{r}}$, derived by an expression of the form of Eqs. (5.10), (5.20) or (5.37), and the discrete constituents of the difference function,

$$\mathbf{d} := \begin{pmatrix} \mathbf{d}(\tau_1) \\ \vdots \\ \mathbf{d}(\tau_K) \end{pmatrix} = \mathbf{T}^{\mathsf{T}} \begin{pmatrix} (\mathbf{E}_c^{2J+1})^{\mathsf{T}} & (\mathbf{B}_c^{2J+1})^{\mathsf{T}} \end{pmatrix} \begin{pmatrix} \mathbf{e}_{2J} \\ \mathbf{b}_{2J+1} \end{pmatrix}, \tag{6.47}$$

with the matrix,

$$\mathbf{T} = \begin{pmatrix} \mathbf{t}_1 & \cdots & \mathbf{t}_K \end{pmatrix} = \begin{pmatrix} \tau_1 & \cdots & \tau_K \\ \vdots & \ldots & \vdots \\ \tau_1^{2J+1} & \cdots & \tau_K^{2J+1} \end{pmatrix}, \tag{6.48}$$

so that it reads with Eqs. (6.8) and (6.9),

$$\mathbf{r} = \mathbf{a}\,\mathbf{r}(\tau_A) + \mathbf{b}\,\mathbf{r}(\tau_B) + \mathbf{T}^{\mathsf{T}} \begin{pmatrix} (\mathbf{E}_c^{2J+1})^{\mathsf{T}} & (\mathbf{B}_c^{2J+1})^{\mathsf{T}} \end{pmatrix} \begin{pmatrix} \mathbf{e}_{2J} \\ \mathbf{b}_{2J+1} \end{pmatrix}. \tag{6.49}$$

Gauss-Markov model for observed positions: If the LEO absolute positions are geometrically determined at the epochs $\tau_1, \ldots, \tau_K$, then the Gauss-Markov model reads in matrix notation,

$$\begin{pmatrix} \mathbf{r}(\tau_1) \\ \vdots \\ \mathbf{r}(\tau_K) \end{pmatrix} = \begin{pmatrix} \mathbf{a} & \mathbf{b} & \mathbf{T}^{\mathsf{T}} \begin{pmatrix} (\mathbf{E}_c^{2J+1})^{\mathsf{T}} & (\mathbf{B}_c^{2J+1})^{\mathsf{T}} \end{pmatrix} \end{pmatrix} \begin{pmatrix} \mathbf{r}_A \\ \mathbf{r}_B \\ \mathbf{e}_{2J} \\ \mathbf{b}_{2J+1} \end{pmatrix}, \quad \mathbf{C_r}. \tag{6.50}$$

The observation model reads,

$$\mathbf{l}_{3K} = \mathbf{A}_{3K \times (6J+6)} \mathbf{x}_{(6J+6)}, \quad \mathbf{C_r}, \tag{6.51}$$

with

$$\mathbf{l} = \begin{pmatrix} \mathbf{r}(\tau_1) \\ \vdots \\ \mathbf{r}(\tau_K) \end{pmatrix}, \quad \mathbf{A} = \begin{pmatrix} \mathbf{a} & \mathbf{b} & \mathbf{T}^{\mathsf{T}} \begin{pmatrix} (\mathbf{E}_c^{2J+1})^{\mathsf{T}} & (\mathbf{B}_c^{2J+1})^{\mathsf{T}} \end{pmatrix} \end{pmatrix}, \quad \mathbf{x} = \begin{pmatrix} \mathbf{r}_A \\ \mathbf{r}_B \\ \mathbf{e}_{2J} \\ \mathbf{b}_{2J+1} \end{pmatrix}. \tag{6.52}$$

The LEO boundary positions and the Euler-Bernoulli polynomials coefficients can be directly estimated as usual by,

$$\hat{\mathbf{x}} = \left(\mathbf{A}^{\mathrm{T}} \mathbf{C}_{\mathbf{r}}^{-1} \mathbf{A}\right)^{-1} \mathbf{A}^{\mathrm{T}} \mathbf{C}_{\mathbf{r}}^{-1} \mathbf{l}, \quad \mathbf{C}_{\hat{\mathbf{x}}} = \left(\mathbf{A}^{\mathrm{T}} \mathbf{C}_{\mathbf{r}}^{-1} \mathbf{A}\right)^{-1}. \tag{6.53}$$

This system of linear observation equation can serve for a pure kinematical orbit determination, if the coefficients $\mathbf{e}_{2J}$ of the Euler polynomials and the coefficients of the Bernoulli polynomials $\mathbf{b}_{2J+1}$ are derived

from the observations by a least squares adjustment process without any dynamical information, together with the boundary values

$$\mathbf{r}_A := \mathbf{r}(t_A), \quad \mathbf{r}_B := \mathbf{r}(t_B), \quad t_A < t_B, \tag{6.54}$$

contained in the reference motion $\bar{\mathbf{r}}(\tau)$. In Sec. 5.4.1.2, it is demonstrated that the approximation quality by a series in terms of Euler and Bernoulli polynomials is limited. Even in case of an upper limit of J_{max} =5 (corresponding to a maximal degree 11 of the Euler and Bernoulli polynomials) the remainder function is in the size of about $15cm$ in case of the straight line and ellipse modes of the reference motion. It can be reduced in the case of a dynamical reference orbit as reference motion down to about $2cm$. Additional computations demonstrate that an increase of J does not improve the approximation quality.

6.1.2.2 SST Carrier Phase Observations

The Euler-Bernoulli coefficients can be derived again directly from the carrier phase GPS-SST observations between the GPS satellites and the LEO. The carrier phase observations between the GPS satellite s and the GPS receiver r on-board LEO at frequency i(Eq. (4.27)) at the normalized epoch τ can be written as

$$\Phi^s_{r,i}(\tau) = \left\|\mathbf{r}^s_m(\tau) - \mathbf{r}(\tau)\right\| + c\delta t_r(\tau) + \lambda_i A^s_{r,i} + d_{M,\Phi_i}(\tau) + e^s_{r,\Phi_i}(\tau) + \varepsilon^s_{r,\Phi_i}(\tau).$$

If the LEO orbit representation Eq. (6.44) with the approximation Eq. (6.43) is inserted in Eq. (6.22), then the carrier phase SST observation equation reads

$$\begin{aligned}\Phi^s_{r,i}(\tau) = &\left\|\mathbf{r}^s_m(\tau) - \bar{\mathbf{r}}(\tau) - \sum_{j=1}^{J} \mathbf{e}_{2j} E_{2j}(\tau) - \sum_{j=1}^{J} \mathbf{b}_{2j+1} B_{2j+1}(\tau)\right\| + c\delta t_r(\tau) + \lambda_i A^s_{r,i} + \\ &+ d_{M,\Phi_i}(\tau) + e^s_{r,\Phi_i}(\tau) + \varepsilon^s_{r,\Phi_i}(\tau).\end{aligned} \tag{6.55}$$

The carrier phase GPS-SST observations are non-linear with respect to the LEO boundary positions and the unknown Euler-Bernoulli coefficients, but linear with respect to the GPS ambiguity terms and the LEO clock offsets. The linear observation equation (Eq. (6.55)) reads as follows,

$$\Phi^s_{r,i}(\tau) = \Phi^s_{r,i,0}(\tau) + \left.\frac{\partial \Phi^s_{r,i}(\tau)}{\partial \mathbf{x}}\right|_{\mathbf{x}=\mathbf{x}_0} (\mathbf{x} - \mathbf{x}_0), \tag{6.56}$$

with,

$$\mathbf{x} := \begin{pmatrix} \mathbf{x}_{eb} \\ \mathbf{x}_t \\ \mathbf{x}_A \end{pmatrix}, \quad \mathbf{x}_{eb} = \begin{pmatrix} \mathbf{r}_A \\ \mathbf{r}_B \\ \mathbf{e}_{2J} \\ \mathbf{b}_{2J+1} \end{pmatrix}, \quad \mathbf{x}_t := \begin{pmatrix} c\delta t_r(\tau_1) \\ \vdots \\ c\delta t_r(\tau_K) \end{pmatrix}, \quad \mathbf{x}_A := \begin{pmatrix} \lambda_i A^{s_1} \\ \vdots \\ \lambda_i A^{s_m} \end{pmatrix}. \tag{6.57}$$

$\mathbf{x}$ contains the LEO boundary positions, the Euler-Bernoulli coefficients, the LEO clock offsets at every of the K observed epochs and the GPS ambiguity parameters for m observed GPS satellites. The design matrix for the ionosphere-free carrier phase GPS-SST observations multiplied by the corrections to the approximations of the unknowns reads

$$\frac{\partial \Phi^s_{r,3}(\tau)}{\partial \mathbf{x}}(\mathbf{x} - \mathbf{x}_0) = \left(\frac{\partial \Phi^s_{r,3}(\tau)}{\partial \mathbf{x}_{eb}} \; \frac{\partial \Phi^s_{r,3}(\tau)}{\partial \mathbf{x}_t} \; \frac{\partial \Phi^s_{r,3}(\tau)}{\partial \mathbf{x}_A}\right) \begin{pmatrix} \mathbf{x}_{eb} - \mathbf{x}^0_{eb} \\ \mathbf{x}_t - \mathbf{x}_{t,0} \\ \mathbf{x}_A - \mathbf{x}_{A,0} \end{pmatrix}. \tag{6.58}$$

The partial derivatives of the carrier phase observations with respect to the LEO clock offsets and the ambiguity parameters were discussed in Sec. 6.1.1.2. The partial derivatives of the carrier phase GPS-SST observations with respect to the Euler-Bernoulli coefficients can be performed by applying the chain rule.

Partial derivatives of the carrier phase observations with respect to the Euler-Bernoulli coefficients: The partial derivatives of ionosphere-free carrier phase SST observations between the GPS satellite s and the GPS receiver r on-board LEO with respect to the Euler-Bernoulli parameters can be written as follows,

$$\frac{\partial \Phi^s_{r,3}(\tau)}{\partial \mathbf{x}_{eb}} = \frac{\partial \Phi^s_{r,3}(\tau)}{\partial \mathbf{r}(\tau)} \frac{\partial \mathbf{r}(\tau)}{\partial \mathbf{x}_{eb}}, \tag{6.59}$$

or in a matrix form,

$$\mathbf{A}^s_{\mathbf{x}_{eb}}(\tau) = \mathbf{a}^s_{\mathbf{r}}(\tau)\mathbf{A}^{\mathbf{r}}_{\mathbf{x}_{eb}}(\tau), \tag{6.60}$$

according to Eqs. (4.25) and (4.31),

$$\mathbf{a}^s_{\mathbf{r}}(\tau) = \frac{\partial \Phi^s_{r,3}(\tau)}{\partial \mathbf{r}(\tau)} = \begin{pmatrix} e^s_{r,x}(\tau) & e^s_{r,y}(\tau) & e^s_{r,z}(\tau) \end{pmatrix},$$

$$e^s_{r,x}(\tau) = \frac{x_r(\tau) - x^s(\tau - \tau^s_r)}{\rho^s_r(\tau)}, \quad e^s_{r,y}(\tau) = \frac{y_r(\tau) - y^s(\tau - \tau^s_r)}{\rho^s_r(\tau)}, \quad e^s_{r,z}(\tau) = \frac{z_r(\tau) - z^s(\tau - \tau^s_r)}{\rho^s_r(\tau)},$$

and

$$\mathbf{c}(\tau) := \mathbf{t}^{\mathrm{T}}_\tau \begin{pmatrix} (\mathbf{E}^{2J+1}_c)^{\mathsf{T}} & (\mathbf{B}^{2J+1}_c)^{\mathsf{T}} \end{pmatrix} = \begin{pmatrix} c_1 & \cdots & c_{2J} \end{pmatrix}, \quad \mathbf{t}_\tau = \begin{pmatrix} \tau \\ \vdots \\ \tau^{2J+1} \end{pmatrix}, \tag{6.61}$$

with τ^s_r as the GPS signal travel time between the GPS satellite s and the GPS receiver r on-board LEO and with the factors $a(\tau)$ and $b(\tau)$ according to Eq. (6.9) and the Euler-Bernoulli coefficients in $\mathbf{c}(\tau)$ according to Eq. (6.47),

$$\mathbf{A}^{\mathbf{r}}_{\mathbf{x}_{eb}}(\tau) = \begin{pmatrix} a(\tau)\mathbf{I} & b(\tau)\mathbf{I} & c_1\mathbf{I} & \cdots & c_{2J}\mathbf{I} \end{pmatrix}, \quad \mathbf{I} = \begin{pmatrix} 1 & 0 & 0 \\ 0 & 1 & 0 \\ 0 & 0 & 1 \end{pmatrix}. \tag{6.62}$$

Gauss-Markov model for SST carrier phase observations: The linearized Gauss Markov model of the ionosphere-free carrier phase observations for the GPS satellite s at epoch τ can be written as,

$$\Delta\Phi^s_{r,3}(\tau) = \mathbf{a}^s_{\mathbf{r}}(\tau)\mathbf{A}^{\mathbf{r}}_{\mathbf{x}_{eb}}(\tau)\big(\mathbf{x}_{eb} - \mathbf{x}^0_{eb}\big) + \mathbf{a}^s_{\mathbf{x}_t}(\tau)\big(\mathbf{x}_t - \mathbf{x}^0_t\big) + \mathbf{a}^s_A(\tau)\big(\mathbf{x}_A - \mathbf{x}_{A,0}\big), \tag{6.63}$$

with the weight of the ionosphere-free carrier phase observations from the LEO r to the GPS satellite s,

$$w^s_{r,\Phi_3}(\tau) = \frac{\sigma^2_0}{\sigma^2_{\Phi^s_{r,3}(\tau)}} \cos^2(z^s_r(\tau)). \tag{6.64}$$

If m_τ is the total number of carrier phase observations at time τ from the GPS receiver r on-board LEO to GPS satellites $s_1, \ldots, s_{m_\tau}$ to , the Gauss-Markov model for all unknowns reads,

$$\begin{pmatrix} \Delta\Phi^{s_1}_{r,3}(\tau) \\ \vdots \\ \Delta\Phi^{s_j}_{r,3}(\tau) \\ \vdots \\ \Delta\Phi^{s_{m_\tau}}_{r,3}(\tau) \end{pmatrix} = \begin{pmatrix} \mathbf{a}^{s_1}_{\mathbf{r}}(\tau)\mathbf{A}^{\mathbf{r}}_{\mathbf{x}_{eb}}(\tau) \\ \vdots \\ \mathbf{a}^{s_j}_{\mathbf{r}}(\tau)\mathbf{A}^{\mathbf{r}}_{\mathbf{x}_{eb}}(\tau) \\ \vdots \\ \mathbf{a}^{s_{m_\tau}}_{\mathbf{r}}(\tau)\mathbf{A}^{\mathbf{r}}_{\mathbf{x}_{eb}}(\tau) \end{pmatrix} (\mathbf{x}_{eb} - \mathbf{x}_{eb,0}) + \begin{pmatrix} \mathbf{a}^{s_1}_{\mathbf{x}_t}(\tau) \\ \vdots \\ \mathbf{a}^{s_j}_{\mathbf{x}_t}(\tau) \\ \vdots \\ \mathbf{a}^{s_{m_\tau}}_{\mathbf{x}_t}(\tau) \end{pmatrix} (\mathbf{x}_t - \mathbf{x}_{t,0}) + \begin{pmatrix} \mathbf{a}^{s_1}_{\mathbf{x}_A}(\tau) \\ \vdots \\ \mathbf{a}^{s_j}_{\mathbf{x}_A}(\tau) \\ \vdots \\ \mathbf{a}^{s_{m_\tau}}_{\mathbf{x}_A}(\tau) \end{pmatrix} (\mathbf{x}_A - \mathbf{x}_{A,0}), \tag{6.65}$$

or in matrix notation as,

$$\Delta \mathbf{l}(\tau) = \mathbf{A}(\tau)\Delta \mathbf{x}, \tag{6.66}$$

with the weight matrix of all ionosphere-free carrier phase observations at the epoch τ,

$$\mathbf{W}(\tau) = \begin{pmatrix} w_{r,\Phi_3}^{s_1}(\tau) & \dots & 0 & \dots & 0 \\ \vdots & \ddots & \vdots & \ddots & \vdots \\ 0 & \dots & w_{r,\Phi_3}^{s_j}(\tau) & \dots & 0 \\ \vdots & \ddots & \vdots & \ddots & \vdots \\ 0 & \dots & 0 & \dots & w_{r,\Phi_3}^{s_{m_\tau}}(\tau) \end{pmatrix}. \tag{6.67}$$

If the total number of the carrier phase observations at epochs $\tau_1, \dots, \tau_K$ is $l (l \geq u)$, then the Gauss-Markov model for all tracked GPS satellites and all observed epochs reads,

$$\begin{pmatrix} \Delta \mathbf{l}(\tau_1) \\ \vdots \\ \Delta \mathbf{l}(\tau_K) \end{pmatrix} = \begin{pmatrix} \mathbf{A}(\tau_1) \\ \vdots \\ \mathbf{A}(\tau_K) \end{pmatrix} (\Delta \mathbf{x}), \tag{6.68}$$

or

$$\Delta \mathbf{l}_{(l)} = \mathbf{A}_{(l\times u)} \Delta \mathbf{x}_{(u)}, \quad \mathbf{W}_l = \begin{pmatrix} \mathbf{W}(\tau_1) & \cdots & \mathbf{0} \\ \vdots & \ddots & \vdots \\ \mathbf{0} & \cdots & \mathbf{W}(\tau_K) \end{pmatrix}, \tag{6.69}$$

where it holds for the matrix dimensions

l	the total number of carrier phase observations at epochs $\tau_1, \dots, \tau_K$,
u	the total number of the unknowns as $u = u_{eb} + u_t + u_A$,
u_{eb}	the number of Euler-Bernoulli coefficients for an upper index J ($u_{eb} = 6J$),
u_t	the total number of the LEO clock offsets ($u_t = K - 1$), except the first epoch,
u_A	the GPS ambiguity parameters.

The corrections to the approximate unknown parameters and the a-posteriori variance-covariance matrix can be determined in the batch processing of all carrier phase SST observations according to

$$\Delta \hat{\mathbf{x}} = \left(\mathbf{A}^{\mathrm{T}} \mathbf{W}_l \mathbf{A}\right)^{-1} \mathbf{A}^{\mathrm{T}} \mathbf{W}_l \Delta \mathbf{l}, \quad \mathbf{C}_{\Delta \hat{\mathbf{x}}} = \left(\mathbf{A}^{\mathrm{T}} \mathbf{W}_l \mathbf{A}\right)^{-1}. \tag{6.70}$$

The estimated unknows in Eq. (6.70) are the corrections to the initial Euler-Bernoulli coefficients, the initial LEO clock offsets and the initial ambiguities of all observed GPS satellites from GPS receiver r on-board LEO. Because of the linearization, the estimation procedure has to be performed in an iterative manner. The convergence of the unknowns can be achieved after a few iterations as,

$$\hat{\mathbf{x}}_{(i)} = \hat{\mathbf{x}}_{(i-1)} + \Delta \hat{\mathbf{x}}_{(i)} = \hat{\mathbf{x}}_{(i-1)} + \left(\mathbf{A}_{(i)}^{\mathrm{T}} \mathbf{W}_l \mathbf{A}_{(i)}\right)^{-1} \mathbf{A}_{(i)}^{\mathrm{T}} \mathbf{W}_l \Delta \mathbf{l}_{(i)}. \tag{6.71}$$

6.1.3 The Hybrid Case: Fourier Series and Euler-Bernoulli Polynomials

In the hybrid or combination version, the function $\mathbf{d}(\tau)$ is represented by a finite series in terms of Euler- and Bernoulli polynomials and a residual finite Fourier series,

$$\mathbf{d}(\tau) \equiv \bar{\mathbf{d}}_F^{\bar{n}}(\tau) + \mathbf{d}_P^{J_{max}}(\tau). \tag{6.72}$$

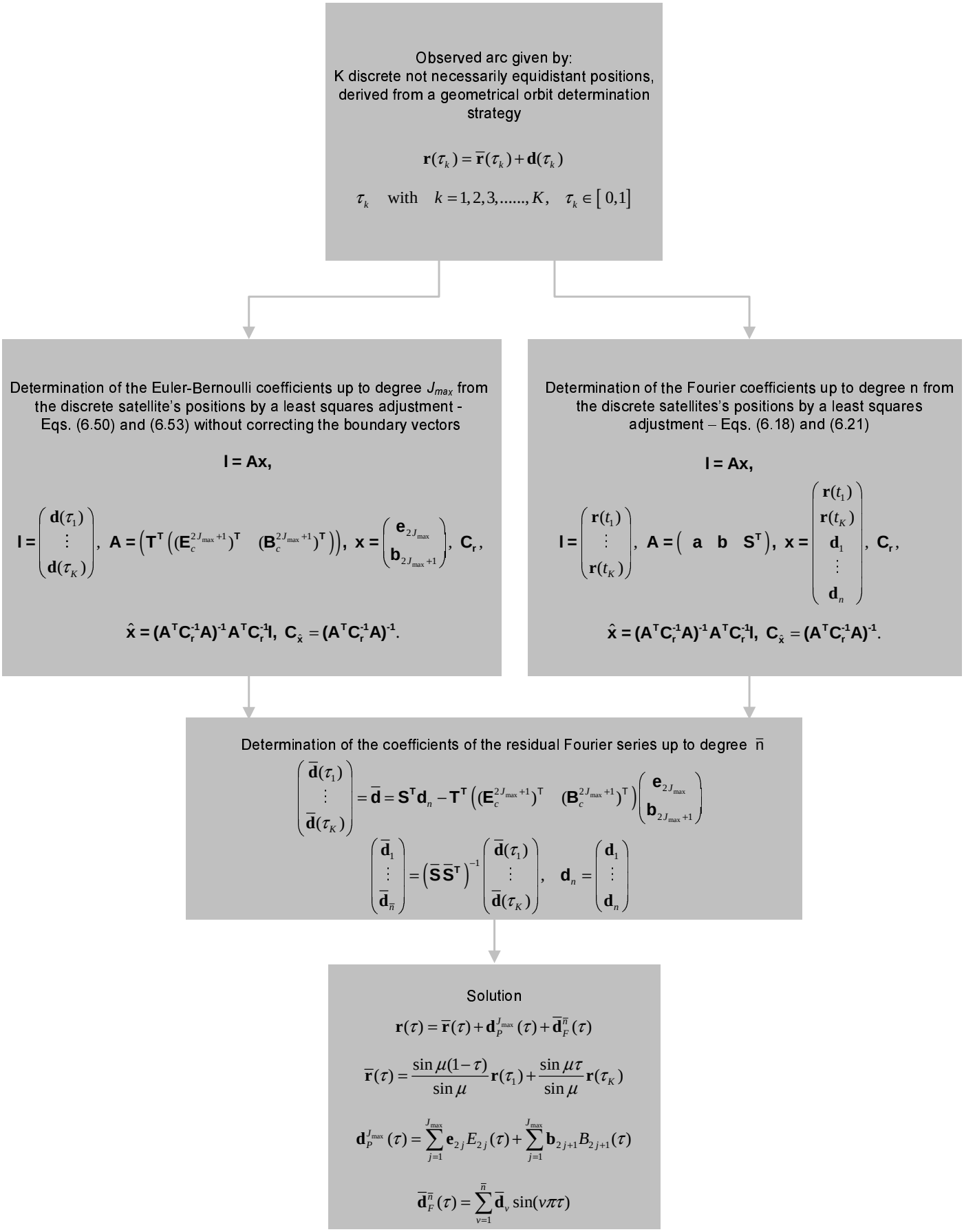

Figure 6.1: Computation scheme of the kinematical orbit determination procedure, with Euler-Bernoulli coefficients calculated from given LEO absolute positions.

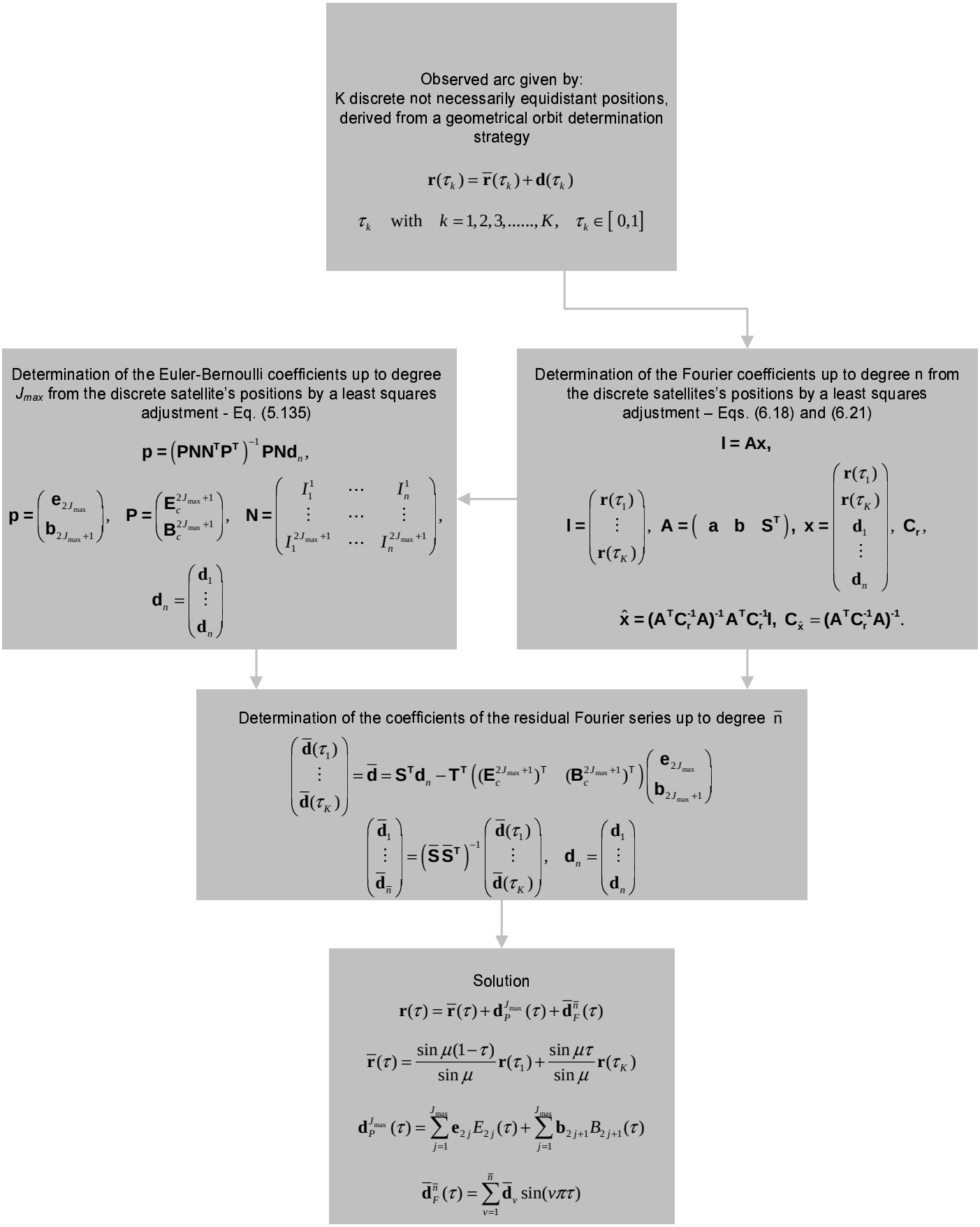

Figure 6.2: Computation scheme of the kinematical orbit determination procedure, with Euler-Bernoulli coefficients calculated from amplitudes of Fourier series.

The residual Fourier series is restricted by an upper index $\bar{n}$ and the Euler-Bernoulli polynomials by an upper index J_{max}. As demonstrated in Sec. 5.4.1.3, the approximation quality of a combination of both series is superior compared to the approximation of either one of these series as discussed in the Secs. 6.1.1 and 6.1.2.

Because of the fact that both orbit representations could be used exclusively, the combination of both series requires a specific strategy, otherwise a linear dependency occurs in the observation equation. As demonstrated in Sec. 5.4.1.3, a fit of a series in terms of Euler-Bernoulli polynomials to the orbit up to a reasonable upper degree J_{max} (e.g. $J_{max} = 4$) will guarantee a sufficient confident determination of the Euler-Bernoulli coefficients. In that case, the residual sine series $\bar{\mathbf{d}}_F^{\bar{n}}(\tau)$ will show an improved fast convergence and low residuals of the combined series when compared to the true ephemerides. Therefore, in a first step, the Euler-Bernoulli polynomial coefficients are derived based on the geometrically determined positions (Sec. 6.1.2.1) or by using directly the carrier phase GPS-SST observations (Sec. 6.1.2.2). Because of the reduced approximation accuracy of the orbit by a series in terms of Euler-Bernoulli polynomials up to a maximum degree $J_{max} = 4$ according to the Eq. (5.119), it is sufficient to determine the coefficients of the Euler-Bernoulli polynomials without correcting the boundary vectors but taking the observation weights into account. Another possibility is to perform a least squares fit of the Fourier series to the pseudo observed positions or based on the observed carrier phase GPS-SST observations, respectively, following the procedures as described in Sec. 6.1.1, and to determine the coefficients of the Euler-Bernoulli polynomials subsequently from the coefficients of the sine functions according to Eq. (5.135). The coefficients of the Euler-and Bernoulli polynomials differ slightly depending on the selected procedure. But the differences will be compensated by the residual sine series. Both alternatives are illustrated in the flowcharts Fig. 6.1 and Fig. 6.2. The flowcharts show only the case where the observations are given as K discrete not necessarily equidistant positions, derived from geometrical orbit determination strategy. The use of the carrier phase GPS-SST measurements is similar but not shown here.

With the Euler-Bernoulli coefficients, the Euler-Bernoulli part of the difference function can be determined:

$$\mathbf{d}_P^{J_{\max}}(\tau) = \sum_{j=1}^{J_{\max}} \mathbf{e}_{2j} E_{2j}(\tau) + \sum_{j=1}^{J_{\max}} \mathbf{b}_{2j+1} B_{2j+1}(\tau), \tag{6.73}$$

and the difference function,

$$\bar{\mathbf{d}}(\tau) = \mathbf{d}(\tau) - \mathbf{d}_P^{J_{\max}}(\tau) = \sum_{\nu=1}^{\bar{n}} \bar{\mathbf{d}}_\nu \sin(\nu\pi\tau), \tag{6.74}$$

is modelled by a sine series $\bar{\mathbf{d}}_F^{\bar{n}}(\tau)$, again by a least squares adjustment fitting to the difference function $\bar{\mathbf{d}}(\tau)$. The upper degree $\bar{n}$ of this series depends on its convergence behaviour. It will depend on the smoothness conditions at the boundaries of this function, if it is periodically continued. The system of equations reads for the epochs $\tau_1, \ldots, \tau_K$,

$$\begin{pmatrix} \bar{\mathbf{d}}(\tau_1) \\ \vdots \\ \bar{\mathbf{d}}(\tau_K) \end{pmatrix} = \bar{\mathbf{d}} = \mathbf{S}^{\mathrm{T}}\mathbf{d}_n - \mathbf{T}^{\mathrm{T}} \begin{pmatrix} (\mathbf{E}_c^{2J_{\max}+1})^{\mathrm{T}} & (\mathbf{B}_c^{2J_{\max}+1})^{\mathrm{T}} \end{pmatrix} \begin{pmatrix} \mathbf{e}_{2J_{\max}} \\ \mathbf{b}_{2J_{\max}+1} \end{pmatrix}, \tag{6.75}$$

and the Fourier amplitudes up to the index $\bar{n}$ are derived based on the sine analysis of the difference function,

$$\begin{pmatrix} \bar{\mathbf{d}}_1 \\ \vdots \\ \bar{\mathbf{d}}_{\bar{n}} \end{pmatrix} = \left(\bar{\mathbf{S}}\,\bar{\mathbf{S}}^{\mathrm{T}}\right)^{-1} \begin{pmatrix} \bar{\mathbf{d}}(\tau_1) \\ \vdots \\ \bar{\mathbf{d}}(\tau_K) \end{pmatrix}, \quad \bar{\mathbf{S}}^{\mathrm{T}} = \begin{pmatrix} \sin(\pi\tau_1) & \cdots & \sin(\bar{n}\pi\tau_1) \\ \vdots & \vdots & \vdots \\ \sin(\pi\tau_K) & \cdots & \sin(\bar{n}\pi\tau_K) \end{pmatrix}. \tag{6.76}$$

The smoothness is defined by the degree of differentiability of the periodically continued function $\bar{\mathbf{d}}(\tau)$. If the (unknown) real orbit and the Euler-Bernoulli polynomials have identical derivatives up to a high degree, then the difference function $\bar{\mathbf{d}}(\tau)$ shows differentiability up to this degree as well. The convergence behaviour

of the Fourier series $\bar{\mathbf{d}}_F^{\bar{n}}(\tau)$ is closely related to this degree of differentiability. Because of the fact that the Euler-Bernoulli polynomials are constructed such that the derivatives of the satellite's arcs coincide with those of the Euler-Bernoulli polynomials, the coincidence should be realized up to a high degree. But this holds only theoretically, because the quality of the approximation depends on the maximum index $J_{\max}$ of $\mathbf{d}_P^{J_{\max}}(\tau)$ and of the accuracy of the real orbit which is known only point-wise by carrier phase GPS-SST observations. The Fig. 5.13 shows the residual functions $\bar{\mathbf{d}}(\tau) = \mathbf{d}(\tau) - \mathbf{d}_P^{J_{\max}}(\tau)$ for various upper indices $J_{\max} = 1, 2, 3, 4, 5$ and Fig. 5.19 shows the residuals of the sum of both functions for the Euler-Bernoulli up to $J_{max} = 4$ and different upper indices $\bar{n}$ compared to the error-free values in the ellipse mode.

6.2 Reduced-Kinematical and Dynamical Orbit Determination

The kinematical orbit determination is based on discrete measurements, either positions derived from a GNSS processing strategy as described in chapter 4, or used directly as observations to derive the parameters of any of the kinematical orbit determination modes described in Sec. 6.1. The kinematical orbit parameters contain no dynamic information of the force function model; they are only based on empirical observations, taken at discrete epochs of the satellite's motion along the orbit. In the following, we will extend the hybrid case of the kinematical orbit determination procedures as treated in Sec. 6.1.3 in such a way that dynamical restrictions can be introduced in the orbit determination procedure. This dynamical information is contained in the orbit coefficients $\mathbf{d}_\nu$ which are related to the force function according to Eqs. (5.13), (5.23) or (5.34) and the respective reference motion types Eqs. (5.10), (5.20) or (5.37). To show the principle behind this idea, we demonstrate it in case of Eq. (5.23),

$$\tilde{\mathbf{d}}_\nu = -\frac{2T^2}{\nu^2\pi^2 - \mu^2} \int_{\tau'=0}^{1} \sin(\nu\pi\tau')\, \mathbf{a}^{II}(\tau; \mathbf{r}, \dot{\mathbf{r}})\, d\tau'.$$

If we restrict the dynamical model to the gravitational field of the Earth, expressed by a spherical harmonics expansion up to degree l_{max}, then it holds,

$$\mathbf{a}^{II}(\tau; \mathbf{r}, \dot{\mathbf{r}}) = \mathbf{a}(\tau; \mathbf{r}, \dot{\mathbf{r}}) - \frac{GM}{a^3}\mathbf{r}(\tau), \quad \mathbf{a}(\tau; \mathbf{r}, \dot{\mathbf{r}}) = \nabla V(\tau; \mathbf{r}, \dot{\mathbf{r}}), \tag{6.77}$$

with the gravitational potential,

$$V = \frac{GM}{\|\mathbf{r}\|} \sum_{l=0}^{l_{\max}} \sum_{m=0}^{l} \left(\frac{R}{\|\mathbf{r}\|}\right)^l \left(c_{lm} C_{lm}(\vartheta, \lambda) + s_{lm} S_{lm}(\vartheta, \lambda)\right), \tag{6.78}$$

the surface spherical harmonics of degree l and order m,

$$C_{lm}(\vartheta, \lambda) = P_l^m(\cos\vartheta)\sin(m\lambda), \quad S_{lm}(\vartheta, \lambda) = P_l^m(\cos\vartheta)\cos(m\lambda), \tag{6.79}$$

and the associated Legendre functions $P_l^m(\cos\vartheta)$. The dynamical restrictions can be introduced in the system of observation equations as a-priori information and an appropriate a-priori variance-covariance matrix. If we consider for simplification the case of pseudo observed positions, then it reads according to Eq. (6.18),

$$\begin{pmatrix} \mathbf{r}(\tau_1) \\ \vdots \\ \mathbf{r}(\tau_K) \\ \tilde{\mathbf{d}}_i \\ \vdots \\ \tilde{\mathbf{d}}_j \end{pmatrix} = \begin{pmatrix} a(\tau_1) & b(\tau_1) & \sin(\pi\tau_1) & \cdots & \sin(i\pi\tau_1) & \cdots & \sin(j\pi\tau_1) & \cdots & \sin(n\pi\tau_1) \\ \vdots & \vdots & \vdots & \vdots & \vdots & \vdots & \vdots & \vdots & \vdots \\ a(\tau_K) & b(\tau_K) & \sin(\pi\tau_K) & \cdots & \sin(i\pi\tau_K) & \cdots & \sin(j\pi\tau_K) & \cdots & \sin(n\pi\tau_K) \\ 0 & 0 & 0 & \cdots & 1 & \cdots & 0 & \cdots & 0 \\ \vdots & \vdots & \vdots & \vdots & \vdots & \vdots & \vdots & \vdots & \vdots \\ 0 & 0 & 0 & 0 & 0 & \cdots & 1 & \cdots & 0 \end{pmatrix} \begin{pmatrix} \mathbf{r}(\tau_1) \\ \mathbf{r}(\tau_K) \\ \mathbf{d}_1 \\ \vdots \\ \mathbf{d}_i \\ \vdots \\ \mathbf{d}_j \\ \vdots \\ \mathbf{d}_n \end{pmatrix}$$

(6.80)

with the variance-covariance matrix

$$\mathbf{C}_\mathbf{l} = \begin{pmatrix} \mathbf{C}(\tau_1) & \cdots & \mathbf{0} & \mathbf{0} & \cdots & \mathbf{0} \\ \vdots & \ddots & \vdots & \vdots & \ddots & \vdots \\ \mathbf{0} & \cdots & \mathbf{C}(\tau_K) & \mathbf{0} & \cdots & \mathbf{0} \\ \mathbf{0} & \cdots & \mathbf{0} & \mathbf{C}(\tilde{\mathbf{d}}_i) & \cdots & \mathbf{0} \\ \vdots & \ddots & \vdots & \vdots & \ddots & \vdots \\ \mathbf{0} & \cdots & \mathbf{0} & \mathbf{0} & \cdots & \mathbf{C}(\tilde{\mathbf{d}}_j) \end{pmatrix}. \tag{6.81}$$

The quantities $\tilde{\mathbf{d}}_i$ to $\tilde{\mathbf{d}}_j$ are considered as a-priori information with the variance-covariance matrices $\mathbf{C}(\tilde{\mathbf{d}}_i)$ to $\mathbf{C}(\tilde{\mathbf{d}}_j)$. The indices i and j define the sine coefficients with a-priori information and can be selected so that they cover the total index domain $i = 1$ and $j = n$ or some specific amplitudes. If we split up the design matrix Eq. (6.80) with the variance-covariance matrix $\mathbf{C}_\mathbf{l}$,

$$\mathbf{l} = \mathbf{A}\mathbf{x}, \tag{6.82}$$

in the following way (do not mix up the observation column matrix $\mathbf{l}$ in Eq. (6.82) with the unit matrix $\mathbf{I}$ in Eq. (6.83)),

$$\begin{pmatrix} \mathbf{l}_1 \\ \mathbf{l}_2 \end{pmatrix} = \begin{pmatrix} \mathbf{A}_1 & \mathbf{A}_2 \\ \mathbf{0} & \mathbf{I} \end{pmatrix} \begin{pmatrix} \mathbf{x}_1 \\ \mathbf{x}_2 \end{pmatrix}, \tag{6.83}$$

with the a-priori variance-covariance matrix Eq. (6.81),

$$\mathbf{C}_\mathbf{l} = \begin{pmatrix} \mathbf{C}_1 & \mathbf{0} \\ \mathbf{0} & \mathbf{C}_2 \end{pmatrix}, \tag{6.84}$$

with

$$\mathbf{l}_1 = \begin{pmatrix} \mathbf{r}(\tau_1) & \cdots & \mathbf{r}(\tau_K) \end{pmatrix}^\mathrm{T}, \quad \mathbf{l}_2 = \begin{pmatrix} \tilde{\mathbf{d}}_i & \cdots & \tilde{\mathbf{d}}_j \end{pmatrix}^\mathrm{T}, \quad \mathbf{A}_1 = \begin{pmatrix} \mathbf{a} & \mathbf{b} \end{pmatrix}, \quad \mathbf{A}_2 = \mathbf{S}^\mathrm{T}, \tag{6.85}$$

$$\mathbf{C}_1 = \begin{pmatrix} \mathbf{C}(\tau_1) & \cdots & \mathbf{0} \\ \vdots & \ddots & \vdots \\ \mathbf{0} & \cdots & \mathbf{C}(\tau_K) \end{pmatrix}, \quad \mathbf{C}_2 = \mathbf{C}(\tilde{\mathbf{d}}) = \begin{pmatrix} \mathbf{C}(\tilde{\mathbf{d}}_i) & \cdots & \mathbf{0} \\ \vdots & \ddots & \vdots \\ \mathbf{0} & \cdots & \mathbf{C}(\tilde{\mathbf{d}}_j) \end{pmatrix}. \tag{6.86}$$

The least squares solution reads (Ilk 1977, Eq. (90))

$$\begin{pmatrix} \hat{\mathbf{x}}_1 \\ \hat{\mathbf{x}}_2 \end{pmatrix} = \mathbf{N}^{-1} \begin{pmatrix} \mathbf{A}_1^\mathrm{T}\mathbf{C}_1^{-1}\mathbf{l}_1 \\ \mathbf{A}_2^\mathrm{T}\mathbf{C}_1^{-1}\mathbf{l}_1 + \mathbf{C}_2^{-1}\mathbf{l}_2 \end{pmatrix}, \tag{6.87}$$

with the inverse normal matrix

$$\mathbf{N}^{-1} = \begin{pmatrix} \mathbf{Q}_{\hat{\mathbf{x}}_1\hat{\mathbf{x}}_1} & \mathbf{Q}_{\hat{\mathbf{x}}_1\hat{\mathbf{x}}_2} \\ \mathbf{Q}_{\hat{\mathbf{x}}_2\hat{\mathbf{x}}_1} & \mathbf{Q}_{\hat{\mathbf{x}}_2\hat{\mathbf{x}}_2} \end{pmatrix}, \tag{6.88}$$

and its sub-matrices

$$\mathbf{Q}_{\hat{\mathbf{x}}_1\hat{\mathbf{x}}_1} = \left(\mathbf{A}_1^\mathrm{T}\bar{\mathbf{C}}^{-1}\mathbf{A}_1\right)^{-1}, \tag{6.89}$$

$$\mathbf{Q}_{\hat{\mathbf{x}}_1\hat{\mathbf{x}}_2} = -\mathbf{Q}_{\hat{\mathbf{x}}_1\hat{\mathbf{x}}_1}\mathbf{A}_1^\mathrm{T}\bar{\mathbf{C}}^{-1}\mathbf{A}_2\mathbf{C}_2, \tag{6.90}$$

$$\mathbf{Q}_{\hat{\mathbf{x}}_2\hat{\mathbf{x}}_1} = -\mathbf{C}_2\mathbf{A}_2^\mathrm{T}\bar{\mathbf{C}}^{-1}\mathbf{A}_1\mathbf{Q}_{\hat{\mathbf{x}}_1\hat{\mathbf{x}}_1}, \tag{6.91}$$

$$\mathbf{Q}_{\hat{\mathbf{x}}_2\hat{\mathbf{x}}_2} = \mathbf{C}_2 - \mathbf{C}_2\mathbf{A}_2^{\mathrm{T}}\bar{\mathbf{C}}^{-1}\mathbf{A}_2\mathbf{C}_2 + \mathbf{C}_2\mathbf{A}_2^{\mathrm{T}}\bar{\mathbf{C}}^{-1}\mathbf{A}_1\mathbf{Q}_{\hat{\mathbf{x}}_1\hat{\mathbf{x}}_1}\mathbf{A}_1^{\mathrm{T}}\bar{\mathbf{C}}^{-1}\mathbf{A}_2\mathbf{C}_2, \tag{6.92}$$

$$\bar{\mathbf{C}} = \mathbf{C}_1 + \mathbf{A}_2\mathbf{C}_2\mathbf{A}_2^{\mathrm{T}}. \tag{6.93}$$

The unknowns can be written explicitly,

$$\hat{\mathbf{x}}_1 = \mathbf{Q}_{\hat{\mathbf{x}}_1\hat{\mathbf{x}}_1}\mathbf{A}_1^{\mathrm{T}}\mathbf{C}_1^{-1}\mathbf{l}_1 + \mathbf{Q}_{\hat{\mathbf{x}}_1\hat{\mathbf{x}}_2}\mathbf{A}_2^{\mathrm{T}}\mathbf{C}_1^{-1}\mathbf{l}_1 + \mathbf{Q}_{\hat{\mathbf{x}}_1\hat{\mathbf{x}}_2}\mathbf{C}_2^{-1}\mathbf{l}_2, \tag{6.94}$$

$$\hat{\mathbf{x}}_2 = \mathbf{Q}_{\hat{\mathbf{x}}_2\hat{\mathbf{x}}_1}\mathbf{A}_1^{\mathrm{T}}\mathbf{C}_1^{-1}\mathbf{l}_1 + \mathbf{Q}_{\hat{\mathbf{x}}_2\hat{\mathbf{x}}_2}\mathbf{A}_2^{\mathrm{T}}\mathbf{C}_1^{-1}\mathbf{l}_1 + \mathbf{Q}_{\hat{\mathbf{x}}_2\hat{\mathbf{x}}_2}\mathbf{C}_2^{-1}\mathbf{l}_2. \tag{6.95}$$

The last terms of these equations can be written with the respective sub-matrices from Eq. (6.89) to Eq. (6.93),

$$\mathbf{Q}_{\hat{\mathbf{x}}_1\hat{\mathbf{x}}_2}\mathbf{C}_2^{-1}\mathbf{l}_2 = -\mathbf{Q}_{\hat{\mathbf{x}}_1\hat{\mathbf{x}}_1}\mathbf{A}_1^{\mathrm{T}}\bar{\mathbf{C}}^{-1}\mathbf{A}_2\mathbf{l}_2, \tag{6.96}$$

$$\mathbf{Q}_{\hat{\mathbf{x}}_2\hat{\mathbf{x}}_2}\mathbf{C}_2^{-1}\mathbf{l}_2 = \mathbf{l}_2 - \mathbf{C}_2\mathbf{A}_2^{\mathrm{T}}\bar{\mathbf{C}}_1^{-1}\mathbf{A}_2\mathbf{l}_2 + \mathbf{C}_2\mathbf{A}_2^{\mathrm{T}}\bar{\mathbf{C}}^{-1}\mathbf{A}_1\mathbf{Q}_{\hat{\mathbf{x}}_1\hat{\mathbf{x}}_1}\mathbf{A}_1^{\mathrm{T}}\bar{\mathbf{C}}^{-1}\mathbf{A}_2\mathbf{l}_2. \tag{6.97}$$

If the pseudo observations $\mathbf{l}_2$ are determined based on the integrals Eq. (5.23) with a specific gravitational potential and the a-priori variance-covariance matrix $\mathbf{C}_2 \rightarrow \mathbf{0}$ then it follows,

$$\hat{\mathbf{x}}_1 = \left(\mathbf{A}_1^{\mathrm{T}}\mathbf{C}_1^{-1}\mathbf{A}_1\right)^{-1}\mathbf{A}_1^{\mathrm{T}}\mathbf{C}_1^{-1}\left(\mathrm{l}_1 - \mathbf{A}_2\mathbf{l}_2\right), \tag{6.98}$$

$$\hat{\mathbf{x}}_2 = \mathbf{l}_2. \tag{6.99}$$

In that case, the amplitudes are fixed according to the gravitational potential used and only the boundary values are corrected. The result corresponds to the result of a dynamical orbit determination. Besides this strict dynamical restrictions, there are basically three different possibilities to influence the kinematical orbit determination by dynamical information and to come up with a reduced kinematical orbit determination modification,

1. introduction of an approximate force function for the determination of the values $(\mathbf{d}_i \cdots \mathbf{d}_j)$, combined with an approximate a-priori variance-covariance matrix $\mathbf{C}_2 = \mathbf{C}(\tilde{\mathbf{d}})$,
2. fixing only some orbit parameters $(\mathbf{d}_i \cdots \mathbf{d}_j)$ by setting a low variance-covariance matrix for $\mathbf{C}_2 = \mathbf{C}(\tilde{\mathbf{d}}) \rightarrow \mathbf{0}$,
3. down- or up-weighting of the a-priori variance-covariance matrix $\mathbf{C}_2$ in relation to $\mathbf{C}_1$.

Because of these various possibilities to adopt the character of the orbit to a variety of applications covering the spectrum from a pure kinematical on the one end to a pure dynamical orbit determination on the other end makes this approach very flexible.

Fig. 6.3 shows a flowchart of the computation steps. Because of the fact that the force function depends on the knowledge of the orbit, the procedure requires an iteration. Therefore, a kinematical orbit determination has to be performed first, and subsequently a reduced-kinematical modification can be performed as shown in the flowchart.

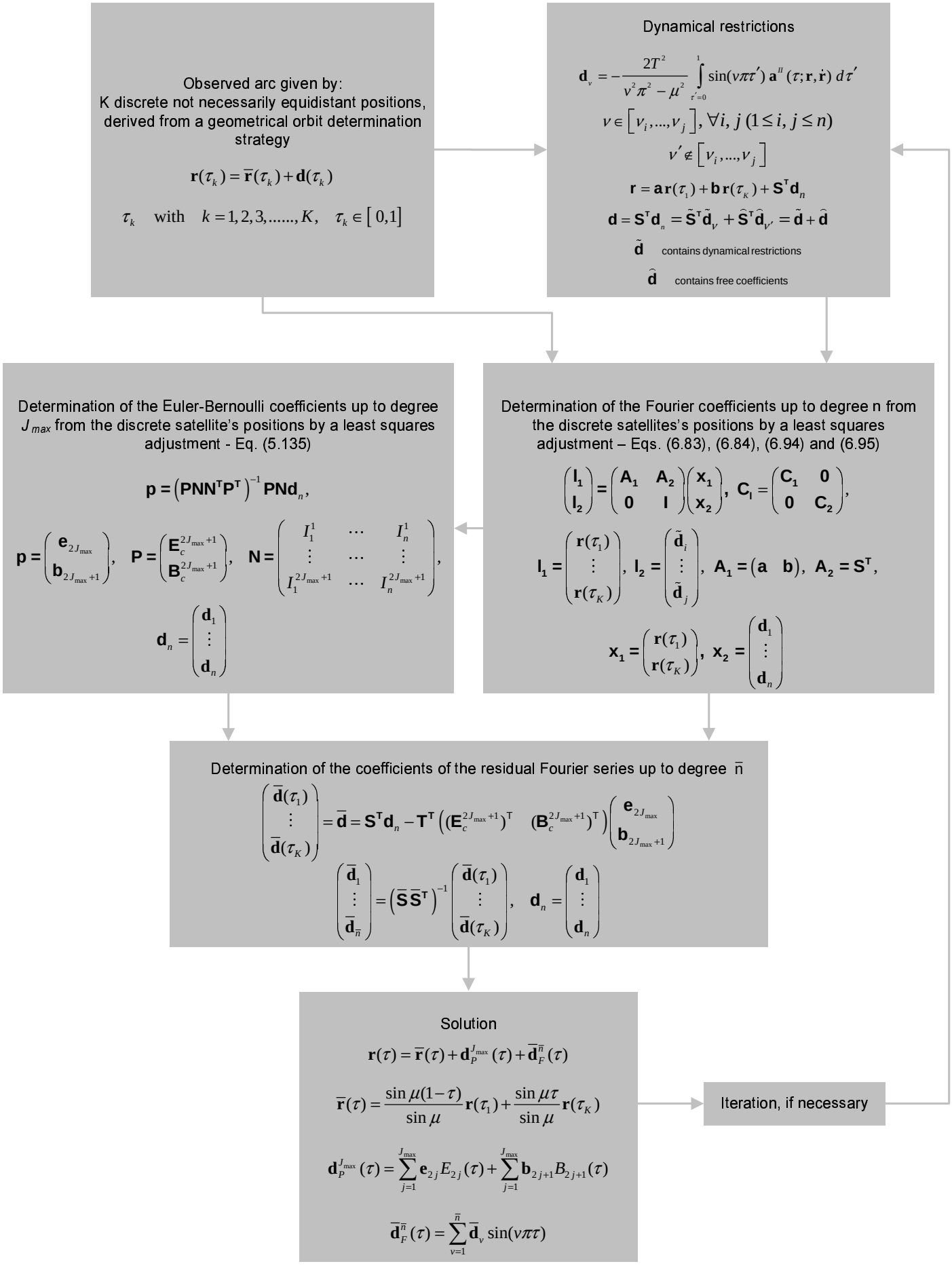

Figure 6.3: Computation scheme of the reduced-kinematical orbit determination strategy, with Euler-Bernoulli calculated from amplitudes of Fourier series.

7. Test Computations

7.1 GPS-SST Observation Preparations

7.1.1 SC7 Dataset

To determine the LEO's orbits, code pseudo-range and carrier phase Satellite-to-Satellite Tracking (SST) measurements between a sufficient number of GNSS satellites and the LEO will be used in the following. To simulate the geometrical precise orbit determination procedure, the ephemerides of the GNSS satellites and the LEO are necessary. In this research, the simulated SC7 data set (Special Commission of IAG-SC7, www.geod.uni-bonn.de) has been used. In this data set, the mission scenarios of CHAMP, GRACE and GOCE as LEOs have been simulated to provide a unique easily accessible data set for various comparisons. The SC7 data set covers a time period of 30 days and includes the absolute positions, velocities and accelerations of the GPS satellites as well as the LEOs and reference frame specifications. The simulation scenarios are simplified in so far as there is no noise in the data for the LEOs and GPS orbits. The files of the GPS-satellites and CHAMP contain observation epochs in Modified Julian Date (MJD), absolute positions ($\mathbf{r}$), velocities ($\dot{\mathbf{r}}$) and accelerations ($\ddot{\mathbf{r}}$) of LEOs and GPS satellites. The absolute coordinates refer to a (quasi) inertial system with origin in the center of mass of the Earth and the axes directed to the principal axes of inertia. The relation of this quasi-inertial system to the Earth fixed coordinate system is defined by the sidereal time as rotation angle between the two specified coordinate systems.

7.1.2 GPS-SST Observation in the RINEX

Standard format for the GPS observations in case of ground-tracked and space-tracked GPS satellites is the **R**eceiver **IN**dependent **E**xchange (**RINEX**) format. To unify the simulation cases with the real cases and to enable a simple processing of the GPS data, the GPS observation file for the simulated observations have to be provided in the RINEX format. To mitigate the effect of low elevated GPS satellites on the accuracy of a point-wise positioning of LEOs, a proper cut-off angle is necessary in the processing. The elevation angle of the GPS receiver on-board LEO has to be applied in the data preparation of the simulated observations.

To generate the observation file which contains the GPS-SST observations in the simulated case, the ephemerides of the GPS satellites and the LEOs have been selected with an interval of 30 sec. Some comparisons are performed with a 10 sec. sampling rate. With the application of a 15° cut-off angle, the code pseudo-range observations as GPS-SST observations read in the RINEX format as shown in Fig. 7.1. In this observation file, only code pseudo-range observations between the GPS satellites (as sender) and GPS receiver on-board LEO (as receiver) have been simulated.

7.1.3 Simulation Scenarios

To test the proposed orbit determination strategies, different scenarios have been simulated in the undifferenced (zero difference) observation mode. The simulation of a geometrical scenario has been designed based on error free zero difference GPS-SST observations. Then errors (white noise) in the GPS-SST observations simulate the real geometrical orbit determination environment. The geometrically determined orbits will be used as pseudo observations together with the error variance-covariance matrices for the sub-sequent kinematical and reduced-kinematical orbit determination modes. But also the direct GPS-SST observations can be used as original observations for the different orbit determination modifications, as shown in the following.

The geometrical precise orbit determination strategy has been tested in the simulation case with the SC7 data set. For the tests based on real observations, data sets of CHAMP have been used, which are provided by the ISDC-GFZ Potsdam, Germany.

```
    1    C1                                                    # / TYPES OF OBSERV
                                                               END OF HEADER
00  7 17  8  0  0.0000000  0  8G30G25G23G21G 9G 6G 5G 1
 20091106.04000
 22984660.68300
 22519093.24900
 21541999.37800
 23806393.26700
 22435297.82200
 21862286.32400
 20615971.76500
00  7 17  8  0 10.0000000  0  8G30G25G23G21G 9G 6G 5G 1
 20114432.91800
 23004950.85600
 22462466.03500
 21514728.30300
 23840276.93100
 22377084.79500
 21916119.78200
 20652183.74400
00  7 17  8  0 20.0000000  0  8G30G25G23G21G 9G 6G 5G 1
 20139060.24400
 23025917.81700
 22406273.42500
 21488097.59600
 23874499.96800
 22319618.98900
 21970748.29200
 20689166.69300
00  7 17  8  0 30.0000000  0  7G30G25G23G21G 6G 5G 1
 20164979.31900
 23047558.81400
 22350524.93100
 21462113.07900
 22262914.59900
 22026156.75000
 20726912.93300
```

Figure 7.1: GPS observation file in the RINEX format

7.2 Geometrical Precise Orbit Determination (GPOD)

7.2.1 Simulated Case

To test the proposed geometrical orbit determination strategy to estimate the LEOs absolute positions from code pseudo-range and carrier phase observations in the zero differenced mode, a simulation example will be considered. Based on the SC7 data set, one satellite revolution has been selected and carrier phase observations have been simulated. In the pre-processing step, a cut off angle of 15° has been applied to the GPS-SST observations to simulate the real case of a geometrical orbit determination. The GPS-SST observations are contaminated with white noise of a standard deviation of 1cm, 2cm and 5cm, respectively. In Fig. 7.2, a simulated CHAMP orbit is shown.

In Fig. 7.3, the number of processed GPS satellites and the position dilution of precision (PDOP) is shown. This gives an impression of the geometrical strength of the GPS satellite configuration. There are always at least 5 GPS satellites available and occasionally up to 10 GPS satellites. The PDOP remains between 1 and 1.5, which represents a strong geometrical satellite configuration. In Fig. 7.4, elevation of the GPS satellites and PDOP values at every observation epoch are shown. It should be pointed out that PODP values are used to estimate the position precision.

The results of the processing of the GPS-SST observations in the simulation case are shown in Fig. 7.6 as differences of the point-wise estimated and given absolute positions. In Fig. 7.5, the corresponding GPS-SST observation residuals are presented. As can be seen, the differences between the estimated LEO absolute

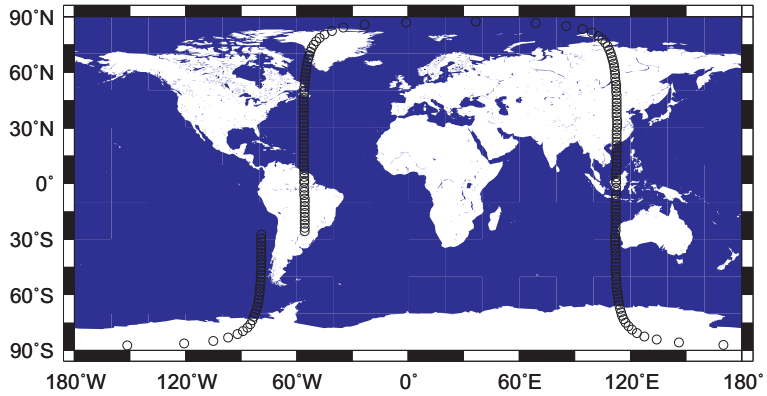

Figure 7.2: One revolution ground track of CHAMP.

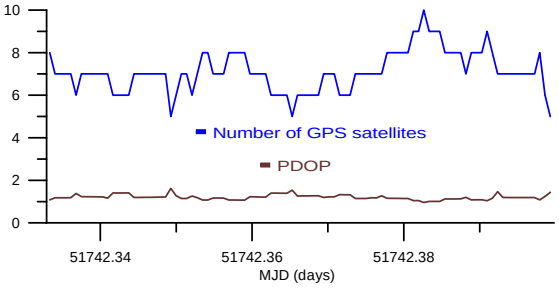

Figure 7.3: The number of processed GPS satellites and PDOPs at the observed epochs.

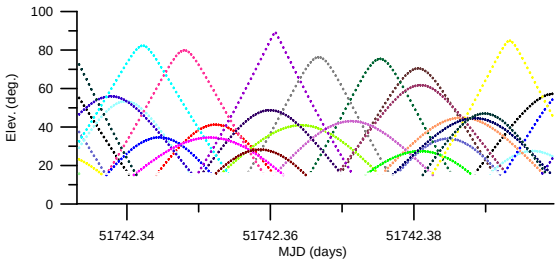

Figure 7.4: Elevation of tracked GPS satellites.

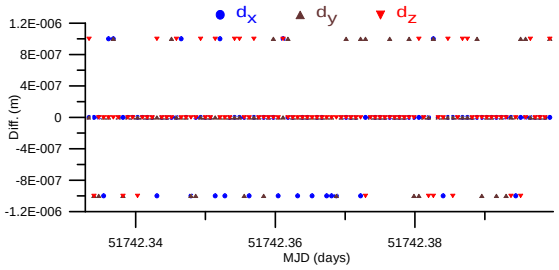

Figure 7.5: The GPS-SST observation residuals *(error free case)*.

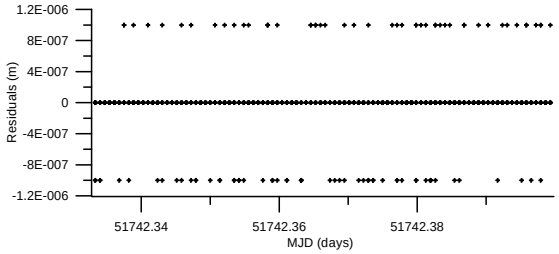

Figure 7.6: The differences of point-wise estimated and given absolute positions *(error free case)*.

positions and the given positions as well as the corresponding GPS-SST observation residuals are in the range of the calculation accuracy of the computer.

To test the proposed geometrical LEO orbit determination strategy in the error case, the GPS-SST observations have to be contaminated with different white noise levels. In the following white noise levels of 1cm, 2cm and finally 5cm in the GPS-SST observations have been selected. In Fig. 7.7, the absolute position differences referred to the SC7 positions are shown for a white noise of 1cm. As can be seen, most of the differences are in the range of the observation noise of 1cm. It should be pointed out that in the GPS data processing, especially in zero difference mode of data processing, there is a linear dependency between the observation precision and the estimated absolute position precision. For example, if the GPS observations are preprocessed and the precision of observations is in the range of 1cm, then the precision of estimated absolute position is in the range of 1cm as well. But it is clear that the configuration of tracked GPS satellites plays an important role in the precision of the estimated positions as well (which is expressed by the PDOP

value). Therefore, the PDOP value is a factor, which indicates the factor of precision of the position (Xu 2007). It can reduce the accuracy of the estimated positions in case of a high PDOP value. In Fig. 7.8 the GPS-SST observation residuals are shown for the white noise case of 1cm. Figs. 7.9 and 7.10 show the situation for a white noise level of 2cm. Nowadays, the accuracy of the estimated LEO orbit is in the size between 2cm to 5cm. Figs. 7.11 and 7.12 show the corresponding results for a white noise level of 5cm.

It should be mentioned that the geometrical orbit determination produces an ephemerid of position coordinates where the accuracy depends on the configuration of the GPS satellites and on the precision of the GPS-SST observations. For the simulation cases, the processing of the GPS-SST observations can be performed either in the single epoch processing mode or in the batch processing mode. The single and batch processing modes have to deliver the same results.

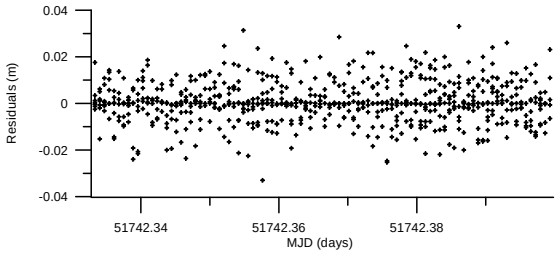

Figure 7.7: The GPS-SST observation residuals *(white noise of 1cm).*

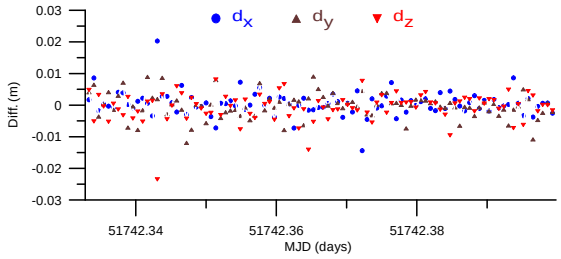

Figure 7.8: Point-wise estimated CHAMP orbit minus SC7 absolute positions *(white noise of 1cm).*

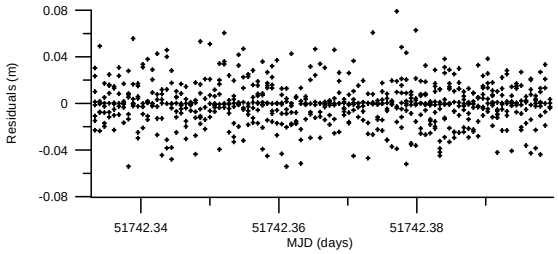

Figure 7.9: The GPS-SST observation residuals *(white noise of 2cm).*

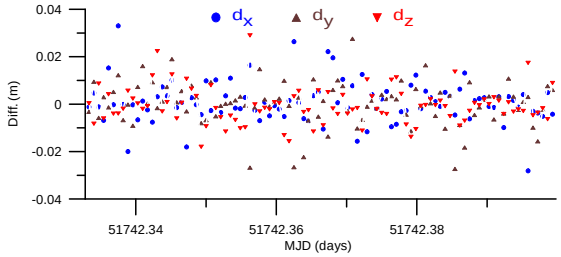

Figure 7.10: Point-wise estimated CHAMP orbit minus SC7 absolute positions *(white noise of 2cm).*

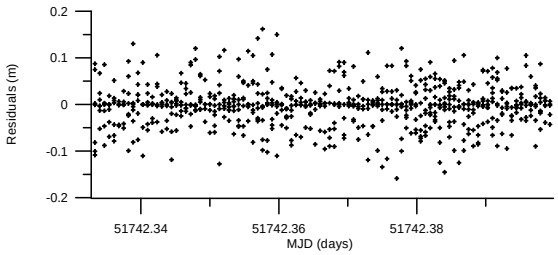

Figure 7.11: The GPS-SST observation residuals *(white noise of 5cm).*

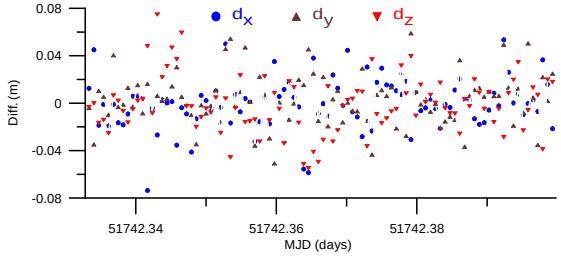

Figure 7.12: Point-wise estimated CHAMP orbit minus SC7 absolute positions *(white noise of 5cm).*

7.2.2 Analysis of Real GPS-SST Observations

The precise absolute positions of the LEOs can be determined either from the carrier phase GPS-SST observations or from the subsequent time differenced carrier phase GPS-SST observations at two sequential epochs in the batch processing mode. If the difference between two carrier phase GPS-SST observations at subsequent epochs has been built and the observation epochs are close together, then the GPS ambiguity parameters are canceled out. Additionally, many errors in the ZD mode of GPS-SST observations can be eliminated or mitigated with the corresponding models (e.g. ionosphere error, antenna phase center offsets and its variations, multi-path, etc.). Therefore, besides the batch processing of carrier phase GPS-SST observations, the sequential time differenced carrier phase observations have been proved to be very efficient for the geometrical LEO precise orbit determination. To determine the geometrical LEO precise orbits, in the real case, initial LEO absolute positions with an accuracy of a few meters have to be estimated based on the Bancroft method with the code pseudo-ranges as a first step. These absolute positions can be used subsequently as initial values for the LEOs absolute positions based on the ionosphere-free code pseudo-range observations to reduce the number of iterations in the data processing. To avoid the GPS satellites with low elevations, at first, a 15° elevation cut-off angle has to be applied to the GPS-SST observations. With the estimated absolute positions in the code pseudo-range process and with the help of the GPS receiver clock offset between two subsequent epochs, the outliers (or cycle slips) are detected and removed in the iteration process. In this method, the estimated LEO orbit is determined point-wise. The geometrical configuration (expressed by the Position Dilution Of Precision, PDOP) of the GPS satellites plays an important role for the GPS data processing accuracy.

To verify the proposed geometrical orbit determination procedure, a 30 minute arc of CHAMP (2002 07 20 12h 48m 00.0s - 2002 07 20 13h 18m 00.0s) with an interval rate of 30 sec. has been selected. The CHAMP ground track is shown in Fig. 7.13(b). The number of the GPS satellites, the corresponding PDOPs and the elevations of the GPS satellites are shown in Figs. 7.14 and 7.15, respectively. In a first step, the approximate estimation of absolute LEO positions are determined based on the Bancroft method (Bancroft 1985). Fig. 7.16 shows the absolute position differences and Fig. 7.17 the corresponding code pseudo-range observation residuals. The precision of the estimated LEO positions are in the range of a few meters.

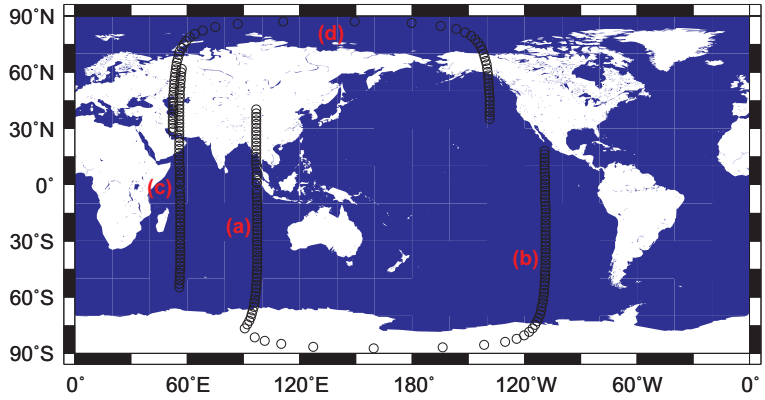

Figure 7.13: The ground track of the 30 minute CHAMP short arc for the time: (a) *2002 03 21 13h 30m 0.0s–14h 00m 0.0s* (b) *2002 07 20 12h 48m 0.0s–13h 18m 0.0s* (c) *2003 03 21 17h 20m 0.0s–17h 50m 0.0s* (d) *2003 03 31 17h 00m 0.0s–17h 30m 0.0s.*

To improve the accuracy of the LEO positions, the approximate positions are used as initial values to screen the GPS-SST observations for outliers (as described in chapter 3). Then they are used as initial values to estimate the LEO absolute positions with the code pseudo-range GPS-SST observations. In Figs. 7.18 and 7.19, the absolute position differences and the observation residuals are shown. The position differences are in the range of the accuracy of the code pseudo-range GPS-SST observations in the size of smaller than two meter.

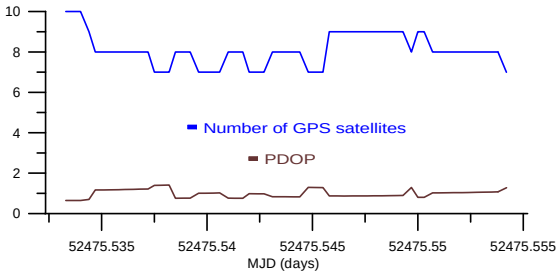

Figure 7.14: The number of tracked GPS satellites and the corresponding PDOPs.

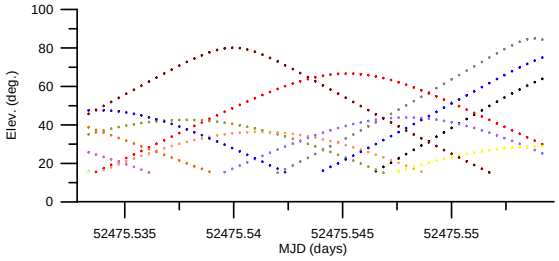

Figure 7.15: Elevations of the tracked GPS satellites applying a 15° cut-off angle.

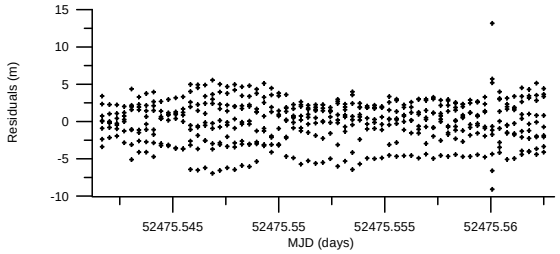

Figure 7.16: GPS-SST observation residuals with the Bancroft method at every observation epochs *(30 sec. sampling)*

.

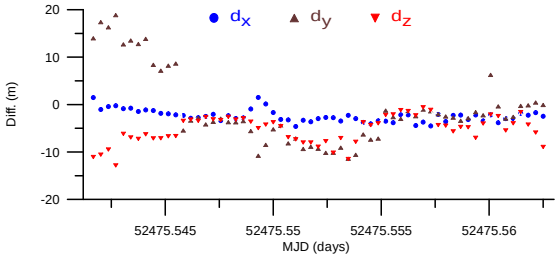

Figure 7.17: Estimated CHAMP absolute positions with the Bancroft method - CHAMP PSO orbit at the observation epochs *(30 sec. sampling)*.

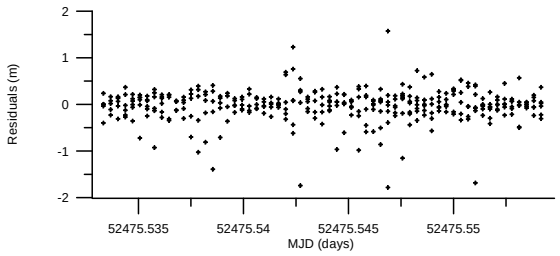

Figure 7.18: Code pseudo-range GPS-SST observation residuals.

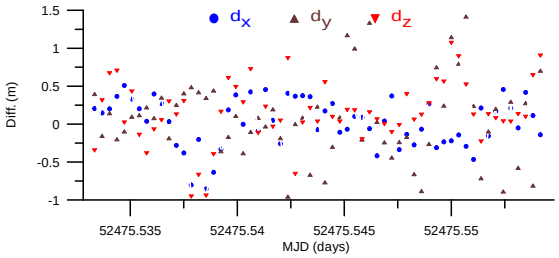

Figure 7.19: Estimated CHAMP absolute position with the code pseudo-range observations - CHAMP PSO orbit at at the observation epochs *(30 sec. sampling)*.

Final improvements can be performed based on the carrier phase GPS-SST observations between the GPS satellites and the GPS receiver on-board LEO. The carrier phase observations are very precise (in the size of *mm*) and play an important role in the precise point positioning (PPP or 3P), either in the static or in the kinematical mode of the geometrical point positioning.

Because of the fact that the accuracy of carrier phase observations are in the range of some millimeters, one can expect millimeter accuracy of GPS receiver positions. In case of GPS receivers at the ground stations, the problematic modeling of atmospheric parameters can reduce the accuracy of the estimated positions. The situation is less critical for GPS receivers at satellite altitude. There is no troposphere in the altitude of LEOs, but at this altitude the ionosphere can affect the GPS-SST observations. The multi-path is another problem in the data processing. Therefore, the LEO absolute positions based on the carrier phase GPS-SST observations can be estimated with an accuracy of 2 to 5cm. The absolute position differences with respect to the CHAMP PSO dynamical orbit provided by GFZ as well as the corresponding GPS-SST residuals are shown in Fig. 7.20(b) to Fig. 7.23(b).

To validate the geometrically determined point-wise CHAMP orbits, different short arcs of 30 minutes are selected. In Figs. 7.20(b) and 7.20(c), the CHAMP absolute position differences with respect to the PSO CHAMP orbit and the dynamical orbits (provided by Švehla, 2003) are shown for the time window of 2002 03 21 13h 30m 0.0s–14h 00m 0.0s. Fig. 7.20(d) shows the position differences of the PSO CHAMP dynamical orbit with respect to Švehla's dynamical orbit and Fig. 7.20(a) the carrier phase GPS-SST observation residuals. The difference plots show a clear systematic deviation pattern caused by the fact that the GFZ PSO as well as Švehla's solution are based on dynamical models. If these systematic effects are removed by a polynomial of degree 5, then the trend reassessed RMS values can be determined. The trend reassessed RMS values for the three coordinates x, y and z are given for the comparisons b, c and d. To show the validation of geometrically determined CHAMP orbit, another three examples at different times are selected. Figs. 7.21(a), 7.21(b), 7.21(c) and 7.21(d) show the carrier phase GPS-SST observation residuals and the position differences for the different CHAMP reference orbits for the time window 2002 07 20 12h 48m 0.0s–13h 18m 0.0s. An approximate trend reassessed RMS value of about 1cm is achieved for the CHAMP absolute positions with respect to the PSO CHAMP orbit. Figs. 7.22(a) to 7.23(d) show the carrier phase GPS-SST observation results and position differences for the time windows 2003 03 21 12h 00m 0.0s–12h 30m 0.0s and 2003 03 31 17h 00m 0.0s–17h 30m 0.0s, respectively. In all cases, the trend reassessed RMS values with respect to PSO and Švehla's dynamical orbits are in the range of 1 to 2cm, but the GPS-SST observation residuals show the smallest observation residuals.

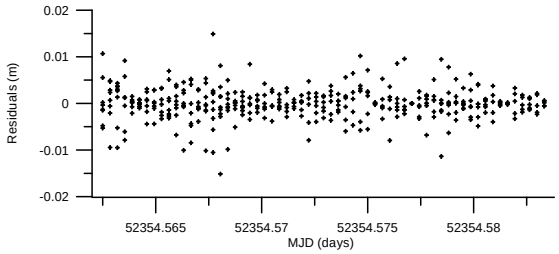

(a)

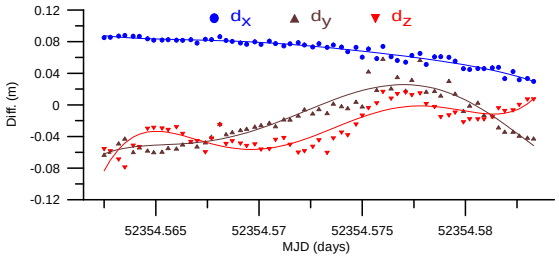

(c)

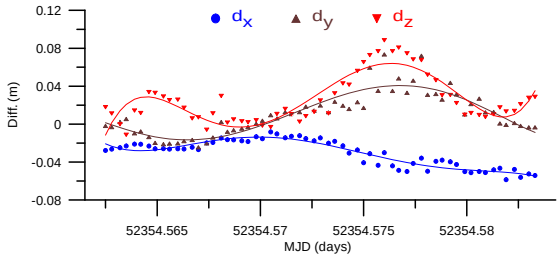

(b)

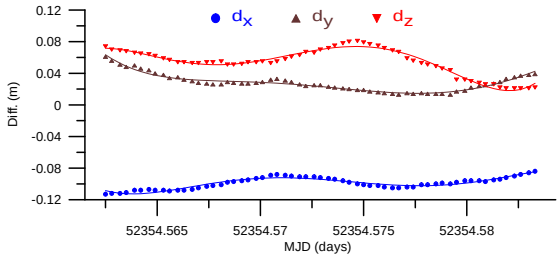

(d)

Figure 7.20: Geometrically determined CHAMP arc (a) carrier phase GPS-SST observation residuals (b) position differences: IGG solution - *CHAMP PSO orbit* (c) IGG solution - *TUM dynamic solution (Švehla, 2002)* (d) *TUM dynamic solution (Švehla, 2003) - CHAMP PSO orbit* for the time *2002 03 21 13h 30m 0.0s–14h 00m 0.0s.*

trend reassessed RMS

method	x(m)	y(m)	z(m)
b	0.0047	0.0096	0.0122
c	0.0038	0.0102	0.0120
d	0.0024	0.0023	0.0030

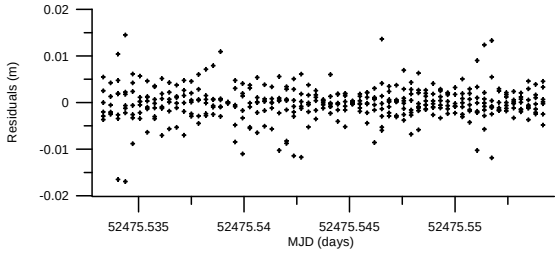

(a)

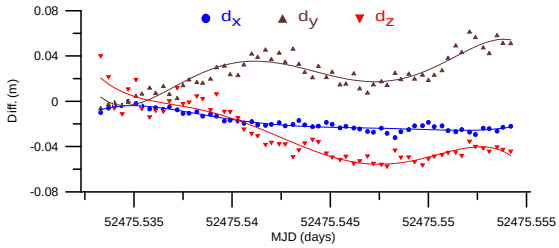

(c)

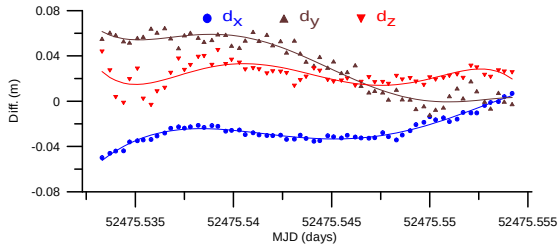

(b)

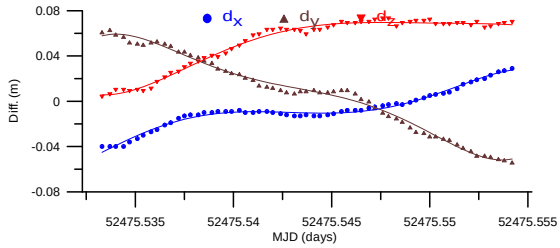

(d)

Figure 7.21: Geometrically determined CHAMP arc (a) carrier phase GPS-SST observation residuals (b) position differences: IGG solution - *CHAMP PSO orbit* (c) IGG solution - *TUM dynamic solution (Švehla, 2002)* (d) *TUM dynamic solution (Švehla, 2003) - CHAMP PSO orbit* for the time *2002 07 20 12h 48m 0.0s–13h 18m 0.0s.*

trend reassessed RMS

method	x(m)	y(m)	z(m)
b	0.0024	0.0062	0.0075
c	0.0024	0.0065	0.0080
d	0.0019	0.0033	0.0024

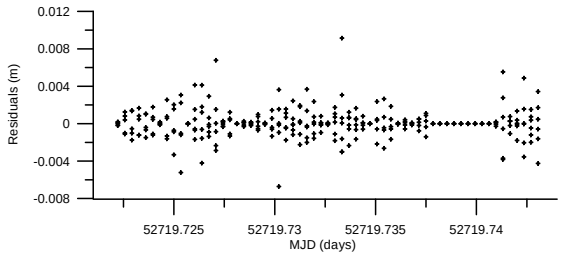

(a)

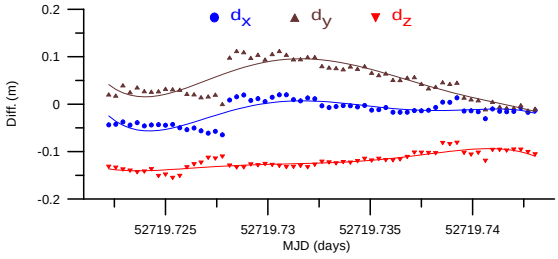

(b)

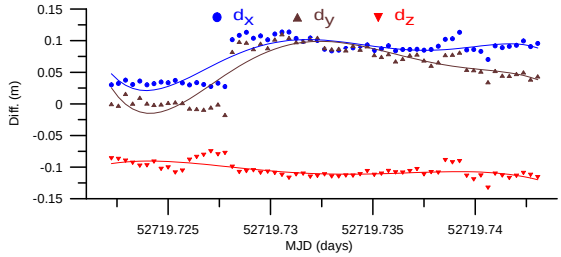

(c)

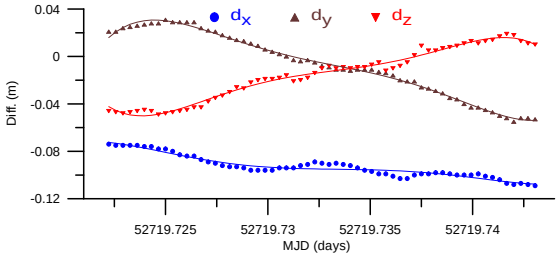

(d)

Figure 7.22: Geometrically determined CHAMP arc (a) carrier phase GPS-SST observation residuals (b) position differences: IGG solution - *CHAMP PSO orbit* (c) IGG solution - *TUM dynamic solution (Švehla, 2002)* (d) *TUM dynamic solution (Švehla, 2003) - CHAMP PSO orbit* for the time *2003 03 21 17h 20m 0.0s–17h 50m 0.0s.*

trend reassessed RMS

method	x(m)	y(m)	z(m)
b	0.0140	0.0171	0.0085
c	0.0142	0.0174	0.0088
d	0.0027	0.0019	0.0028

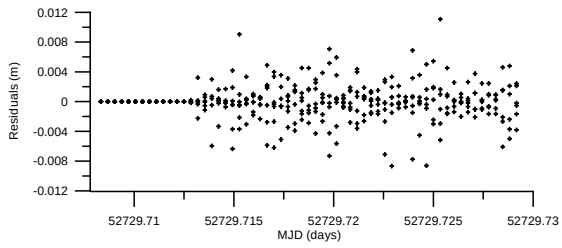

(a)

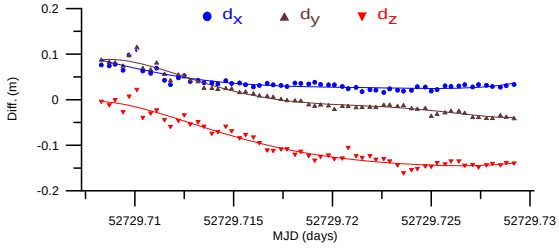

(b)

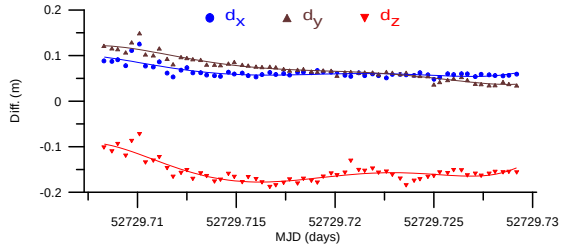

(c)

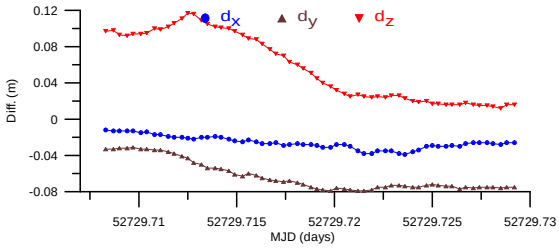

(d)

Figure 7.23: Geometrically determined CHAMP arc (a) carrier phase GPS-SST observation residuals (b) position differences: IGG solution - *CHAMP PSO orbit* (c) IGG solution - *TUM dynamic solution (Švehla, 2002)* (d) *TUM dynamic solution (Švehla, 2003) - CHAMP PSO orbit* for the time *2003 03 31 17h 00m 0.0s–17h 30m 0.0s.*

trend reassessed RMS

method	x(m)	y(m)	z(m)
b	0.0087	0.0073	0.0105
c	0.0082	0.0072	0.0116
d	0.0020	0.0017	0.0043

7.3 Kinematical Precise Orbit Determination (KPOD)

As described in Sec. 6.1, the proposed kinematical orbit determination approach can be interpreted as continuous representation of the LEO's arc. The continuous representation of the satellite's arc is realized by a combination of the Euler-Bernoulli polynomials up to degree J_{max} and the sine series up to index $\bar{n}$. This procedure can be performed either based on the GPS-SST observations directly or based on the LEO's geometrically determined absolute positions. Both methods have to deliver the same results if the full variance-covariance information (with the correlation information between the points in case of positions as pseudo observations) are used in both cases. To verify the proposed kinematical precise orbit determination strategy, different scenarios are simulated based on the SC7 data set. After the verification, the proposed strategy is used for the real case, i.e. the CHAMP's data which are provided by the ISDC-GFZ, Potsdam.

7.3.1 Simulated Case

The orbit determination approach is tested based on a simulation scenario for a 30 minute arc of a simulated CHAMP orbit, adapted from the SC7 simulation scenarios as described in Sec. 7.1. To be as close as possible to the reality, a 15° cut-off angle has been chosen for the measurements between the GPS receiver, fixed to CHAMP, and the GPS satellites. In a first test based on simulated data, the error-free case is investigated (Sec. 7.3.1.1) and, in a second simulation test, the case of a white noise of $2cm$ for the GPS-SST measurements to derive positions so that they are used as pseudo-observations for the subsequent kinematical orbit determination procedure (Sec. 7.3.1.2). In the case of high-low GPS-SST observations (e.g. as carrier phase observations) for the kinematical orbit determination, a white noise corresponding to $2cm$ pseudo-range accuracy has been modeled. This GPS-SST observation error produces also an error of approximately $2cm$ in each of the position coordinates. The Table 7.1 shows the various simulation examples. Despite the fact that the computation procedure shown in Fig. 6.1 and Fig. 6.2 are very similar, they are considered separately. For each computation alternative, the observations for the determination of the kinematical orbit are considered either as positions (introduced as pseudo observations) or directly as carrier phase GPS-SST observations. In many applications of kinematical orbits, the position coordinates derived from the geometrical orbit determination procedure are used instead of the high-low GPS-SST observations. Therefore, the difference of both solutions shall be discussed.

Table 7.1: Summary of all kinematical precise orbit determination cases.

error case	noise free				white noise 2cm			
computation type	Fig. 6.1		Fig. 6.2		Fig. 6.1		Fig. 6.2	
observation type	*SST*	*Pos.*	*SST*	*Pos.*	*SST*	*Pos.*	*SST*	*Pos.*
Figure	Fig.7.24	Fig.7.25	Fig.7.26	Fig.7.27	Fig.7.28	Fig.7.29	Fig.7.30	Fig.7.31

7.3.1.1 Noise Free Case

In a first step, the GPS-SST observations with the corresponding variance-covariance information are used to estimate the kinematical precise orbit of CHAMP as described in the flowchart of Fig. 6.1. As shown in Fig. 6.1, the LEO arc boundary positions and the sine amplitudes are estimated based on the GPS-SST observations. The Euler-Bernoulli polynomial coefficients up to degree $J_{max} = 4$ are estimated independently from the GPS-SST observations as well. In a first step, the residual sine series are estimated by a least squares estimation. Figs. 7.24(a) to 7.27(a) show the absolute position differences at a time interval of $10sec.$, while the orbit determination is based on a sampling rate of $30sec.$ The upper limit of the sine series are chosen as $\bar{n} = 20$, 30, 30, and 59. The latter case represents the interpolation case, that means no redundancy exists.

In judging the results in the following figures, we want to point out that the orbits are determined from observations sampled at a 30 seconds rate while the comparisons with the true values are performed at every

10 seconds. This is the reason that we see RMS values different from zero also in the interpolation cases. To avoid the influence of remaining Gibb's effects in the RMS results as shown in the RMS tables to each orbit determination example, the boundary sections in the size of 5% of the total arc are blanked out. We will see later that this is important only in the error-free cases; in case of noisy observations the Gibb's effects are not visible anymore compared to the general errors in the orbit determination results (compare the Fig. 7.32 for the error-free case and the Fig. 7.33 for the noise case).

The RMS table of Fig. 7.24 shows, as expected, that the best result is achieved for the interpolation case. As mentioned before, the RMS values represent the differences of the computed coordinates and the true values given at every 10 second. This holds also for the velocities (shown in Fig. 7.24(b)) and for the accelerations (shown in Fig. 7.24(c)). The velocities and accelerations can be determined by analytical differentiation as outlined in Sec. 5.3.3. Especially, the interpolation cases demonstrate the high accuracy of the orbit representation by the mixed series approximation of sine series and Euler-Bernoulli polynomials. As expected, these differences will be larger in the error examples as discussed in Sec. 7.3.1.2.

If the point-wise LEOs positions are determined with the geometrical orbit determination strategy based on the GPS-SST observations (see Chapter 4), then the estimated absolute positions and their variance-covariance can be used as pseudo-observations in the kinematical data processing procedure. As shown in Fig. 6.1, the boundary positions as well as the sine amplitudes are estimated based on the point-wise absolute positions with their variance-covariance information. The Euler-Bernoulli coefficients up to degree $J_{max} = 4$ are estimated from the geometrically determined positions independently. Finally, the residual sine amplitudes are estimated based on the sine analysis of the residual function. The LEO orbit can be represented with the boundary positions, the Euler-Bernoulli polynomials up to degree $J_{max} = 4$ and the residual sine series (with the upper indices 20, 30, 40 or 59).

The results shown in Fig. 7.25 correspond to the results shown in Fig. 7.24 with the only difference that they are derived from a position ephemeris with a 30sec. sampling rate, derived geometrically in a prior step from the GPS-SST observations. The variance-covariance matrices of the three coordinates x, y and z of the absolute positions are used in the kinematical orbit determination procedure as well. The results are similar to those of Fig. 7.24, with the minimal RMS values in the positions, velocities and accelerations for the interpolation case. The comparison of the cases shown in the Figs. 7.24 and 7.25 show that there are slightly smaller RMS values for the case where the positions and its variance-covariance matrices are introduced in the computation procedure as pseudo observations than in case of using directly the GPS-SST observations.

The flowchart in Fig. 6.2 shows the procedure, where the Euler-Bernoulli polynomial coefficients are estimated based on the sine series amplitudes. In the other words, the Euler-Bernoulli coefficients are estimated in the spectral domain. This procedure can again be performed either based on the GPS-SST observations or based on the geometrically determined LEO absolute positions. The results shown in the Figs. 7.26 and 7.27 correspond to the results shown in the Figs. 7.24 and 7.25 with the only difference that the Euler-Bernoulli polynomials are determined from the amplitudes of the sine series as shown in the flowchart of Fig. 6.2. This procedure differs slightly from the procedure as shown in the flowchart of Fig. 6.1, because in the case of Fig. 6.2, the Euler-Bernoulli coefficients are determined implicitly also under a simultaneous correction of the boundary vectors of the short arc. The comparison of the results in the Figs 7.26 and 7.27 shows identical results (at least in the RMS values of the positions, velocities and accelerations) with the minimal RMS values for the interpolation case (as expected) and also slightly better than the results shown in Fig. 7.25.

Summarizing the results of the error-free simulation cases, we conclude that the best case with minimal RMS values for a 10sec. ephemeris (in the positions, velocities and accelerations) based on an observation series with a 30 sec sampling rate is that of using either GPS-SST observations directly or positions as pseudo observations indirectly by following the determination procedure as shown in the flowchart of Fig. 6.2. Obviously, it is preferable to derive the Euler-Bernoulli series from the sine series coefficients, which are determined in a prior least squares adjustment step by simultaneous correcting the boundary values together with the sine coefficients.

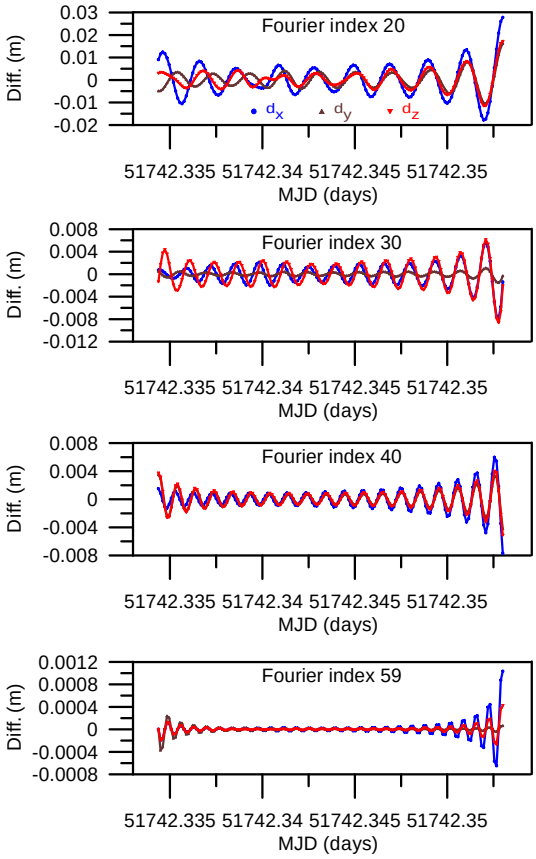

(a)

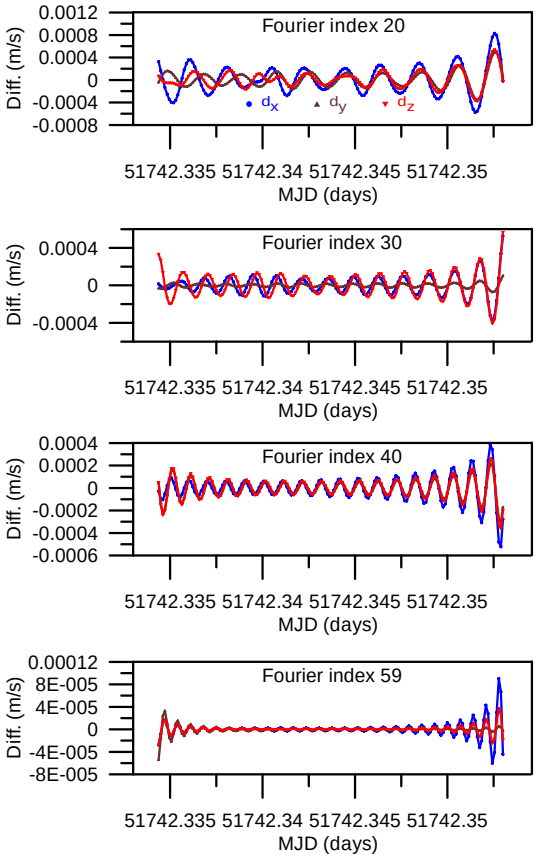

(b)

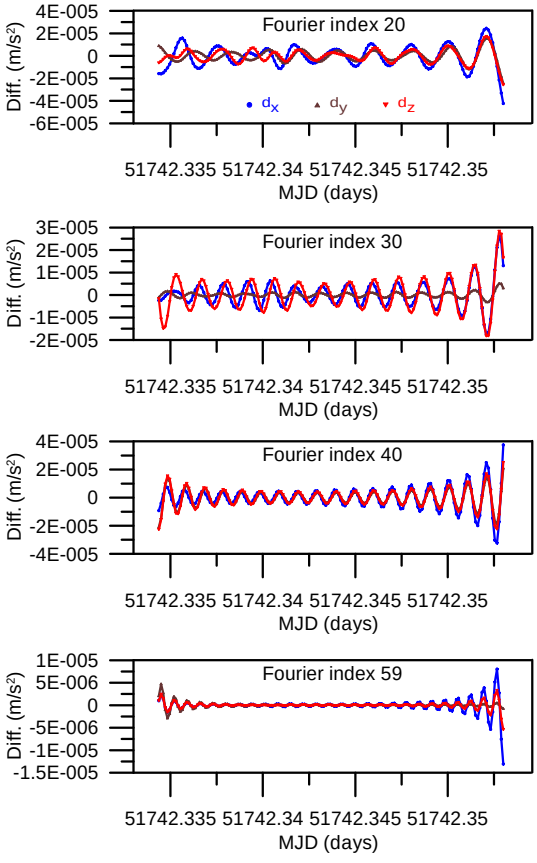

(c)

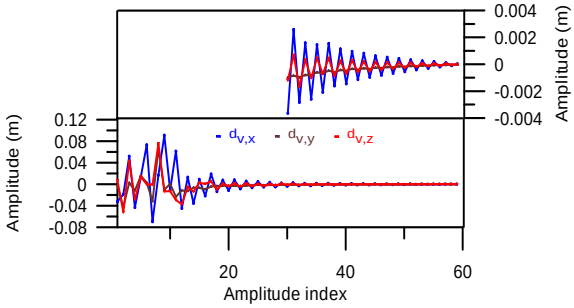

(d)

Figure 7.24: (a) Position differences (b) velocity differences (c) acceleration differences (d) Fourier spectrum (reference motion: *ellipse mode*, J_{max}=4, N_F =300, *error free case*, observation type: *SST*, method: *flowchart Fig. 6.1*, observation sampling rate: *30 sec.*, test sampling rate: *10 sec.*, without $\approx 5\%$ at boundaries $\equiv$ 9 points or 80 sec.).

RMS

index	Pos.(m)	Vel.(m/s)	Acc.(m/s^2)
20	0.008742	0.000322	0.000012
30	0.003012	0.000159	0.000009
40	0.002163	0.000164	0.000011
59	0.000149	0.000016	0.000002

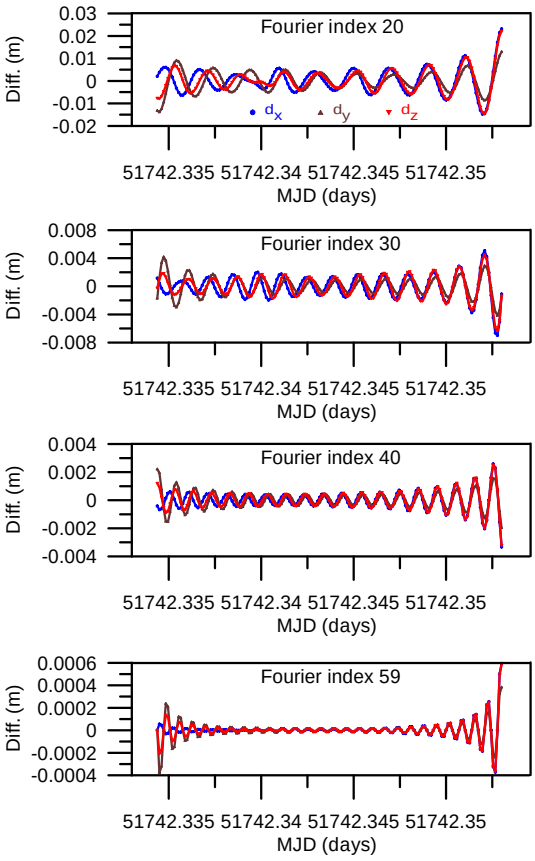

(a)

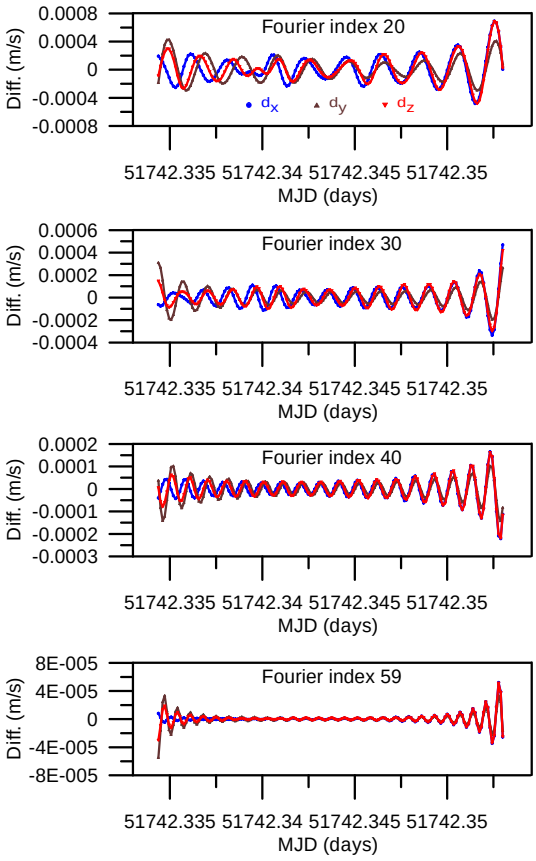

(b)

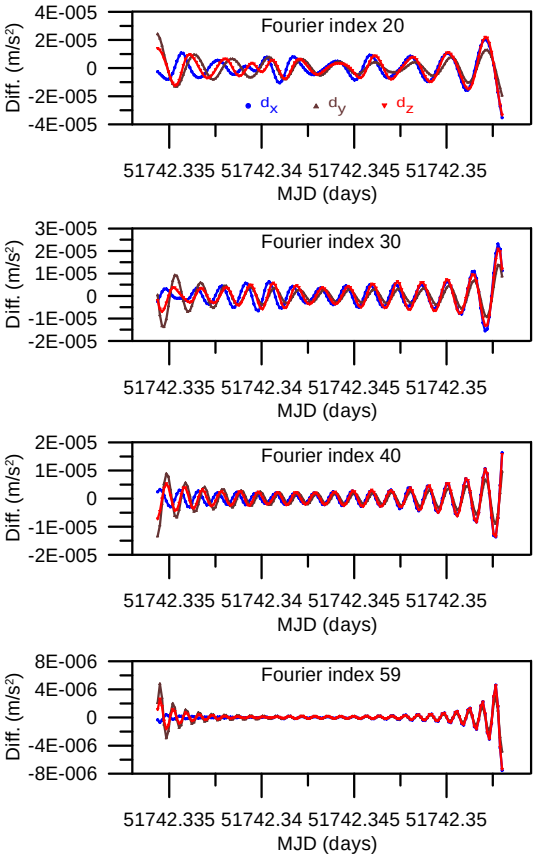

(c)

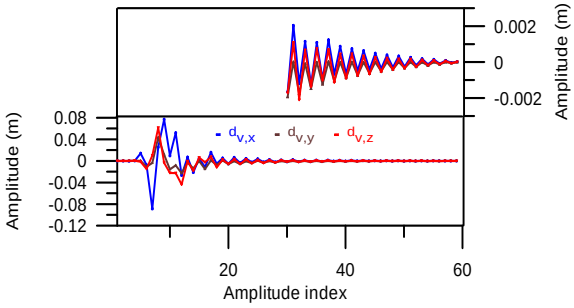

(d)

Figure 7.25: (a) Position differences (b) velocity differences (c) acceleration differences (d) Fourier spectrum (reference motion: *ellipse mode*, J_{max}=4, N_F =300, *error free case*, observation type: *Positions*, method: *flowchart Fig. 6.1*, observation sampling rate: *30 sec.*, test sampling rate: *10 sec.*, without $\approx$ 5% at boundaries $\equiv$ 9 points or 80 sec.).

RMS

index	Pos.(m)	Vel.(m/s)	Acc.(m/s^2)
20	0.008496	0.000319	0.000012
30	0.002708	0.000144	0.000008
40	0.001077	0.000081	0.000006
59	0.000126	0.000014	0.000001

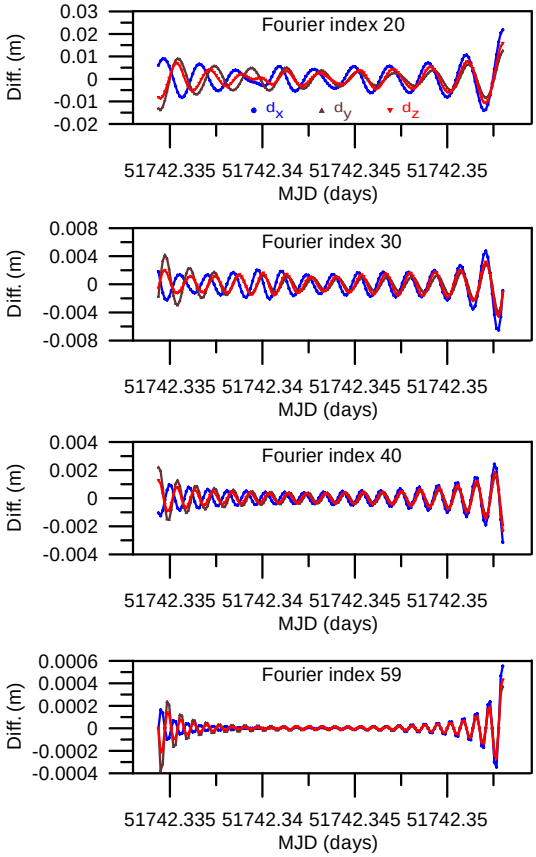

(a)

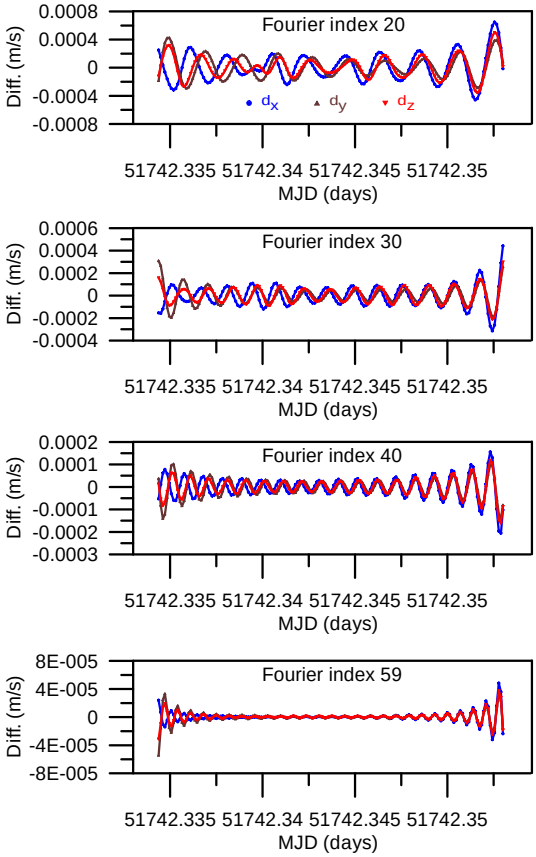

(b)

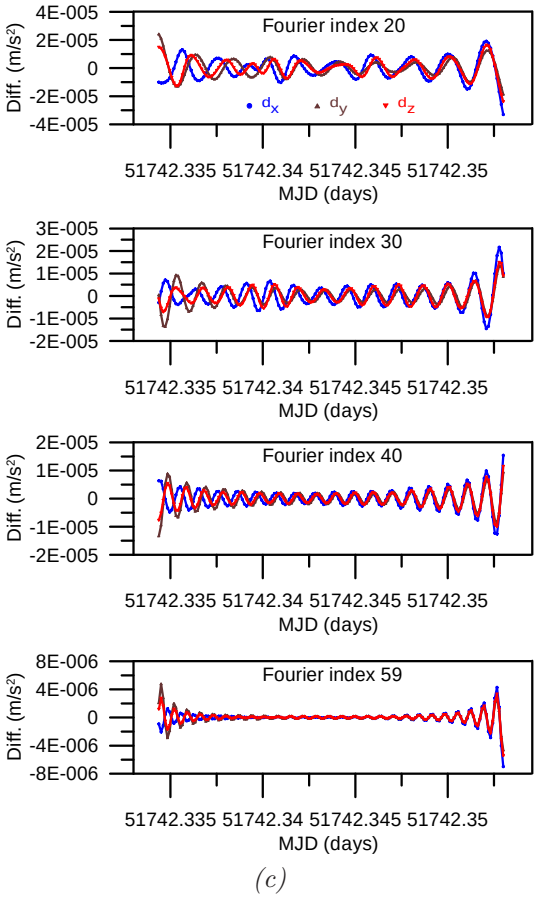

(c)

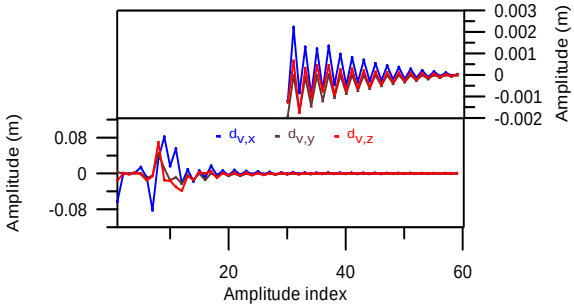

(d)

Figure 7.26: (a) Position differences (b) velocity differences (c) acceleration differences (d) Fourier spectrum (reference motion: *ellipse mode*, J_{max}=4, N_F =300, *error free case*, observation type: *SST*, method: *flowchart Fig. 6.2*, observation sampling rate: *30 sec.*, test sampling rate: *10 sec.*, without $\approx 5\%$ at boundaries $\equiv$ 9 points or 80 sec.).

RMS

index	Pos.(m)	Vel.(m/s)	Acc.(m/s^2)
20	0.007975	0.000296	0.000011
30	0.002480	0.000134	0.000008
40	0.000999	0.000074	0.000005
59	0.000116	0.000013	0.000001

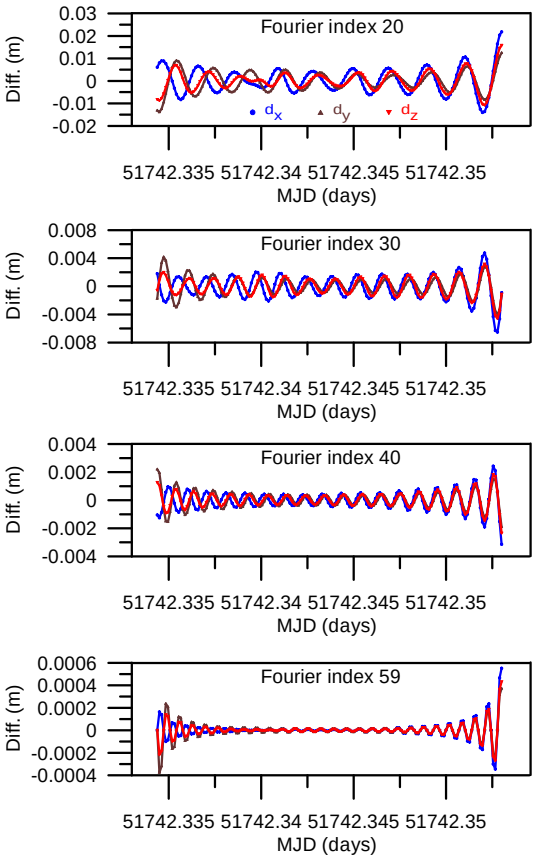

(a)

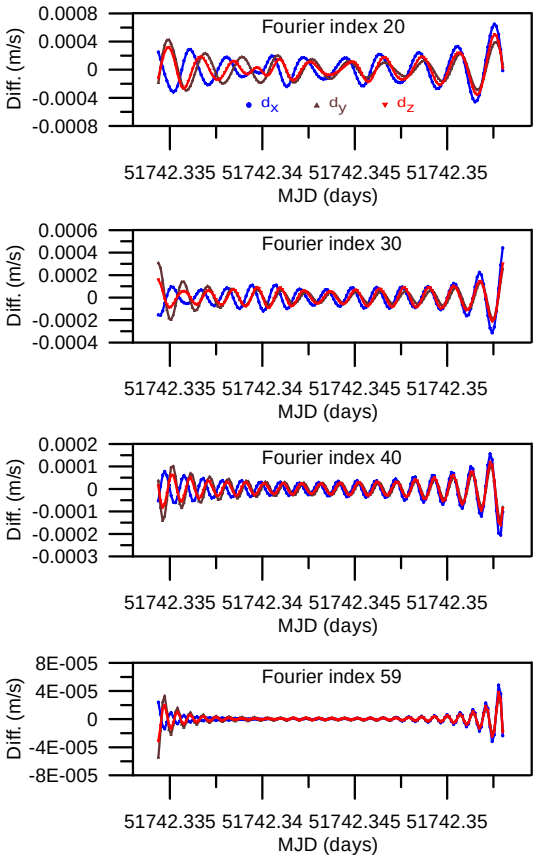

(b)

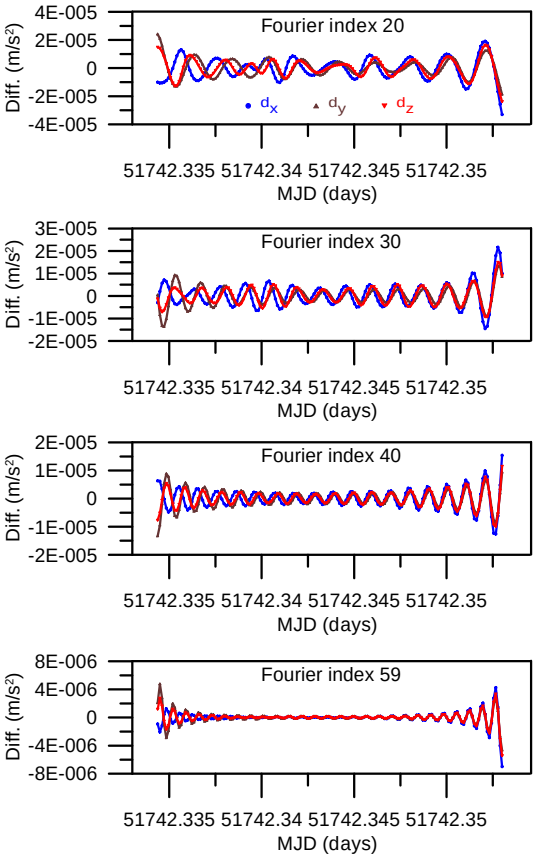

(c)

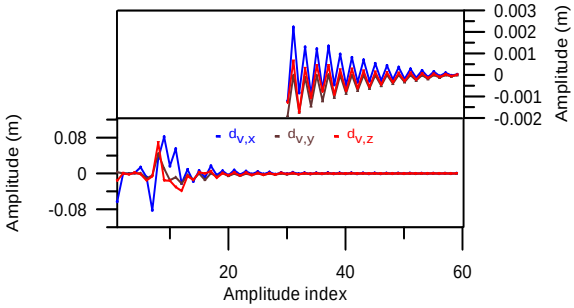

(d)

Figure 7.27: (a) Position differences (b) velocity differences (c) acceleration differences (d) Fourier spectrum (reference motion: *ellipse mode*, J_{max}=4, N_F =300, *error free case*, observation type: *Positions*, method: *flowchart Fig. 6.2*, observation sampling rate: *30 sec.*, test sampling rate: *10 sec.*, without $\approx$ 5% at boundaries $\equiv$ 9 points or 80 sec.).

RMS

index	Pos.(m)	Vel.(m/s)	Acc.(m/s^2)
20	0.007975	0.000296	0.000011
30	0.002479	0.000134	0.000008
40	0.000999	0.000074	0.000005
59	0.000116	0.000013	0.000001

7.3.1.2 Error Case

In a second simulation test, the orbit determination examples presented in the Figs. 7.24 to 7.27 are repeated with noise contaminated observations. These examples are shown in the Figs. 7.28 to 7.31 and will be compared in the following with the results in case of error-free simulation scenarios. A white noise of $2cm$ is modeled for the GPS-SST observations to derive positions so that they are used as pseudo-observations for the subsequent kinematical orbit determination procedure. In the case of high-low GPS-SST observations (e.g. carrier phase observations) for the kinematical orbit determination, a white noise corresponding to $2cm$ pseudo-range accuracy has been modeled. This GPS-SST observation error produces also an error of approximately $2cm$ in each of the position coordinates.

The orbit determination case, shown in Fig. 7.28, corresponds to the example of Fig. 7.24 for the error-free scenario. Two aspects are of interest: first of all, the minimum RMS values for the positions, velocities and accelerations are not achieved for the so-called interpolation case (by extending the upper summation index of the sine series to 59) but for a much lower upper index, namely about 30. Obviously, the restriction to a lower upper index acts as a filtering. Secondly, we observe that the influence of white noise of the observations is reduced with the number of differentiations. While the RMS value for the positions is about four times larger for the noise case relative to the error-free case, for the accelerations this factor is reduced to only 2, in case of an upper limit of the residual sine series of 30. Furthermore, it is interesting to note (the expected result) that for an upper index of 59 (interpolation case), the RMS value represents a certain basic noise level which corresponds to the white noise level of the observations. These values can only be reduced by an additional filtering procedure, as it is realized in case of reducing the upper summation index to 30, but alternative filtering techniques might be even more successful.

The comparisons of the examples presented in the Figs. 7.28 and 7.29 show similar characteristics as in case of the Figs. 7.24 and 7.25. Obviously, the use of the geometrically determined positions as pseudo-observations has slight advantages compared to the case where the high-low GPS-SST observations are introduced directly, at least if the computation sequence of the flowchart of Fig. 6.1 is applied. The results shown in the Figs. 7.30 and 7.31 correspond to the results shown in the Figs. 7.28 and 7.29 again with the difference that the Euler-Bernoulli polynomials are determined from the amplitudes of the sine series as shown in the flowchart of Fig. 6.2. We want to repeat that this procedure differs only in the procedure as shown in the flowchart of Fig. 6.1 by a different computation of the Euler-Bernoulli coefficients. The comparison of the results in the Figs. 7.30 and 7.31 again show identical results (at least in the RMS values of the positions, velocities and accelerations) with the minimal RMS values for an upper index of about 30 to 40 and also slightly better than the results shown in Figs. 7.28 and 7.29, respectively.

7.3.1.3 Gibb's Effect

The Gibb's phenomenon, named after the American physicist *J. Willard Gibbs*, is the peculiar manner in which the Fourier series of a piecewise continuously differentiable periodic function f behaves at a jump discontinuity. The nth partial sum of the Fourier series has large oscillations near the jump. The overshoot becomes smaller as the frequency increases. The overshoot is a consequence of trying to approximate a discontinuous function with a finite sum of continuous functions. A finite sum of continuous functions is necessarily continuous, and therefore cannot approximate the discontinuity to within any arbitrarily chosen accuracy. An infinite sum of continuous functions can be discontinuous, and the point-wise limit of the partial sums of a Fourier series does not exhibit an overshoot near a jump discontinuity as do the partial sums themselves (Carslaw 1930).

The orbit determination approach based on a combined representation of the short arc by a series in terms of Euler and Bernoulli polynomials, $\mathbf{d}_P^{J_{max}}(\tau)$ and a residual Fourier series $\bar{\mathbf{d}}_F^{\bar{n}}(\tau)$ (which becomes a sine series because of the fact that the residual function $\bar{\mathbf{d}}_F^{\bar{n}}(\tau)$ is an odd periodic function if continued with the period $2T$) has the property that the Gibb's effect of the sine series $\bar{\mathbf{d}}_F^{\bar{n}}(\tau)$ is significantly reduced. Because of the fact that the Euler-Bernoulli series is constructed such that the derivatives of $\mathbf{d}_P^{J_{\max}}(\tau)$ coincide up to the maximum index $J_{\max}$ with the corresponding number of derivatives of the difference function $\mathbf{d}(\tau)$

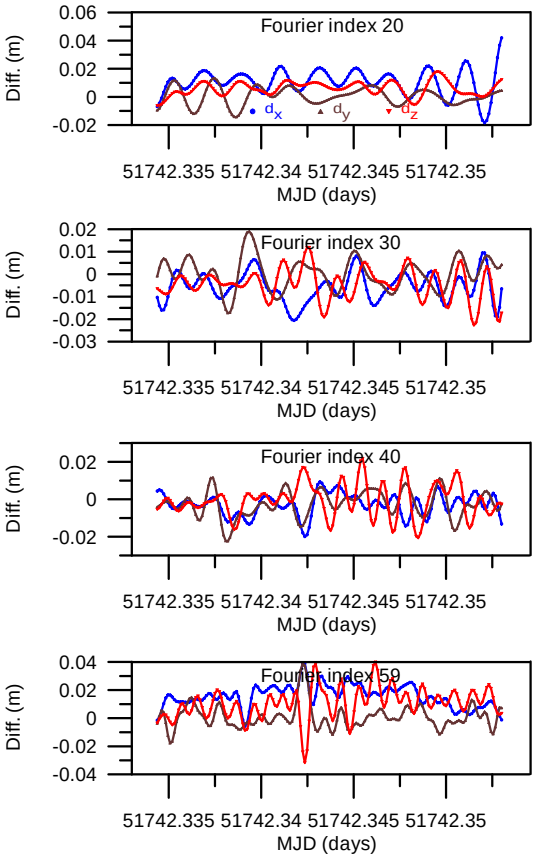

(a)

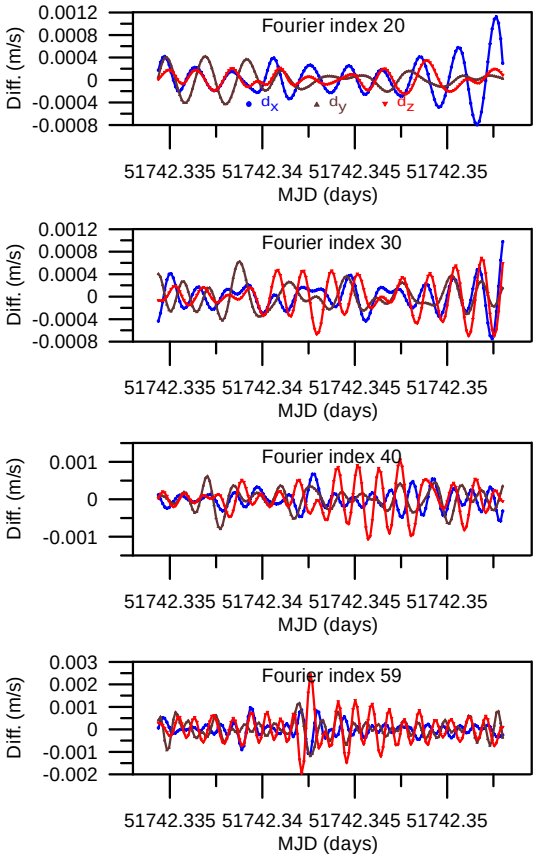

(b)

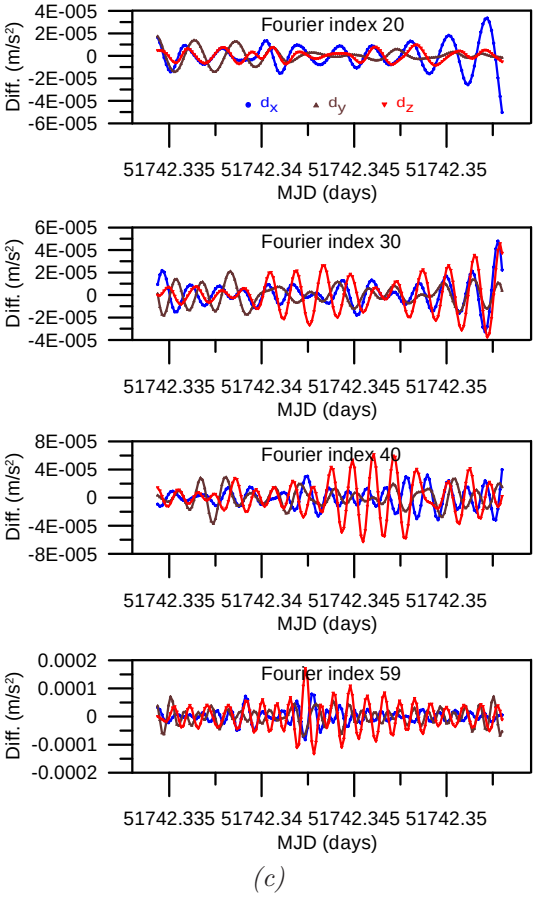

(c)

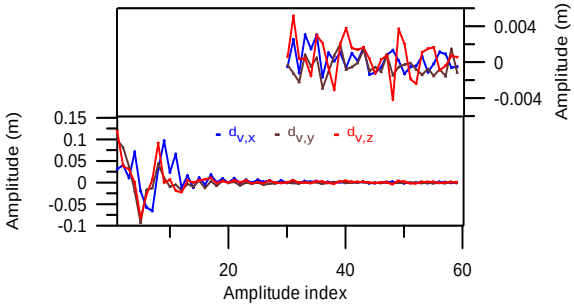

(d)

Figure 7.28: (a) Position differences (b) velocity differences (c) acceleration differences (d) Fourier spectrum (reference motion: *ellipse mode*, J_{max}=4, N_F =300, *white noise of* 2 *cm*, observation type: *SST*, method: *flowchart Fig. 6.1*, observation sampling rate: *30 sec.*, test sampling rate: *10 sec.*, without $\approx$ 5% at boundaries $\equiv$ 9 points or 80 sec.).

RMS

index	Pos.(m)	Vel.(m/s)	Acc.(m/s^2)
20	0.016681	0.000381	0.000013
30	0.013784	0.000427	0.000021
40	0.012959	0.000541	0.000031
59	0.024851	0.000802	0.000060

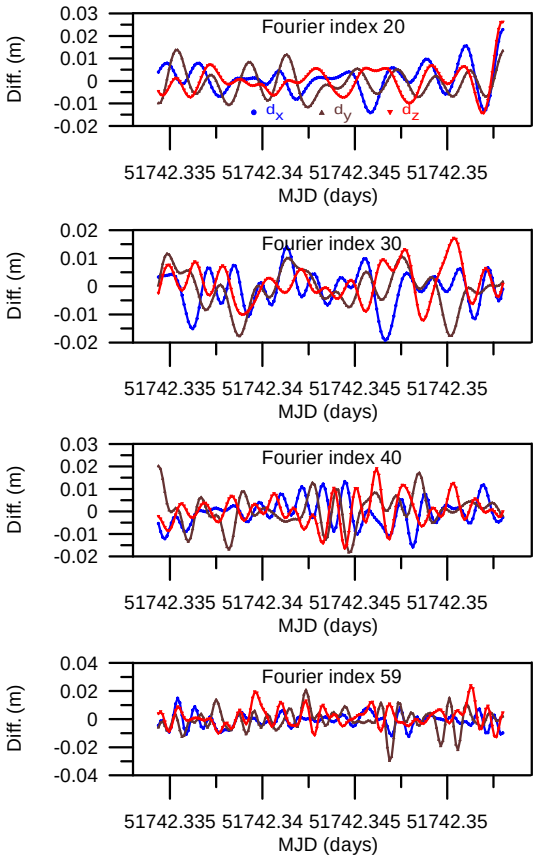

(a)

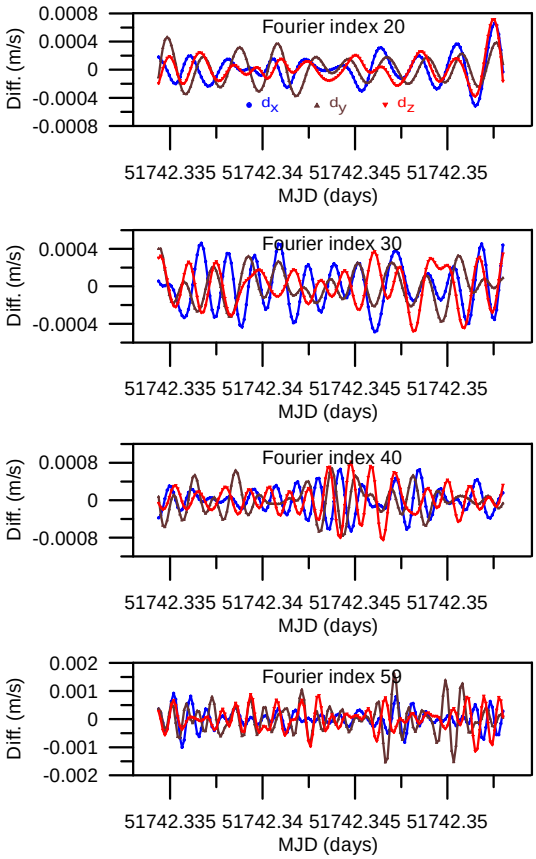

(b)

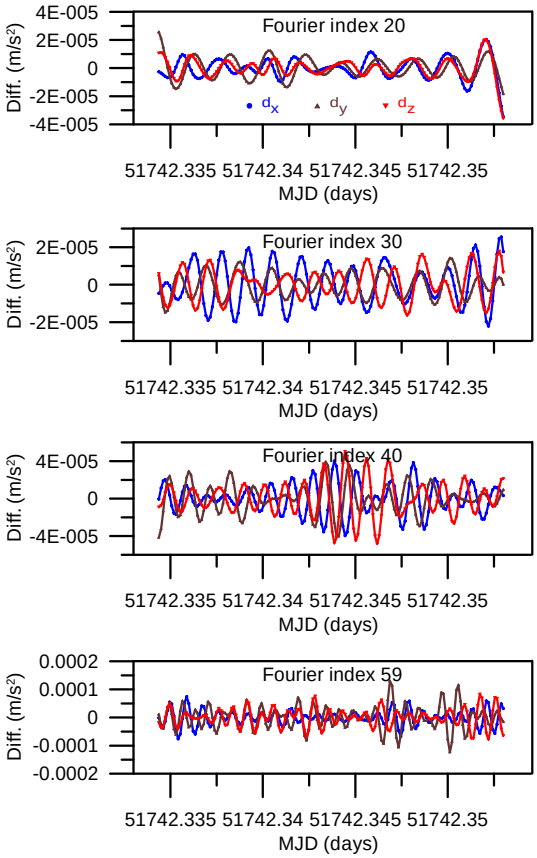

(c)

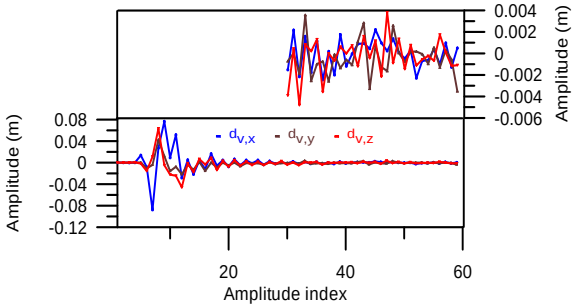

(d)

Figure 7.29: (a) Position differences (b) velocity differences (c) acceleration differences (d) Fourier spectrum (reference motion: *ellipse mode*, J_{max}=4, N_F =300, *white noise of* 2 *cm*, observation type: *Positions*, method: *flowchart Fig. 6.1*, observation sampling rate: *30 sec.*, test sampling rate: *10 sec.*, without $\approx$ 5% at boundaries $\equiv$ 9 points or 80 sec.).

RMS

index	Pos.(m)	Vel.(m/s)	Acc.(m/s^2)
20	0.010397	0.000330	0.000012
30	0.011339	0.000351	0.000015
40	0.011133	0.000500	0.000029
59	0.011348	0.000724	0.000059

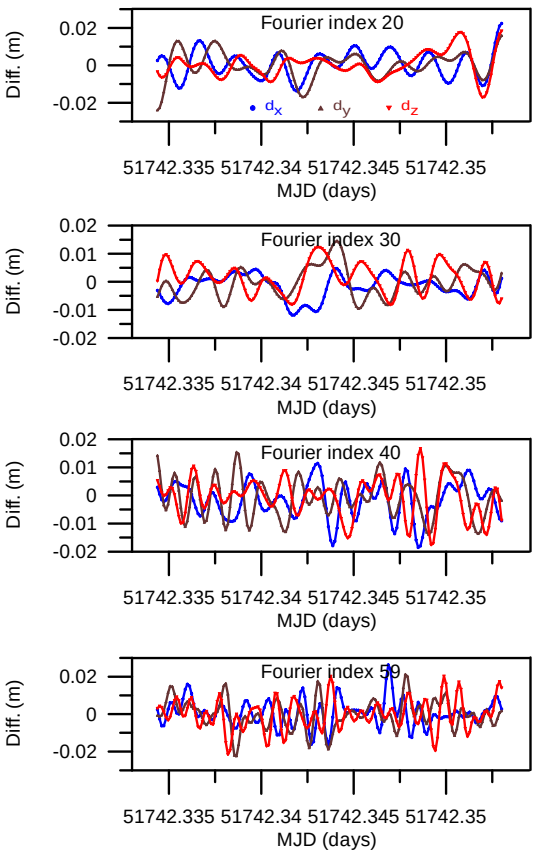

(a)

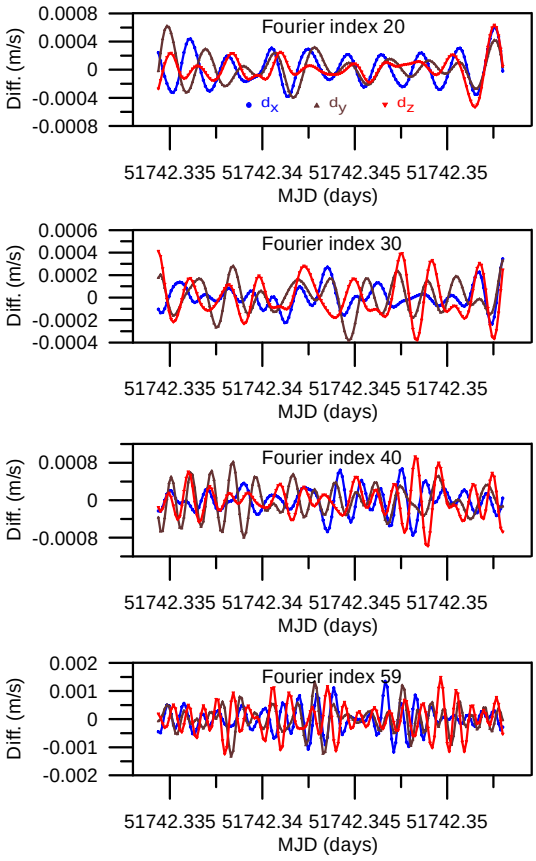

(b)

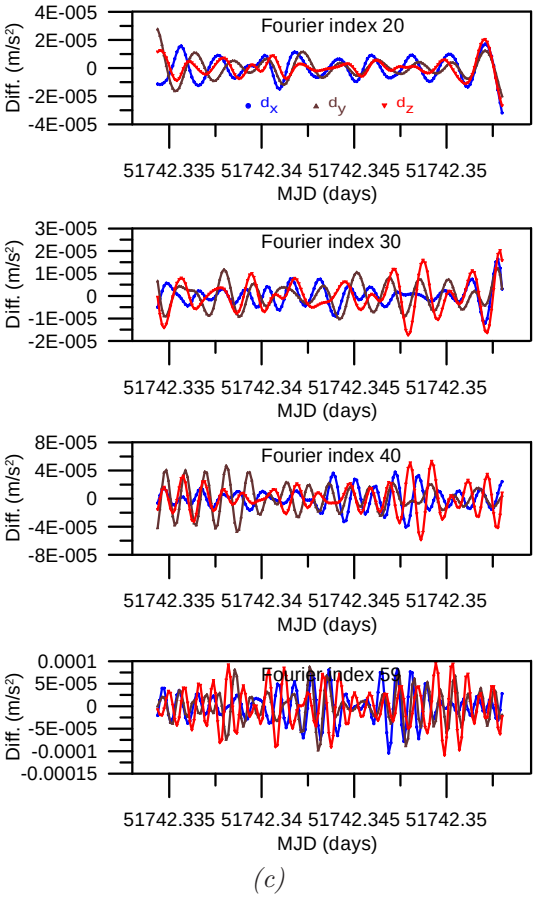

(c)

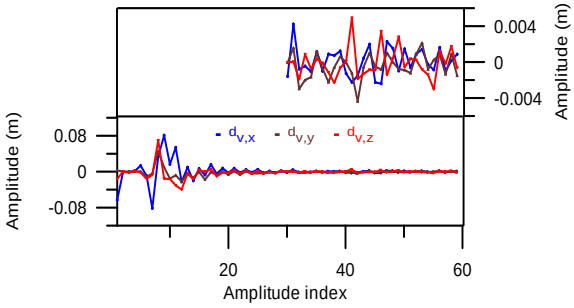

(d)

Figure 7.30: (a) Position differences (b) velocity differences (c) acceleration differences (d) Fourier spectrum (reference motion: *ellipse mode*, J_{max}=4, N_F =300, *white noise of* 2 *cm*, observation type: *SST*, method: *flowchart Fig. 6.2*, observation sampling rate: *30 sec.*, test sampling rate: *10 sec.*, without $\approx$ 5% at boundaries $\equiv$ 9 points or 80 sec.).

RMS

index	Pos.(m)	Vel.(m/s)	Acc.(m/s^2)
20	0.011638	0.000342	0.000012
30	0.008821	0.000239	0.000010
40	0.011581	0.000531	0.000031
59	0.013065	0.000823	0.000065

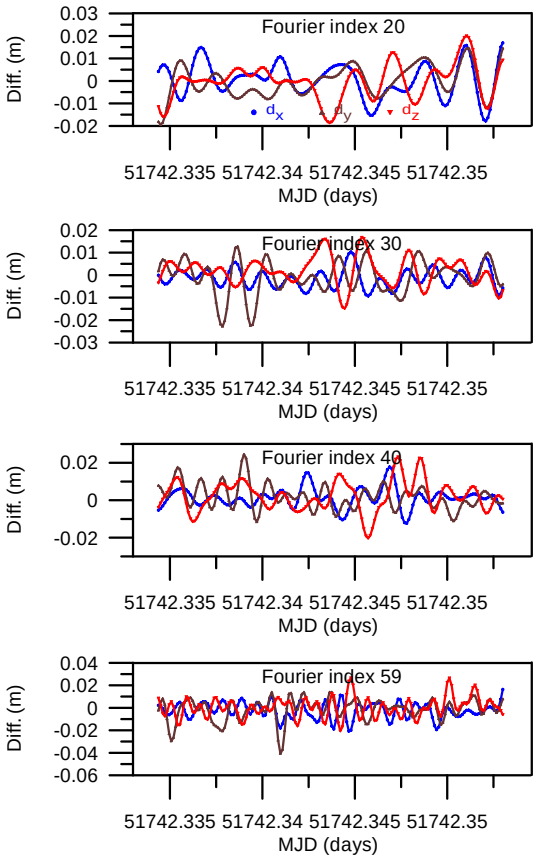

(a)

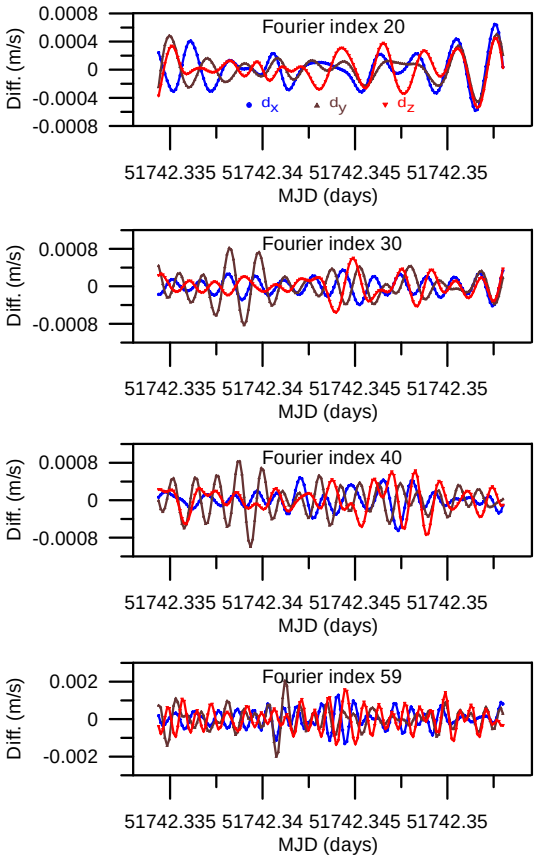

(b)

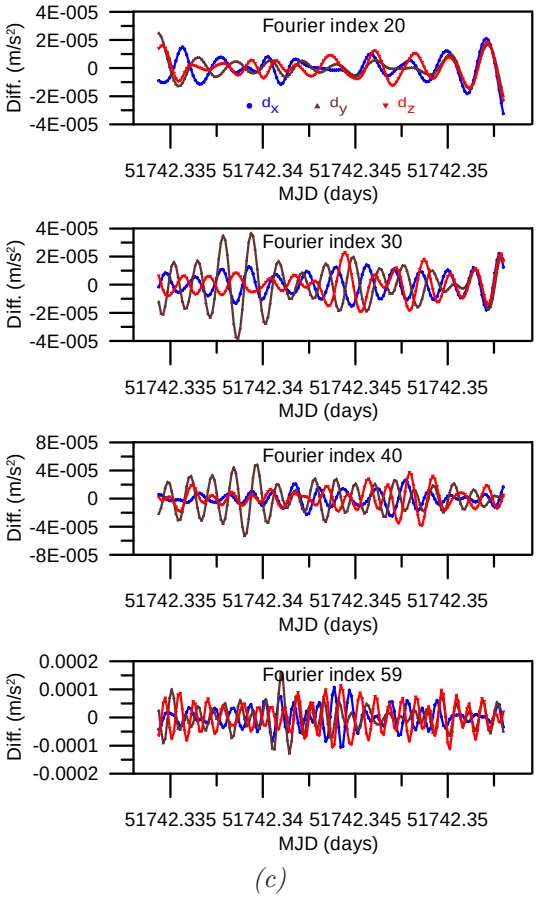

(c)

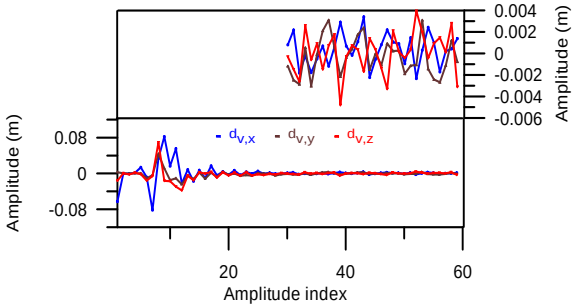

(d)

Figure 7.31: (a) Position differences (b) velocity differences (c) acceleration differences (d) Fourier spectrum (reference motion: *ellipse mode*, J_{max}=4, N_F =300, *white noise of* 2 *cm*, observation type: *Positions*, method: *flowchart Fig. 6.2*, observation sampling rate: *30 sec.*, test sampling rate: *10 sec.*, without $\approx$ 5% at boundaries $\equiv$ 9 points or 80 sec.).

RMS

index	Pos.(m)	Vel.(m/s)	Acc.(m/s^2)
20	0.012644	0.000353	0.000012
30	0.010717	0.000397	0.000018
40	0.011997	0.000463	0.000025
59	0.014737	0.000941	0.000077

(refer to Eq. (6.72), all derivatives up to the index $J_{\max}$ of the residual function $\bar{\mathbf{d}}_F^{\bar{n}}(\tau)$ become zero and a smooth function results, if $\bar{\mathbf{d}}_F^{\bar{n}}(\tau)$ is periodically continued with the period $2T$. This property does not hold rigorously because of the fact that the Euler-Bernoulli polynomial coefficients are derived only approximately (refer to Secs. 5.4.1.3 and 6.1.3). On the other hand, it is important that the Gibb's effect can be reduced down to a level of the maximum orbit representation accuracy of approximately 1cm. Fig. 7.33 demonstrates that in case of noisy observations, the Gibb's effects are not visible anymore already in case of an upper sine series index of 30 compared to the general errors in the orbit determination results as a consequence of the observations errors, while in the error-free case, the Gibb's effect is still clearly visible at the boundaries (Fig. 7.32). In any case it is useful to blank out the boundary regions in the size of 5% of the total arc length.

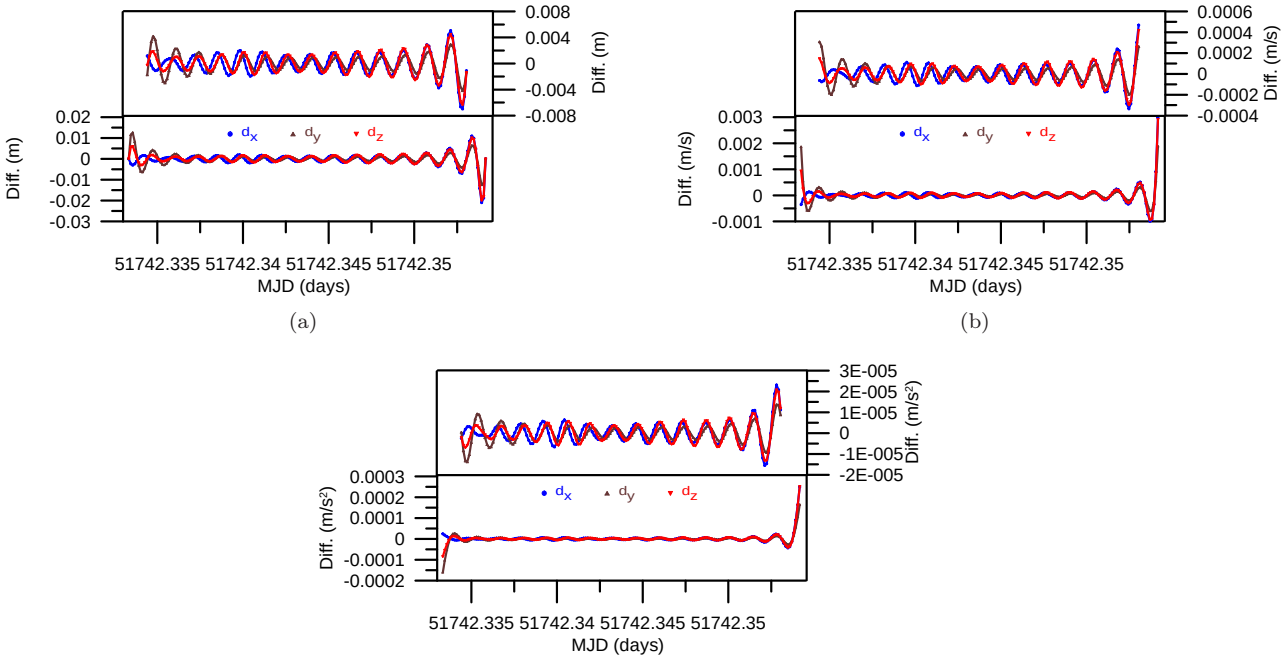

Figure 7.32: Gibb's effect, N_F =300, *error free case*, Fourier upper index $\bar{n} = 30$ ((a) absolute position differences (b) velocity differences (c) acceleration differences).

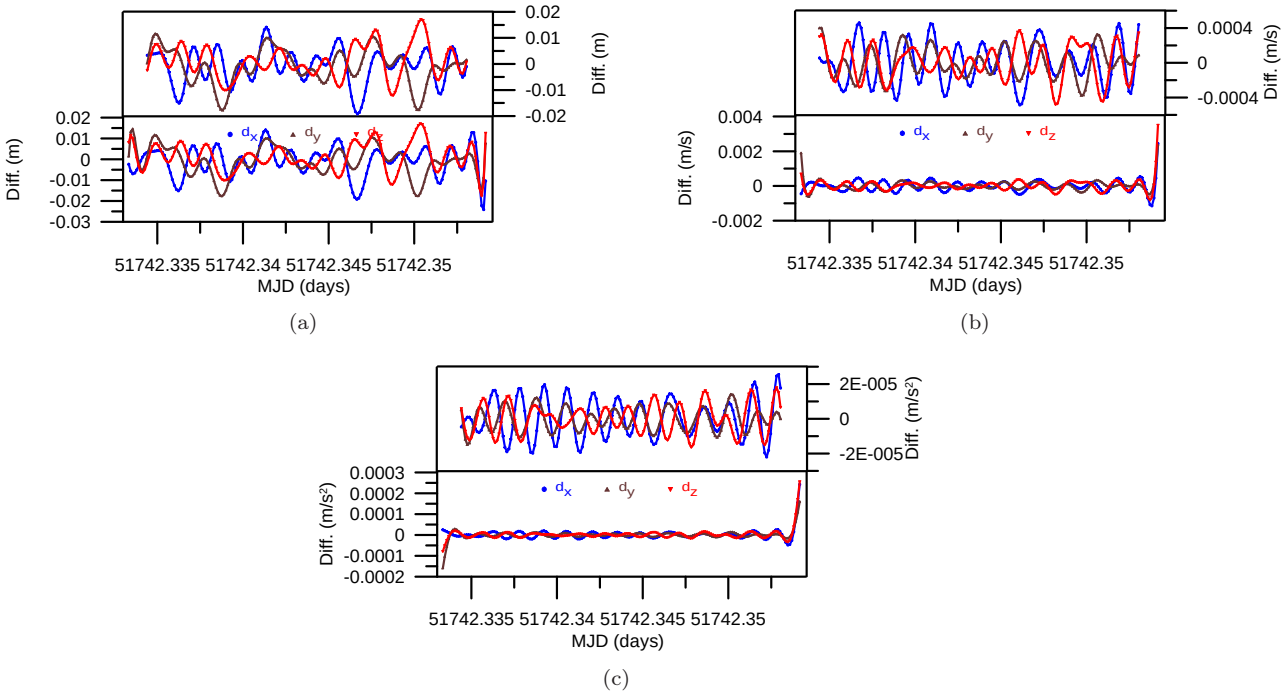

Figure 7.33: Gibb's effect, $N_F = 300$, *white noise of* $2cm$, Fourier upper index $\bar{n} = 30$ ((a) absolute position differences (b) velocity differences (c) acceleration differences).

7.3.2 Real Case

The tests of the kinematical precise orbit determination technique for simulation scenarios give satisfactory results. In this section, we try to validate the orbit determination approach based on real high-low GPS-SST observations. Generally, it is very difficult to find an objective criterion to validate the results. We selected two different possibilities, all of them describe the quality imperfectly, but may give a first impression of the quality of the kinematical precise orbit determination results:

- Validation by comparisons with the PSO (Post-processed Scientific Orbits) results provided by GFZ Potsdam,
- Validation by inspection of carrier phase GPS-SST observation residual at interpolated epochs.

For comparison reasons, the orbit determination examples are restricted also to 30 minute short arcs of the CHAMP satellite. The Table 7.2 shows the various real CHAMP short arc examples for the different estimated time periods. These examples correspond to those which are used in Sec. 7.2.2 for the geometrical orbit determination and shown in the Figs. 7.20 to 7.23.

Table 7.2: Summary of all real kinematical precise orbit determination cases.

Figure	Observation Type	Computation Type	Time
Fig. 7.34	Positions	flowchart Fig. 6.1	2002 03 21 13h 30m 0.0s-14h 00m 0.0s
Fig. 7.35	Positions	flowchart Fig. 6.1	2002 07 20 12h 48m 0.0s-13h 18m 0.0s
Fig. 7.36	Positions	flowchart Fig. 6.1	2003 03 21 17h 20m 0.0s-17h 50m 0.0s
Fig. 7.37	Positions	flowchart Fig. 6.1	2003 03 31 17h 00m 0.0s-17h 30m 0.0s

7.3.2.1 Comparison with the PSO Dynamical Ephemerides

In the simulated case, the proposed kinematical precise orbit determination strategy has been proved to be an efficient method to determine the LEO orbit based on the high-low GPS-SST observations. Therefore, to test the proposed kinematical orbit determination strategy based on the real data, four different CHAMP short arcs are selected (Table 7.2). To simplify the problem, the point-wise absolute positions of the selected short arcs are estimated with the geometrical orbit determination strategy based on the carrier phase observations. Subsequently, the estimated CHAMP positions with their variance-covariance information are used in the kinematical precise orbit determination procedure.

As described in Fig. 6.1, as a first step, the CHAMP boundary positions and the sine series amplitudes of the short arc are estimated based on geometrically determined CHAMP positions. In a second step, the Euler-Bernoulli polynomial coefficients up to degree $J_{max} = 4$ are estimated based on the positions independently. The residual sine amplitudes with the index 20, 30, 40 and 59 are estimated based on a sine analysis of the remaining function (or by a least squares adjustment procedure) in a third step.

As a first test example, the CHAMP arc with the time period 2002 03 21 13h 30m 0.0s - 14h 00m 0.0s is selected (ground track (a) in Fig. 7.13). The absolute positions are determined for this short arc based on the carrier phase GPS-SST observations. It should be mentioned that in the geometrical orbit determination procedure, a cut off angle 15° is applied to the GPS-SST observations on-board the CHAMP satellite and subsequently the code pseudo-range and carrier phase GPS-SST observations are screened with respect to outliers and cycle slips. As a result, Fig. 7.34(a) shows the calculated carrier phase GPS-SST observation residuals after the kinematical orbit determination procedure for the different residual sine series with the upper indices 20, 30, 40 and 59. The bottom graph of Fig. 7.34(a) corresponds to the graph 7.20(a). The three graphs at the top reflect also the additional errors caused by the sine series of the residual function

limited by the respective upper index 20, 30 and 40. Figs. 7.34(b) and 7.34(c) show the corresponding position and velocity differences from the positions and velocities given for the CHAMP PSO arcs at the interpolated epochs (at every 10 sec.). The results show the accuracy of the estimated kinematical orbit based on the geometrical orbit as input. Fig. 7.34(b), bottom, corresponds to the geometrical position differences at the observation epochs shown in Fig. 7.20(b). In Fig. 7.34(d), the residual sine series amplitudes for the index 59 are shown. The RMS values in the Table of Fig. 7.34 show the results for the residual sine series for different upper indices at the interpolation epochs. The results are more or less identical for the different upper indices because of the large systematic derivations. The differences (bias or/and trend) between the kinematical solution and the PSO in the positions and velocities show probably systematical mis-modeling effects of the CHAMP dynamical PSO orbits.

The Figs. 7.35 to 7.37 correspond to the results of the geometrical orbit determination results as shown in Figs 7.21 to 7.23. Despite the large systematic differences in the positions and velocities, the small residuals in panels (a) of the Figures demonstrate the quality of the kinematical orbit determination procedure, so that the systematic deviations are caused mainly by the dynamical model used for the PSO orbits.

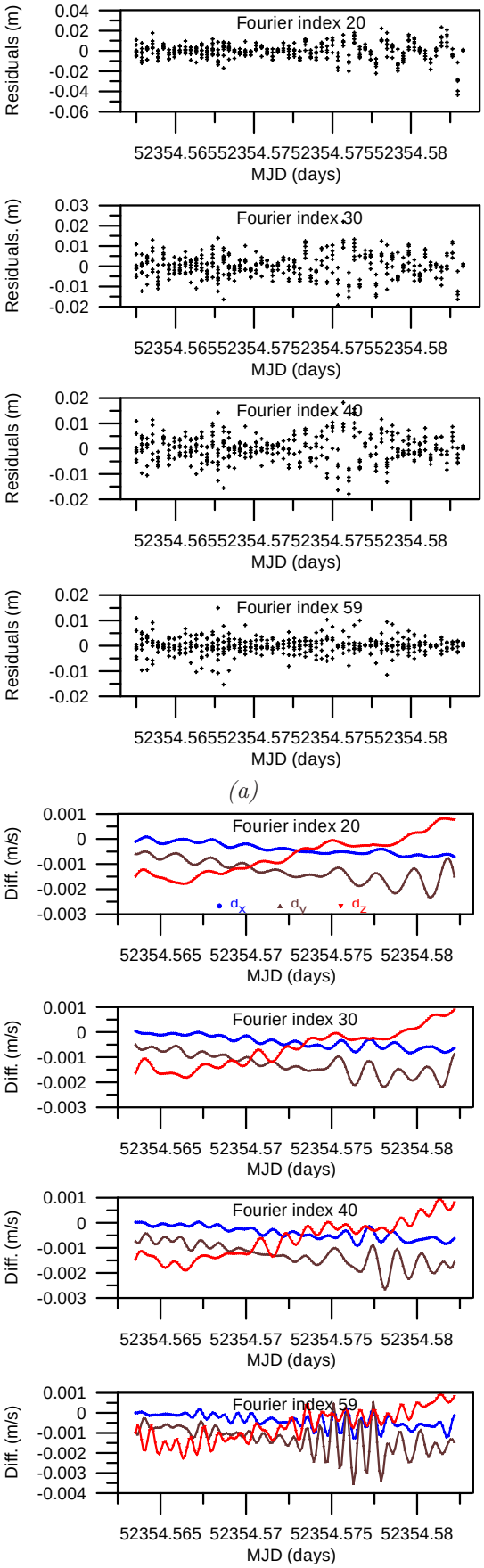

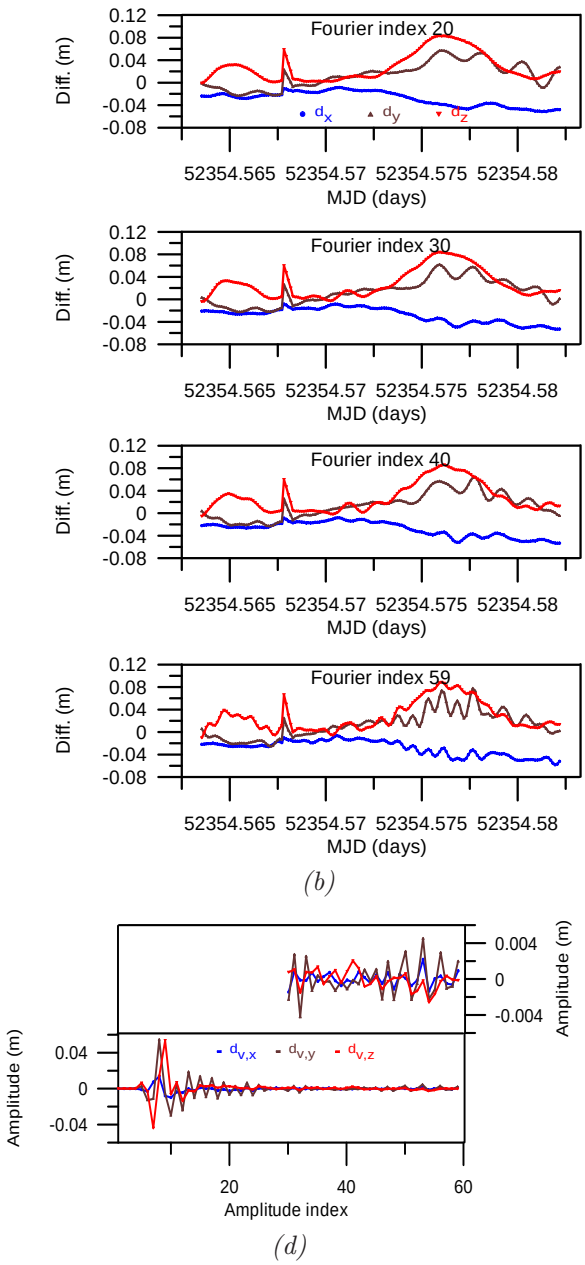

Figure 7.34: (a) Carrier phase GPS-SST observation residuals after KPOD at observation epochs (b) position differences at interpolated epochs (refer to *PSO* ephemerides) (c) velocity differences at interpolated epochs (refer to *PSO* velocities)(d) Fourier spectrum (reference motion: *ellipse mode*, J_{max}=4, method: *flowchart Fig. 6.1*, without $\approx 5\%$ at boundaries $\equiv 9$ points or 80 sec.) for the time of *2002 03 21 13h 30m 0.0s–14h 00m 0.0s*.

RMS

index	Pos.(m)	Vel.(m/s)
20	0.0513	0.0017
30	0.0513	0.0017
40	0.0515	0.0018
59	0.0520	0.0019

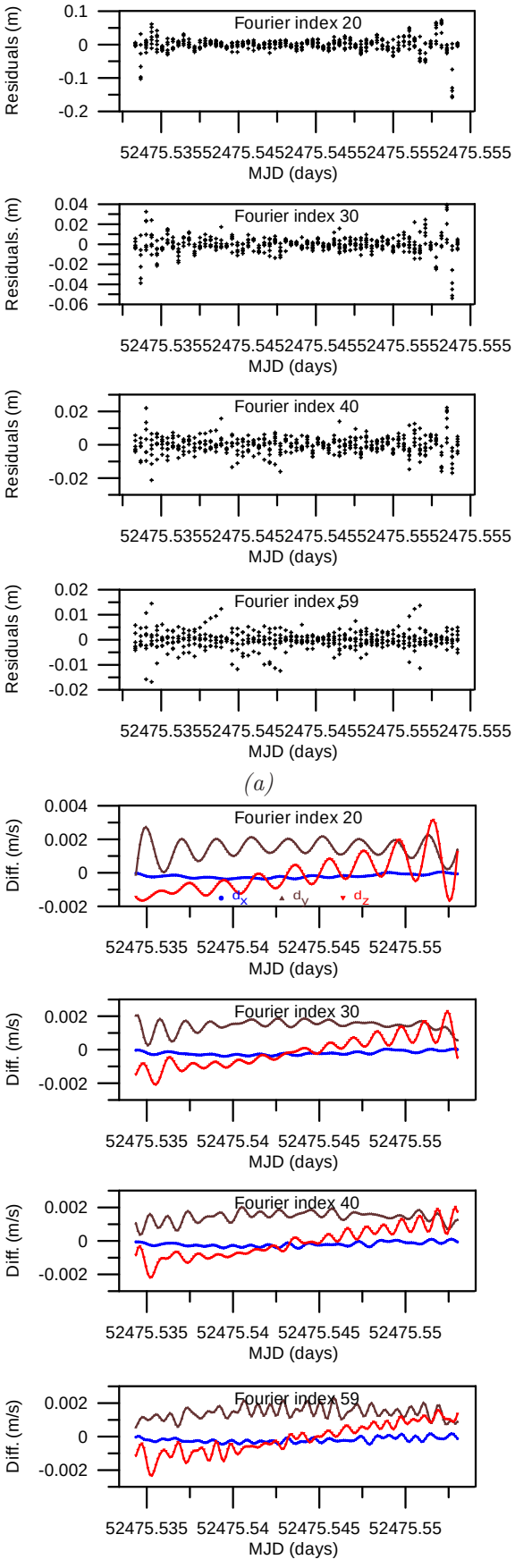

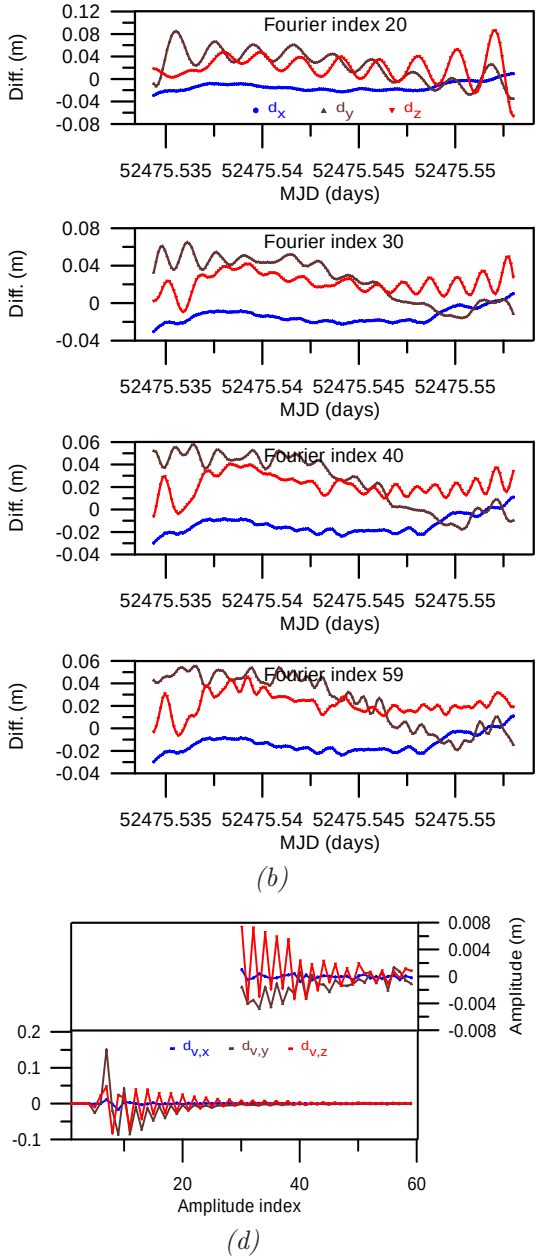

Figure 7.35: (a) Carrier phase GPS-SST observation residuals after KPOD at observation epochs (b) position differences at interpolated epochs (refer to *PSO* ephemerides) (c) velocity differences at interpolated epochs (refer to *PSO* velocities)(d) Fourier spectrum (reference motion: *ellipse mode*, J_{max}=4, method: *flowchart Fig. 6.1*, without $\approx 5\%$ at boundaries $\equiv$ 9 points or 80 sec.) for the time of *2002 07 20 12h 48m 0.0s–13h 18m 0.0s*.

RMS

index	Pos.(m)	Vel.(m/s)
20	0.0503	0.0019
30	0.0455	0.0018
40	0.0449	0.0017
59	0.0449	0.0017

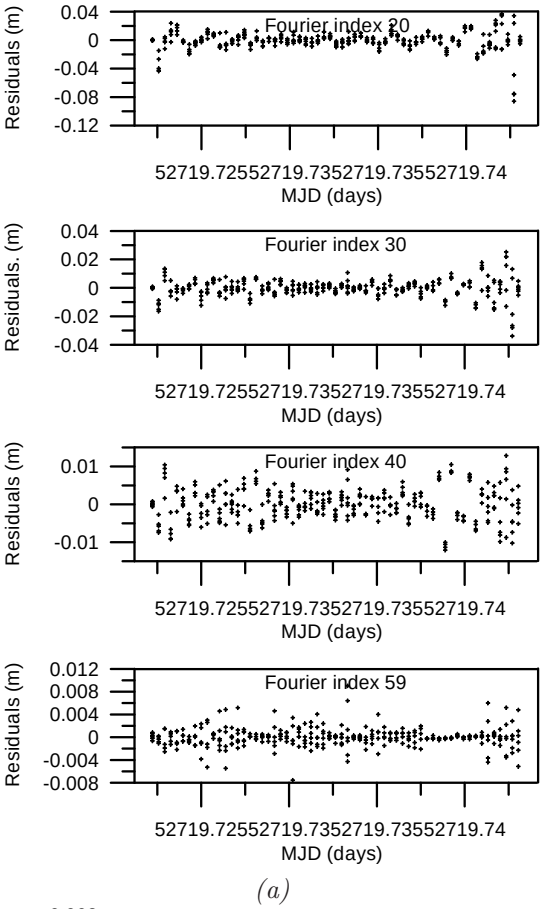

(a)

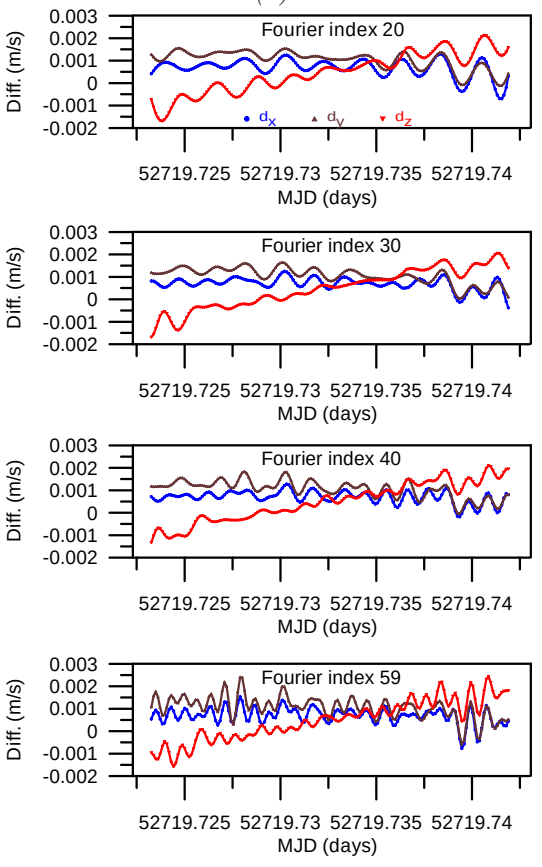

(c)

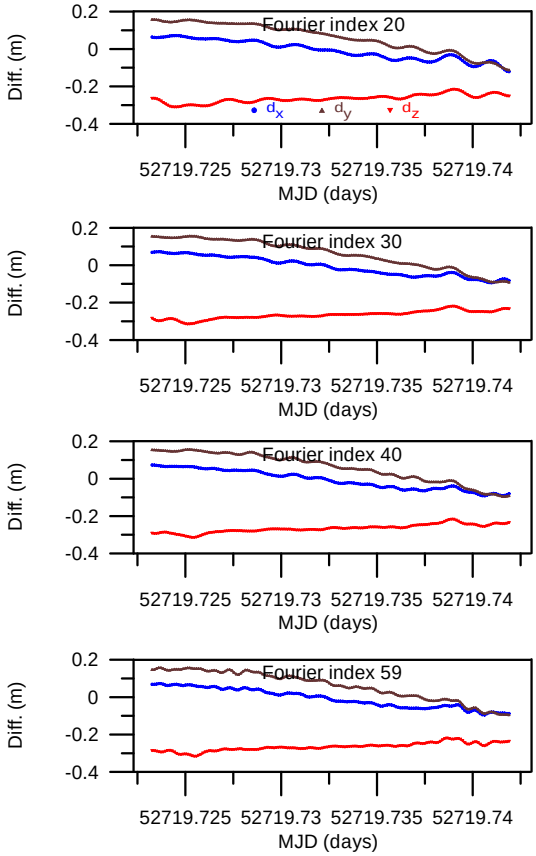

(b)

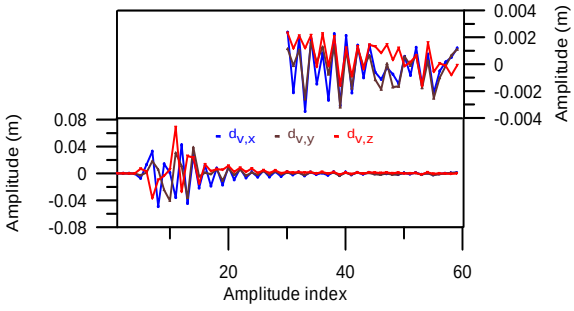

(d)

Figure 7.36: (a) Carrier phase GPS-SST observation residuals after KPOD at observation epochs (b) position differences at interpolated epochs (refer to *PSO* ephemerides) (c) velocity differences at interpolated epochs (refer to *PSO* velocities)(d) Fourier spectrum (reference motion: *ellipse mode*, J_{max}=4, method: *flowchart Fig. 6.1*, without $\approx 5\%$ at boundaries $\equiv 9$ points or 80 sec.) for the time of *2003 03 21 17h 20m 0.0s–17h 50m 0.0s*.

RMS

index	Pos.(m)	Vel.(m/s)
20	0.1402	0.0019
30	0.1402	0.0019
40	0.1403	0.0019
59	0.1404	0.0020

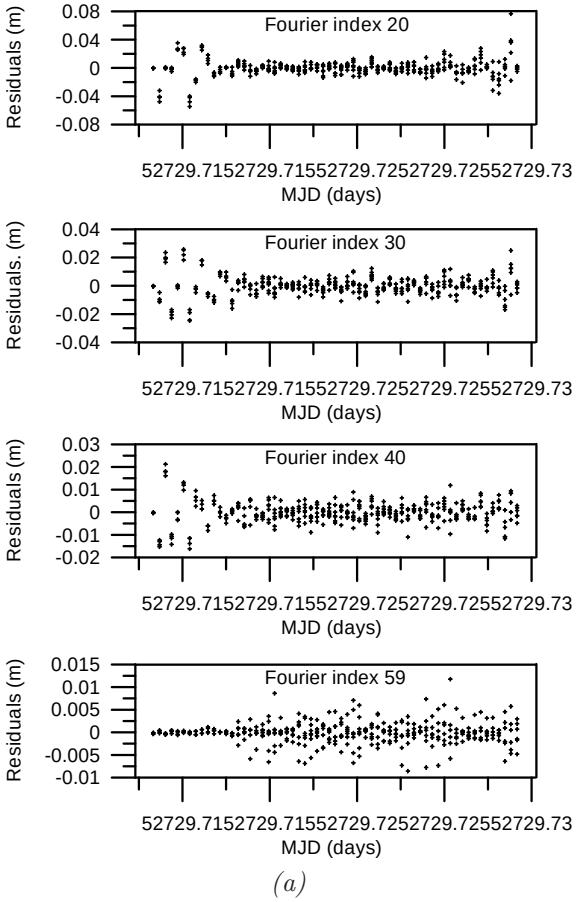

(a)

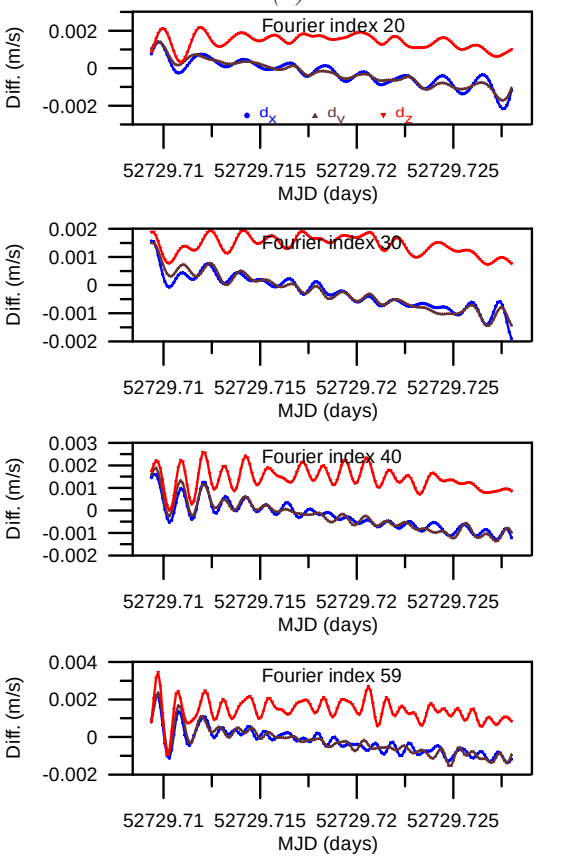

(c)

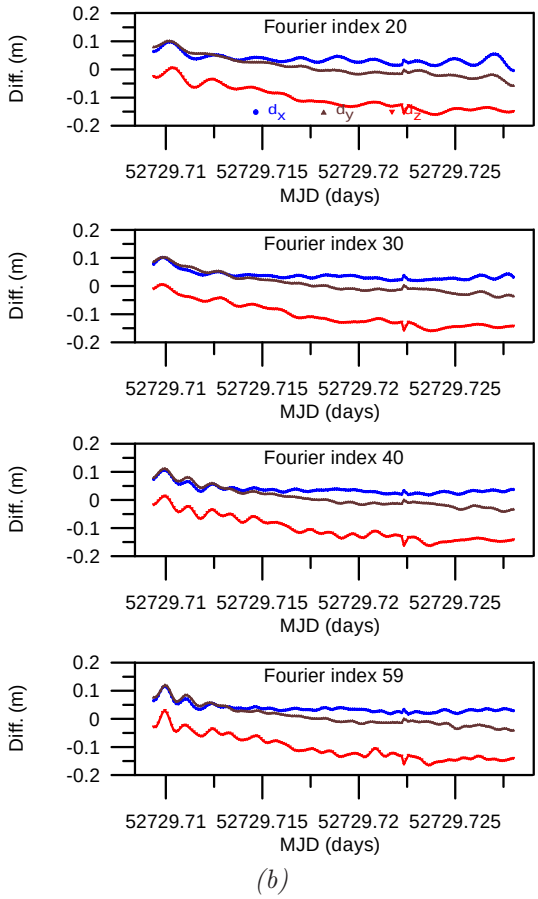

(b)

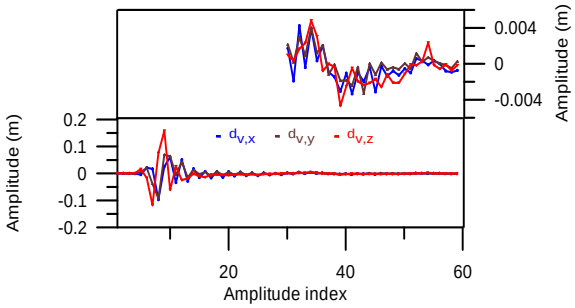

(d)

Figure 7.37: (a) Carrier phase GPS-SST observation residuals after KPOD at observation epochs (b) position differences at interpolated epochs (refer to *PSO* ephemerides) (c) velocity differences at interpolated epochs (refer to *PSO* velocities)(d) Fourier spectrum (reference motion: *ellipse mode*, J_{max}=4, method: *flowchart Fig. 6.1*, without $\approx 5\%$ at boundaries $\equiv$ 9 points or 80 sec.) for the time of *2003 03 31 17h 00m 0.0s–17h 30m 0.0s*.

RMS

index	Pos.(m)	Vel.(m/s)
20	0.1202	0.0018
30	0.1201	0.0017
40	0.1204	0.0018
59	0.1204	0.0019

7.3.2.2 Comparison with Carrier Phase GPS-SST Observation at Interpolated Epochs

The proposed kinematical precise orbit determination approach is tested based on the simulated SC7 data set and on the real data from the GPS receiver on-board CHAMP. Both cases show the capabilities of the procedure. In the real case, the comparison with kinematically estimated short arcs, the PSO dynamical orbits and Švehla's dynamical solutions are used for comparison. In both cases, the comparisons show systematic differences. They can be the effects of the dynamical mis-modelings of the CHAMP orbits.

Therefore, as an additional quality check, the carrier phase GPS-SST observations at every 10 sec. are compared with the kinematically determined carrier phase observations. For this task, the GPS satellite position and velocity coordinates are interpolated with a polynomial of degree 9 at epochs with a time difference of 10 sec. To avoid the non-linear effect of the CHAMP clock offsets at the interpolated epochs, the clock offset are estimated based on the geometrical precise orbit determination technique and used in the following test. At the interpolation epochs, the carrier phase GPS-SST observations between the CHAMP and the GPS satellites can be calculated based on the interpolated GPS satellites ephemerides, the kinematically determined CHAMP positions and, under consideration of the CHAMP and GPS clock offsets, the GPS ambiguity parameters as well as the relativistic effects of the satellites. To simplify the problem, the ionosphere-free carrier phase observations are used in the computation. This comparison method is applied for the four selected CHAMP short arcs (ground tracks (a) to (d) in Fig. 7.13). Figs. 7.38(a) to 7.38(d) show the carrier phase GPS-SST observation difference at the interpolation epochs (at every 10 sec) for the four selected short arcs (30 minute) separately for the different residual sine series indices, respectively. The residual sine series with an upper index of 40 shows already sufficient good results in case of all four CHAMP short arcs. It should be mentioned that the kinematical positions are calculated based on the estimated kinematical parameters for the different residual sine series 20, 30, 40 and 59. Therefore, the Gibb's effect may be the reason for some jumps at the beginning and the end of the short arcs especially for the lower indices.

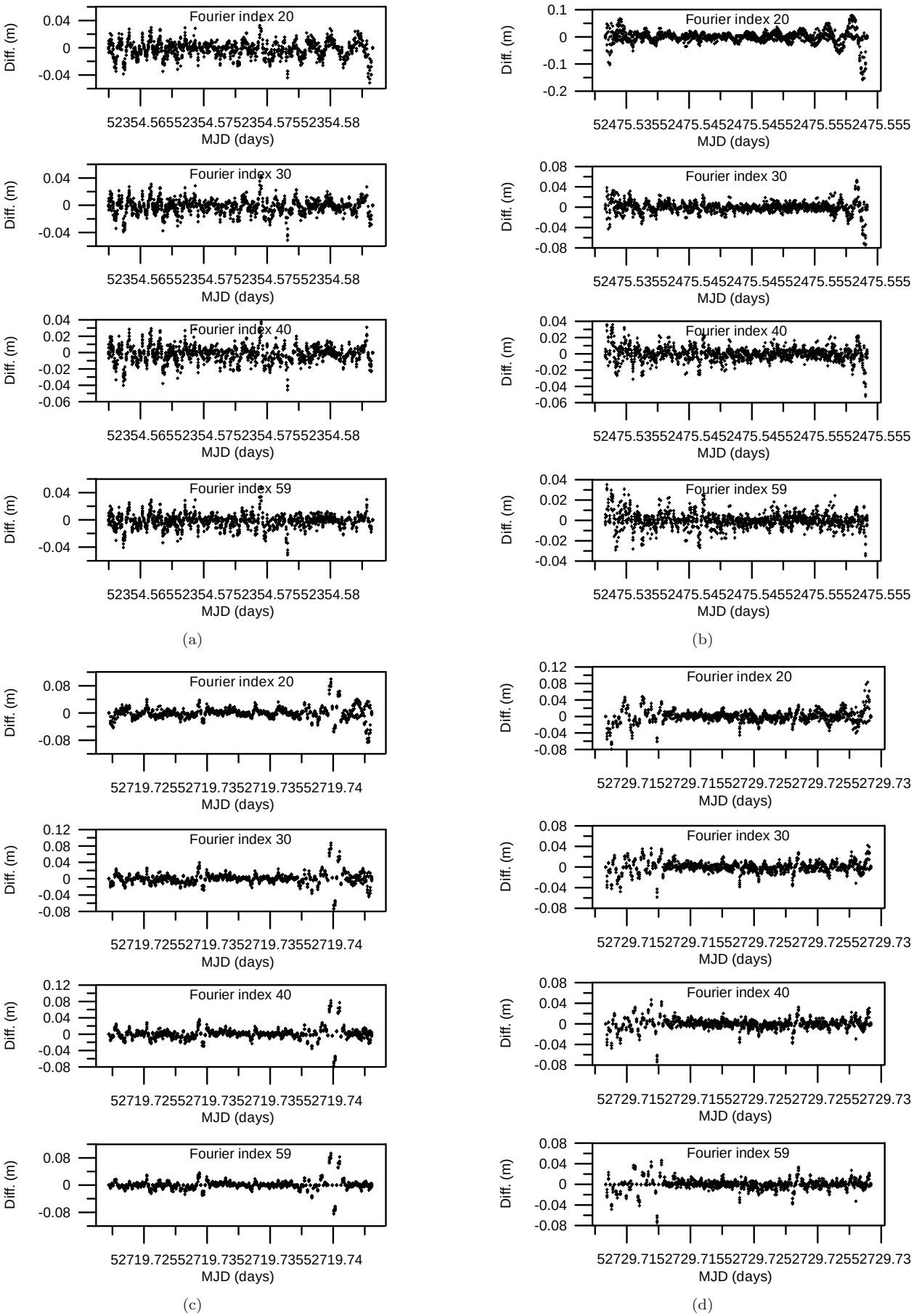

Figure 7.38: Carrier phase GPS-SST observation differences at every *10 sec.* (at interpolation epochs) for the time periods of (a) *2002 03 21 13h 30m 0.0s–14h 00m 0.0s* (b) *2002 07 20 12h 48m 0.0s–13h 18m 0.0s* (c) *2003 03 21 17h 20m 0.0s–17h 50m 0.0s* (d) *2003 03 31 17h 00m 0.0s–17h 30m 0.0s.*

7.4 Reduced-Kinematical Precise Orbit Determination (RKPOD)

The sine coefficients $\mathbf{d}_\nu$ can be considered as coefficients of a linear approximation of the satellite's orbit. If we determine these coefficients by a least squares fitting based on the geometrically determined satellite's positions then we end up with a pure kinematical orbit determination. But the quantities $\tilde{\mathbf{d}}_i$ to $\tilde{\mathbf{d}}_j$ can be considered also as a-priori information for the amplitudes $\mathbf{d}_i \cdots \mathbf{d}_j$ in Eq. (6.80) with the variance-covariance matrices $\mathbf{C}(\tilde{\mathbf{d}}_i)$ to $\mathbf{C}(\tilde{\mathbf{d}}_j)$ in Eq. (6.81). The indices i to j define the sine coefficients with a-priori information and can be selected so that they cover the total index domain $i = 1$ and $j = n$ or some specific amplitudes. Then the unknowns $\mathbf{x}_2(\mathbf{d}_i, \cdots, \mathbf{d}_j)$ can be determined according to Eq. (6.97),

$$\mathbf{Q}_{\hat{\mathbf{x}}_2\hat{\mathbf{x}}_2}\mathbf{C}_2^{-1}\mathbf{l}_2 = \mathbf{l}_2 - \mathbf{C}_2\mathbf{A}_2^{\mathrm{T}}\bar{\mathbf{C}}_1^{-1}\mathbf{A}_2\mathbf{l}_2 + \mathbf{C}_2\mathbf{A}_2^{\mathrm{T}}\bar{\mathbf{C}}^{-1}\mathbf{A}_1\mathbf{Q}_{\hat{\mathbf{x}}_1\hat{\mathbf{x}}_1}\mathbf{A}_1^{\mathrm{T}}\bar{\mathbf{C}}^{-1}\mathbf{A}_2\mathbf{l}_2,$$

with the 'pseudo observation', Eq (6.85)

$$\mathbf{l}_2 = \begin{pmatrix} \tilde{\mathbf{d}}_i & \cdots & \tilde{\mathbf{d}}_j \end{pmatrix}^{\mathrm{T}},$$

and the a-priori variance-covariance matrix Eq. (6.86)

$$\mathbf{C}_2 = \mathbf{C}(\tilde{\mathbf{d}}) = \begin{pmatrix} \mathbf{C}(\tilde{\mathbf{d}}_i) & \cdots & \mathbf{0} \\ \vdots & \ddots & \vdots \\ \mathbf{0} & \cdots & \mathbf{C}(\tilde{\mathbf{d}}_j) \end{pmatrix}.$$

If all coefficients are determined as pseudo-observations,

$$\mathbf{l}_2 = \begin{pmatrix} \tilde{\mathbf{d}}_1 & \cdots & \tilde{\mathbf{d}}_n \end{pmatrix}^{\mathrm{T}},$$

based on a specific gravitational potential and the a-priori variance-covariance matrix $\mathbf{C}_2 \to \mathbf{0}$ then it follows, Eq. (6.99)

$$\hat{\mathbf{x}}_2 = \mathbf{l}_2.$$

In that case, the amplitudes are fixed according to the gravitational potential used and only the boundary values are corrected. The result corresponds to the result of a dynamical orbit determination. Besides this strict dynamical restrictions, there are basically three different possibilities to influence the kinematical orbit determination by dynamical information and to come up with a reduced-kinematical orbit determination modification, as outlined in Sec. 6.2. The dynamical restrictions can be defined by

1. introduction of an approximate force function for the determination of the values $(\mathbf{d}_i \cdots \mathbf{d}_j)$, combined with an approximate a-priori variance-covariance matrix $\mathbf{C}_2 = \mathbf{C}(\tilde{\mathbf{d}})$,
2. fixing only some orbit parameters $(\mathbf{d}_i \cdots \mathbf{d}_j)$ by setting a low variance-covariance matrix for $\mathbf{C}_2 = \mathbf{C}(\tilde{\mathbf{d}}) \to \mathbf{0}$,
3. down- or up-weighting of the a-priori variance-covariance matrix $\mathbf{C}_2$ in relation to $\mathbf{C}_1$.

Because of these various possibilities to adopt the character of the orbit to a variety of applications covering the spectrum from a pure kinematical on the one end to a pure dynamical orbit determination on the other end makes this approach very flexible. Table 7.3 summarizes all investigated examples. The results of the pure kinematical orbit determination (KPOD) are shown in Fig. 7.27 (see Sec. 7.3) for the orbit characteristics and for the determination mode.

Table 7.3: Summary of all reduced-kinematical precise orbit determination cases.

rest. type	error case	noise free		white noise(2cm)		white noise (5 cm)	
1	gravity field	300	300	300		60	60
2	dynamical restriction	[1-5]	[1-59]	[1-5]	[1-59]	[1-59]	[1-59]
3	var.-cov. matrix	$\|\mathbf{C}_2\| << \|\mathbf{C}_1\|$		$\|\mathbf{C}_2\| << \|\mathbf{C}_1\|$		variance $\|\mathbf{C}_2\|$	
	Figure	Fig.7.39	Fig.7.40	Fig.7.41	Fig.7.42	Fig.7.43	Fig.7.44

7.4.1 Noise Free Case

As first example demonstrates the effect of fixing sine coefficients for the indices $\nu = 1$ to $\nu = 5$. This example corresponds to the restriction type 2 based on 'true' gravity field introduced with a large weight (small variance). Fig. 7.39 shows the results in case of different upper index limits for the sine series. Fig. 7.39(a) shows the position differences, Fig. 7.39(b) the velocity and Fig. 7.39(c) the acceleration differences between the solutions and the SC7 'true' data. The comparison with the kinematical orbit determination (Fig. 7.27) shows more or less identical results; the restriction of the amplitudes with the indices $\nu = 1$ to $\nu = 5$ has no improvement effect and degrades the results in the positions slightly. The dynamical orbit determination case is achieved in case of an upper index of 59 (Fig. 7.40), if all amplitudes are restricted by the force function model. The differences of all cases show similar results in terms of RMS values for positions, velocities and accelerations with slightly better results for the dynamical orbit determination case. In judging the results, one has to keep in mind that, similar to the results for the KPOD cases in Sec. 7.3, the orbit determination is performed by positions with a sampling rate of 30 sec., while the sampling rate of the comparisons with the SC7 'true' data is 10 sec. Therefore, the RMS values contain also interpolation errors.

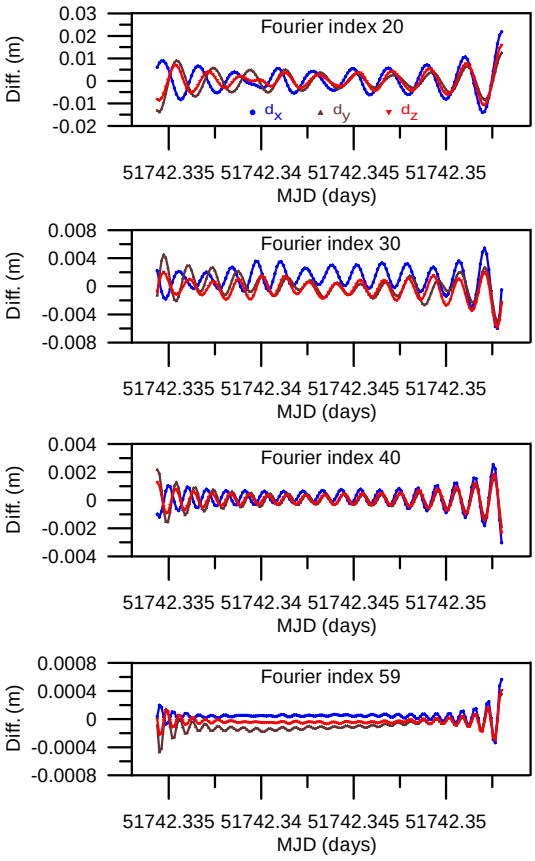

(a)

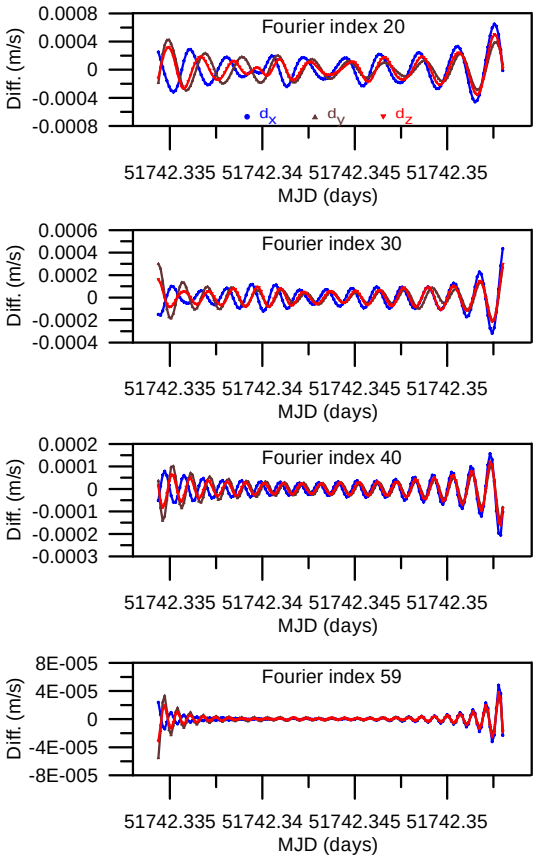

(b)

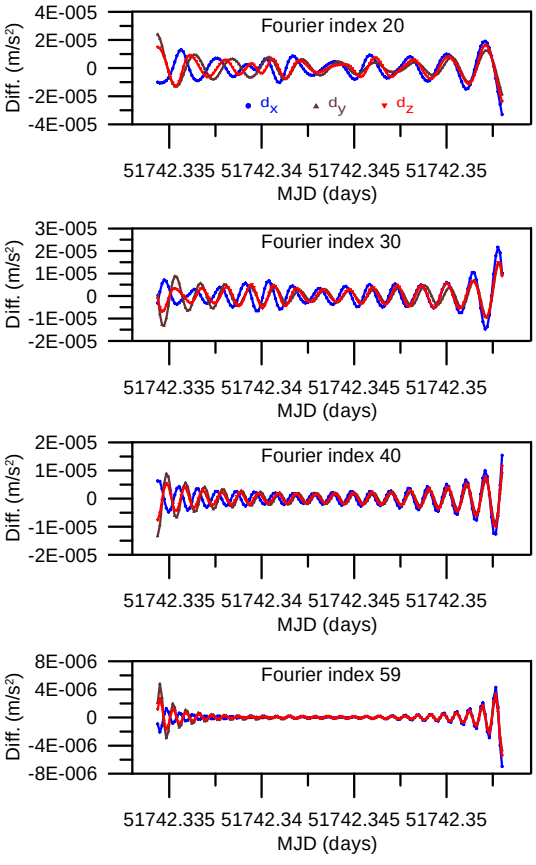

(c)

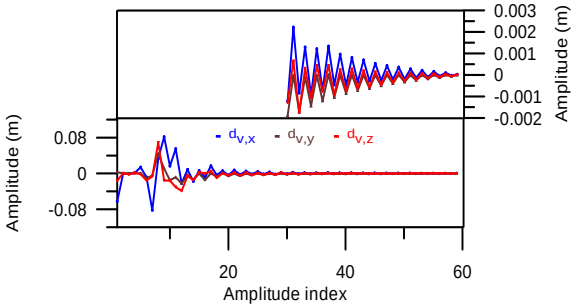

(d)

Figure 7.39: (a) Position differences (b) velocity differences (c) acceleration differences (d) Fourier spectrum (dynamical restriction index window [1-5], reference motion: *ellipse mode*, J_{max}=4, N_F =300, *error free case*, observation type: *Positions*, method: *flowchart Fig. 6.2*, observation sampling rate: *30 sec.*, test sampling rate: *10 sec.*, without $\approx$ 5% at boundaries $\equiv$ 9 points or 80 sec.).

RMS

index	Pos.(m)	Vel.(m/s)	Acc.(m/s^2)
20	0.007975	0.000296	0.000011
30	0.002924	0.000135	0.000008
40	0.001019	0.000074	0.000005
59	0.000169	0.000013	0.000001

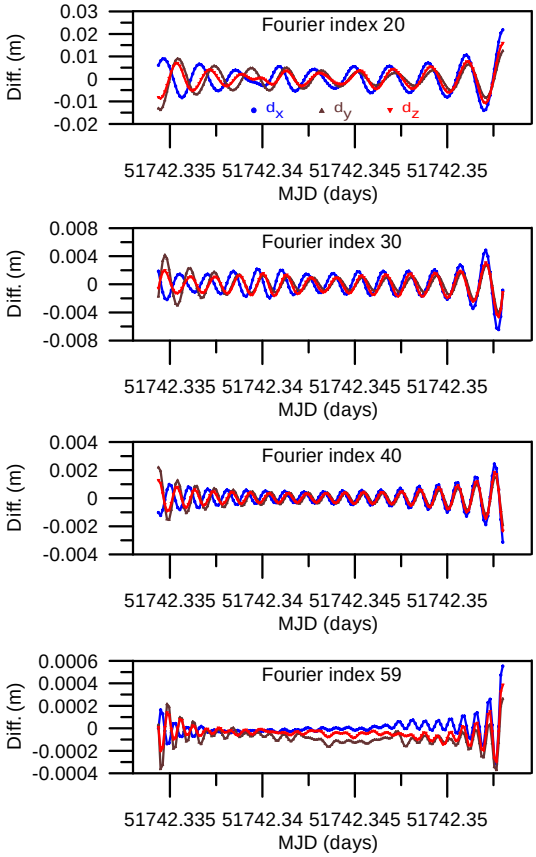

(a)

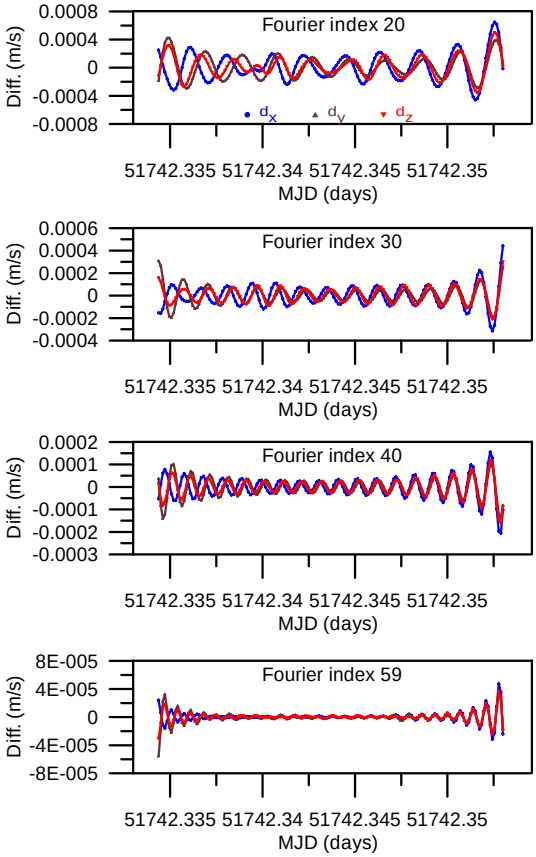

(b)

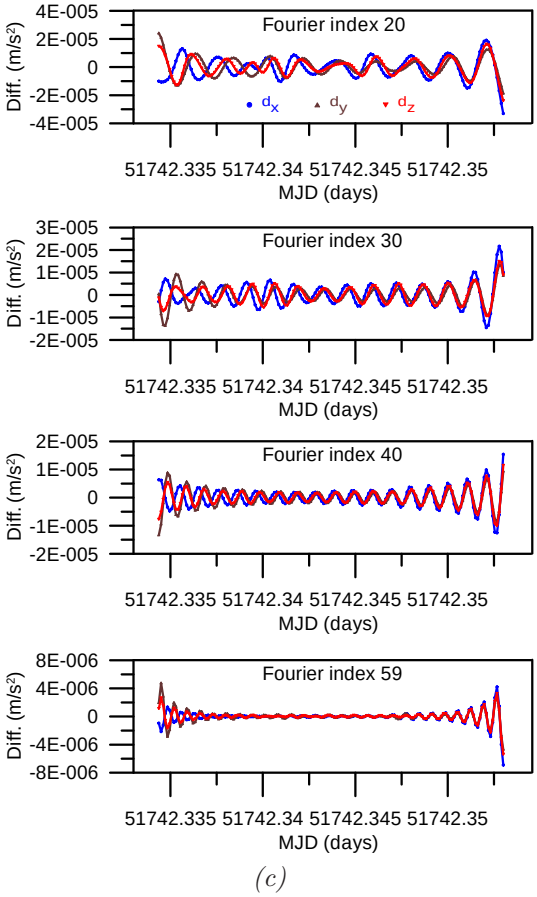

(c)

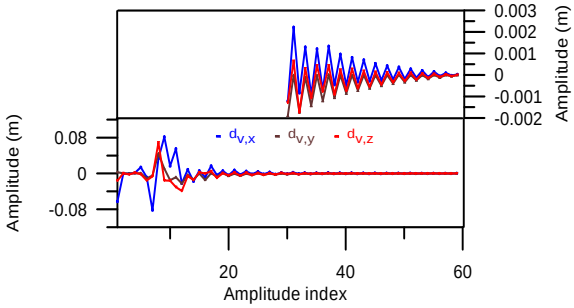

(d)

Figure 7.40: (a) Position differences (b) velocity differences (c) acceleration differences (d) Fourier spectrum (dynamical restriction index window [1-59], reference motion: *ellipse mode*, J_{max}=4, N_F =300, *error free case*, observation type: *Positions*, method: *flowchart Fig. 6.2*, observation sampling rate: *30 sec.*, test sampling rate: *10 sec.*, without ≈ 5% at boundaries ≡ 9 points or 80 sec.).

RMS

index	Pos.(m)	Vel.(m/s)	Acc.(m/s^2)
20	0.007974	0.000296	0.000011
30	0.002486	0.000134	0.000008
40	0.000999	0.000074	0.000005
59	0.000157	0.000013	0.000001

7.4.2 Error Case

To show the reduced-kinematical orbit determination strategy in the error case, the GPS-SST observations are contaminated with different levels of white noise ($2cm$ and $5cm$). The same CHAMP arcs as in Sec. 7.4.1 are considered here. The GPS-SST observations are contaminated with a white noise of $2cm$. Then the dynamical restriction windows $[\tilde{\mathbf{d}}_1$ to $\tilde{\mathbf{d}}_5]$ and $[\tilde{\mathbf{d}}_1$ to $\tilde{\mathbf{d}}_{59}]$ are added to the observations equations. Figs. 7.41(a) to (c) show the position coordinate, velocity and acceleration differences between the orbit determination results and the SC7 'true' values. This case corresponds to the kinematical orbit determination case shown in Fig. 7.31. The dynamical restrictions only have a small improvement effect. Figs. 7.42(a) to (c) show the dynamical case with a full dynamically restricted spectrum. If the results are compared with the unrestricted case, then we see a clear improvement with respect to the case shown in Fig. 7.31. The systematic effects in the position differences are caused by small corrections of the boundary vectors as a result of the least squares adjustment.

In theses two simulation cases, an Earth gravity field up to degree and order 300 is used for the reduced-kinematical orbit determination. It represents a full and accurate dynamical information of the Earth gravity field at the altitude of the low flying satellite . To investigate the effect of an approximate dynamical information, an Earth gravity field up to degree and order $N_F = 60$ is selected. Fig. 7.43, based on a white noise level of $2cm$, shows the results of a reduced-kinematical orbit determination by restricting all amplitudes based on this approximate gravity field. The panels of the Figs. 7.43(a) to (c) show the results with different weights. A low weight (top panel) produces a low dynamical restriction while a high weight (bottom panel) generates a dynamical orbit with the respective gravity field. To get an impression about the size of the influence of the band limited gravity field on a short 30 minute arc, Fig. 7.45 shows the deviations of the CHAMP arc determined dynamically up to a varying upper degree and order of the spherical harmonics expansion and compared to an orbit determined with a gravity field up to degree and order 300. The boundary vectors are selected to be identical for all cases. In case of degree and order 60, the systematic deviations are in the size of 0 to $15cm$ for the coordinates x, y and z and corresponds approximately to the differences shown in the bottom panel of Fig. 7.43(a). The differences shown in the top panel are approximately in the size of the observation noise of $2cm$. The case shown in Fig. 7.44 corresponds to the case shown in Fig. 7.43 with only difference that the white noise level is $5cm$. The qualitative character of the difference graphs are identical while the overall accuracy is lower corresponding to the lower observation accuracy.

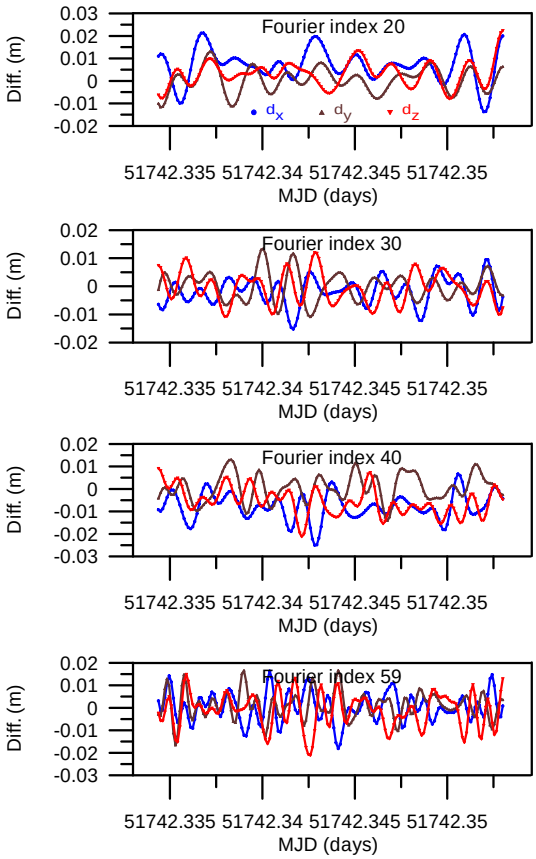

(a)

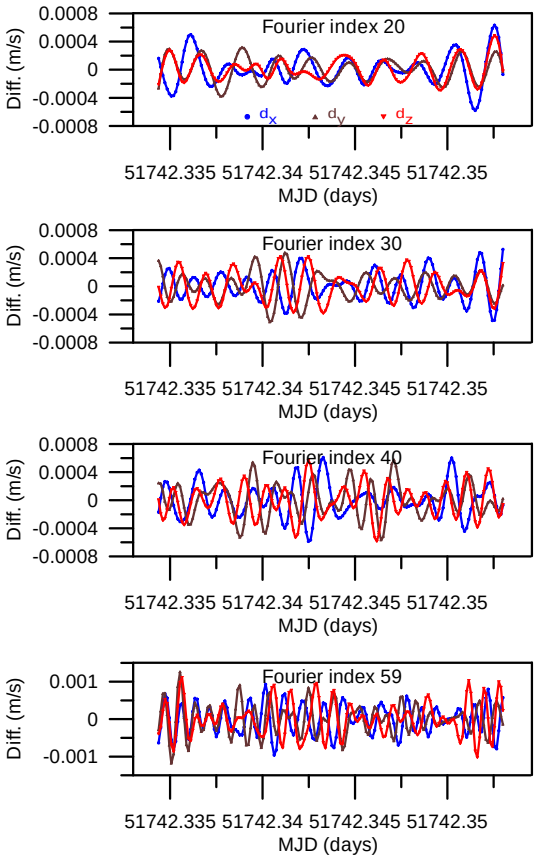

(b)

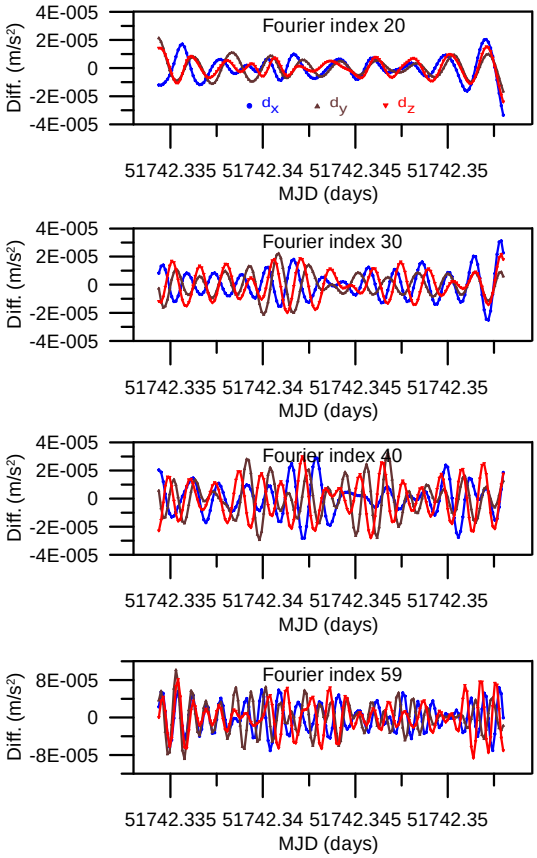

(c)

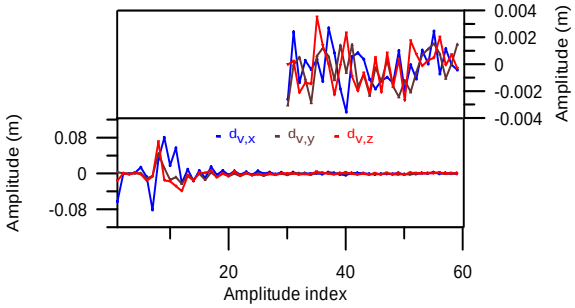

(d)

Figure 7.41: (a) Position differences (b) velocity differences (c) acceleration differences (d) Fourier spectrum (dynamical restriction index window [1-5], reference motion: *ellipse mode*, J_{max}=4, N_F =300, *white noise of* 2 *cm*, observation type: *Positions*, method: *flowchart Fig. 6.2*, observation sampling rate: *30 sec.*, test sampling rate: *10 sec.*, without $\approx$ 5% at boundaries $\equiv$ 9 points or 80 sec.).

RMS

index	Pos.(m)	Vel.(m/s)	Acc.(m/s^2)
20	0.012831	0.000316	0.000012
30	0.008873	0.000337	0.000016
40	0.014034	0.000402	0.000021
59	0.011553	0.000721	0.000056

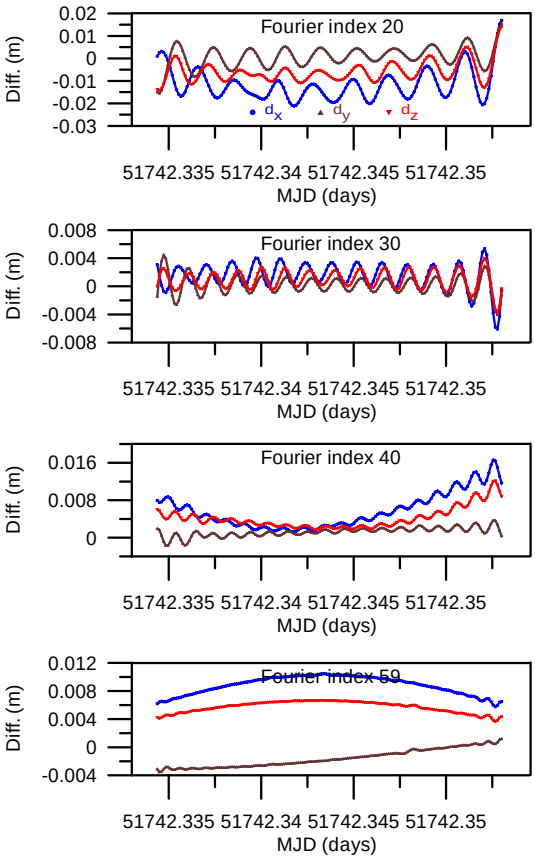

(a)

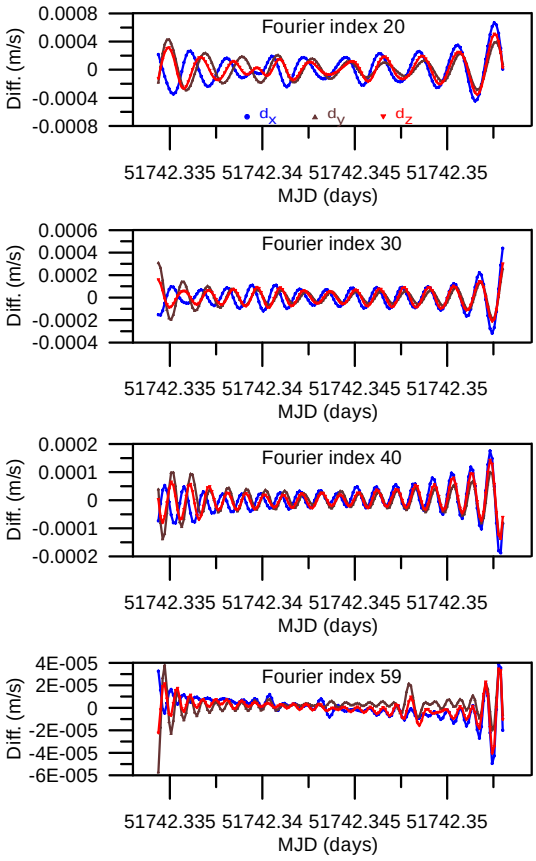

(b)

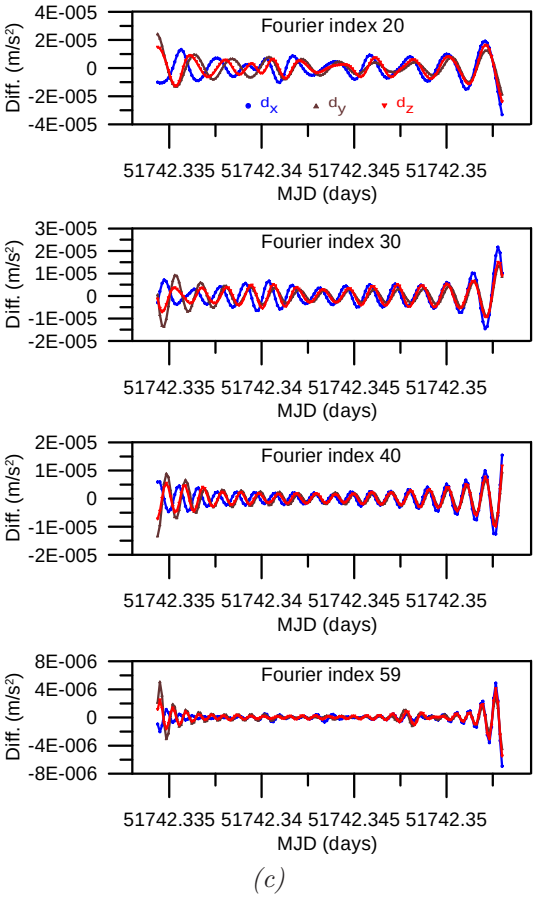

(c)

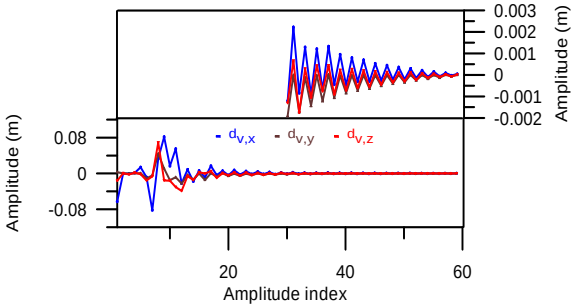

(d)

Figure 7.42: (a) Position differences (b) velocity differences (c) acceleration differences (d) Fourier spectrum (dynamical restriction index window [1-59], reference motion: *ellipse mode*, J_{max}=4, N_F =300, *white noise of* 2 *cm*, observation type: *Positions*, method: *flowchart Fig. 6.2*, observation sampling rate: *30 sec.*, test sampling rate: *10 sec.*, without $\approx 5\%$ at boundaries $\equiv$ 9 points or 80 sec.).

RMS

index	Pos.(m)	Vel.(m/s)	Acc.(m/s^2)
20	0.016108	0.000299	0.000011
30	0.003113	0.000134	0.000008
40	0.008375	0.000076	0.000005
59	0.010821	0.000016	0.000001

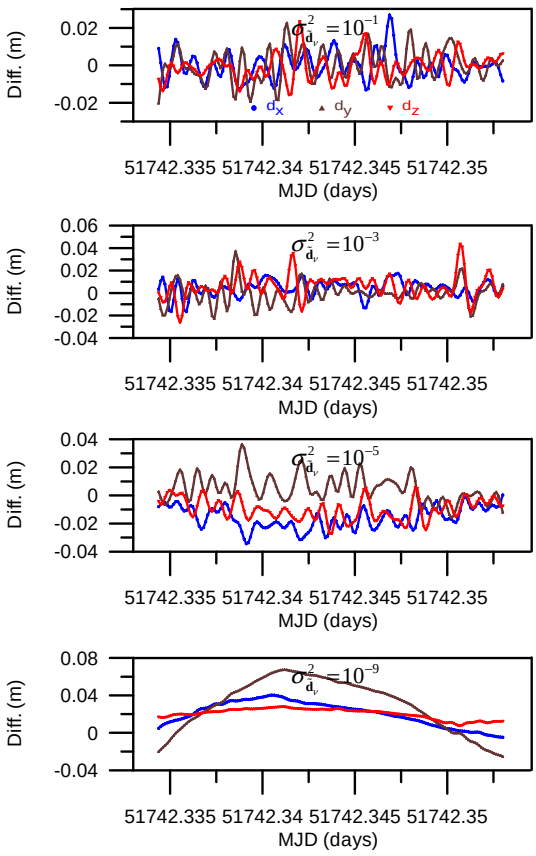

(a)

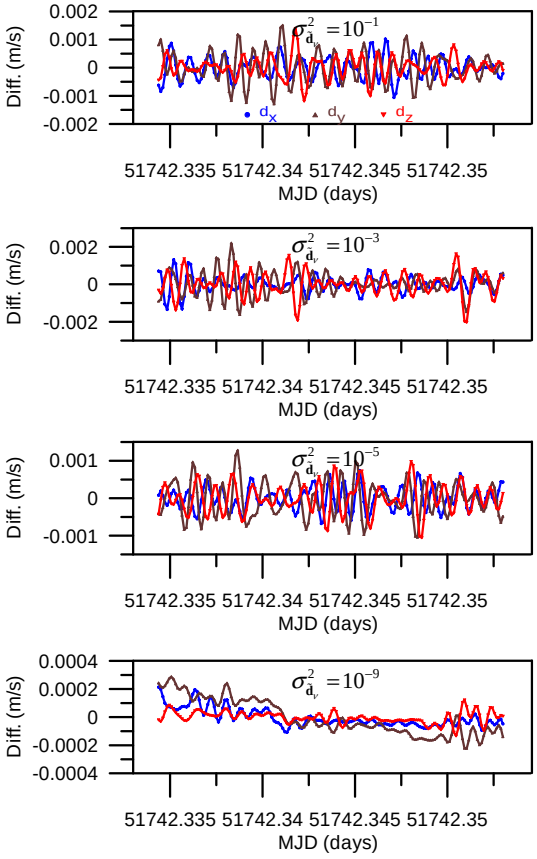

(b)

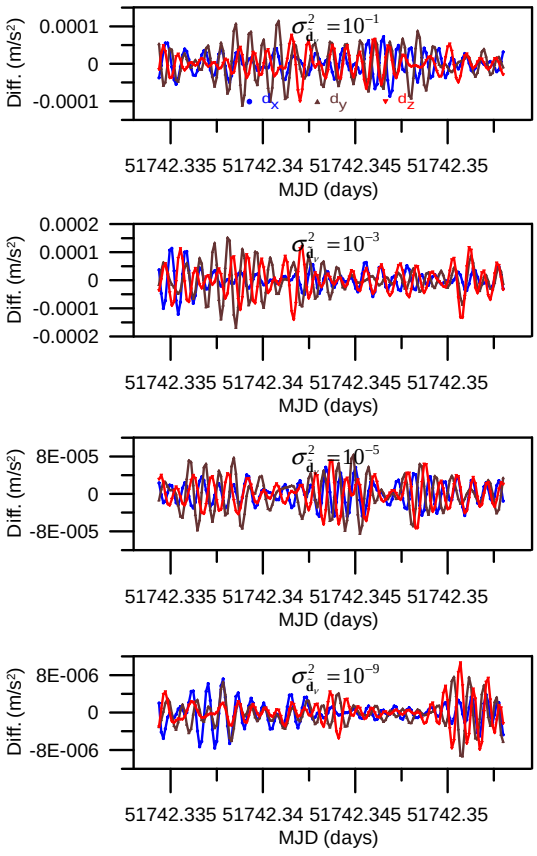

(c)

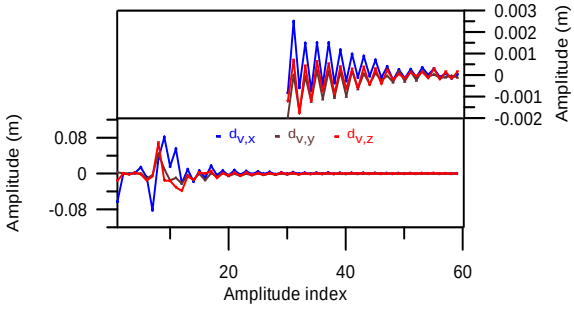

(d)

Figure 7.43: (a) Position differences (b) velocity differences (c) acceleration differences (d) Fourier spectrum (dynamical restriction index window [1-59], reference motion: *ellipse mode*, J_{max}=4, N_F =60, *white noise of* 2 *cm*, observation type: *Positions*, method: *flowchart Fig. 6.2*, observation sampling rate: *30 sec.*, test sampling rate: *10 sec.*, without $\approx$ 5% at boundaries $\equiv$ 9 points or 80 sec.).

RMS

$\sigma^2_{\tilde{d}_\nu}$	Pos.(m)	Vel.(m/s)	Acc.(m/s^2)
10^{-1}	0.013007	0.000777	0.000061
10^{-3}	0.017380	0.000987	0.000080
10^{-5}	0.024032	0.000681	0.000051
10^{-9}	0.052265	0.000150	0.000004

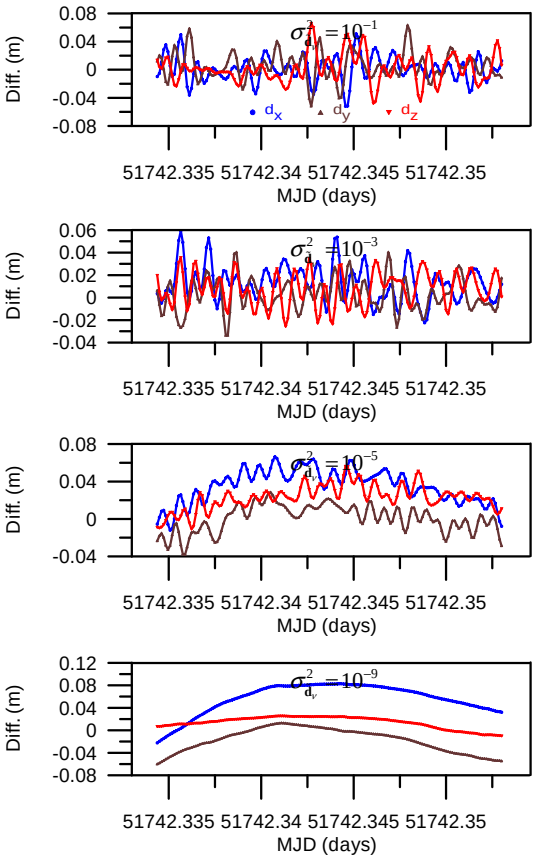

(a)

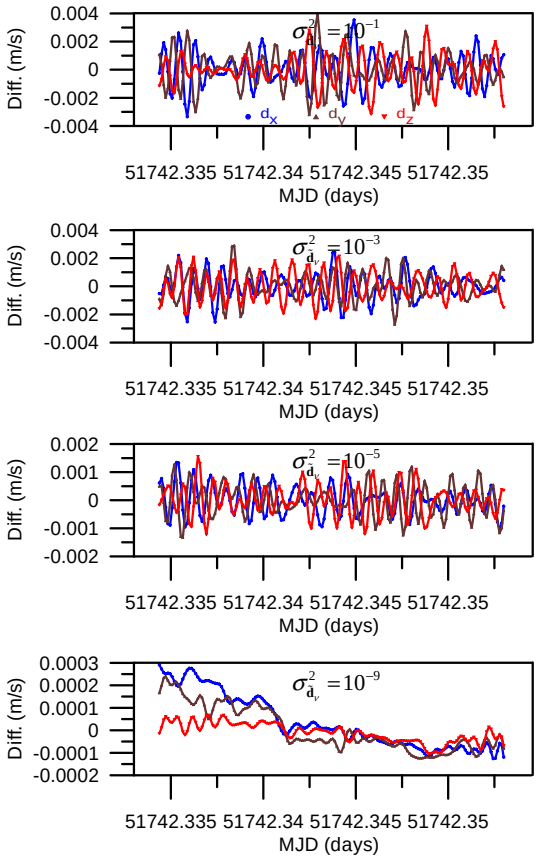

(b)

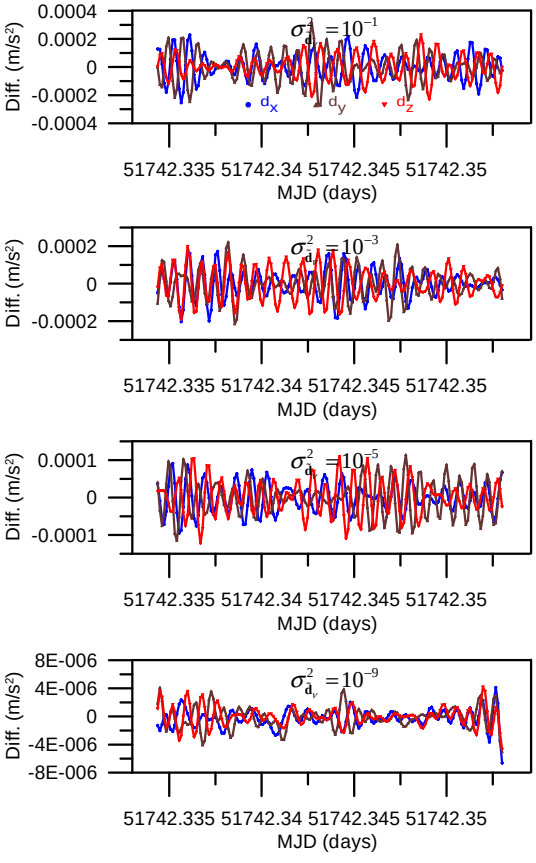

(c)

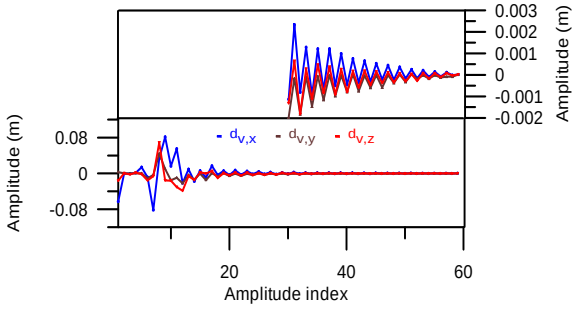

(d)

Figure 7.44: (a) Position differences (b) velocity differences (c) acceleration differences (d) Fourier spectrum (dynamical restriction index window [1-59], reference motion: *ellipse mode*, J_{max}=4, N_F =60, *white noise of* 5 *cm*, observation type: *Positions*, method: *flowchart Fig. 6.2*, observation sampling rate: *30 sec.*, test sampling rate: *10 sec.*, without $\approx$ 5% at boundaries $\equiv$ 9 points or 80 sec.).

RMS

$\sigma^2_{\ddot{d}_v}$	Pos.(m)	Vel.(m/s)	Acc.(m/s^2)
10^{-1}	0.033348	0.002076	0.000167
10^{-3}	0.029720	0.001674	0.000138
10^{-5}	0.049789	0.000932	0.000077
10^{-9}	0.070613	0.000166	0.000002

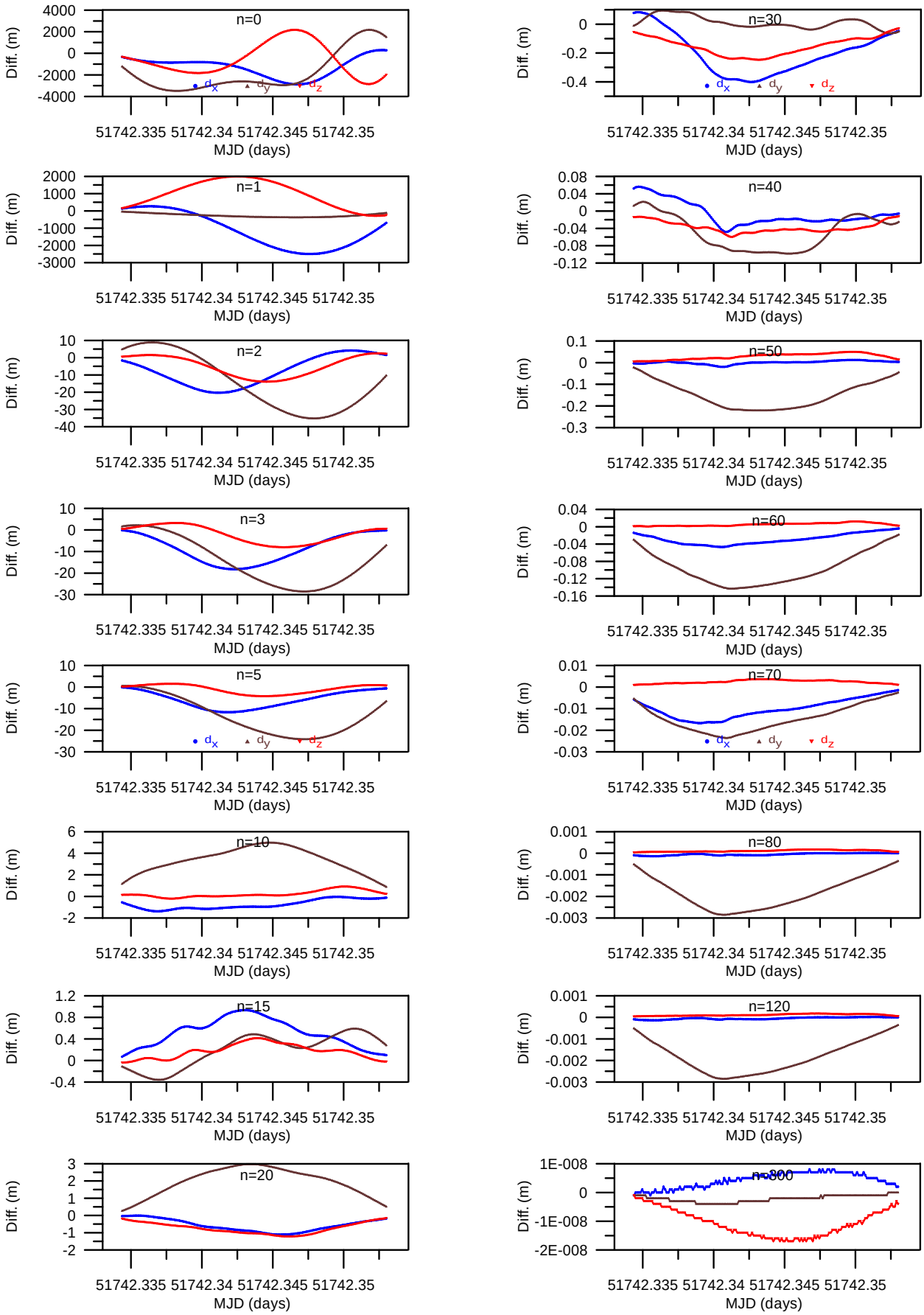

Figure 7.45: Difference between CHAMP dynamical orbit of different degree and order of the Earth gravity field and full CHAMP dynamical orbit with an Earth gravity field degree and order N_F=300 without $\approx 5\%$ at boundaries.

8. Discussion and Conclusions

In this dissertation, a new approach for the determination of satellite orbits based on densely and homogeneously distributed observations is presented. These observations are code pseudo-range and carrier phase measurements between a Low Earth Orbiter (LEO) and the satellites of any of the Global Navigation Satellite Systems (GNSS) such as GPS, GLONASS or in future GALILEO. The orbit determination is restricted to short arcs; the use of precise short arcs of low-flying satellites has been demonstrated recently to be the proper tool for various applications in Satellite Geodesy, especially for the determination of static and temporal gravity field models, based on the observations related to the new satellite gravity missions such as CHAMP and the twin satellite mission GRACE.

The approach investigated in this research is characterized by the fact that the satellite arcs are represented by a semi-analytical series. This kind of orbit representation not only allows to determine arbitrary functionals of the satellite's orbit, such as velocities and accelerations of the satellite, but it is also possible to use geometrical, kinematical, but also dynamical observations for the determination of the orbit parameters. The interpretation of the term "kinematical" is different from that what is usually understood by kinematical positioning in the context of GPS positioning methods. Here, the notion "kinematics" used as in physics which is defined as the theory of the motion of mass points and closely related to terms such as velocity and acceleration. While the definition of the term "geometrical" is reserved for the point-wise determination of positions by purely geometric observations. In that case, there is no connection between subsequent positions, and consequently, no information about the velocity or the acceleration of the satellite.

The orbit determination approach is based on the formulation of a boundary value problem to Newton-Euler's equation of motion, either as absolute or relative orbit, in form of an integral equation of Fredholm type. The solution of this integral equation is formulated as a function which consists of three parts: a first one describing a linear combination of the boundary position vectors (either a straight line or an ellipse connecting the end points of the arc or a dynamical reference orbit), a second one which consists of polynomials of Euler and Bernoulli type of various degrees and a third one consisting of a series of sine functions, described by an - in principle - infinite number of terms. Because of the limited number of observations in an orbit determination process, the number of parameters has to be restricted adequately, ensuring the envisaged accuracy. Theoretically, the series in terms of Euler and Bernoulli polynomials could completely represent the orbit in addition to the linear combination of the boundary vectors. But it turned out that this is not possible with sufficient numerical accuracy. Also, the sine series as the solution of the Fredholm integral equation could be used to represent the orbit in addition to the linear combination of the boundary vectors. This is possible also numerically by extending the upper summation index of the sine series to a sufficient high number. But in that case, there are not enough observations to determine a sufficient number of series terms, on the one hand, or the Gibb's effect is too large, if the summation index is selected corresponding to the number of equally distributed observations, on the other hand. A compromise is achieved by combining both representations. Because of the fact that the Euler-Bernoulli polynomial series are constructed such that its derivatives coincide up to a sufficient high degree with the number of derivatives of the satellite arc at the boundaries, the derivatives of the difference function becomes zero at the arc's boundaries and a smooth difference function results. This function can be represented by a very fast converging sine series with small resulting Gibb's effect at the arc boundaries, if periodically continued with the period of twice of the arc length.

Because of the close relation of the series coefficients with the force function model, the orbit determination can be designed as a pure dynamical but also as a pure kinematical orbit determination technique. If only weak dynamical restrictions are introduced in the adjustment process then a reduced kinematical orbit results. The series coefficients of this approximation function can be fixed by the adapted force function model and the boundary vectors can be determined as free parameters by fitting the observations in a best possible way representing a dynamical orbit. If all free parameters are determined completely by a least squares adjustment procedure then a kinematical orbit results. The observations are based on precise GNSS measurements of various types. GNSS provides accurate code pseudo-range and carrier phase observations that can be used to estimate the geometrical absolute positions of the LEOs.

In Chapter 1, the subject of orbit determination was introduced along with its applications especially in the field of Satellite Geodesy. Then the pre-requisites of the orbit determination were treated in Chapter 2, including some essentials of the GNSS, the reference systems and transformation issues as well as a discussion of various error sources of the GNSS point positioning.

In Chapter 3, some important aspects of the pre-processing of code pseudo-range and carrier phase GPS-SST observations were represented. Among various observation techniques to determine the LEO orbit, the GNSS observations especially the high-low GPS-SST observations play an important role. Among the GPS-SST observations, the code pseudo-range GPS-SST observations are frequently used to determine initial LEO orbits. Final improvements are performed based on high-low GPS-SST carrier phase observations. The code pseudo-range and carrier phase GPS-SST observations have to be cleaned from outliers and cycle slips, respectively. Therefore, the outliers in the code pseudo-range observations were screened using the majority-voting strategy, which was described in Sec. 3.1.2. With this method, the outliers in the code pseudo-range observations could be detected. It was found in this research that some of the low elevated GPS satellites show outliers, and it is recommended for the zero difference data processing mode if only GPS satellites with a sufficient high elevation are used. Therefore, a cut-off angle of 15° was applied to the GPS-SST processing procedure. The same screening algorithm can be applied for the subsequent time differenced carrier phase observations. In this case, the limiting criterion of the performance of the screening algorithm is the quality of the LEO absolute positions which are determined based on the code pseudo-range observations. Therefore, alternative observation combination techniques (described in Sec. 3.2.4) have to be used along with the screening algorithm to ensure the removal of the outliers (or cycle slips) in the carrier phase GPS-SST observations. In case of the GPS-SST data processing, proper observation weights have to be used in the adjustment. Different weighting methods were proposed in Sec. 3.3. The GPS-SST data weighting has to be based on geometrical or physical criteria, or both of them. One useful criterion is the weighting according to the zenith distance. Especially in case of the CHAMP and the GRACE satellites, SNR (Signal to Noise Ratio) values are given in RINEX format. Therefore, they can be used as a physical interpretation of the GPS signal strength of the GPS-SST observations. The geometrical and physical weighting methods show approximately the same results for the LEO precise orbit determination. Because of the dependency of the SNR values on the GPS receiver, their interpretation in case of CHAMP is difficult with respect to the geometrical criteria, e.g. based on the zenith distance. Therefore, in this research, only the zenith distance weighting method was used in the GPS-SST data processing.

In Chapter 4, the geometrical precise orbit determination strategy was discussed. In this method, only geometrical connections (in the sense of distances) between the GPS satellites and the LEOs are used to determine the position coordinates of the LEOs . With this approach, the absolute positions are determined point-wise based on the code pseudo-range and carrier phase observations. With the ionosphere-free code pseudo-range GPS-SST observations, the absolute positions are estimated with meter-accuracy. Improved LEO positions can be estimated based on the accurate carrier phase GPS-SST observations. If the correction models are applied to the observation equation then an accuracy of $2-3cm$ can be expected for low-flying satellites like CHAMP. From the various important key factors, the accuracy of the h-l GPS-SST carrier phase observations, the geometrical strength of the GPS satellites and the number of GPS satellites at every epoch are the most important pre-requisites to estimate successfully the geometrical orbit with high precision. From the different GPS-SST data processing techniques, the zero difference mode proved to be an efficient choice for the LEO precise orbit determination using only undifferenced GPS-SST observations. To externally validate and compare the estimated geometrical results, the PSO CHAMP dynamical orbit of the GFZ Potsdam and Švehla's CHAMP dynamical solution orbit were used. The geometrical results show systematic differences from both dynamical reference orbits. They can be interpreted as dynamical mis-modelings of the PSO orbits and Švehla's solution in the years 2002 and 2003 as described in Chapter 7.

In Chapter 5, various important theoretical and numerical features related to the representation of the short arc of the proposed integrated orbit determination approach were presented. The geometrically estimated LEO orbit is given point-wise; therefore there is no connection between subsequent positions, and consequently, no information about the velocity or even the acceleration of the LEO is available. To describe the time dependency of the satellite motion, the semi-analytical orbit representation based on the boundary positions, the Euler-Bernoulli polynomials and the residual sine series was used. The semi-analytical representation function is based on the reference motion (a straight line, an ellipse or a dynamical reference orbit)

of the LEO. It was found in this research that the type of reference motion is important for the size of the sine amplitudes, and also for the size of the remainder function of the approximate orbit representation. The accuracy of the LEO is much better when using the dynamically determined arc as reference motion than a straight line or an ellipse reference motion. Because of the fact that the computation of the dynamical reference LEO orbit is much more costly than the use of an ellipse reference motion, the ellipse reference motion was used as an acceptable compromise.

As already pointed out, the LEO arc can be represented by the reference motion and the Fourier series up to index n or by the reference motion and the Euler-Bernoulli polynomials up to an upper index J_{max}, or by a combination of them. For the representation of the LEO arc by the boundary positions and the Fourier series, it was shown that this combination causes large Gibb's effect at the arc boundaries in case of a low Fourier upper index. Due to the fact that there exists a functional dependency between the Fourier amplitudes and the Euler-Bernoulli coefficients, a series in terms of Euler-Bernoulli up to a sufficient high degree can be used to represent the LEO arc as well. It could be shown that the convergence of the Euler-Bernoulli polynomials requires a large upper index J_{max}. In the practical application, the Euler-Bernoulli series has to be limited because of stability problems by a rather low index J_{max}. But it was found that the orbit approximation of the series in terms of the Euler-Bernoulli polynomials is not better than a couple of centimeters in case of a maximum index $J_{max} = 4$. Both orbit representation can be used exclusively. Because of the disadvantages of both alternatives, a combined solution was proposed. A series in terms of Euler-Bernoulli polynomials has to be fitted to the geometrically determined arc with a reasonable upper degree $J_{max} = 4$, corresponding to sufficiently precise arc derivatives at the arc boundaries. In that case, the residual sine series shows a fast convergence and low residuals of the combined series when compared to the true ephemerides. Concluding it was proposed that the LEO short arc should be represented by the LEO arc boundary positions (connected by an ellipse), the Euler-Bernoulli polynomials up to degree $J_{max} = 4$ and a residual sine series up to a properly selected index $\bar{n}$.

In Chapter 6, the integrated kinematic-dynamic orbit determination approach was formulated explicitly as well as different determination algorithms. In this chapter, it was found that the determination of the kinematical or dynamical orbits (or any reduced-kinematical orbit modification) can be performed based on the positions, derived in a first preparation step by a geometrical precise orbit determination procedure, or directly by the carrier phase GPS-SST observations, together with observation specific corrections. Both observation types have to deliver the same results if the full variance-covariance information (with the correlation information between the points in case of positions as pseudo-observation) are used in both algorithms. The estimated kinematical orbit is not only a continuous approximation of the LEO orbit in a kinematical sense, but it is also a solution of Newton-Euler's equation of motion. If the LEO representation parameters are estimated by a least squares procedure only based on the carrier phase GPS-SST observations (or positions) without any dynamical information, then the LEO short arc is determined kinematically. By introducing dynamical information for the solution, a reduced-kinematical or a pure dynamical orbit determination can be realized. It was shown that a smooth transition from a kinematical orbit determination procedure to a dynamical orbit determination is possible by adding dynamical information (in the sense of Fourier amplitudes) together with its variance-covariance matrices to the observation equations. In other words, the estimated kinematical LEO short arc can be reduced with respect to the introduced dynamical information to the observation equation by loosing continuously the empirical orbit character.

In this research, two LEO short arc determination strategies were proposed. In a first step, the Euler-Bernoulli polynomial coefficients up to degree $J_{max} = 4$ were derived based on the geometrically determined positions or directly by the carrier phase GPS-SST observations together with its variance-covariance matrices. Because of the reduced approximation accuracy of the orbit by a series in terms of the Euler-Bernoulli polynomials up to a maximum degree $J_{max} = 4$, it is sufficient to determine the coefficients of the Euler-Bernoulli polynomials without correcting the boundary positions. Another possibility is to perform a least squares fit of the Fourier series to the (pseudo) observations to determine the Euler-Bernoulli coefficients from the Fourier series amplitudes. The coefficients of the Euler-Bernoulli coefficients differ slightly depending on the estimation procedure, but the differences can be compensated by the residual sine series. In other words, the Euler-Bernoulli estimation procedure in the first case is performed in the space domain, and in the second estimation procedure, it is performed in the spectral domain.

Chapter 7 was dedicated to test computations, partly based on CHAMP orbit information of the SC7 simulation data set, partly based on real CHAMP data provided by GFZ Potsdam. In this chapter, geometrical, kinematical, reduced-kinematical and dynamical precise orbit determination modifications were tested. To unify the simulated cases with the real ones, the GPS-SST observations were provided in the RINEX format. A 15° cut-off angle was used to avoid the processing of low elevated GPS satellites, and the zero difference GPS data processing mode was used for the orbit determination procedures.

It was found in the geometrical test computations of the real CHAMP data that the point-wise LEO orbit can be estimated based on the carrier phase GPS-SST observations with an accuracy of $2-3cm$. It should be mentioned that the geometrical strength of the GPS satellites, the accuracy of the GPS-SST observations, and the number of GPS satellites plays an important role in the GPS data processing, especially for the geometrical orbit determination procedure. In all real geometrical orbit determination cases, the trend reassessed RMS values with respect to PSO and Švehla's dynamical orbits are in the range of 1 to $2cm$, but the GPS-SST observation residuals show the smallest observation residuals. It should be mentioned that the geometrical orbit determination methods can not deliver directly the LEO kinematical parameters such as velocity and acceleration.

In Sec. 7.3.1, the kinematical orbit determination strategy was tested based on a 30 minute CHAMP short arc simulation scenario. Based on the results of the error-free simulation cases, it was concluded that the best case with minimal RMS values for ephemerides of positions, velocities and accelerations of 10 sec time difference based on observation series with a 30 sec sampling rate are achieved of using either GPS-SST observations directly or positions as pseudo observations indirectly by following the determination procedure as shown in the flowchart of Fig. 6.2. It is preferable to derive the Euler-Bernoulli series from the sine series coefficients, which are determined in a prior least squares adjustment step by simultaneous correcting the boundary values together with the sine coefficients.

If the observations (carrier phase GPS-SST observations or positions) are contaminated with white noise, two outcomes are of interest: first of all, the minimum RMS values for the positions, velocities and accelerations are not achieved for the so-called interpolation case (by extending the upper summation index of the sine series corresponding to the number of equi-distant observations) but for a much lower upper index, e.g. 30. Obviously, the restriction to a lower upper index acts as a filtering. Secondly, it was observed that the influence of white noise in the observations is reduced with the number of differentiations. While the RMS value for the positions is about four times larger for the noise case relative to the error-free case, for the accelerations this factor is reduced to only two, in case of an upper limit of the residual sine series of 30. Furthermore, it was noted that for an upper index of 59 (interpolation case), the RMS value represents a certain basic noise level which corresponds to the white noise level of the observations. These values can only be reduced by an additional filtering procedure, as it is realized in case of reducing the upper summation index to e.g. 30, but alternative filtering techniques might be even more successful.

The Gibb's effect in the kinematical orbit determination procedure can be reduced down to a level of the maximum orbit representation accuracy of approximately 1cm. It should be mentioned that in case of noisy observations, the Gibb's effect is not visible anymore in the residuals; already in case of an upper sine series index of 30 compared to the general errors in the orbit determination results as a consequence of the observations errors. In the error-free case the Gibb's effect is still clearly visible at the boundaries. In any case, it is useful to blank out the boundary regions in the size of 5% of the total arc length.

In Sec. 7.3.2, four examples of kinematical orbit determinations are discussed. All cases document the efficiency of the kinematical orbit determination strategy for the LEO short arcs. The results are more or less identical for the different upper indices of the residual sine series because of the large systematic derivations. The differences (bias and/or trend) between the results of the kinematical orbit determination and the PSO in the positions and velocities show (most probably) systematic mis-modeling effects of the dynamical CHAMP PSO orbits. Despite the large systematic differences in the positions and velocities, the small carrier phase observation residuals demonstrate the quality of the kinematical orbit determination procedure, so that the systematic deviations are caused mainly by the dynamical model used for the PSO orbits.

To show the flexibility of the proposed orbit determination strategy to vary between a kinematical orbit determination and a pure dynamical orbit determination by covering all levels of reduced-kinematical orbit determination cases, different simulation scenarios were tested in the error-free and error cases based on a 30 minute CHAMP short arc in Sec. 7.4. In the error-free case, no improvement of the orbit accuracy could be observed. In the error cases, an Earth gravity field up to degree and order 300 was used for the reduced-kinematical orbit determination. It represents a full and accurate dynamical information of the Earth gravity field at the altitude of the low-flying satellite.

The geometrical, kinematical, reduced-kinematical and dynamical precise orbit determination of low-flying satellites based on only high-low GPS-SST observations can be performed with sufficient accuracy. Further test with real data, based on the relative motion of the GRACE twin satellites, on Satellite Laser Ranging (SLR) data and altimetry cross-over tests are necessary. The proposed orbit determination strategy opens also new applications in the case of kinematical and dynamical observables in connection with satellite formation flight configurations.

List of Abbreviations

AC	**A**nalysis **C**enter	see Sec. 2.2
ANTEX	**ANT**enna **EX**change format	see Sec. 2.2
CCD	**C**harge **C**oupled **D**evice	see Sec. 1.3.1
CHAMP	**CHA**llenging **M**inisatellite **P**ayload	see Sec. 1.2.3
CNES	**C**entre **N**ational d'**E**tudes **S**patiales	see Sec. 1.3.1
DD	**D**ouble **D**ifference	see Sec. 4
DOD	**D**epartment **O**f **D**efense	see Sec. 2.1.1
DOP	**D**ilution **O**f **P**recision	see Sec. 4
DORIS	**D**oppler **O**rbitography and **R**adiopositioning **I**ntegrated by **S**atellite	see Sec. 1.3.1
DPOD	**D**ynamical **P**recise **O**rbit **D**etermination	see Sec. 6.2
EGM	**E**arth **G**ravitational **M**odel	see Sec. 7.4
EIGEN	**E**uropean **I**mproved **G**ravity model of the **E**arth by **N**ew techniques	see Sec. 1.2.3
ERP	**E**arth **R**otation **P**arameter	see Sec. 2.5
GFZ	**G**eo**F**orschung**Z**entrum	see Sec. 7.2.2
GLONASS	**G**lobal **N**avigation **S**atellite **S**ystem	see Sec. 8
GNSS	**G**lobal **N**avigation **S**atellite **S**ystem	see Sec. 2.1
GOCE	**G**ravity field and steady-state **O**cean **C**irculation **E**xplorer	see Sec. 1.2.3
GMM	**G**auss-**M**arkov **M**odel	see Sec. 4.2.3
GPOD	**G**eometrical **P**recise **O**rbit **D**etermination	see Sec. 4
GPS	**G**lobal **P**ositioning **S**ystem	see Sec. 2.1.1
GRACE	**G**ravity **R**ecovery **A**nd **C**limate **E**xperiment	see Sec. 1.2.3
ICRF	**I**nternational **C**elestial **R**eference **F**rame	see Sec. 2.4.4
IERS	**I**nternational **E**arth **R**otation **S**ervice	see Sec. 2.4.5
IAG	**I**nternational **A**ssociation of **G**eodesy	see Sec. 7.1.1
IGG	**I**nstitute for **G**eodesy and **G**eoinformation at university of Bonn	see Sec. 7.2.2
IGS	**I**nternational **G**NSS **S**ervice	see Sec. 2.2
ITRF	**I**nternational **T**errestrial **R**eference **F**rame	see Sec. 2.4.4
JPL	**J**et **P**ropulsion **L**aboratory	see Sec. 2.7.5
KPOD	**K**inematical **P**recise **O**rbit **D**etermination	see Sec. 6.1
LC	**L**inear **C**ombination	see Sec. 3.2.4
LEO	**L**ow **E**arth **O**rbiter	see Sec. 4
LOS	**L**ine **O**f **S**ight	see Sec. 3.3.5
LS	**L**east **S**quares	see Sec. 4.2.3
MEO	**M**edium **E**arth **O**rbiter	see Sec. 2.1.1
POD	**P**recise **O**rbit **D**etermination	see Sec. 2.1.1
PPP(3P)	**P**recise **P**oint **P**ositioning	see Sec. 4
PRARE	**P**recise **R**ange **A**nd **R**ange rate **E**quipment	see Sec. 1.3.1
PSO	**P**ost-processed **S**cience **O**rbit	see Sec. 7.2.2
RKPOD	**R**educed-**K**inematical **P**recise **O**rbit **D**etermination	see Sec. 6.2
RINEX	**R**eceiver **IN**dependent **EX**change format	see Sec. 7.1.2
SC7	**S**pecial **C**ommission **7** of IAG	see Sec. 7.1.1
SCA	**S**tar **C**amera **A**ssembly	see Sec. 2.7.6.2
SD	**S**ingle **D**ifference	see Sec. 4.1
SGG	**S**atellite **G**ravity **G**radiometry	see Sec. 1.2.3
SGPS	**S**paceborne **G**lobal **P**ositioning **S**ystem	see Sec. 4.1
SLR	**S**atellite **L**aser **R**anging	see Sec. 1.3.1
SNR	**S**ignal to **N**oise **R**atio	see Sec. 3.3.3
SP3	**S**tandard **P**roduct **3**	see Sec. 2.7.5
SPP	**S**tandard **P**oint **P**ositioning	see Sec. 4.1
SST	**S**atellite-to-**S**atellite **T**racking	see Sec. 1.2.3
SVN	**S**atellite **V**ehicle **N**umber	see Sec. 2.1.1
TD	**T**riple **D**ifference	see Sec. 4
TUM	**T**echnical **U**niversity **M**unich	see Sec. 1.2.3
VLBI	**V**ery **L**ong **B**aseline **I**nterferometry	see Sec. 2.3
WGS84	**W**orld **G**eodetic **S**ystem **84**	see Sec. 2.4.5.2
ZD	**Z**ero **D**ifference	see Sec. 4

List of Figures

List of Tables

References

Abramowitz, M. and I.A. Stegun (1972) *Handbook of Mathematical Functions with Formulas, Graphs, and Mathematical Tables*. Dover Publications Inc.

Ashby, N. (2003) Relativity in the Global Positioning System. *Living Rev. Relativity*, Vol. 6, No. 1.

Balmino, G., C. Reigber and B. Moynot (1976) A Geopotential Model Determined from Recent Satellite Observation Campaigns (GRIM1). *manuscripta geodaetica*, Vol. 1:41–69.

Bancroft, S. (1985) An algebraic solution for the GPS equations. *IEEE Transactions on Aerospace and Electronic Systems AES*, Vol. 21, No. 7:56–59.

Bassiri, S. and A. Hajj (1992) Higher order ionospheric effects on the Global Positioning System observables and means of modeling them. *manuscripta geodaetica*, Vol. 18:280–290.

Bastos, L. and H. Landau (1988) Fixing cycle slips in dual frequency kinematic GPS-applications using kalman filtering. *manuscripta geodaetica*, Vol. 13, No. 4:249–256.

Beutler, G. (2005) *Methods of Celestial Mechanics Vol II, Application to Planetary System, Geodynamic and Satellite Geodesy*. Springer Verlag Berlin Heidelberg.

Beutler, G., A. Jäggi, U. Hugentobler and L. Mervart (2006) Efficient satellite orbit modelling using pseudo-stochastic parameters. *Journal of Geodesy*, Vol. 80, No. 7:353–372.

Birmingham, W. P., B. L. Miller and W. L. Stein (1983) Experimental results of using the GPS for LANDSAT 4 onboard navigation. *ION Meeting Proceedings*, National Aerospace Meeting Proceedings.

Bisnath, S.B. (2000) Efficient, automated cycle-slip correction of dual-frequency kinematic GPS data. *Geodetic Research Laboratory, Department of Geodesy and Geomatics Engineering, University of New Brunswick*.

Bisnath, S.B. (2004) *Precise Orbit Determination of Low Earth Orbiters with a Single GPS Receiver-Based, Geometric Strategy*. Dissertation, Department of Geodesy and Geomatics Engineering, Technical Report No. 220, University of New Brunswick, Fredericton, New Brunswick, Canada.

Bjerhammar, A. (1967) *On the energy integral for satellites*. Dissertation, Royal Institute of Technology, Stockholm, Sweden.

Blewitt, G. (1990) An automatic editing algorithm for GPS data. *Geophysical Research Letters*, Vol. 17, No. 3:199–202.

Bock, H. (2003) *Efficient Methods for Determining Precise Orbits for Low Earth Orbiters Using the Global Positioning System (GPS)*. Dissertation, Astronomisches Institut, University of Bern, Schwitzerland.

Bock, H., U. Hugentobler, T.A. Springer and G. Beutler (2002) Efficient Precise Orbit Determination of LEO Satellites using GPS. *Advances in Space Research*, Vol. 30, No. 2:295–300(6).

Braasch, M.S. and A.J. Dierendonck (1999) GPS receiver architectures and Measurements. *Proc. IEEE*, Vol. 87, No. 1:48–64.

Byun, S. H. (2003) Satellite orbit determination using triple-differenced GPS carrier phase in pure kinematic mode. *Journal of Geodesy*, Vol. 76, No. 9-10:569–585.

Carslaw, H.S. (1930) *Introduction to the theory of Fourier's series and integrals*. Third Edition, New York: Dover Publications Inc., Chapter IX.

Collins, J.P. and R.B. Langley (1999) Possible Weighting Schemes for GPS carrier phase observations in the presence of multipath. Technical Report, Department of Geodesy and Geomatics Engineering, University of New Brunswick.

Földvary, l., d. Švehla, c. Gerlach, m. Wermuth, t. Gruber, r. Rummel, m. Rothacher, b. Frommknecht, t. Peters and p. Steigenberger (2004) Gravity model TUM-2sp based on the energy balance approach and kinematic CHAMP orbits. Earth Observation with CHAMP - Results from Three Years in Orbit. *Reigber Ch., H. Lühr, P. Schwintzer, J. Wickert (Eds.) ISBN: 3-540-22804-7 Springer*, 13–18.

Fricke, W., H. Schwan and T. Lederle (1988) (in collaboration with U. Bastian, R. Bien, G. Burkhardt, B. du Mont, R. Hering, R. Jährling, H. Jahreiss, S. Roeser, H.M. Schwerdtfeger and H.G. Walter) Fifth Fundamental Catalogue (FK5), Part I. The Basic Fundamental Stars. *Veroeff. Astron. Rechen-Institut Heidelberg*, No. 32.

Gao, Y. and Z. Li (1999) Cycle slip detection and ambiguity resolution algorithms for dual-frequency GPS data processing. *Marine Geodesy*, Vol. 22, No. 3:169–181.

Gao, Y. and X. Shen (2002) A new method for carrier-phase-based precise point positioning. *Journal of Navigation*, Vol. 49, No. 2:109–116.

Gao, Y. and A. Wojciechowski (2004) High Precision Kinematical Positioning Using Single Dual Frequency GPS Receiver. *International Archives of Photogrammetry Remote Sensing and Spatial Information Sciences*, Vol. XXXV-B3:845–850.

Gerlach, C., L. Földvary, D. Švehla, T. Gruber, M. Wermuth, N. Sneeuw, B. Frommknecht, H. Oberndorfer, T. Peters, M. Rothacher, R. Rummel and P. Steigenberger (2003) A CHAMP-only gravity field model from kinematic orbits using the energy integral. *Geophys. Res. Lett.*, Vol. 30, No. 20, 2037, DOI:10.1029/ 2003GL018025.

Goad, C.C. (1988) Investigation of an Alternate Method of Processing Global Positioning Survey Data Collected in Kinematic Mode. In:. *Lecture Note in Earth Science, 19, GPS Technique Applied to Geodesy and Surveying, E. Groten, R. Strauss (Hrsg.), Springer Verlag Berlin / Heidelberg*, Vol. 19, DOI 10.1007/BFb0011315:93–106.

Grejner-Brzezinska, D.A., C.K. Shum and J.H. Kwon (2002) A practical algorithm for LEO orbit determination. *Journal of Navigation*, Vol. 49, No. 3:127–135.

Herring, T.A. (1992) Modeling Atmospheric Delays in the Analysis of Space Geodetic Data. In: *Proceedings of Symposium on Refraction of Transatmospheric Signals in Geodesy, (Eds. de Munck, J.C. and Spoelstra, T.A.), pp. 4487–4499.*

Hofmann-Wellenhof, B., H. Lichtenegger and J. Collins (2001) *GPS - Theory and Practice.* Springer Verlag New York Inc.

Hugentobler, U., S. Schär and P. Fridez (2001) Bernese GPS-Software, Version 4.2. *Astronomical Institute, University of Berne.*

IGS (2008) International GNSS Service (IGS). Technical Report, NASA–http://igscb.jpl.nasa.gov/.

Ilk, K.H. (1972) Zur vorläufigen Bahnbestimmung künstlicher Erdsatelliten. Technical Report, Forschungsbericht W 72-16, Weltraumforschung, Bundesministeriums für Bildung und Wissenschaft, Institut für Astronomische und Physikalische Geodäsie der Techni-schen Universität München, München.

Ilk, K.H. (1973) Bahnbestimmung aus Richtungs-und Entfernungsmessungen künstlicher Erdsatelliten als Randwertaufgabe. Technical Report, Veröff. Bayer. Kommission Int. Erdmess. S.27 ff, München.

Ilk, K.H. (1976) *Berechnungvon Referenzbahnen durch Lösung selbstadjungierter Randwertaufgaben.* Dissertation, Deutsche Geodätische Kommission bei der Bayrischen Akademie der Wissenschaften, Dissertationen, Reihe C, Heft Nr.228.

Ilk, K.H. (1977) Vermittelnde Ausgleichung und Kollokation. Technical Report, Die Arbeiten des Sonderforschungsbereiches 78 Satellitengeodäsie der Technischen Universität München im Jahr 1976, Veröffentlichungen der Bayerischen Kommission für die Internationale Erdmessung der Bayerischen Akademie der Wissenschaften, Heft Nr. 36., München.

Ilk, K.H. (1983a) *Ein Beitrag zur Dynamik ausgedehnter Körper-Gravitationwechselwirkung.* Dissertation, Band 288 der Reihe C. Deutsche Geodätische Kommission, München.

Ilk, K.H. (2007) Bezugssysteme und Bezugsrahmen, Rotation der Erde. PDF file, *http : //www.geod.uni − bonn.de/apmg/pdf$_d$oc/7$_R$otationErde.pdf*.

Ilk, K.H., R. Rummel and M. Thalhammer (1995) Refined Method for the Regional Recovery from GPS/SST and SGG, CIGAR III/2. Technical Report, ESA contract No. 10713/93/F/FL, European Space Agency.

Ilk, K.H., M. Feuchtinger and T. Mayer-Gürr (2003) Gravity Field Recovery and Validation by Analysis of Short Arcs of a Satellite-to-Satellite Tracking Experiment as CHAMP and GRACE. In: *F. Sansó (ed.) A Window on the Future of Geodesy, IUGG General Assembly 2003, Sapporo, Japan, International Association of Geodesy Symposia, Vol. 128, pp. 189-194, Springer Verlag Berlin.*

Jäggi, A., U. Hugentobler and G. Beutler (2006) Pseudo-Stochastic Orbit Modeling Techniques for Low-Earth Orbiters. *Journal of Geodesy*, Vol. 80, No. 1:47–60.

Jekeli, C. (1999) The determination of gravitational potential differences from satellite-to-satellite tracking. Technical Report, Celestial Mechan-ics and Dynamical Astronomy 7582:85-100.

Kaula, W. M. (2000) *Theory of Satellite Geodesy: Applications of Satellites to Geodesy.* Dover ed., USA.

Kleusberg, A. and P.J.G. Teunissen (1998) *GPS for geodesy.* Springer Verlag Berlin.

Klose, U. (1985) Beiträge Zur Lösung Einer Integralgleichung vom HAMMERSTEINschen Typ. Diplomarbeit, Mathematisches Institut, Technische Universität München, München.

Kouba, J. and P. Heroux (2001) Precise Point Positioning Using IGS Orbit and Clock Products. *GPS Solutions*, Vol. 5, No. 2:12–28.

Kovalevsky, J. and I.I. Müller (1981) IAU Colloquium No. 56, Reference Coordinate Systems for Earth Dynamics. *ed. E.M. Gaposchkin and B. Kolaczek: (D. Reidel Publishing Co., Dordrecht, Holland), 375.*

Kovalevsky, J. and I.I. Müller (1989) Reference Frames in Astronomy and Geophysics. *J. Kovalevsky, I.I. Müller and B. Kolaczek (eds.), Kluwer Acad. Publ., 1.*

Langley, R.B. (1997) GPS Receiver System Noise. *GPS World*, Vol. 8, No. 6:40–45.

Leick, A. (1995) *GPS Satellite Surveying.* Wiley & Sons, USA.

Mayer-Gürr, T. (2006) *Gravitationsfeldbestimmung aus der Analyse kurzer Bahnbögen am Beispiel der Satellitenmission CHAMP und GRACE.* Dissertation, Institut für Geodäsie und Geoinformation, Bonn Universität, Deustchland.

McCarthy, D.D. and G. Petit (2003) IERS Technical Note 32, IERS Convetions. Technical Report, U.S Naval Observatory and Bureau International des Poids et Mesures.

Melbourne, W.G., B.D. Tapley and T.P. Yunck (1994) The GPS flight experiment on TOPEX/POSEIDON. *Geophysical Research Letters*, Vol. 21, No. 19:2171–2174.

Montenbruck, O. and E. Gill (2000) *Satellite Orbits. Models, Methods and Applications.* Springer Verlag Berlin.

Moritz, H. and I. Müller (1987) *Earth Rotation - Theory and Observation.* The Ungar Publishing Company, New York, ISBN 0-8044-4671-7, 617 S.

O'Keefe, J.A. (1960) Determination of the Earth's Gravitational Filed. *Space Research 1*, 448–457.

Parkinson, B.W. (1996) *Global Positioning System: Theory and Applications, chap. 1: Introduction and Heritage of NAVSTAR, the Global Positioning System. pp. 3-28.* American Institute of Aeronautics and Astronautics, Washington, D.C.

Reigber, C. (1969) *Zur Bestimmung des Gravitationsfeldes der Erde aus Satellitenbeobachtungen.* Dissertation, DGK, Reihe C, Heft Nr. 137, München.

Reigber, C. (1989) *Gravity field recovery from satellite tracking data.* Springer Verlag Berlin / Heidelberg.

Reigber, C., G. Balmino, P. Schwintzer, R. Biancale, A. Bode, J.M. Lemoine, R. Koenig, S. Loyer, H. Neumayer, J.C. Marty, F. Barthelmes, F. Perosanz and S.Y. Zhu (2003a) Global Gravity Field Recovery Using Solely GPS Tracking and Accelerometer Data from CHAMP. *Space Science Reviews*, Vol. 29:55–66.

Reigber, C., P. Schwintzer, K.H. Neumayer, F. Barthelmes, R. König, C. Förste, G. Balmino, R. Biancale, J.M. Lemoine, S. Loyer, S. Bruinsma, F. Perosanz and T. Fayard (2003b) The CHAMP-only Earth Gravity Field Model EIGEN-2. *Advances in Space Research*, Vol.31, No. 8:1883–1888, DOI: 10.1016/S0273–1177(03)00162–5.

Reigber, C., G. Balmino, P. Schwintzer, R. Biancale, A. Bode, J.M. Lemoine, R. König, S. Loyer, H. Neumayer, J.C. Marty, F. Barthelmes, F. Perosanz and S. Y. Zhu (2003c) Global gravity field recovery using solely GPS tracking and accelerometer data from CHAMP. *Space science reviews*, Vol. 108, No.1:55–66.

Remondi, B.W. (1984) *Using The Global Positioning System (GPS) Phase Observable for Relative Geodesy Modelling.* Processing and Results Ph.D.Thesis, The University of Texas at AUSTIN.

Reubelt, T., G. Austen and E.W. Grafarend (2003) Harmonic analysis of the Earth's gravitational field by means of semi-continuous ephemerides of a low Earth orbiting GPS-tracked satellite. Case study: CHAMP. *Journal of Geodesy*, Vol. 77, No. 5-6:257–278.

Rim, H.J. and B.E. Schutz (2002) Precise Orbit Determination (POD). Technical Report, Geo-science Laser Altimeter System(GLAS) Project, Algorithm Theoretical Basic Document Version 2.2.

Rothacher, M., S. Schaer, G. Beutler, W. Schlueter and H. O. Hase (1996) Phase Center Variations of GPS Antennas Derived From GPS Observations of Specially Designed Calibration Campaigns. In: *Supplement to EOS, American Geophysical Union, Spring Meeting, May 20-24, Baltimore, Mayland, AGU, 77, April 23, 17, G11A-6.*

Rothacher, M., T. Springer, S. Schaer and G. Beutler (1998) Processing Strategies for Regional GPS Networks. In: *International Association of Geodesy Symposia Advances in Positioning and Refernce Frames, Brunner, F., 93-100, Springer Verlag Berlin-Heidelberg.*

Schneider, M. (1968) *A General Method of Orbit Determination.* Dissertation, Library Translation, Band 1279, Royal Aircraft Establishment, Ministry of Technology, Farnborough, England.

Schneider, M. (1984) Observation equations based on expansions into eigenfunctions. *manuscripta geodaetica*, Vol. 9:169–208.

Schneider, M. (1992) *Himmelsmechanik, 4 Bde., Bd.1, Grundlagen.* Spektrum Akademischer Verlag.

Schneider, M. (1993) *Himmelsmechanik, 4 Bde., Bd.2, Systemmodelle.* Spektrum Akademischer Verlag.

Schneider, M. (1997) *Satellitengeodäsie.* Wiley-VCH.

Schneider, M. (2002a) *Himmelsmechanik, 4 Bde., Bd.3, Gravitationstheorie.* Spektrum Akademischer Verlag.

Schneider, M. (2002b) *Himmelsmechanik, 4 Bde., Bd.4, Theorie der Satellitenbewegung, Bahnbestimmung.* Spektrum Akademischer Verlag.

Seeber, G. (2003) *Satellite Geodesy, second edition.* Walter de Gruyter, Berlin, New York.

Seidelmann, P. K. (1980) IAU Theory of Nutation 1980 : The final report of the IAU Working Group on Nutation. Technical Report, U.S. Naval Observatory, Nautical Almanac Office, 20390 Washington, D.C., U.S.A.

Seidelmann, P. K. (1992) *Explanatory Supplement to the Astronomical Almanac.* Mill Valley.

Strang, G. and K. Borre (1997) *Linear Algebra, geodesy and GPS.* Wellwsley-Cambridge Press.

Teunissen, P.J.G., N.F. Jonkmann and C.C.J.M. Tiberius (1998) Weighting GPS dual frequency observations: Bearing the cross of cross-correlation. *GPS Solutions*, Vol. 2, No. 2:28–37.

Tiberius, C., N. Jonkmann and F. Kenselaar (1999) The stochastics of GPS observables. *GPS World*, Vol. 10, No. 2.

Van der Marel, H. (2003) GPS Data Processing Lecture notes. TU Delft, Netherlands.

Visser, P. N. A. M., N. Sneeuw and C. Gerlach (2003) Energy integral method for gravity field determination from satellite orbit coordinates. *Journal of Geodesy*, Vol. 77, No. 3-4:207–216, DOI 10.1007/s00190–003–0315–8.

Švehla, D. and M. Rothacher (2002) Kinematic Orbit Determination of LEOs Based on Zero or Double Difference Algorithms Using Simulated and Real SST Data. *Vistas for Geodesy in the New Millenium, Springer Verlag*, Vol. 125:322–328.

Švehla, D. and M. Rothacher (2003) CHAMP double difference kinematic POD with ambiguity resolution. In: *First CHAMP Science Meeting, Potsdam, Germany.*

Wells, D.E., N. Beck, D. Delikaraoglou, A. Kleusberg, E.J. Krakiwsky, G. Lachapelkle, R.B. Langley, M. Nakiboglu, K.P. Schwarz, J.M. Tranquilla and P. Vaníček (1987) *Guide to GPS Positioning.* Canadian GPS Associates, Fredericton, New Brunswick, Canada, 2nd. edition.

Wuebbenna, G., A. Bagge and M. Schmitz (2001) RTK Networks based on Geo++ GNSMART-Concepts, Implementation, Results. In: *ION GPS-2001.*

Xu, G. (2007) *GPS. Theory, Algorithms and Applications.* Springer Verlag Berlin, 2nd edition.

In der Schriftenreihe des Instituts für Geodäsie und Geoinformation
der Rheinischen Friedrich-Wilhelms-Universität Bonn sind erschienen:

Heft 14 2008	Akbar Shabanloui A New Approach for a Kinematic-Dynamic Determination of Low Satellite Orbits Based on GNSS Observations
Heft 13 2008	Frank Friesecke Stadtumbau im Konsens!? Zur Leistungsfähigkeit und Fortentwicklung des städtebaulichen Instrumentariums unter Schrumpfungsbedingungen
Heft 12 2008	Heinz Rütz Zur Kostenanalyse der privaten Umlegung als Teil der konsensualen integrierten Baulandentwicklung
Heft 11 2008	Gaby Alexandra Boele-Keimer Kommunales Kennzahlenmanagement am Beispiel von Vermessungs- und Katasterämtern in Nordrhein-Westfalen
Heft 10 2008	Annette Eicker Gravity Field Refinement by Radial Basis Functions
Heft 9 2008	Torsten Mayer-Gürr Gravitationsfeldbestimmung aus der Analyse kurzer Bahnbögen
Heft 8 2008	Boris Kargoll On the Theory and Application of Model Misspecification Tests
Heft 7 2008	Hamza Alkhatib On Monte Carlo Methods
Heft 6 2008	Klaus Borchard Annäherungen an Städtebau und Raumentwicklung
Heft 5 2008	Jens Jähnke Zur Teilmarktbildung beim Landerwerb der öffentlichen Hand
Heft 4 2008	Atef Abd-Elhakee Makhloof The Use of Topographic Isostatic Mass Information
Heft 3 2008	Markus Vennebusch Singular Value Decomposition and Cluster Analysis
Heft 2 2007	Christian Beder Grouping Uncertain Oriented Projective Geometric Entities
Heft 1 2007	Klaus Börger Geodäsie und Quantenphysik

Vertrieb: Rheinische Friedrich-Wilhelms-Universität Bonn
Institut für Geodäsie und Geoinformation
· Bibliothek ·
Nußallee 17
53115 Bonn

Tel.: +49 (0)228 73-3566
Fax: +49 (0)228 73-2988

Internet: http://www.igg.uni-bonn.de

ISSN 1864-1113